SÉRGIO JOSÉ COELHO DO CARMO

STUDIES ON LOW-ENERGY
PARTICLE-INDUCED SOFT X-RAY EMISSION

· U **C** ·

UNIVERSIDADE DE COIMBRA

2010

SÉRGIO JOSÉ COELHO DO CARMO

STUDIES ON LOW-ENERGY
PARTICLE-INDUCED SOFT X-RAY EMISSION

ESTUDOS SOBRE A EMISSÃO DE RAIOS X DE BAIXA ENERGIA
INDUZIDOS POR PARTÍCULAS DE BAIXA ENERGIA

SUPERVISOR: PROFESSOR DOCTOR FILIPA ISABEL GOUVEIA DE MELO BORGES BELO SOARES

CO-SUPERVISOR: PROFESSOR DOCTOR CARLOS ALBERTO NABAIS CONDE

Dissertation submitted to the Faculty of Sciences and Technology of the University of
Coimbra for the obtention of the degree of Doctor of Philosophy in Physics

FCTUC

2010

Aos meus pais,
por todos os sacrifícios que fizeram por mim

AGRADECIMENTOS

Agora no final de quatro anos de trabalho, não posso de modo algum deixar de agradecer neste momento tão especial para mim a todos aqueles que contribuíram de alguma forma para o bom termo desta dissertação.

Em primeiro lugar, gostaria de agradecer à Professora Doutora Filipa Isabel Gouveia de Melo Borges Belo Soares e ao Professor Doutor Carlos Alberto Nabais Conde, respectivamente orientadora e co-orientador desta tese, pela oportunidade que me deram e pelos ensinamentos transmitidos. Estou grato pelos inúmeros conselhos, pela constante disponibilidade, assim como pela confiança demonstrada durante a realização dos trabalhos. Estas poucas palavras são demasiado "simplistas" para exprimir o meu agradecimento que vai além do contexto da supervisão científica: penso que a nossa colaboração não pode, nem deve, acabar com esta dissertação.

O meu obrigado ao Professor Paul Indelicato por me ter recebido nas instalações do seu laboratório. Agradeço a oportunidade de poder explorar uma área de investigação diferente.

Cabe-me igualmente agradecer à Doutora Teresa Dias e à Doutora Filomena Santos pela ajuda diária.

Agradeço aos meus colegas de laboratório Liliana Carita, Pedro Neves, Ana Conceição, Fernando Amaro, Alexandre Trindade, José Escada e Luís Coelho o apoio diário: partilhámos muito mais do que um local de trabalho.

Ao Augusto Cordeiro e ao Carlos Carvalho, agradeço a disponibilidade e a competência na elaboração dos vários componentes, mas sobretudo a paciência demonstrada ao "aturar-me" (e eu sei que não foi fácil!).

Por último, e não sendo por isso menos sentido (antes pelo contrário!), um agradecimento muito especial vai para à minha tia Madalena e para a minha tia Fernanda pela constante preocupação demonstrada desde o primeiro dia em que vim viver para Portugal. A ambas, o meu eterno obrigado.

RESUMO

A emissão de raios X induzidos por partículas (Particle-Induced X-ray emission - PIXE) é uma técnica analítica utilizada para determinar quantitativamente concentrações de elementos residuais com uma sensibilidade invejável. Esta ferramenta de análise multi-elementar mostrou ser particularmente bem sucedida num grande número de aplicações em diversas áreas desde arqueologia, biologia, medicina às ciências ambientais.

Entre estas aplicações podemos igualmente referir a análise de superfícies de materiais utilizando iões de baixa velocidade devido ao seu alcance reduzido em sólidos (até centenas de nanómetros). No entanto, para esta aplicação em particular, a falta de secções eficazes de produção de raios X para partículas incidentes de baixa energia limita a precisão da análise PIXE de baixa energia.

Neste trabalho, um acelerador de partículas recentemente construído foi estudado, caracterizado, melhorado e utilizado em conjunto com um sistema experimental PIXE, desenvolvido por nós, para determinar secções eficazes de produção de raios X induzidos por protões de baixa energia de 10 a 50 keV.

Na altura em que começámos os trabalhos descritos na presente dissertação, o acelerador de partículas estava numa fase muito precoce. Consequentemente, tivemos de implementar várias melhorias antes de o utilizar para irradiar amostras e realizar os estudos planeados. Estas melhorias incidiram na fonte de iões, na aceleração dos iões, na caracterização do feixe e em diversos componentes da câmara de reacções.

Além disso, também desenvolvemos um sistema de detecção de raios X baseado num Contador Gasoso de Cintilação Proporcional, CGCP, para adquirir os espectros PIXE. Este detector foi optimizado para a detecção dos raios X de baixa energia induzidos pela interacção dos iões acelerados com alvos de elementos leves e foi também adaptado para o sistema experimental PIXE desenvolvido. O detector de raios X teve de preencher alguns requisitos para esta aplicação particular, nomeadamente a detecção de raios X até algumas centenas de eV e a necessidade de ter uma grande área de detecção devido às reduzidas secções eficazes de produção de raios X envolvidas. Por estas razões, decidimos equipar este CGCP com uma grelha elipsoidal, ao invés de uma planar, para delimitar as regiões de absorção e de cintilação de modo a melhorar o seu desempenho para grandes áreas de detecção. Também considerámos encher este CGCP com misturas de Ar-Xe em vez de Xe puro para reduzir a perda de electrões primários para a janela do detector, resultante dos comprimentos de absorção reduzidos envolvidos

na detecção de raios X de baixa energia, e a consequente deterioração do desempenho do detector.

Demonstrámos que o uso da técnica da grelha elipsoidal com misturas Ar-Xe como meio de detecção permite boa compensação para todas as misturas estudadas tanto em relação à resolução em energia como ao ganho do detector. Por exemplo, para a mistura 80%Ar-20%Xe, quando o diâmetro da janela de radiação do detector aumenta de 2 até 38 mm a resolução em energia deteriora-se de 7.8% para 9.5% ao utilizar a grelha elipsoidal enquanto se verifica uma deterioração até 11.5% com uma grelha planar convencional. Da mesma forma, o ganho do detector diminui 2% com o aumento do diâmetro da janela ao utilizar uma grelha elipsoidal e 4 % com uma grelha planar. Um estudo sistemático do desempenho do detector mostrou que as melhores condições de operação dependem da composição da mistura gasosa.

As misturas de Ar-Xe estudadas foram caracterizadas em termos do seu rendimento de electroluminescência, dos limiares de excitação e ionização, dos valores w e dos factores de Fano. O desempenho do detector foi avaliado em termos do seu ganho, da sua resolução em energia e da relação pico-vale (Peak to Valley Ratio - PVR). As misturas Ar-Xe demonstraram apresentar resoluções em energia similares às obtidas com Xe puro, excepto para a gama dos 250-630 eV como já era de esperar, e apresentam melhores factores de Fano para misturas com concentrações de xénon inferiores a 10 %. Por exemplo, resoluções em energia de 17,5% foram obtidos com misturas de 95%Ar-5%Xe ou 90%Ar-10%Xe para raios X de 1.2 keV, enquanto um valor de 16,9% foi alcançado com Xe puro. Além disso, o PVR melhora por um factor de 2 ou 3 com o aumento da concentração de Ar. Foi demonstrado que as misturas de Ar-Xe são uma boa alternativa ao Xe puro como gás de enchimento de CGCP.

O CGCP desenvolvido foi também utilizado para realizar outro trabalho complemente distinto, nomeadamente um estudo da cintilação primária induzida por raios X em Xe gasoso à pressão atmosférica. Nestes estudos, detectámos a luz de cintilação primária produzida por raios X de 5.9 keV absorvidos em Xe puro e quantificámos a sua intensidade comparando o seu sinal com o do rendimento de luz de cintilação secundária através de uma técnica desenvolvida por nós. Estes estudos revelaram que a energia média necessária para originar um fotão de cintilação primária em Xe gasoso à pressão atmosférica é igual a 111 ± 16 eV.

Uma vez concluídos estes estudos relativos ao acelerador de partículas e ao sistema de detecção de raios X, realizámos alguns estudos preliminares de PIXE. Começámos por estudar a influência de alguns parâmetros do sistema experimental durante irradiações com o intuito de optimizar o desempenho geral do sistema. Posteriormente, obtivemos alguns resultados de secções eficazes produção de raios X ao irradiar alvos espessos de alumínio, através da determinação da curva de rendimento de alvo espesso. Determinámos secções eficazes de produção de raios X em alumínio de 8.43×10^{-4}, 1.30×10^{-3} e 1.81×10^{-3} barn para protões de 15, 20 e 25 keV respectivamente. Estes primeiros resultados são promissores e estão de acordo com

dados publicados, apesar de algumas limitações do acelerador de partículas serem responsáveis pela incerteza relativamente elevada dos valores obtidos. Identificámos essas limitações e apresentamos possíveis melhorias que visam eliminar estas últimas.

Por último, sugerimos também trabalho futuro para poder fazer uso de todas as potencialidades do sistema experimental PIXE que desenvolvemos. Algumas dessas sugestões já estão a ser implementadas.

ABSTRACT

Particle-Induced X-ray emission (PIXE) is an analytical technique used for determining quantitatively trace-elements concentrations with an enviable sensibility. This multi-elemental analysis tool was shown to be particularly well suited in a large number of applications in various fields ranging from archaeology, biology, medicine to environmental sciences.

Among these applications we can also distinguish the analysis of material surfaces using low-velocity ions due to their reduced range in solids (down to hundreds of nanometers). However, for this particular purpose, the lack of reliable and accurate X-ray production cross-sections for low-velocity impinging particles limits the accuracy of such low-energy PIXE analysis.

In this work, a recently built particle accelerator was studied, characterized, improved and used together with a PIXE experimental set-up, developed by us, in order to determine cross-sections for X-ray production induced by low-energy protons in the 10-50 keV energy range.

At the time we began the works described in this dissertation, the particle accelerator was at a very early stage. We consequently had to implement several improvements before using it to irradiate samples and perform the studies planned; namely in the ion source, in the ion acceleration, in the characterization of the beam and in the components of the reaction chamber.

Besides, we also developed an X-ray detection system based on a Gas Proportional Scintillation Counter (GPSC) to register the PIXE spectra. This detector was optimized for the detection of the soft X-rays induced by the interaction of the accelerated protons with targets of light elements and was also adapted to the PIXE experimental arrangement developed. The X-ray detector had to fulfil some requirements for this particular application, namely the detection of soft X-rays down to 200-300 eV and the need of having a large detection area due to the reduced X-ray production cross-sections involved. For these reasons, we decided to instrument this GPSC with an ellipsoidal grid, rather than a planar one, to delimit the absorption and scintillation regions in order to improve its performance for large detection areas. We also considered filing this latter with Ar-Xe mixtures instead of pure Xe to reduce the loss of primary electrons to the detector window, resulting from the very low absorption lengths involved in the detection of soft X-rays, and the subsequent worsening of the detector performance.

The use of the ellipsoidal grid technique with Ar-Xe mixtures as the detection media was shown to allow good compensation for all the studied mixtures regarding

both the energy resolution and the detector gain. For instance, for the 80%Ar-20%Xe mixture, the energy resolution worsens from 7.8 to 9.5 % as the detector radiation window diameter increases from 2 to 38 mm when using the ellipsoidal grid, whereas it worsens up to 11.5 % with a conventional planar grid. Also as the window diameter increases, the detector gain decreases 2 % when using the ellipsoidal grid and 4 % with the planar grid. A systematic study of the best detector performance showed that the best operating voltages depend on the gas mixture composition.

The Ar-Xe mixtures studied were characterized for their electroluminescence yield, the excitation and ionization thresholds, the w-values and Fano factors. The detector performance was evaluated in terms of the detector gain, its energy resolution and the Peak-to-Valley Ratio (PVR). Ar-Xe mixtures were shown to present similar energy resolutions than pure Xe, apart from the 250-630 eV energy range as expected, and to have improved Fano factor with Xe concentrations below 10%. For instance, energy resolutions of 17.5 % were obtained with either 95%Ar-5%Xe or 90%Ar-10%Xe mixtures for 1.2 keV X-rays while a value of 16.9 % was reached with pure Xe. In addition, the PVR improves by a factor 2 or 3 as the Ar concentration increases. Ar-Xe mixtures were consequently shown to be a valid alternative to pure Xe as the filling gas of GPSCs.

The developed GPSC was additionally used to carry out another completely distinct study regarding the primary scintillation induced by X-rays in pure gaseous Xe at atmospheric pressure. In these studies, we detected the primary scintillation light produced by 5.9 keV X-rays absorbed in pure Xe and quantified its intensity by comparing its signal to the one due to the secondary scintillation light yield with a technique that we developed. These studies revealed than the average energy spent to create a primary scintillation photon in gaseous Xe at atmospheric pressure is equal to 111 $\pm$ 16 eV.

Once these studies concerning both the particle accelerator and the X-ray detection system were completed, preliminary PIXE studies were finally conducted. We began by studying the influence of some parameters of the experimental arrangement during irradiation with the purpose of optimizing the overall system performance. Afterwards, X-ray production cross-sections results were obtained by irradiating thick targets and through the determination of the thick target yield curve. We determined aluminium X-ray production cross-sections of 8.43×10^{-4}, 1.30×10^{-3} and 1.81×10^{-3} barn for 15, 20 and 25 keV protons respectively. These first results are promising and in agreement with the very few published data, although some limitations of the particle accelerator are responsible for relatively high uncertainty in the results. We have identified those limitations and presented possible improvements to eliminate these.

Finally, future work has also been suggested to use the full capabilities of the PIXE experimental set-up we developed. Some of these suggestions are already being implemented.

CONTENTS

CHAPTER II

THE PARTICLE ACCELERATOR 53

CHAPTER III

THE X-RAY DETECTION SYSTEM 81

CHAPTER IV

CHAPTER V

INTRODUCTION

Particle-Induced X-ray emission (PIXE) is a technique for multi-elemental analysis which consists on irradiating the specimen to analyze with accelerated, charged light particles, usually protons in the Mega-Electron Volt energy range, and studying the X-ray yield resulting from the interaction of the ion beam with the target material. The PIXE technique was shown to be very useful for analytical purposes and has been developed over the past decades into a fully quantitative analytical tool for determining trace-elements concentrations with detection limits below the part-per-million level, corresponding to amounts of matter below 10^{-12} g. This particularly great sensitivity, together with its non-destructive character, allows this powerful analytical tool to be very well suited in a variety of application fields.

The determination of such low amounts of matter relies on the knowledge of several parameters and the accuracy of the technique is usually limited by their precision. Among these parameters are the X-ray production cross-sections, whose knowledge is fundamental to perform any quantitative elemental analysis. Although some accurate, and experimentally obtained, X-ray cross-sections are available in the literature for the most conventional impinging particle energies, the X-ray production cross-sections usually used are approximate values calculated from theoretical models with an uncertainty above 10 %. The situation is even worse when considering low-energy incident particles since the data available in the literature is scarce or even inexistent and because the cross-sections predicted by the theoretical models differ widely in this low-energy range. As a result, the accuracy of an important application of the PIXE technique, which is the characterization of material surfaces by using low-energy impinging particles due to their very low range in solids (down to a few hundreds of nanometers), is limited by the lack of available data in the literature.

In this work, making use of a recently built low-energy particle accelerator at the Atomic and Nuclear Instrumentation Group (Grupo de Instrumentação Atómica e Nuclear – GIAN) in the Physics Department of the University of Coimbra, we conceived and built a low-energy PIXE set-up with the aim of determining of low-energy particle induced X-ray production cross-sections suitable for the analysis of material surfaces. The present dissertation is divided in five Chapters:

- Chapter I is a review of the PIXE technique whose goal is presenting this analytical tool to readers not familiar with the field. The different characteristics of the technique are briefly described, as well as some of its main applications, in

order to provide enough information for a correct understanding of the work and the decisions made during the study described along this thesis. This review also points out some limitations of the technique, among which is the lack of available cross-sections in the literature for low velocity ions which is at the origin of the present work.

▪ Chapter II presents the recently built particle accelerator used to irradiate the samples. This description reports its early stage at the moment we began the work described here and presents the improvements implemented and the studies performed in order to adapt and prepare this experimental set-up to our particular PIXE application.

▪ Chapter III describes the Gas Proportional Scintillation Counter built to register the PIXE spectra. After a brief description in which we justify some of the decisions taken regarding its optimization for both large detection area and soft X-ray detection, this section presents the projection, construction and performance characterization of the X-ray detection system developed. Besides, this section also presents a distinct study dealing with the primary scintillation yield induced by X-rays absorbed in gaseous Xe at atmospheric pressure.

▪ Chapter IV describes the first studies performed with the developed PIXE experimental arrangement by irradiating metal specimens with protons with energy up to 50 keV. Aluminium X-ray production cross-sections were deduced for protons in the 15, 20 and 25 keV protons through the thick target yield curve. The discussion of the results obtained and their associated accuracy enables us to point out the limitations of the present experimental arrangement. This section ends with a discussion concerning the future work to be done to improve both the particle accelerator and the present PIXE set-up.

▪ Chapter V resumes the main achievements of the work presented.

The studies described in this dissertation were carried out in the Atomic and Nuclear Instrumentation Group (GIAN – Grupo de Instrumentação Atómica e Nuclear) of the Physics Department of the University of Coimbra.

Besides, the work presented in this dissertation gave rise to the following publications:

PUBLICATIONS IN INTERNATIONAL REFEREED JOURNALS

- "Absolute primary scintillation yield of gaseous xenon under low drift electric fields for 5.9 keV X-rays", **S.J.C. do Carmo**, F.I.G.M. Borges, F.P. Santos, T.H.V.T. Dias and C.A.N. Conde, Journal of Instrumentation 3, P07004 (2008).

-"Experimental study of the *w*-values and Fano factors of gaseous xenon and Ar-Xe mixtures for X-rays", **S.J.C. do Carmo**, F.I.G.M. Borges and C.A.N. Conde, IEEE Transactions on Nuclear Science 55(5), pp. 2637-2642 (2008).

-"Ar-Xe mixtures and their use in curved grid gas proportional scintillation counters for X-rays", **S.J.C. do Carmo**, A.M.F. Trindade and F.I.G.M. Borges, Journal of Instrumentation 4, P03015 (2009).

-"Performance of Argon-Xenon mixtures in a gas proportional scintillation counter for the 0.1-10 keV X-ray region", **S.J.C. do Carmo**, F.I.G.M. Borges and C.A.N. Conde, IEEE Transactions on Nuclear Science 56(2), pp. 437-440 (2009).

-"Mossbauer study of Haltern 70 amphora sherds from Castro do Vieito, North of Portugal", B.F.O. Costa, G. Pereira, A.J.M. Silva, M. Ramos Silva and **S.J.C. do Carmo**, Journal of Physics: Conference Series 217, nº 012060 (2010).

PUBLICATIONS IN THE PROCEEDINGS OF INTERNATIONAL CONFERENCES

- "A large area room temperature gas proportional scintillation counter for soft X-rays with Ar-Xe mixtures: Preliminary results", **S.J.C. do Carmo**, F.I.G.M. Borges and C.A.N. Conde, Conference Record of the 2007 IEEE Nuclear Science Symposium and Medical Imaging Conference, pp. 581-584 (2007).

-"Performance of a room temperature gas proportional scintillation counter in X-ray analysis of metallic alloys excited with alpha particles", F.I.G.M. Borges, **S.J.C. do Carmo**, T.H.V.T. Dias, F.P. Santos, F.P.S.C. Gil, A.M.F. Trindade, R.M. Curado da Silva and C.A.N. Conde, 2007 Denver X-ray conference, Advances in X-Ray Analysis 51, pp. 249-254 (2008).

- "Performance of Argon-Xenon mixtures in a gas proportional scintillation counter for the 0.1-10 keV X-ray region", **S.J.C. do Carmo**, F.I.G.M. Borges and C.A.N. Conde, Conference Record of the 2008 IEEE Nuclear Science Symposium and Medical Imaging Conference, pp. 173-176 (2008).

– CHAPTER I –

PARTICLE INDUCED X-RAY EMISSION

Following the work of Röentgen that culminates with the discovery of the X-rays in 1895 [I.1], Moseley observed in 1913 that the X-rays emitted from several excited elements of the periodic table have characteristic energies, related to their atomic number [I.2]. Although Moseley also demonstrated qualitatively that the X-rays resulting from the excitation of brass were the characteristic X-rays lines from its components, it was only with Glocker and Schreiber in 1928 [I.3], by detecting secondary fluorescent X-rays obtained from the irradiation of targets with primary X-rays, that the first quantitative analysis of materials was performed. Their proposal to apply X-ray excitation as a multi-element analysis tool appeared to be at the origin of the X-ray fluorescence analysis technique (XRF).

Although the emission of characteristic X-rays was also observed earlier in 1912 by Chadwick by bombarding matter with heavy charged particles instead of primary X-rays [I.4], it was only much later with the works of Merzbacher and Lewis [I.5],[I.6] and Khan *et al.* [I.7], in 1953 and 1966 respectively, that the potential of Charged-Particle X-ray Fluorescence (CPXRF) received noticeable attention for multi-elemental analysis purposes despite the fact that charged-particle induced X-ray emission was shown to be more sensitive than XRF. However, Khan *et al.* used a proportional counter to detect the X-rays emitted from the irradiated targets, whose poor energy resolution did not allow resolving characteristic X-rays from adjacent elements. As a result, they were not able to perform any quantitative multi-element analysis.

In this line of thought, using the recently invented Si(Li) X-ray detector with improved energy resolution that was not available when Khan *et al.* performed their studies, Johansson *et al.* [I.8] presented in 1970 a pioneer experimental work that became the starting point of a powerful multi-elemental analysis technique, known nowadays as Particle Induced X-ray Emission (PIXE). This non-destructive technique consists in bombarding a specimen with heavy charged particles from accelerators, such as protons, α-particles or heavier ions, in order to originate the emission of X-rays, characteristics of the irradiated atoms. These X-rays result from the de-excitation of the inner shell vacancies created in ionized atoms due to the interaction of the ion beam with the target and are detected by either a wavelength-dispersive or an energy-dispersive detector.

This Ion Beam Analysis (IBA) technique is highly sensitive and enables quantitative analysis because there is a relationship between the amount of a particular element present in the irradiated sample and the intensity of its characteristic K- or L-X-ray lines in the PIXE spectrum. Accurate knowledge of X-ray production cross-sections, detector efficiency and absorption coefficients allow the quantification of very small amounts of matter for several elements in a large variety of materials, down to 10^{-12} g [I.8] which corresponds to typical detection limits for trace elements lying in the 0.1-1 Parts Per Million (ppm) range. Furthermore, this method is almost insensitive to the chemical state of the atom, i.e. it distinguishes atoms rather than molecules [I.9].

In PIXE, the incident charged-particle beam, which is usually formed by light ions with energy between 1 and 4 MeV, is usually generated by particle accelerators and goes through an irradiation chamber maintained in vacuum, where it bombards a target. The target is usually a thin sample of the specimen to be analysed deposited onto a thin carbon or plastic support layer, although the irradiation of thick targets is also possible. The beam passes though the sample and is dumped in a Faraday cup connected to a charge integrator. The X-rays emitted from the sample are detected and separated in an energy spectrum. A typical spectrum is shown in Figure I.1 where several K- and L-characteristic peaks are superimposed upon a continuous radiation background. The cut-off in the low energy range of the spectrum is due to both the high absorption of these low energy X-rays in the windows of the chamber and/or the detector and in the sample itself and to the low detector efficiency for this low-energy range.

Besides traditional bombardment in vacuum, known as macro-PIXE, in which the irradiation is performed with millimetre-sized beams (1-10 mm diameter typically), PIXE analysis can also be performed with focused micro-beams with only a few micrometers diameter in such a way that, with scanning techniques, it allows analysis with high spatial resolution, this variant being usually referred to as micro-PIXE. When the examination of delicate and/or large objects is required, PIXE analysis can also be performed with an external beam irradiating the sample either in the laboratory air or in a nitrogen or helium atmosphere. Moreover, the combination of PIXE with other IBA techniques, such as Rutherford backscattering spectrometry (RBS), was found to be useful in several applications [I.10].
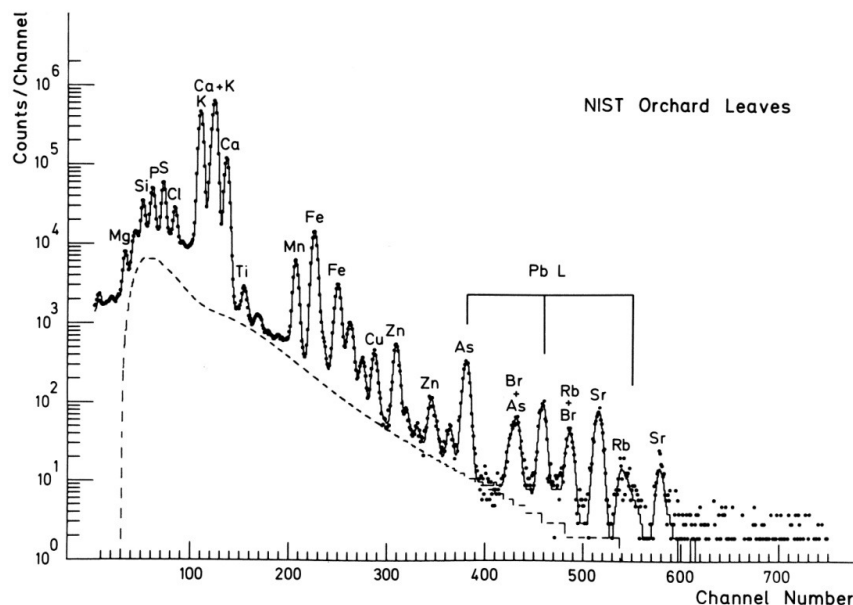
Figure I.1 – PIXE spectrum obtained for a NIST Orchard Leaves specimen with incident protons of 2.4 MeV [I.11].

The PIXE technique presents many advantages over common XRF due to the fact that it uses charged particles instead of X-rays to irradiate a target, the major one being its greater sensitivity [I.12]. Another advantage is the fact that the ion beam can be focussed by electrostatic or (electro)magnetic lenses and may be transported over large distances without loss of beam intensity, resulting in much higher incident beam densities in PIXE rather than in ordinary XRF. We also have to refer that, although beam focusing is also possible with electrons as it occurs in the Electron Probe Micro-Analyzer technique (EPMA), these originate much larger radiation continuum background intensity in the X-ray spectrum (due to bremsstrahlung) and so much poorer detection limits.

As a result of its applicability, versatility and sensitivity for solving numerous trace element analytical problems for almost all the elements of the periodic table, PIXE became nowadays a technique of great importance when material analysis is required. It is consequently used in many practical applications for the examination of a wide variety of distinct samples from metals and alloys, rocks, environmental samples, medical and biological specimens, surface of thick samples of technological and industrial interest, to valuable art pieces for origin identification.

In the next section, the physical processes underlying the PIXE method will be outlined, while the following ones present considerations about experimental arrangements and technical details that have to be taken into account when intending to develop a PIXE experimental set-up to be used as a multi-elemental analytical tool. Then, another section illustrates the usefulness of PIXE by describing briefly a few practical applications. Finally, the last section of this chapter deals with the sensitivity and the accuracy of this technique and also evidences the lack of available X-ray production cross-sections in the literature for low-energy beams, despite the fact that PIXE surface

analysis (which is one of the main applications of PIXE) relies on the knowledge of such cross-sections.

I.1 INTERACTION OF CHARGED PARTICLES WITH MATTER

I.1.1 X-RAY PRODUCTION

While penetrating into matter, heavy charged particles interact mainly through Coulomb forces between the positive charge of the incoming ions and the negative charge due to the Coulombic fields of the bound electrons of the absorber atoms. In such inelastic encounters, ions interact simultaneously with several electrons which sense the attractive Coulomb force from the travelling ions; and depending on the proximity of the encounter this interaction leads to either excitation or ionization.

As a result of these inelastic Coulombic encounters, the travelling charged particle transmits some of its energy to the excited/ionized electrons and its velocity therefore decreases. However, since the maximum energy T_m that can be transferred from a charged particle of mass m with kinetic energy E_p to an electron of mass m_e ($m >> m_e$) in a collision is $4E_p m_e / m$, this corresponds to a small fraction of the total energy of the ions in contrast to the case of electron beams. In consequence, the direction of travel of an incident ion beam is scarcely altered during its continuous slowing process and the ions have to undergo many interactions until they are stopped.

Many of the Coulombic interactions between charged particles and matter result in ionization of the target atoms, i.e. ejection of inner-shell electrons and so creation of inner-shell vacancies. These interactions are of great importance for PIXE since they may lead to the emission of the desired characteristic X-rays. The following theoretical approaches have been used through the years to describe this interaction and to calculate cross-sections for inner-shell vacancy creation in elements of atomic number Z, σ_Z^I:

- ✓ The Plane Wave Born Approximation (PWBA). This approach is due to Merzbacher and Lewis [I.6] and describes the inner-shell ionization process in terms of a quantum mechanical model. Although this approach explains the dependence of the ionization cross-section σ_Z^I for high projectiles energies, corrections for the binding energy of the target atom electrons and the Coulombic deflection of the approaching projectile are needed to obtain quantitative agreement for lower projectile energies.
- ✓ The Binary Encounter Approximation (BEA), used by Garcia [I.13], considers the interaction to be that of an incident particle and a free electron with an effective mass in order to take into account the target atom mass.
- ✓ The semi-classical approximation (SCA), developed by Bang and Hansteen [I.14] and Hansteen and Mosebeke [I.15], uses an impact parameter which directly takes into account the projectile deflection.

✓ The EPCSSR approach is an improvement of the PWBA theory performed by Brandt and Lapicki [I.16],[I.17] that takes into account the deflection and velocity change of the particles due to nuclear Coulomb field (C), perturbation of the atomic stationary states (PSS) by the projectile, relativistic effects (R) and energy loss (E) during the collision.

All these models are based on the assumption that the production of an inner-shell vacancy results from a Coulombic interaction and are only valid for incident particle energies much larger than the binding energy of the electrons. All these approaches can explain the following dependence and variation of ionization cross-section, σ_Z^I:

✓ The ionization cross-section increases rapidly with projectile energy.
✓ The ionization cross-section is proportional to the square of the projectile atomic number Z_p (for projectile of equal velocity).
✓ The ionization cross-section decreases rapidly with the target atomic number Z_T.
✓ Atomic shells having higher ionization potentials have lower ionization cross-sections.

One would immediately assume from the Z_p^2 dependence of σ_Z^I that heavier ions would preferentially be chosen to perform PIXE analysis. However, heavy ions interactions with matter lead to much more complex X-ray spectra because of the additional interaction between the two electron systems from the target and impinging atoms [I.12],[I.18]. Therefore, and despite their higher ionization cross-sections, the use of heavy ions to perform multi-elemental trace analysis is improbable.

The ionization cross-sections calculated thanks to these theories have been compared to experimental results [I.13],[I.19],[I.20]. Agreement within $\pm$ 20 % has been observed in the energy range and atomic number region of interest (target atomic numbers, Z_T, typically between 20 and 40), which is however far from being sufficient for accurate trace analysis by PIXE. On the contrary, the σ_Z^I K-shell predictions provided by the ECPSSR theory agree within a few percent with the best experimental data, except for very low atomic number of the target, Z_T.

An interesting characteristic to point out is that the magnitude of the ionization cross-section for 1-3 MeV protons is similar to those of electrons in the energy region of 10-30 keV employed in electron probe micro-analysis. This is because the principal determinant of the interaction is the velocity ratio between the projectile and bound electron, and this ratio is similar for kilo-electron-volt electrons and mega-electron-volt protons.

By using the BEA model, Garcia [I.13] found out a scaling law for the ionization cross-section σ_Z^I of all elements which only relates the electron binding energy u_i (where i=K or L) and the projectile energy E_p. A universal curve is obtained by plotting $u_i^2 \sigma_Z^I$ as a function of $E_p/\lambda u_i$, where λ is the ratio of the proton mass to the electron mass. Johansson and Johansson [I.12] compiled experimentally obtained ionization

cross-sections available in the literature to verify the adequacy of this relationship and found out that theses curves (shown in Figure I.2) indeed allow the estimation of the ionization cross-sections with a typical uncertainty of 10-20 % for Z_T=20-40 and MeV ion beams. However, although the values of σ_Z^I easily obtained from this scaling law are useful when studying the feasibility of a particular experiment, they are not sufficiently accurate to carry out an absolute PIXE analysis.
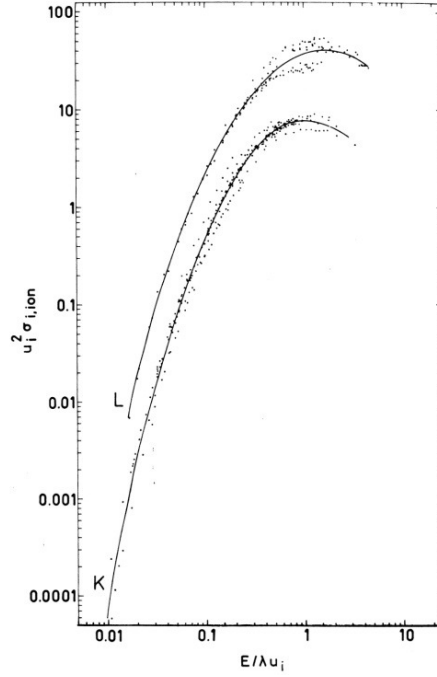
Figure I.2 – The semi-empirical fit of Johansson and Johansson [I.12] for K- and L- ionization cross-sections σ_Z^I by plotting $u_i^2\sigma_Z^I$ as a function of $E_p/\lambda u_i$. The dots correspond to experimental values obtained from thin target measurements.

As a result of the creation of an inner-shell vacancy, the excited target atoms seek to return to a stable energy state through de-excitation, i.e. an outer-shell electron which drops down to a lower energy level filling so the inner-shell vacancy. The vacancy moves therefore towards the outer shells while the superfluous energy results in the emission of either X-rays or Auger or Coster-Kronig electrons. While X-rays correspond to the radiative emission of the redundant energy resulting from the electron migration to an inner-shell (K, L, M... lines produced by electron transition to the K, L, M... shells of the target atom respectively), Auger electrons consist in outer-shell electrons ejected from the atomic orbit (creating therefore a vacancy in an outer-shell) due to the redundant energy. Alternatively, the Coster-Kronig effect which is similar to the Auger effect with the difference that it occurs between sub-shells of an atomic shell (and therefore does not take place in the K-shell), corresponds to the shift of a vacancy created in a lower sub-shell to a higher sub-shell.

Since the energy gap between atomic shells is well defined and characteristic of a given element, the X-rays emitted have discrete and characteristic energy, hence being denominated as characteristic X-rays.

Since PIXE analysis relies on the detection of X-rays, only the emission of characteristic X-rays is relevant among these three competitive processes. Hence, for practical purposes in any quantitative trace-elements analysis, accurate X-ray production cross sections for individual X-ray lines $\sigma_{p,Z}^{X}$, with p the X-ray line considered for analysis, are required rather than the ionization cross-section σ_Z^I. However, the X-ray production cross-section $\sigma_{p,Z}^{X}$ for a given radiative transition (i.e. for a line in a spectrum) of a given element of atomic number Z is related to the ionization cross sections σ_Z^I through atomic parameters, namely fluorescence yields and relative line transition probabilities in the case of the K-shell; and fluorescence yields, Coster-Kronig yields, and relative line transition probabilities for the L-shell. For instance, the X-ray production cross-section for a K-shell radiative transition, $\sigma_{p,Z}^{X}$, is related to σ_Z^I as:

$$\sigma_{p,Z}^{X} = \omega_{p,Z} \ \ \sigma_{p,Z}^{I} \ \ T_p \qquad\qquad \text{(Eq. I.1)}$$

where $\omega_{p,Z}$ is the fluorescence yield and T_p the relative line transition probability to fill the p-shell vacancy.

The fluorescence yield $\omega_{p,Z}$ of a shell, which increases gradually with atomic number Z, can be described as the fraction of emitted X-rays due to transitions to a particular shell of a given number of primary vacancies created in that shell, i.e. the probability for X-ray emission as a vacancy is created. The K- fluorescence yields are known with great accuracy (within 5 %) for atomic numbers Z between 20 and 60, but the situation for the lighter elements is less clear [I.21]. Moreover, the relationship between the X-ray production and ionization cross-sections also takes into account the relative X-ray transition probability since more than one X-ray line (K_α or K_β lines for the K-shell, for instance) can occur as the result of the radiative transition to a particular energy level due to different initial energy states. The fraction of a specific X-ray line emitted with respect to the total number of X-rays emitted from that shell is referred to as relative X-ray line transition probability T_p (Equation I.1).

In Figures I.3, I.4 and I.5, we have compiled data available in the literature (see references in the captions) for proton induced X-ray production cross-sections of K-lines and represented them as a function of both the incident proton energy E_p and the target atomic number, Z_T. We can observe that $\sigma_{p,Z}^{X}$ is a rapidly increasing function of the incident projectile energy up to 2-4 MeV, depending on Z_T. X-ray yield for high X-ray energies, i.e. high Z elements (Z > 25), increases proportionally to E_p^4 (where E_p is the projectile energy) but for low X-ray energies the increase is less pronounced [I.22]. It reaches a maximum for the i'th shell of a given element when the velocity of the projectile equals the mean velocity of the electron of the shell under consideration. Then, for higher energies of the projectile, the cross-sections decrease slowly. Another conclusion of great importance that is also in evidence in Figure I.4 is that $\sigma_{p,Z}^{X}$ decreases sharply with increasing atomic number of the target atom, Z_T. Furthermore, we also have to refer at this point that, as for ionization cross-sections, X-ray production cross-sections are proportional to Z_p^2 for equal velocity ions, as illustrated in Figure I.6.
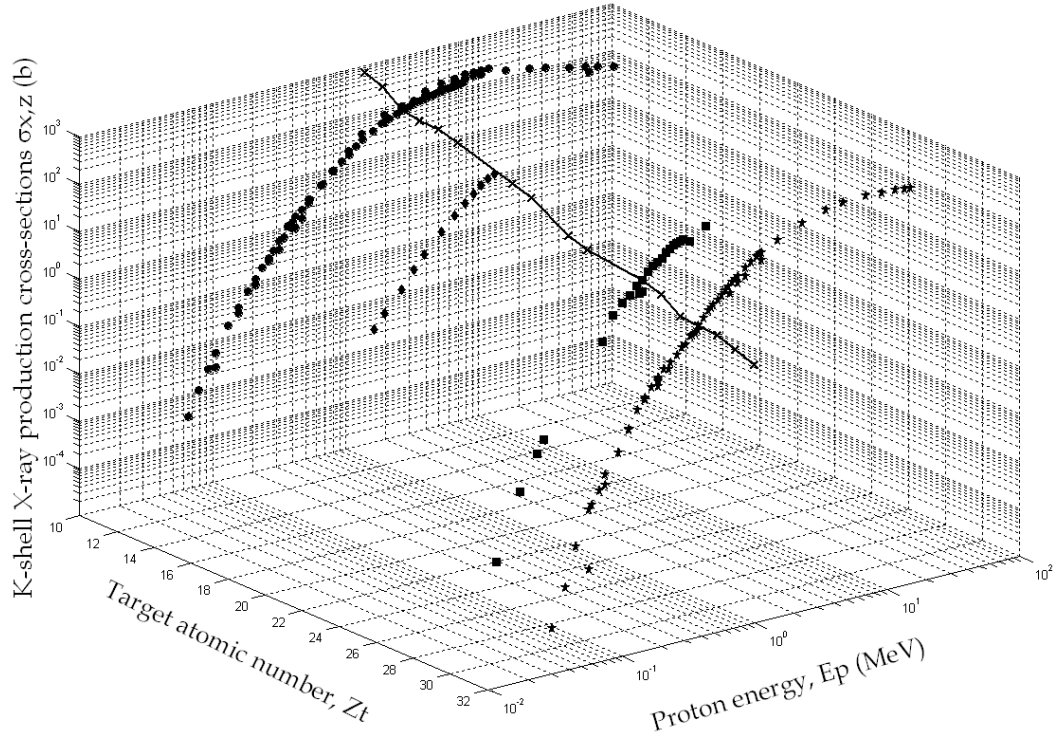
Figure I.3 – Experimentally obtained K-shell X-ray production cross-sections $\sigma_{p,Z}^{X}$ (logarithmic scale) in proton impact for aluminium (●), argon(♦), iron (■) and copper (*) as a function of the incident proton energy E_p and of the target atomic number Z_T [I.23]-[I.34]. The solid curve corresponds to X-ray production cross-sections for protons with a constant energy of 1 MeV and for target of different atomic number Z_T.
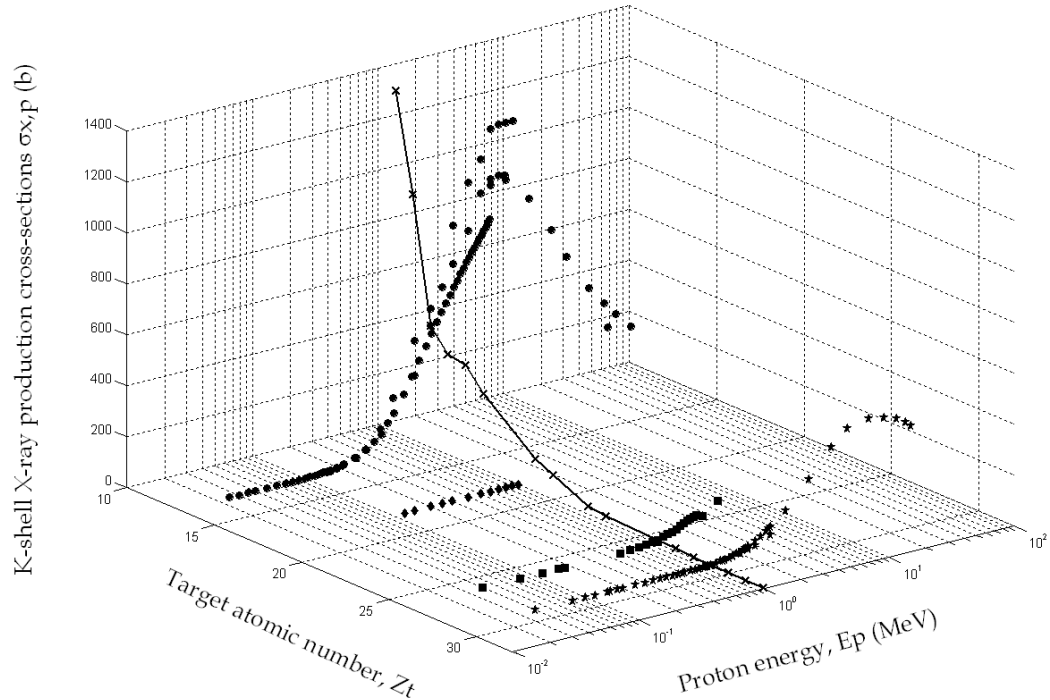
Figure I.4 – Experimentally obtained K-shell X-ray production cross-sections $\sigma_{p,Z}^{X}$ (linear scale) in proton impact for aluminium (●), argon(♦), iron (■) and copper (*) as a function of the incident proton energy E_p and of the target atomic number Z_T [I.23]-[I.34]. The solid line represents the same as in Figure I.3 but the difference that a linear scale is used to represent $\sigma_{p,Z}^{X}$ in order to focus its rapid decrease with the target number Z_T.

12
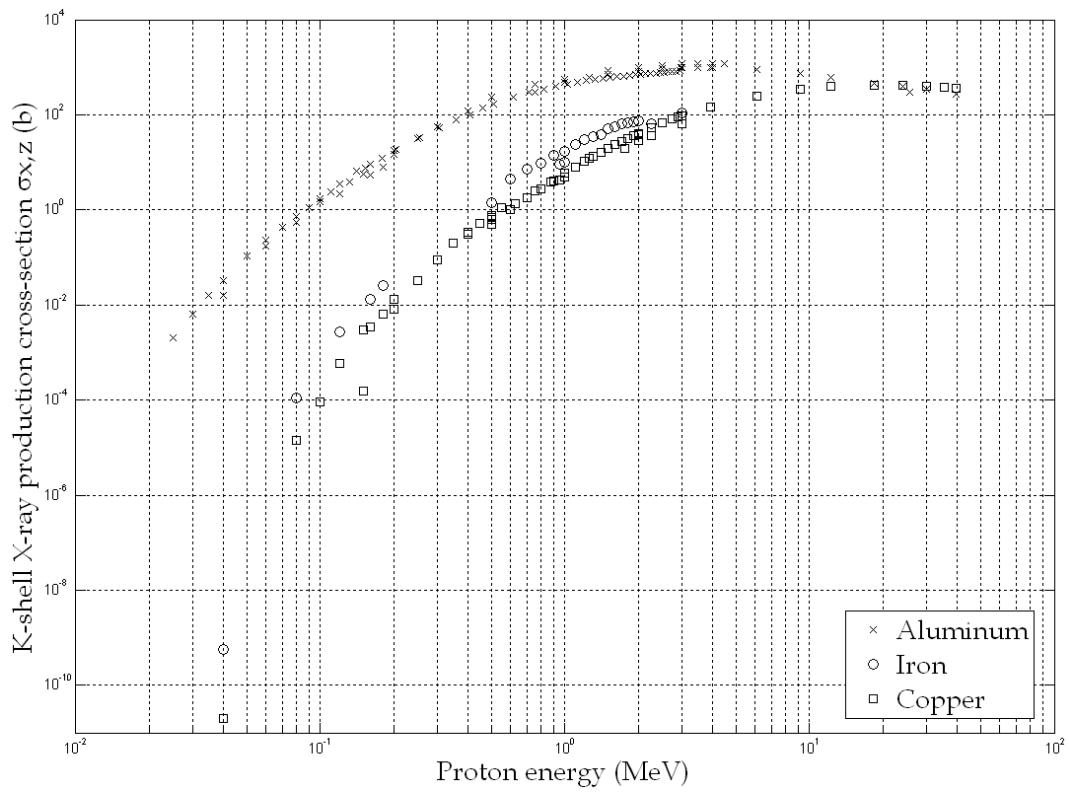
Figure I.5 – Experimentally obtained K-shell X-ray production cross-sections for proton impact in aluminium, iron and copper as a function of the incident proton energy E_p and the target atomic number Z_T [I.23]-[I.26],[I.28]-[I.31],[I.33] and [I.34].
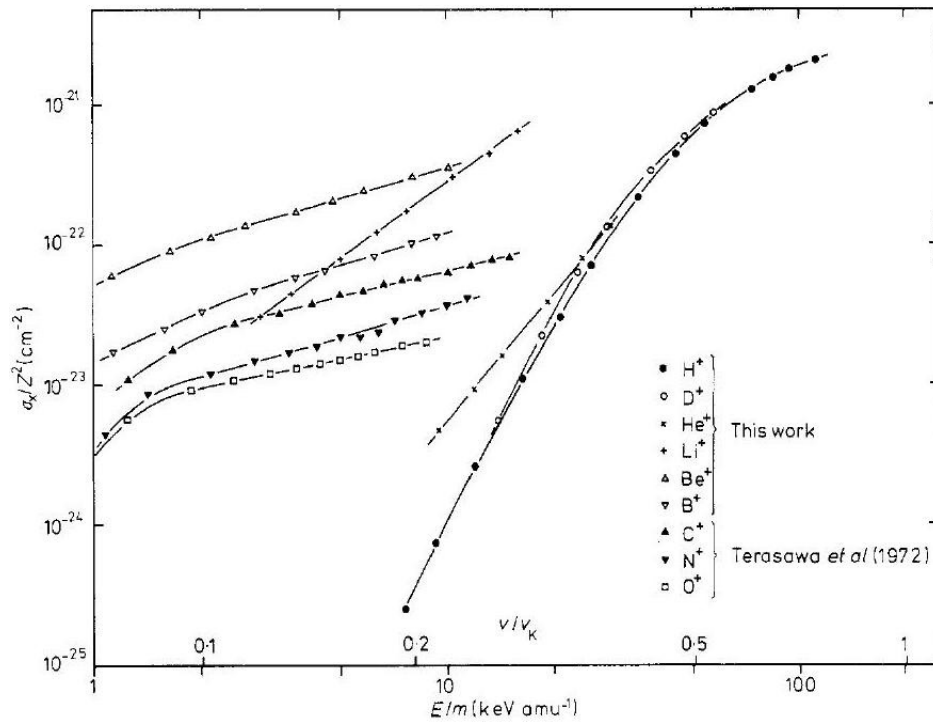
Figure I.6 – Reduced Be K-line production cross sections σ_x/Z^2 (where Z is the projectile atomic number) for various projectile ions as a function of kinetic energy per atomic mass unit [I.35].

13

I.1.2   RADIATION BACKGROUND

In a typical PIXE analysis, beyond the desired characteristic X-rays from the trace elements to detect, the X-ray detector also registers a large amount of unwanted background radiation. This can result from the beam interaction with the trace elements of interest through additional competitive processes (proton and electron bremsstrahlung, for instance) or, on the other hand, might arise from the impact of the impinging ions with either the bulk of the host material of the sample or any element from the backing material. This radiation background, which is the main determinant of the limit of detection for any element, may be in the form of a continuum distribution or it may also be composed by discrete peaks corresponding to X- or γ-rays from the matrix material (by matrix material, we consider all the elements that are not the ones under consideration). As a result, the characteristic X-ray lines of interest are superimposed on a continuous spectrum of electromagnetic radiation similar to that observed in EPMA technique, as we can observe in Figure I.1. The high background at low X-ray energies, combined to the significant drop in the detector efficiency for this low-energy range because of X-ray absorption in the windows of the experimental set-up and/or the detector, prohibits accurate analysis of light elements, typically below sulphur, in the spectrum. This also demonstrates that, although a high X-ray production cross-section is a necessary condition for high sensitivity, it is not enough.

Therefore, the understanding of this background is as important as the understanding of the generation of the characteristic X-rays. One has to be aware that several processes contribute to this radiation background, namely primary proton bremsstrahlung, electron bremsstrahlung, and nuclear reaction gamma-rays for high values of E_p.

I.1.2.1   ELECTRON BREMSSTRAHLUNG

The low energy background of PIXE spectra, which is actually where the background is much more intense (as illustrated in Figure I.1), is largely due to electron bremsstrahlung as it occurs in the EPMA technique but with the difference that in this case it is caused by the secondary electrons ejected from the target atoms during the inelastic collision process rather than with the deceleration of incident electrons. This assumption is experimentally confirmed by observing PIXE spectra since this bremsstrahlung decreased rapidly above an energy threshold T_m corresponding to the maximum energy that a projectile of mass M_p and energy E_p can transfer to a free electron of mass m_e, which is given by $4(m_e/M_p)E_p$.

Much of the early work concerning the theoretical understanding of the *secondary electron bremsstrahlung* was realized by Folkmann *et al.* [I.36]. They gave a comprehensive understanding of the physical processes involved in the production of the *electron bremsstrahlung* and, as it can be seen in Figure I.7, their theoretical estimations (which also took into account the projectile bremsstrahlung, PB, which we discuss in more detail in

next section) are in good agreement with experimental data. Besides, Figure I.7 also illustrates the fact that the intensity of the electron bremsstrahlung background increases with both the incident projectile energy E_p and the atomic number of the target, Z_T. From an experimental point of view, this last observation means that, beyond E_p, the matrix composition of the target also plays a critical role in both the shape and intensity of the electron bremsstrahlung background.
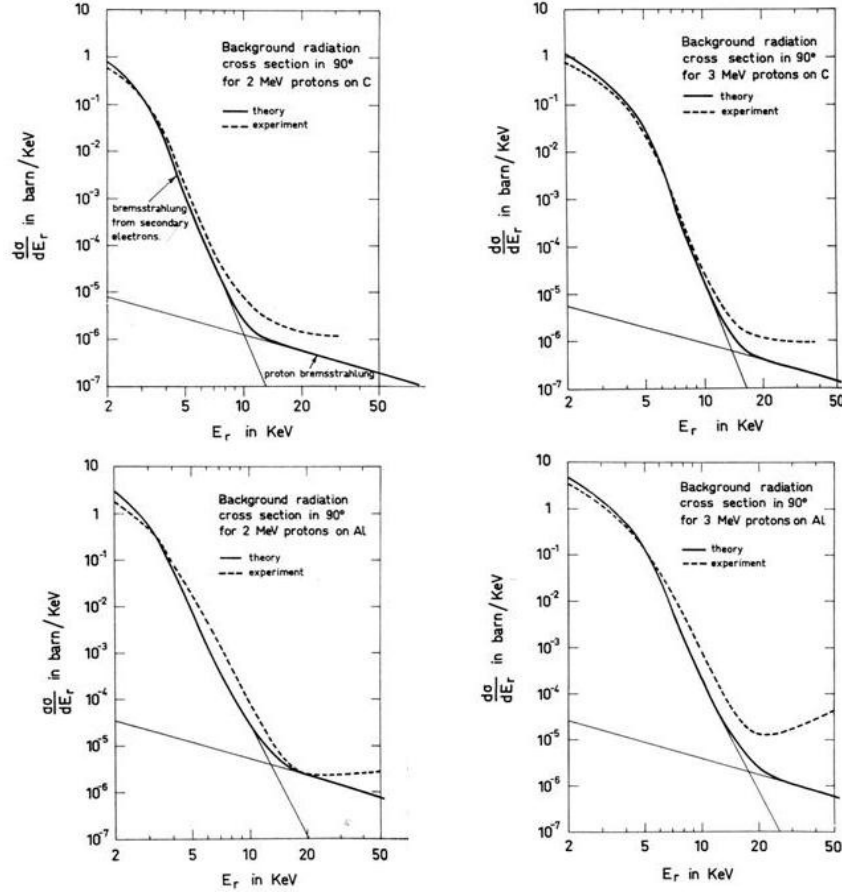
Figure I.7 – Experimental and theoretical background radiation cross-sections for thin samples of carbon and aluminium [I.36].

The work of Folkmann *et al.* was then complemented later, in the mid-1980s, by Ishii and Morita and various coworkers [I.37]-[I.40]. Their work demonstrated that electron bremsstrahlung in PIXE is originated by the following three processes:

- ✓ *Secondary Electron Bremsstrahlung* (SEB): SEB is formed by a two-step process. The incident particle first ejects an electron from a target atom, and the secondary electron is subsequently scattered in the Coulomb field of a target nucleus, thus producing the bremsstrahlung with maximum energy equal to T_m as referred earlier.

- ✓ *Quasi-Free Electron Bremsstrahlung* (QFEB): QFEB arises when the projectile velocity v_p is so large compared with orbital electron velocities that these electrons are effectively free and at rest; then an electron can be scattered by the projectile´s Coulomb field and emit QFEB. The QFEB end-point energy is $T_r=(1/2)m_e v_p^2$, which is also equal to $T_m/4$.

✓ *Atomic Bremsstrahlung* (AB): The AB process occurs when a bound target electron is excited to a continuum state by the projectile and, returning to its original state, emits a photon. Atomic bremsstrahlung is the main contribution of the electron bremsstrahlung to the continuous spectrum at photon energy above T_m.

The relative contributions of QFEB, SEB and AB to the electron bremsstrahlung background are represented schematically in Figure I.8.
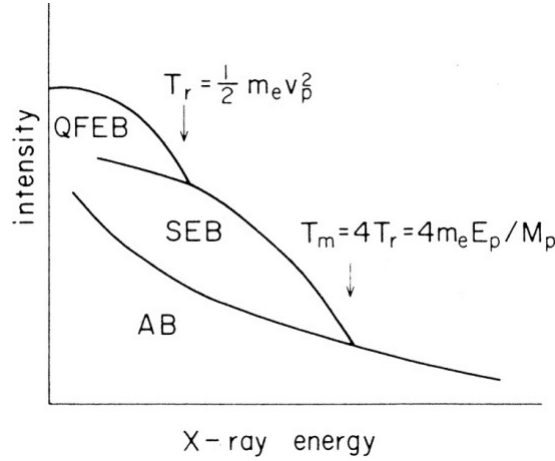
Figure I.8 – Schematic representation of the relative contributions of QFEB, SEB and AB [I.40].

In addition, Ishii and Morita also carried out a large number of experiments to test the veracity of their theoretical calculations. That work culminates in reference [I.40] in which the agreement between the theory and measurements is shown to be excellent, as illustrated in Figure I.9.
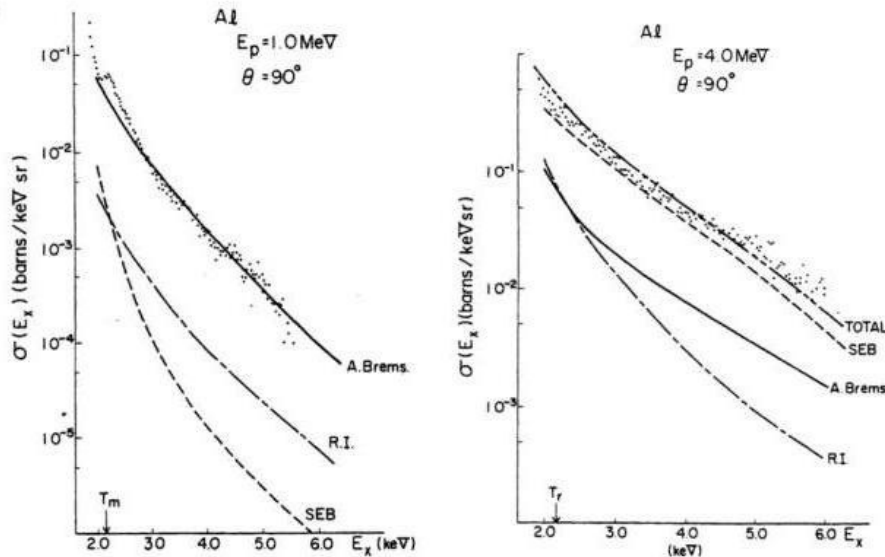
Figure I.9 – Bremsstrahlung spectra obtained from aluminium bombarded by 1 and 4 MeV protons. The curves show calculated contributions of different processes [I.40].

Since both the production of characteristic X-rays and electron bremsstrahlung are consequences of the same primary process which is the ionization event, i.e. the

16

creation of inner-shell vacancy by the incident particles, the ratio of the X-ray peaks to the bremsstrahlung background is the same for all projectiles having the same velocity. Consequently, as long as the electron bremsstrahlung is the dominant form of radiation background, the signal-to-noise ratio is independent of the projectile specie despite the Z_p^2 dependence of the X-ray production cross-section. There is therefore, from this point of view, no reason to use charged particles heavier than protons. In fact, heavier charged particles also have the inconvenient of leading to more complex radiation background spectra. Although the contribution of this radiation background can theoretically be reduced by using extremely thin samples in a way that the electrons can escape before they have the chance of radiating most of their kinetic energy as bremsstrahlung in a second collision, this improvement is impossible to accomplish experimentally because the thicknesses needed are impractical to achieve.

Another important characteristic of electron bremsstrahlung relies on the fact that, contrary to the X-ray production process, this radiation is emitted anisotropically being lower at forward and backward angles than at 90º with respect to the direction of the beam. This statement has been confirmed experimentally by Ishii *et al.* [I.41], who also explained it theoretically latter by them by incorporating a relativistic retardation effect in the bremsstrahlung production [I.42]. This matter was again subject of discussion by Gonzalez *et al.* [I.43] who compared experimental data from Folkmann *et al.* [I.44] (Figure I.10) to their theoretical calculations as illustrated in Figure I.11. From an experimental point of view, this observation is of great importance since it suggests preferential positioning of the X-ray detector in order to reduce the detection of this kind of bremsstrahlung. The maximum possible angle between the incident beam direction and the X-ray detector (typically 135º) was found to reduce significantly the background in PIXE spectra, as it can be seen in Figure I.10.
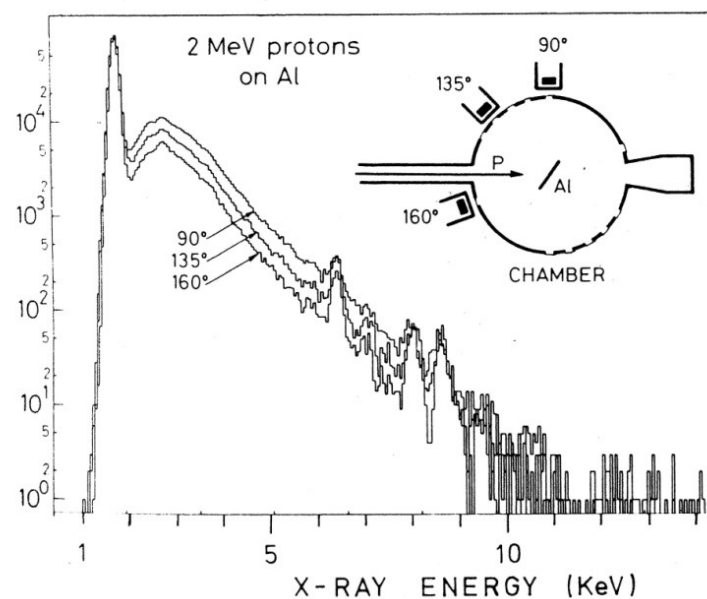
Figure I.10 – Experimental spectra obtained by bombarding a 130 μg/cm² Al foil with 2 MeV protons and with the Si(Li) X-ray detector positioned at different angles with respect to the direction of the incident beam [I.44].
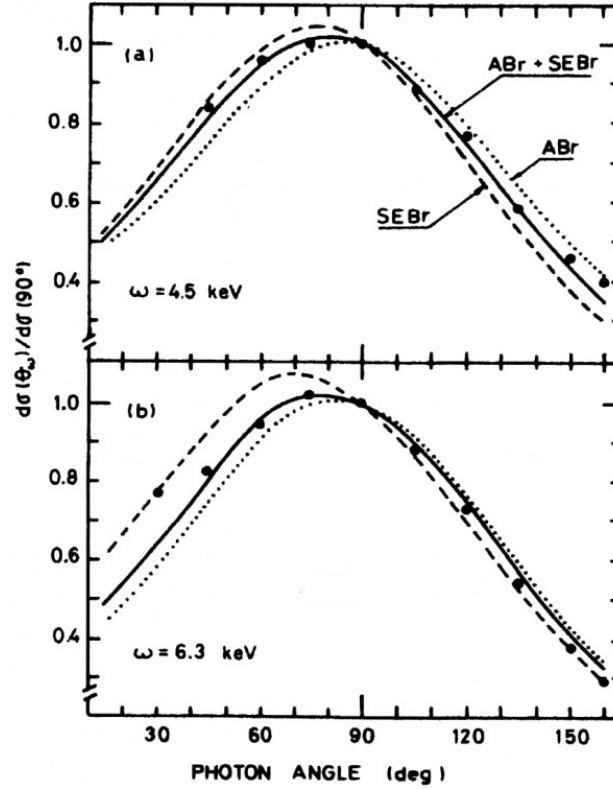
Figure I.11 – X-rays angular distributions for 2 MeV protons impinging on aluminium for photon energies of 4.5 and 6.3 keV [I.43].

I.1.2.2   INCIDENT PROJECTILE BREMSSTRAHLUNG

Another component of the continuous radiation background observed in PIXE spectra is due to *incident projectile bremsstrahlung* (PB). This radiation continuum results from the deceleration of the incident charged particles while passing through the sample because of the Coulomb field of atomic nuclei. The cross-section σ_{PB} for this process is given by the following formula:

$$\frac{d\sigma_{PB}}{dE_{pX}} = C \; \frac{A_p \, Z_p^2 \, Z_T^2}{E_p \, E_{pX}} \left(\frac{Z_p}{A_p} - \frac{Z_T}{A_T} \right)^2 \qquad \text{(Eq. I.2)}$$

where E_{pX} is the energy of the background radiation; Z_p, A_p, E_p are the atomic number, mass and energy of the incident particle and Z_T and A_T those for the matrix. C is a slowly varying factor dependent on Z_p, Z_T and E_p having a value of about 2-3 eV.

The intensity of primary bremsstrahlung emitted by a charged particle is proportional to the square of its deceleration. The Coulombic forces are the same for electron and heavy charged particles, but since the masses differ by a factor of at least 2000 in the worst case from this point of view (which corresponds to the lighter heavy charged particles, i.e. protons) the intensity of the projectile bremsstrahlung due to heavy charged particles is much less than that when induced by electron beams. As a result, the intensity of the proton´s primary bremsstrahlung is negligible in comparison

18

with that of the electron in the case of the electron microprobe analysis, as illustrated in Figure I.12.
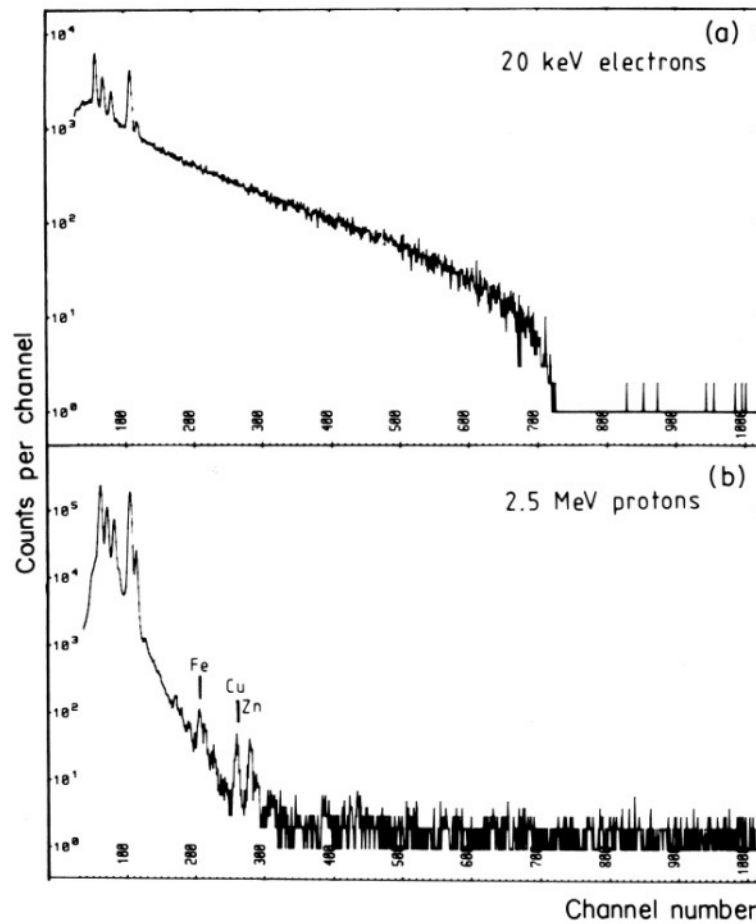
Figure I.12 – X-ray spectra from a thin biological specimen (human brain) obtained with a) electron and b) nuclear microprobe excitation. [I.45].

Although its contribution is much less important than *electron bremsstrahlung* (EB) in the low energy region of PIXE spectra, PB background continuum is the major component of the radiation background of PIXE spectra for the high energy part, above 10-20 keV for typical incident particles energies.

An important behaviour of PB that can be deduced from Equation I.2 is that, contrary to X-ray production cross-sections and other background processes behaviour, its yield (i.e. cross-section) increases with decreasing projectile energy. As a result, this background process is expected to be of great importance for low energy incident particles as it occurs for surface analysis applications.

On the other hand, Equation I.2 also demonstrates that if the mass to charge ratio Z/A is the same for the projectile and an element of the matrix, the contribution of this bremsstrahlung vanishes. However, even if this term does not vanishes, since most of the elements of a matrix present a ratio Z_T/A_T of approximately 0.5, there should be little or no incident projectile bremsstrahlung PB for impinging charged particles as α-particles and heavier ions for which Z_p/A_p almost equals 0.5 too, but not for protons

(for which equals 1). This effect has been experimentally verified by Watson *et al.* [I.46] as it can be seen in Figure I.13.
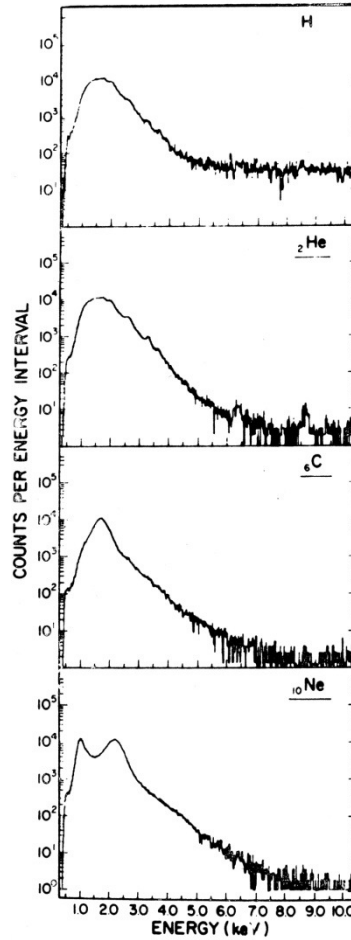
Figure I.13 – X-ray spectra produced by bombarding a 530 μg/cm2 Mylar® foil with 1.7 MeV/amu particles [I.46].

I.1.2.3   OTHER SOURCES OF BACKGROUND

As explained earlier, charged particles interact with matter mainly through inelastic Coulomb encounter with bound electrons which lead to ionization. However, one has to be aware that other kinds of interactions of charged particles with matter are possible. Despite the fact that the large majority of the interactions of the ions are inelastic ones, elastic encounters may also occur. The measurement of the elastically scattered particles provides information on the elemental composition of the sample and on the distribution of the elements with depth. This information is at the origin of the Rutherford Backscattering technique (RBS) which is actually sometimes performed simultaneously with PIXE for complementary results [I.10]. However, the scattered particles have the great disadvantage of eventually depositing a large amount of energy into the X-ray detector used and consequently harming this latter. This can be easily avoided by placing a thin absorber in front of the detector but always at the expense of a significant reduction of the sensitivity for low energy X-rays from light elements.

Moreover, when PIXE analysis is performed with high energy projectiles bombarding especially light target elements, nuclear reactions appear as a competitive interaction. For instance, nuclear reactions such as (p, γ) present high cross-sections for protons energies from a few MeV up to tens of MeV. The dependence of the cross-sections for these reactions with target nuclide and incident particle energy is irregular but these generally increase with increasing incident energy, while intense resonance peaks at particular energies may also appear. Due to the Coulomb barrier, the cross-sections are smaller for the heavier target elements than for lighter ones. Such interactions may result in the emission of high-energy γ-rays, therefore far outside the 0-30 keV energy range typically observed in PIXE spectra, but which may then give rise to a high energy tail in the spectrum due to Compton scattering in the detector. Furthermore, γ-radiation can reach the detector after multiple scattering in the target chamber (including in the Faraday Cup where the beam is dumped) and so the resulting γ-ray background depends not only on the matrix composition but also on the details of the experimental set-up.

Folkmann *et al.* [I.47] found out that this background is dominant for $Z_T < 30$ at proton energies from 3 to 5 MeV. Hence, in an attempt to reduce the γ-ray backgrounds to a minimum, the projectile energy must be kept as low as possible whilst still high enough to provide sufficiently intense characteristic X-ray yields. In addition, Folkmann *et al.* [I.47] also concluded from experimental work that ions heavier than protons, but with the same velocity, have much higher incident energies and therefore present the great disadvantage of having much larger cross-sections for γ-ray emission. As a result, protons with energy inferior to 3 MeV are the preferable incident particles from the point of view of γ-ray background production.

Particular attention has therefore to be given to avoid any nuclear reaction with the most abundant nuclides of the matrix, as ^{12}C and ^{16}O for instance. As an example, the observation of some PIXE spectra after the beam was shut off showed that the γ-ray background component decayed with a 10 min half-life and could therefore be attributed to the positron emitter ^{13}N, formed by the (p, γ) reaction on ^{12}C. For this particular case, the proton energy and the foil thickness should be chosen such as the proton energy does not fall through 0.5 or 1.7 MeV while crossing the film in order to avoid enhanced cross-sections for this nuclear reaction, since these particular energies correspond to two resonance energies. In addition, it is highly recommended to avoid dealing with samples or bulk materials with high concentrations of light elements such as aluminium, sodium or especially fluorine since these elements are at the origin of significant γ-ray background [I.48]. For this reason, Kapton$^®$ or polyethylene support films are preferred rather than Teflon$^®$ ones for instance.

These conclusions combined with the fact that, as we already mentioned before, heavier projectiles do not originate improved signal-to-noise ratio despite the Z_p^2 dependence of the X-ray production cross-sections are the main reasons why 1-2 MeV protons are the best choice to perform PIXE analysis.

As a result, , it seems clear from this discussion concerning radiation background production that a rather adequate understanding of the main processes responsible for the continuous background in PIXE has been achieved. However, since the background contributions depend significantly on both the matrix composition and the incident particle energy (which varies as the beam goes through the specimen), it is unlikely to reach a simple and yet universal expression that may be used to describe the background continuum in mathematical terms sufficiently simple to use in routine PIXE analysis. As a result, in practice, the bremsstrahlung encountered in PIXE spectra is usually modelled with exponential polynomials in energy.

I.2 EXPERIMENTAL SET-UPS

The ion beams required in PIXE analysis are almost always provided by an accelerator. Because of the relatively low energy range usually required of 1-4 MeV/amu, small accelerators such as electrostatic ones (usually of the Van de Graff type) or small cyclotrons (especially for high energy PIXE) are sufficient. The ion beam emerging from the accelerator first passes through an analyzing magnet, which sorts out the ions of the correct mass and velocity, and then travels through the accelerator tube where it is normally focused by electrostatic or magnetic quadrupole lenses onto the specimen (the cross-section of the beam has an approximately Gaussian intensity distribution). However, when dealing with specimens that may have a non-uniform areal distribution, a homogenized beam profile is obtained by forcing the beam to pass through a thin metal foil where multiple small-angle scattering occurs. Useful visual inspection of the beam at various points along the beam line may be accomplished by retractable quartz viewers whose fluorescence can be observed by cameras. In addition, the use of several retractable Faraday cups at critical points allows numerous useful beam current measurements. The ion beams produced are then used to perform PIXE analysis in several different ways.

I.2.1 MACRO-PIXE IN VACUUM

Concerning macro-PIXE realized in vacuum, which is probably the most widespread variant of the PIXE experimental set-ups, the ion beam (typically 1-10 mm in diameter) penetrates into a vacuum chamber that operates under moderately high vacuum (10^{-5}-10^{-6} Torr) and where the irradiation of samples occurs. The main features of such irradiation chamber include a multi-specimen disposal, both beam and X-ray collimators, a Faraday cup where the beam is dumped, several exit windows to allocate several radiation and/or particle detectors and an absorber holder. A typical set-up of an irradiation chamber is depicted in Figure I.14.
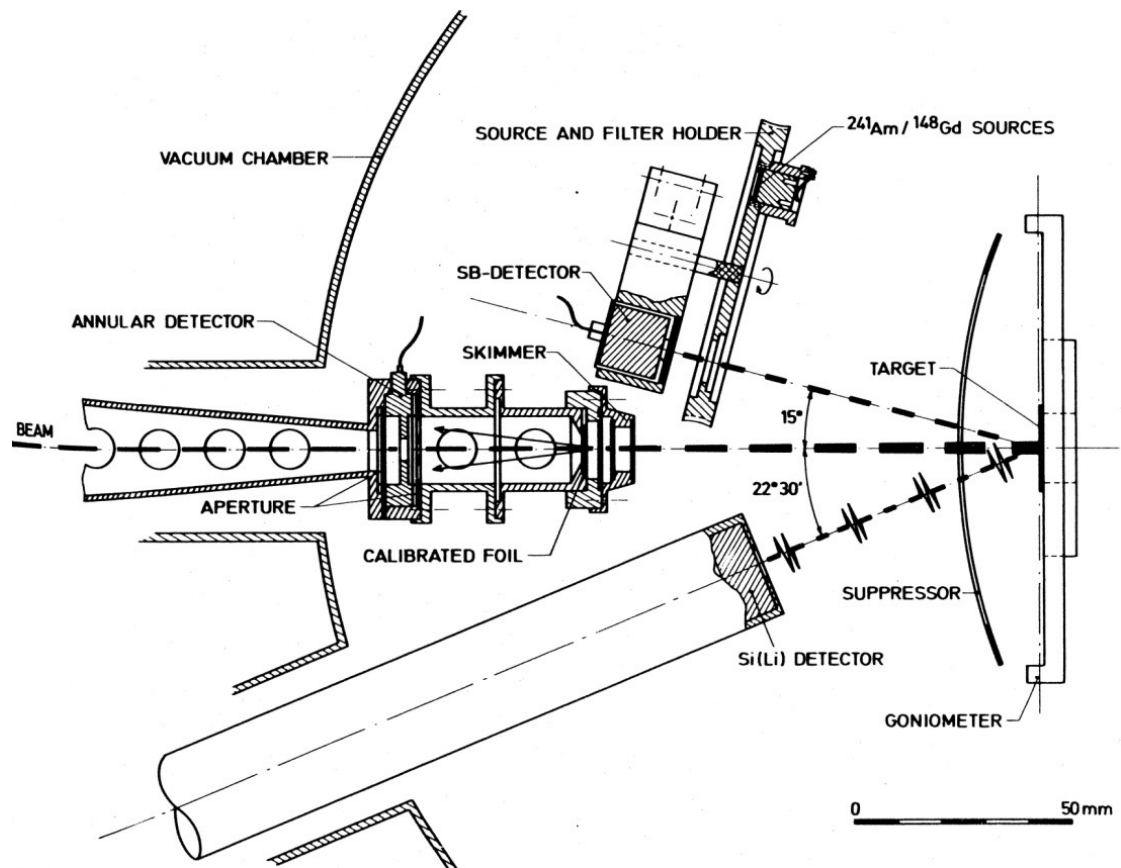
Figure I.14 – Typical Ion beam monitor arrangement [I.49].

It seems important at this point to characterize with some detail each of these elements. First of all, if the irradiation chamber is not connected to the beam line directly, the beam ought to cross a window to penetrate into the vacuum chamber. Even if metal foil windows provide greater longevity, their intense characteristic X-ray emission, coupled sometimes with undesired γ-ray emission via the (p, γ) reaction, forbids their use in this particular case. Instead, beryllium or polymer windows (such as Kapton® or Mylar®) are preferred. Then, the beam passes through collimators in order to guarantee that it impinges exclusively on the target sample. Again the material of theses collimators is chosen in order to withstand bombardment over long periods and simultaneously give rise to negligible amounts of both detectable X-rays and undesired γ-ray radiation background in the PIXE spectra. Although aluminium provides low energy characteristic X-rays, it also originates an intense nuclear gamma-radiation when stopping proton beams. Carbon (graphite foils) is the material of election for beam collimation purposes. However, for the case of protons, it is preferable to use beam energies below the 1.7 or 3.2 MeV thresholds because of the nuclear reactions that occur with ^{12}C and ^{13}C respectively. Also for these reasons, regions of the chamber or of the beam line that are exposed to scattered photons should be lined with graphite foil, including the Faraday cup where the beam is dumped.

A target holder defines the proper position of the sample during irradiation. A typical PIXE chamber should be designed to have a target holder that enables the allocation of several specimens simultaneously. The purpose of such disposal, which may

range from a simple ladder holding a few specimens to an automatic device remotely controlled, is to permit target changing (and hence consecutive PIXE analysis) while maintaining vacuum. Besides, since several analyses may be performed consecutively, each one giving rise to distinct PIXE spectra, many different absorbers are also required simultaneously in the vacuum chamber. Hence, beyond the multi-target holder, a PIXE irradiation chamber also usually provides a multi-absorber disposal that enables a useful variety of absorbers to be placed in front of the detectors, as we will discuss in more detail later in section I.2.6. Furthermore, this device may also be used to install radioactive sources that may be necessary for calibration purposes.

In order to minimize the radiation background contribution to the PIXE spectra, the X-ray detector should be placed at large angles with respect to the beam direction (backward angles of 135° or more), as already referred in section I.1.2.1, and only at a few centimetres from the irradiated target in order to maximize the solid angle subtended. Besides, this geometry has the great advantage of resulting in a sample-detector direction almost perpendicular to the sample surface and so generally gives the smallest X-ray absorption in the sample. This is of critical importance for analysis of low Z element.

In addition, it is useful in many applications to perform other complementary IBA techniques. An irradiation chamber should therefore be designed so that it is possible to incorporate other kind of detectors such as those of the surface barrier type or HPGe detectors. While surface barrier detectors aim to detect charged particles scattered from the target to perform RBS analysis, HPGe enables the detection of γ-rays resulting from nuclear reactions with the great advantage of maintaining almost constant detection efficiency [I.50] well beyond the 25 keV photon energy, which is the energy threshold from which the detection efficiency of Si(Li) detectors begins to decrease significantly.

I.2.2   MICRO-PIXE IN VACUUM

There is sometimes interest, in cases where the material properties depend on the spatial distribution and/or concentration of the component elements present in its matrix, to determine not only the concentrations of these elements but also to obtain spatial information from the specimen. In practice, micro-PIXE analyses are performed just as macro-PIXE ones but with the difference that a scanning system to raster the micro size beam over a sample is required.

Micro-PIXE (also known as nuclear microprobe) is similar to the EPMA technique but, as discussed in section I.1.2.2, heavy charged particle beams from nuclear probe present the significant advantage over electron microprobe from the EPMA technique to produce much less radiation background, leading to sensitivities 100-1000 times better (see further section I.5.1). However, ion beam focusing is also much more difficult to accomplish with heavy charged particles than with electrons. The beam focusing can easily be achieved through severe collimation restrictions [I.51], but always at the expense of a drastic reduction of the beam intensity, and/or either magnetically (the most widespread technique) or electrostatically [I.52]. As

a result, while electron microprobe beams with diameters down to the 0.1-0.5 μm range are commonly obtained, nuclear probes with diameters in the 1-50 μm range already represent quite an achievement. Naturally, micro-PIXE ought to be realized in vacuum to forbid scattering of the beam by the gas. Otherwise, only moderately small beam sizes (20-100 μm) are feasible.

In addition, comparing to macro-PIXE, micro-PIXE involves a remotely controlled data acquisition system to scan the nuclear microprobe over the sample surface [I.53]. Usually such analysis is performed by registering the positional information while acquiring the PIXE spectra event-by-event for each position and then, with off-line sorting of data, by constructing a two dimensional picture of the sample for each trace element. An illustration of the possibilities of such technique is presented in Figure I.15.
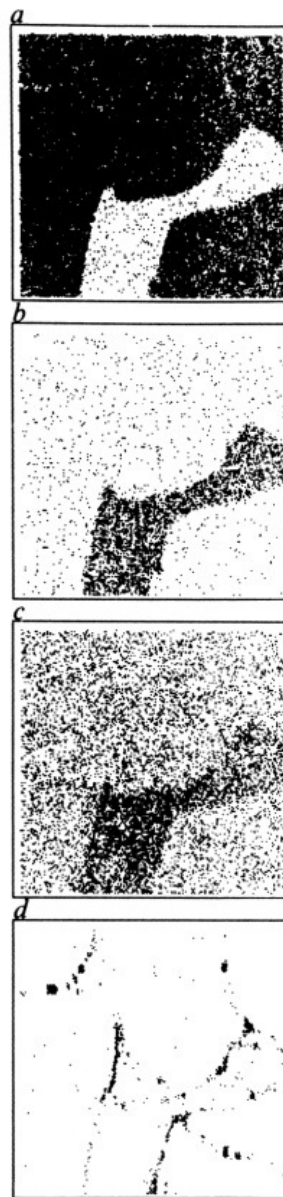

Figure I.15 – Elemental X-rays maps of the distribution of Ni (a), Cr (b), Mn (c) and Sr (d) in a 4×4 mm² thin section of a coarse garnet obtained using the proton microprobe. Dark areas indicate high concentration of the elements [I.54].

I.2.3 NON-VACUUM MACRO-PIXE/EXTERNAL BEAM

Non-vacuum PIXE analysis (also known as external beam analysis) is necessary when large objects are analysed (like in archaeology and art science), or with liquid and biological materials. In this case, the beam normally exits the vacuum beam line via a thin foil window (e.g. Mylar®, Kapton® or beryllium to ensure that it withstands high intensities and a high irradiation dose before mechanical breakdown) towards the sample that, together with the X-ray detection system, is situated in air, nitrogen or helium environment. For this latter case, since some X-ray detector windows are not leak proof to helium, the detector is usually separated from the chamber gas by an additional window.

This alternative of the PIXE analysis presents simultaneously advantages and disadvantages when compared to irradiations performed in vacuum. Among the advantages one can point out the simplified sample preparation and handling and the fact that the specimens are more effectively cooled at atmospheric pressure than in vacuum due to the increase of the heat conductivity, avoiding thermal losses of volatile elements or compounds [I.55]. At this point we should also notice that helium offers better heat removal than air, which is valuable in the analysis of specimens that are easily damaged, such as old documents. However, non-vacuum irradiations present intense X-ray radiation produced in the foil, part of which scattered by the sample into the detector. Moreover, a strong argon peak appears in the PIXE spectrum because the beam passes through air. In fact, since the measurement of the beam current is more complicated in the case of an external beam, the K X-ray peak of argon can be used to provide a useful measurement of the integrated beam charge. However, such interference can be avoided by using an helium atmosphere because the stopping power cross-section in helium is about four times lower than in air. Another disadvantage of bombardment in air is the danger of sample oxidation during irradiation.

A proof of the importance of such variant of the PIXE analysis is the fact that nowadays renowned museums all over the world own at least one accelerator to perform PIXE analysis of art objects on a daily basis [I.56],[I.57]. Indeed, PIXE analyses are common practice when the analysis of old artwork is required without, of course, damaging to the specimen [I.58].

I.2.4 BEAM CURRENT MEASUREMENT

The accurate measurement of the collected charge is not a simple task to accomplish since several experimental difficulties may arise. There are two distinct situations, namely the irradiation of thin or semi-thick samples (for which the beam ions pass through the specimen) and the bombardment of thick targets (for which the beam is totally stopped within the specimen).

For thin samples, including targets of intermediate thickness for which ions lose a considerable part of their initial energy but still cross the whole specimen, the beam is

usually dumped in a Faraday cup located in the beam trajectory behind the target. The measurement of the integrated charge is carried out by connecting the Faraday cup to a sensitive current integrator. Some considerations about the Faraday cup have also to be made. One is to place a negatively biased ring, or grid, in front of the cup to avoid the escape of secondary electrons from the cup, which results in an overestimate of integrated charges. The ratio of secondary electron to incident beam intensity varies markedly among the elements [I.59],[I.60]. On the other hand, in order to prevent the detection of both γ-ray background and characteristic X-rays resulting from the beam interaction with the matrix of the Faraday cup, the use of long cup (eventually lined with graphite foils, as we explained earlier) placed far from the X-ray detector is preferable.

For the case of the irradiation of thick samples, the measurement of the beam current becomes a more complicated matter that requires an indirect approach for insulating samples for which the measurement cannot be accomplished on the specimen itself. A possible way to deal with this problem is to coat the surface of insulating samples with a thin layer of conducting material to perform direct measurement of the beam current [I.61]. Nevertheless, this method cannot be used for surface analysis. Another method consists in using a conducting strip as a beam chopper which periodically intercepts the beam.

In order to avoid these experimental difficulties, methods that do not rely on any current measurement have also been developed. Among them, one possible method consists in interposing a calibrated reference foil in the beam path. While the beam passes un-deviated through the thin reference foil, a surface barrier detector measures the intensity of the backscattered particles from the foil [I.49],[I.62]. This method is not applicable with nuclear micro-probes because the scattering in the foil causes unacceptable beam divergence. It is also possible to irradiate a reference standard before bombarding the specimen of interest and then compare the intensity of the characteristic X-rays lines [I.63]. However, this approach has the inconvenient that it is fundamental to keep exactly the same irradiation conditions between runs to perform any quantitative comparison, and this can represent experimental difficulties that originate larger uncertainties. Another elegant approach consists in spiking the sample with a calibrated, analysis non-disturbing, known amount of an element that serves as an analysis non-disturbing internal reference. The amount (or concentration) of the trace-elements of interest is then obtained by direct comparison between the intensity of their characteristic X-ray line in the PIXE spectrum and the intensity of characteristic peak originated by the internal reference [I.65].

I.2.5   TARGET PREPARATION

Although PIXE analyses can ideally be performed with any kind of specimen, many considerations have to be dealt with depending on the sample to be analyzed. For instance, the irradiation of liquids samples cannot be performed directly in vacuum

without any target preparation because of obvious out-gassing during vacuum pump-down.

Sample preparation differs extremely depending on the state of the sample. This may vary from simple cleaning of the sample (to remove surface contamination), polishing (to eliminate surface roughness effects), and powdering (to homogenize the sample and to reduce the particle size), to some physical or chemical pre-concentration or separation (this can also be simply drying the sample, for example).

In all cases, these preparation procedures aim to obtain a small but representative quantity of specimen material on a substrate. The substrate (or support material) to be used also requires a careful selection since it has to fulfil simultaneously many requirements; namely to have high mechanical strength, good thermal conductivity, to withstand high intensity irradiations, to be as thin as possible to minimize continuous bremsstrahlung background, to be highly pure in order to minimize characteristic X-ray background interferences, to be made of low Z-elements in order to minimize both secondary electron and proton bremsstrahlungs and detectable characteristic X-rays. Although all parameters cannot be optimized simultaneously, plastic foils such as Formvar®, Kapton®, Mylar® and polystyrene have all been successfully used as thin backing materials through the years. One has to point out that for biological tissues and organic material the problems of sample preparation are often more severe.

The contamination issue is the most critical problem. Since a common PIXE analysis aims to measure μg/g levels of trace elements, which typically correspond to absolute amounts of matter in the nanogram region or below, contamination control is fundamental because there is no interest in having a powerful and highly sensitive multi-elemental technique if impurities mask the results. Hence, one should exclusively use acid-cleaned plastic and highly pure chemicals, acids and water during sampling and sample preparations. On the other hand, continuous development on the fabrication of ultrapure backing materials is therefore an important task. In addition, the use of a clean bench with laminar flow during sample preparation is advisable.

On the other hand, the heating of the specimen is another issue of practical importance. When the particles pass through the target, a large amount of energy is deposited in a limited volume (a situation which is even worse in the case of thick targets where the beam is totally stopped) and converted to heat. The consequent rise of the temperature of the target, especially when dealing with material of poor heat conductivity, can lead to the evaporation of some volatile compounds or elements of the specimen, such as bromine, leading so to false results of trace elements concentrations. This issue has been described by many workers of the field [I.12],[I.53]. On the basis of extensive experience, Maenhaut [I.11] suggests that the current density should not exceed 5 nA/mm² for vacuum irradiations of thin targets. Consequently, arrangements to prevent heating of the sample are also needed (especially in micro-PIXE), such as deflecting the beam periodically [I.66]. The beam deflection technique uses a pair of electrostatic plates that are both maintained at equal potential voltage in order to let the beam pass un-deflected between them in normal conditions while, when the X-ray

detector registers an event, its preamplifier triggers fast-acting circuitry to remove the voltage from one plate, establishing therefore an electric field between the plates which is sufficient to deflect the beam off the collimator aperture and so off the specimen. Besides, this eliminates the need of measuring the dead time due to signal processing since, during this dead time, there is no beam interacting with the target to generate X-rays.

Beyond heat induced damages, care with sample charging has also to be considered. When the irradiated sample is an insulator, it becomes highly charged due to the bombardment. Even if this effect does not lead to any electrical discharge resulting in the specimen deterioration/destruction, it results in a huge amount of radiation background in the PIXE spectrum that therefore worsens the sensitivity [I.67],[I.68]. As we can observe in Figure I.16, an easy way to avoid such deterioration is to make the sample conducting. Another efficient technique consists in spraying the sample with electrons during the irradiation, as it can be seen in Figure I.17.
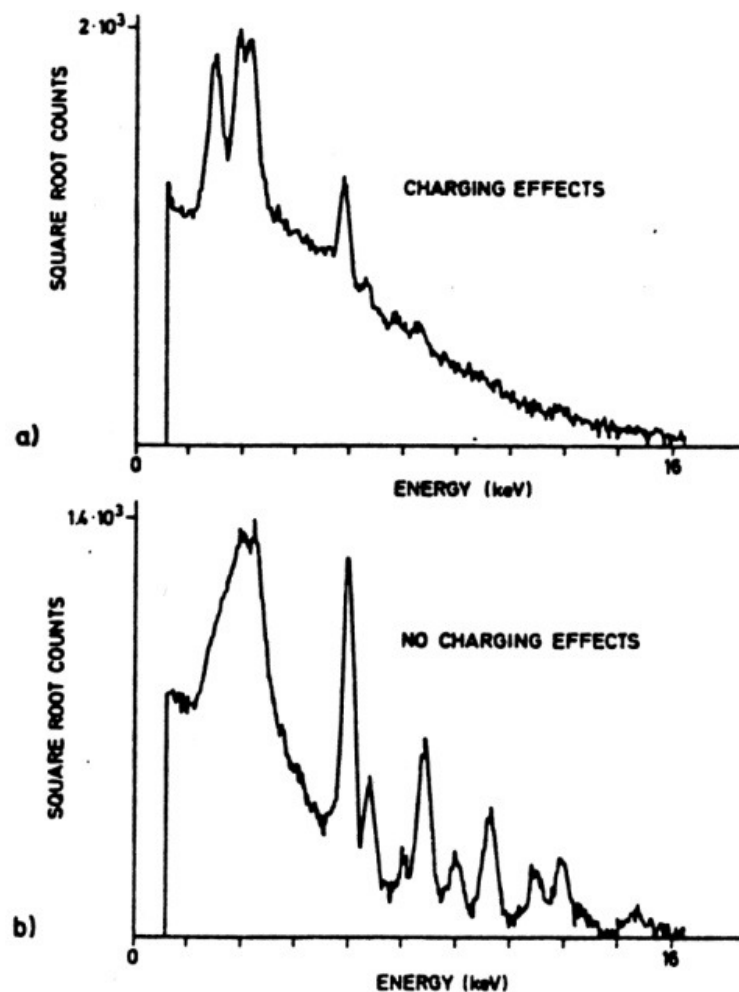
Figure I.16 – Spectra from an insulating air particulate sample before a) and after b) the surface was made conducting thanks to aluminium tape [I.61].
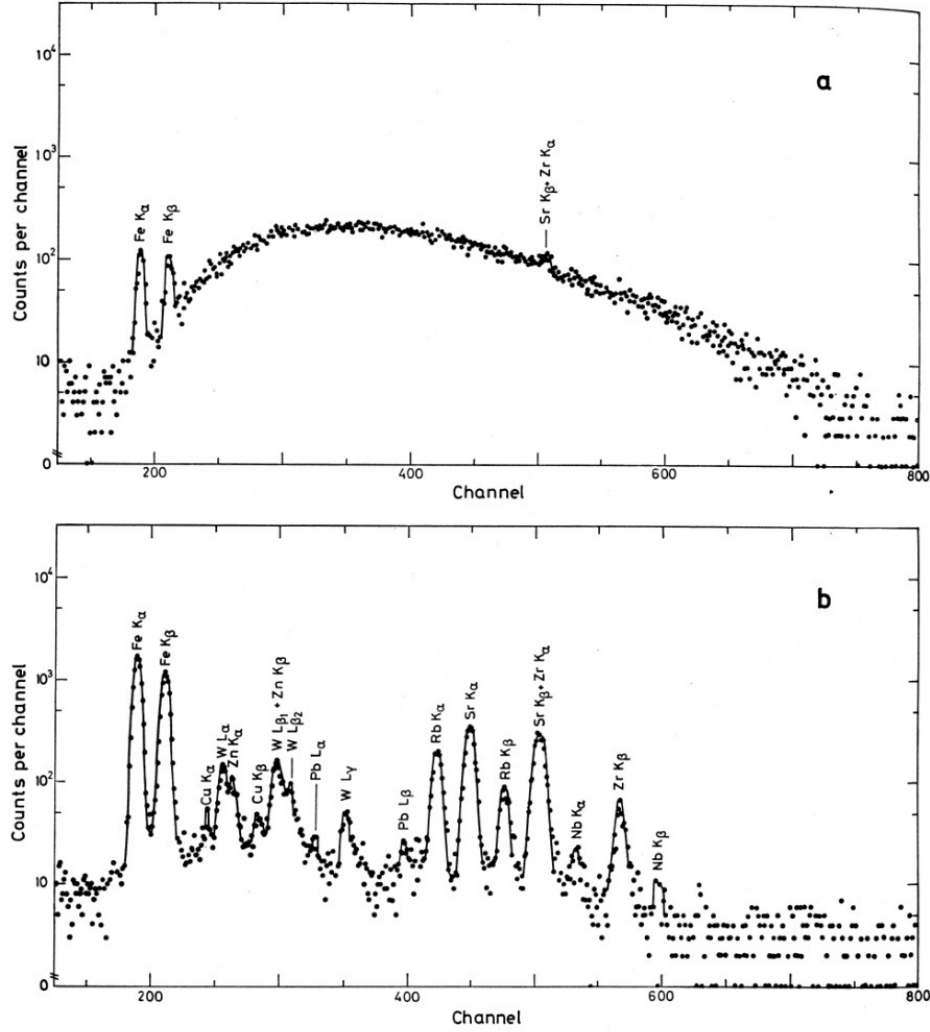
Figure I.17 – Spectra obtained by irradiating of a granite sample with 2 MeV protons and with the low energy X-rays absorbed in an Al absorber; a) when charging limited the proton beam to 3 nA b) with a beam current of 50 nA, charging being eliminated by the use of a heated carbon filament in the sample chamber [I.68].

I.2.6 X-RAY SPECTROMETRY

One can distinguish two kinds of X-ray spectrometry techniques, namely energy-dispersive and wave-length dispersive techniques. Although wavelength dispersive techniques present the best energy resolution (typically some tens of eV, i.e. almost an order of magnitude better than energy dispersive techniques with solid state detectors) allowing almost interference-free spectrum evaluation, they also have disadvantages such as low efficiency, further post-irradiation scanning and low detectable area that result in extremely long irradiations to perform a PIXE analysis with sufficient statistic. As a result, despite giving rise to eventual interferences in the PIXE spectrum, energy-dispersive detectors (mainly Si(Li) ones), are the most widespread X-ray detection systems used in PIXE arrangements. In addition, their relatively large sensitive area

(some tens of mm^2) and high efficiency enables simultaneously convenient, efficient and fast multi-elemental PIXE analyses.

Si(Li) detectors are provided with several different sensitive areas and different detection performances. The simultaneous optimization of both characteristic is not possible since improved energy resolutions exclude large detection and vice versa. As a result, it is common practice to employ two Si(Li) detectors operating simultaneously. While a smaller detector (typically 10-30 mm^2 active area) provides highest energy resolutions for very low energy X-rays, a second detector is employed (with an absorber filter to suppress the low-energy region of the spectrum) in order to be used exclusively for the high-energy region with both large detectable areas (typically 50-80 mm^2 active area) and high efficiency.

Besides, since usual Si(Li) detectors do not allow the detection of very low energy X-rays with energy below 2-3 keV (typically potassium or calcium K-lines) because of its Be window, the use of windowless detectors is required for the analysis of lighter elements down to B or C [I.69]. However, the use of such detectors also demands extra experimental arrangements to avoid the direct interaction of backscattered particles with energy of a few MeV into the detector. This can be done by using permanent magnets between the irradiated specimen and the windowless X-ray detector, but always at the expense of a severe reduction of the detector solid angle. Alternatively, in less critical cases, the use of X-ray detectors with an ultra-thin window combined with incident particles of relatively low energy (less than 1 MeV), so that the backscattered ones are still absorbed in the window, is another solution.

We must point out that the use of a gamma-ray detectors (of the Ge or Na(Tl) types) is often supplied to perform simultaneously Particle-Induced Gamma Emission (PIGE) analysis since some light elements have high cross-sections for production fo gamma-rays through nuclear reactions.

A feature which is characteristic of all energy-dispersive detectors (including therefore Si(Li) solid-state detectors) is the fact that their pulse processing electronic demands large time constants for optimum energy resolution (tens of μs). This is of great importance from an experimental point of view since it results in experimental restrictions of great concern. Indeed, when dealing with relatively high counting rates, this characteristic invariably causes spectral deterioration due to pile-up effects, i.e. a continuum to the right of a given characteristic peak (Figure I.18), which might prevent the detection of other characteristic X-rays from trace elements of interest. Moreover, this pile-up effect can also be observed when an intense characteristic X-ray peak is present in the PIXE spectrum because of the matrix composition (usually from low Z elements). For this reason, the limited counting capability of energy-dispersive detectors must be used wisely. In order to reduce the use of a significant part of the available counting rate in detecting undesired X-ray counts, the spectral shape can advantageously be modulated by placing absorbers in front of the detector.
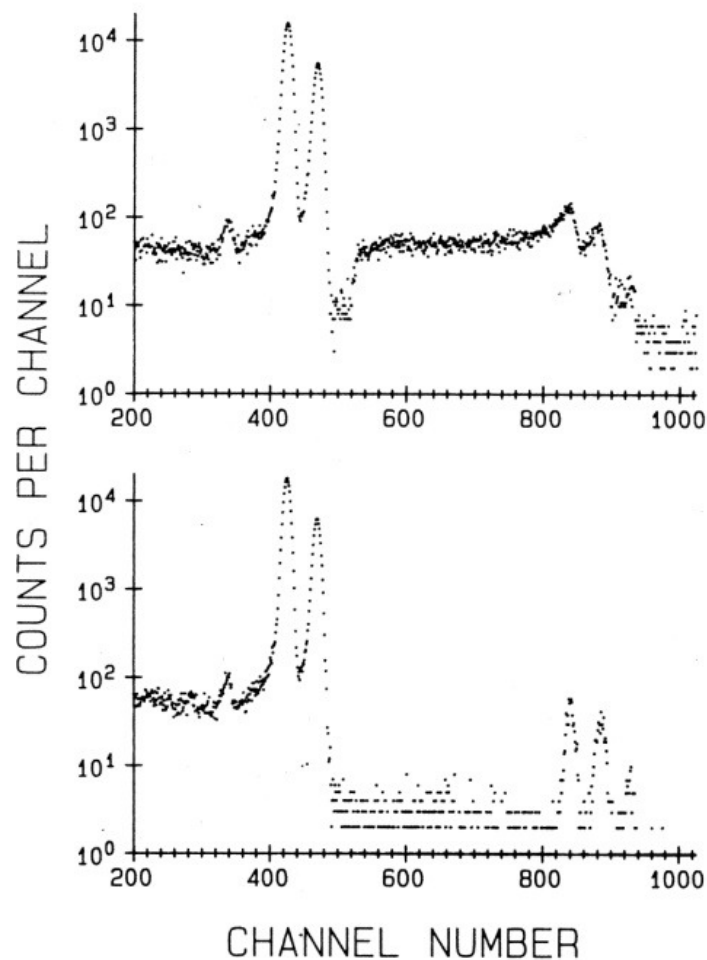
Figure I.18 – Copper K- X-ray spectra recorded with (lower) and without (upper) a beam deflector used to avoid simultaneously pile-up effects and damages of the specimen [I.70].

As it can be seen in Figure I.1, PIXE spectra have a significant part of the X-ray counts in the low-energy region, due to the radiation background contribution, although this region is not of interest, in most of the cases. As a result, most of the detector limited counting capability is wasted. A way to avoid this situation is to use an absorber in front of the detector that significantly absorbs the electron bremsstrahlung background and the characteristic X-rays up to the 3-5 keV energy range depending on its thickness, while transmitting without any interference the characteristic X-rays of higher energies, i.e. from heavier elements. Absorbers consist in thin foils (50-250 μm) made of either light elements, such as beryllium, aluminium or organic materials as Kapton® or Mylar®. Although the use of an absorber is unfortunately at the expense of a significant reduction of detection sensitivity for a number of interesting trace elements with low atomic number, this also permits stopping scattered particles. Another advantage of such absorbers is to reduce the acquisition/irradiation time since higher beam currents are then allowed without pile-up issues.

On the other hand, when an undesired interference consists in a specific X-ray line from an element which is, for example, the main constituent of the backing material (and whose contribution is not significantly reduced with a standard absorber because of a greater X-ray energy), this can interfere with neighbours lines of elements of interest. In

such cases, a "band-pass" absorber is usually used to attenuate selectively, and almost exclusively, the contribution of this specific X-ray line in the spectrum. This latter consists of a thin foil of a specific element whose K-edge absorption is close to the unwanted characteristic X-ray energy. Then, the absorption is almost nil for all the energies of the PIXE spectrum, except in the vicinity of that K-edge. For instance, a chromium absorber suppresses the Fe K- line but still allows high transmission of X-rays below and above that energy [I.71].

On the other hand, when low-energy X-ray lines (from low Z elements) are the ones of interest neither usual nor "band-pass" absorbers can be used since they would suppress the peaks entirely, along with the undesired continuum or provoke a significant counting rate reduction since characteristic X-rays of neighbouring elements have quite close energy values. A clever solution consists in using a "funny filter" which is a thin absorber with a hole in its centre, so that only a fraction of the low-energy X-rays (i.e. with a smaller solid angle) is allowed to reach the detector while the X-rays from heavier trace elements pass unaffected by the interposition of the absorber due to their greater energies. This enables to significantly reduce the number of both low energy X-rays and low-energy bremsstrahlung background detected but still allow a sufficient number of counts to be collected in a reasonable time, as illustrated in Figure I.19. All of the X-rays detected, and so the available counting capability of the X-ray detector, is therefore equally balanced between the high- and low-energy regions of the X-ray spectrum.

Another way to emphasize regions of interest is to perform several irradiations with different absorber thicknesses and/or pinhole diameters and eventually different beam energies.
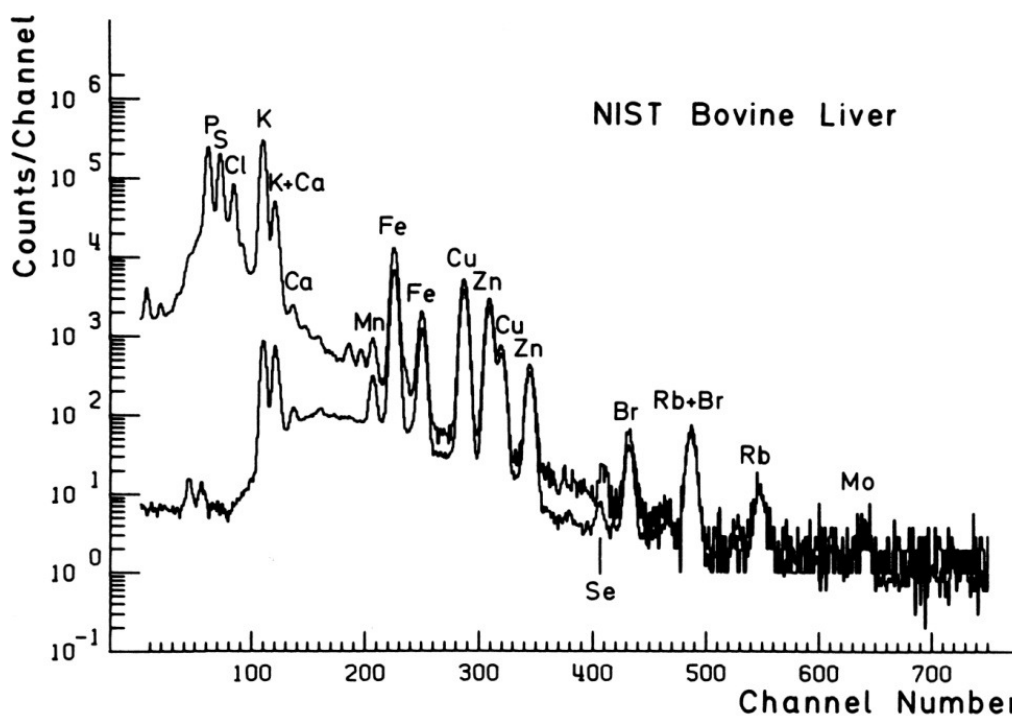

Figure I.19 – PIXE spectra for a bovine liver specimen with an incident beam of 2.4 MeV. Top spectrum taken with a funny filter, a beam current of 10 nA and an integrated charge of 20 μC. Bottom spectrum taken with a 660 μm Mylar® absorber, a beam current of 150 nA and an integrated charge of 200 μC [I.11].

I.3   QUANTITATIVE ANALYSIS

As already explained earlier, the basis for a PIXE quantitative analysis is the relationship between the net area of a characteristic K- or L- X-ray line from a particular element in the PIXE spectrum and the amount of this element present in the sample. Considering protons of initial energy E_0 as incident particles, for a homogeneously distributed trace-element of atomic number Z, atomic mass A_Z, and concentration C_Z, the elemental number of characteristic X-rays of its p-line, $dY_{p,Z}$, originated along an elemental path dx is then

$$dY_{p,Z} = N_p\, \sigma_{p,Z}^X(E) \left(C_Z\, \frac{N_{AV}}{A_Z}\, \rho\right) dx = N_p\, \sigma_{p,Z}^X(E) \left(C_Z\, \frac{N_{AV}}{A_Z}\right) \frac{dE}{S_M(E)} \quad \text{(Eq. I.3)}$$

where N_p is the number of incident protons, N_{AV} Avogadro´s number, ρ the specimen density, $\sigma_{p,Z}^X(E)$ the X-ray production cross section for the p-line of the element Z and $S_M(E)$ the effective stopping power of the matrix (M) of the target, which is defined as $S_M(E) = (1/\rho)\,(dE/dx)$.

By generalizing θ and φ as the angles between the incident beam and the specimen surface and between the specimen surface and the detector direction respectively (Figure I.20), it follows that the number of X-rays $N_{p,Z}$ of the p- (K-, L- or M-) X-ray line in the PIXE spectrum due to an element of atomic number Z is related to X-ray production cross-section $\sigma_{p,Z}^X(E)$ through the following relationship:

$$N_{p,Z} = N_p\, \frac{\Omega}{4\pi}\, \epsilon_{p,Z} \left(C_Z\, \frac{N_{AV}}{A_Z}\right) \int_{E_0}^{E_f} T_{target}(E)\ \sigma_{p,Z}^X(E)\, \frac{dE}{S_M(E)} \quad \text{(Eq. I.4)}$$

where E_f is the final energy of the incident particles, $\epsilon_{p,Z}$ is the detector efficiency for the considered p-line of the element Z (which includes the window transmission, the transmission of eventual absorbers which are especially used to filter low energy X-ray and the eventual loss of primary electrons for low X-ray energy to the detector window), $\Omega/4\pi$ is the solid angle subtended by the detector and $T_{target}(E)$ is the X-ray transmission though the sample itself (i.e. this coefficient takes into account the target X-ray self-absorption). $T_{target}(E)$ is defined as (Figure I.20)

$$T_{target}(E) = \exp\left(-\, \frac{\mu_{p,M}\sin\theta}{\rho\,\sin\varphi}\, \int_{E_0}^{E_f} \frac{dE}{S_M(E)}\right) \quad \text{(Eq. I.5)}$$

with $\mu_{p,M}$ as the linear absorption coefficient for the p-line in the matrix (M).

Alternatively, as explained in [I.5],[I.6], for the case of a thick target in which the ions are totally stopped, $N_{p,Z}$ can also be expressed as

$$N_{p,Z} = N_p\, \frac{\Omega}{4\pi}\, \epsilon_{p,Z} \left(C_Z\, \frac{N_{AV}}{A_Z}\right) \rho \int_0^{x_0} e^{-\mu\frac{\sin\theta}{\sin\varphi}(x_0-x)}\ \sigma_{p,Z}^X(E(x))\, dx \quad \text{(Eq. I.6)}$$

where x_0 is the range of the impinging ions of initial energy E_0.
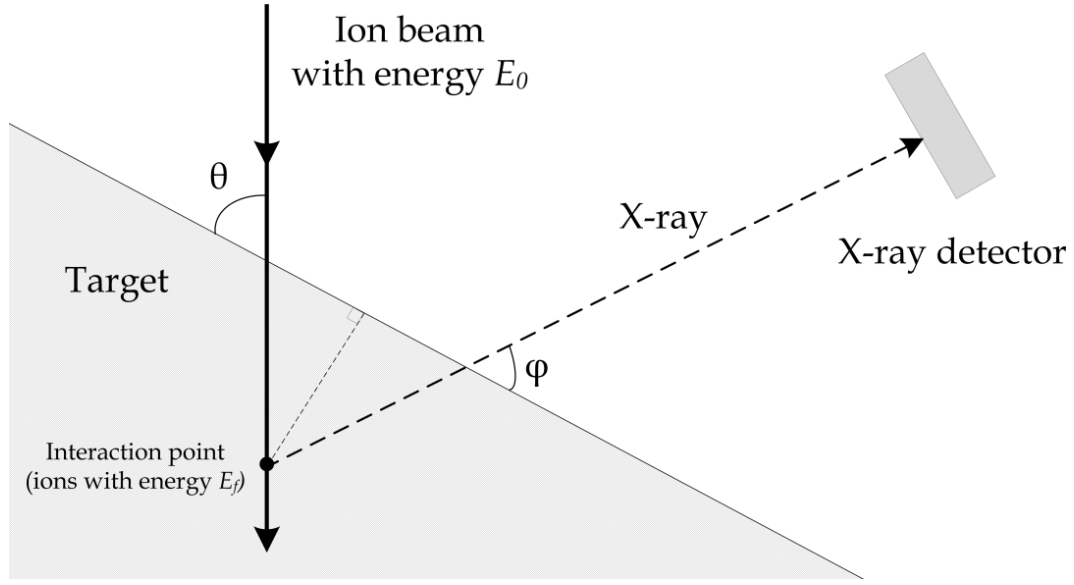
Figure I.20 – Geometric representation of an ion beam impinging on a target.

I.3.1   THIN SPECIMENS

For the case of a thin target with thickness τ, for which self-absportion of X-rays no longer exists (i.e. $T_{\text{target}}(E)$ equals unity in Equation I.4), the ions are almost not slowed down and their energy E_0 is therefore constant within good approximation. Hence, the X-ray production cross-section $\sigma_{p,Z}^X(E)$ no longer varies along the sample, being equal to $\sigma_{p,Z}^X(E_0)$, and $N_{p,Z}$ is then given by:

$$N_{p,Z} \;=\; N_p \;\; \sigma_{p,Z}^X(E_0) \;\; \left(\tfrac{\Omega}{4\pi}\right) \;\; \epsilon_{p,z} \;\left(C_Z \tfrac{N_{AV}}{\sin\theta \; A_z}\right) \left(\tfrac{\rho\tau}{\sin\theta}\right) \qquad\qquad \text{(Eq. I.7)}$$

While $\Omega/4\pi$ is determined by the geometry of the experimental set-up, N_p is experimentally obtained from the integrated charge in the Faraday cup, Q_p, ($N_p=Q_p/qe$ where e is the charge of an electron and q the charge of the ions of the beam). Concerning the efficiency $\varepsilon_{p,z}$ of the detector, although this is usually provided by the manufacturer its accuracy might be insufficient and it is therefore advisable to calibrate the detector, especially in the low-energy X-ray region [I.72].

We can conclude from the above discussion that all the quantities in Equation I.7, except C_Z and $N_{p,Z}$, are either known or can be determined experimentally and independently. This is the reason why PIXE is an absolute method.

Moreover, the knowledge of the specimen mass thickness τ is required to express the results of an analysis in terms of either concentrations or absolute amount of matter. If the determination of τ represents some experimental difficulty [I.73], this latter can be overcame by the use of an internal standard of known amount in the specimen [I.63]-[I.65]. This is realized by doping the sample with this standard prior to the specimen preparation. Then, quantitative calculations involve dividing Equation I.7 for

the trace element considered by the same equation for the internal standard so that the specimen thickness $\tau/\sin\theta$ cancels out. As mentioned earlier in section I.2.4, another advantage of spiking the target is to avoid the measurement of the beam integrated charge since the number of incident particles N_p also cancels out. Alternatively, another possibility consists in bombarding a standard sample of known composition and thickness under the same conditions as the sample to be analysed. Then, the elemental abundances in the unknown specimen are determined by comparing the peaks heights in the two spectra obtained.

I.3.2   THICK SPECIMENS

The considerations of the previous section rely on the assumption that the X-ray production cross-section $\sigma_{p,Z}^{X}(E)$ is constant, i.e. that the energy of the beam particles remains almost equal to E_0 while passing through the target. However, this is no longer true when incident particles are slowed down, i.e. when dealing with target of substantial thickness, since these cross-sections depend significantly on the particle energy E. By targets of considerable thickness, we mean targets for which the incident particles are considerably slowed down and lose a significant fraction of their initial energy E_0 while, on the other hand, thick targets are defined as the ones with thickness larger than the range of the incident particles.

In such case, Equation I.4 must be used to carried out a quantitative analysis and the knowledge of additional parameters is then required when compared to the case of thin targets. These parameters are the energy loss E_0-E_f (determined either indirectly through the knowledge of the specimen thickness or by some experimental determination), the stopping power of the projectile in the matrix (*M*) and the mass absorption coefficients for the self-absorption of the X-rays. These latter might originate difficulties since their determination depends of the knowledge of the composition of the sample.

I.3.3   SPECTRUM ANALYSIS

Either considering thin or thick targets, any quantitative analysis of an element of interest requires the determination of the number of counts $N_{p,Z}$ in each p- (K-, L- or M-) X-ray lines in the PIXE spectrum. Such determination consists in identifying all the peaks arising from the radiation background in a PIXE spectrum, determining their energies, and then extracting the required peak intensities. The intensity of a peak can be determined manually by estimating and subtracting the background but this is obviously an impossible task to realize when dealing with spectra containing several peaks. Consequently, computer programs are invariably used. These programs make use of the least-square method to fit the radiation background with polynomial or exponential polynomial functions upon which gaussian functions are used to model the arising characteristic X-ray peaks.

On the other hand, instead of using only such a purely analytical tool, other fits have been developed by using the physics involved in the X-ray generation and detection for the explanation of the PIXE spectra, originating this way a functional model that depends on several parameters [I.74]. This approach improves the fit to the radiation background by considering its expected shape due to the fact that it is composed by bremsstrahlung emitted from secondary electrons in the low-energy part of the spectrum and projectile bremsstrahlung and Compton scattering processes for higher energies. Then, the gaussians superimposed on this generated background, not only fit the peaks in the spectrum but also present a width that depends on the energy of the X-ray line considered because of the energy resolution of the X-ray detector. Besides, several peaks are also considered to have fixed ratio intensities in order to take into account the fact that a given element gives rise to some characteristic peaks with fixed relative intensities.

In the earlier years of PIXE, these computer programs were actually adapted from codes generated for γ-ray spectroscopy and enabled spectrum evaluation including up to six peaks. Nowadays, software packages such as GUPIX [I.75] not only identify and fit to gaussian the peaks beyond the radiation background but also directly calculate the amount and/or concentration of each trace element present in the sample, by making use of the amassed knowledge of the X-ray production cross-sections for different incident particles and at different energies, solid angles effects, X-ray transmission corrections and calibrated detection efficiencies.

Nevertheless, despite the quality of the software packages, peak interferences are still unavoidable, mainly due to the limited resolving power of the X-ray detectors available. Spectra with only few well distinguished peaks are scarce. Indeed, in most of the practical cases, a multitude of trace and minor component elements compose the specimen analysed, with each of these giving rise to more than one characteristic line because of the K-, L- and M- shell transitions (the X-ray production cross-sections are larger for M- lines than for L-lines, which are themselves larger than for K-lines). K-lines are usually provided by the lighter elements while L- and M- ones result from the interaction of the beam with heavier elements. In addition, the K-, L- and M- X-ray lines are themselves subdivided to give peaks corresponding to K_α, K_β, L_α, L_β, L_γ, etc... As a result, it seems unlikely that neither overlapping nor interfering occurs in typical PIXE spectra. One can distinguish several kind of interference issues encountered, namely the overlapping of the K_α of an element Z and K_β of the element Z-1 for X-ray energies below approximately 8-10 keV (beyond such energies the energy differences allow the detector to separate these interfering lines) or else interferences between the L- X-ray lines of medium atomic number elements and the K- X-ray lines of low Z elements. Illustrating issues encountered in practice are, for instance, the ambiguity between the K_α X-ray of sulphur (2.308 keV) and the $M_{\alpha 1}$ line of lead (2.346 keV) or the coincidence between L_β peak of cadmium (3.317 keV) and the K_α of potassium (3.314 keV).

This complicated task of interpreting the recorded spectrum is a typical issue in PIXE analysis that cannot be minimized. Hence, an initial idea of the major constituents making up the specimen may be valuable to avoid such ambiguities.

I.4 APPLICATIONS OF PIXE ANALYSIS

A demonstration of the potential of PIXE as a multi-elemental analysis tool lies in the remarkable wide range of applications in which this technique has been applied through the years, giving rise to a vast number of publications and dedicated conferences. Among these areas of interest we must point out:

- ✓ Biological and medical samples
- ✓ Environmental specimens
- ✓ Art and archaeology
- ✓ Analysis of materials

The usefulness of PIXE in such distinct and numerous areas is mainly due to the fact that the samples to be irradiated can be provided, almost restriction free, in many ways (which is an advantage of great importance because of the natural severe practical limitations in most of the cases), namely either thick or thin; they can come in a variety of shapes and sizes; can be precious or without material value and may take the form of a solid, liquid or gas. On the other hand, the non-destructive nature of the technique combined to the minimal beam induced effects on the specimen itself are other valuable advantages over more classical physical and chemical methods.

One of the most important applications of PIXE is the analysis of biomedical samples. PIXE is useful for analytical purposes in areas such in physiology and pathology because in some cases there is a relationship between trace elements levels in biological samples and diseases such as cancer formation, brain pathologies or pulmonary disorders. Indeed, trace elements are fundamental in biological systems and the deficiency or overabundance of such trace elements is known to be associated with several diseases. Such investigations are usually accomplished by performing multi-elemental analyses in several biological specimens such as hair, skin, brain, urine, bones, teeth, nails, blood and saliva; in both normal and disease states to enable comparisons. These analyses are focussed in the detection of either "essential" minor or trace elements (such as K, Ca, Mn, Fe, Cu, Zn or Se) or "toxic" trace elements (like Cd and Pb) resultant from pollutants from modern industry. For instance, cadmium concentrations in kidneys might reflect the status of a specific disease under study while copper, zinc and iron concentrations are fundamental in blood and liver tissues, scandium and chromium in marrow specimens and fluorine in teeth samples. When dealing with body fluids and single cells, it is also the ratio between two specific trace elements of interest that can be used as an index of some pathological states.

Another area that represents a significant portion of the PIXE applications is the analysis of environmental samples such as water pollutants, air particles, aerosols, soil and botanical materials (leaves, algae, enzymes and proteins) due to the increasing concern of governments and international agencies in the gradual erosion of the quality of the environment by industrial, man-made and natural pollutants. For instance, an extensive network of aerosol monitoring stations has been developed since the first years of the PIXE technique in order to investigate the harmful effects of the retention of air

pollution in the human respiratory system. Such air pollution analyses are requested indoors (i.e. in hazardous working environments such as found in mining industry, paint spray shops, welding operations or cement works) and outdoors near specific pollution sources or urban pollution of large cities (mainly because of the inhalation of automotive emissions). Besides, the analyses of environmental samples might have totally different purposes. For instance, trace element concentrations in ground water are used as an indicator of ore prospecting while the analysis of oil when oil pollution occurs serves as a "fingerprint" to identify the origin of this pollution. Such samples are typically collected by deposition of the trace-elements onto thin foils of light elements thanks to devices such as streakers, cascade impactors or stacked filter units.

The non-destructive feature of PIXE is very convenient for analysis of priceless, old and unique archaeological and art objects (such as handwriting papyrus or oil paintings) that cannot obviously suffer any kind of damage despite being in most cases very sensitive to heat or radiation (as the Gutenberg Bible and the Vinland map for instance). Such analyses are performed for authenticity, provenance, deterioration and conservation purposes. In many cases these analyses are performed in either large objects and/or very small samples of extremely fragile specimens that cannot bear any target preparation and therefore external beam arrangements are required, which additionally have the advantage of providing improved heat dissipation. For instance, PIXE analysis has revealed population movements and trade routes by allowing the analysis of hundreds of antique objects.

Finally, the last application field that we point out here is the analysis of materials. This latter varies from the analysis of forensic and geological specimens, to metal analysis, and to surface analysis of materials. Indeed, PIXE analyses are performed in geological specimens as a way to study phenomena such as climatic changes or corrosion and erosion through the variations of the trace-elements concentrations with depth in either the earth crust or sea water sediments. Besides, PIXE is used to detect the presence of impurities in the surface of samples of technological and industrial interest such as electronic components and metallic oxide layers. The latter application is also used to provide elemental distributions of bulk impurities in integrated electronic devices or solid-state based materials in order to diagnose errors in the manufacturing process. The nuclear microprobe is also useful to investigate the spatial distribution of the elements present in a sample, especially in cases where the properties of a material depend on it.

Considering the diversity of all the application fields of PIXE, and the still growing interest in using small accelerators and dedicated ion beam facilities, it seems likely that PIXE and other IBA techniques will be increasingly applied analytical tools in the future.

Although the PIXE technique has valuable characteristics that represent practical advantages of great importance, as mentioned before, it is also true that the spectral

interferences combined to complicated analytical corrections represent an important inconvenience in the use of this technique. As a result, it may be useful to make use of another advantage of the PIXE technique, which is the fact that it can be used simultaneously and in-situ with other IBA techniques, such as elastic scattering spectrometry (usually with Rutherford Backscattering Spectrometry - RBS) [I.10] or Nuclear Reaction Analysis (RNA) (mainly Particle Induced Gamma-ray Emission - PIGE) [I.77]. Elastic scattering spectrometry techniques involve the detection of either the elastically scattered incident particles or the elastically recoiled target nuclei. On the other hand, RNA techniques are based on nuclear reactions of interest between the impinging particles and the target nuclei and are implemented by detecting the resulting γ-radiation, usually with a germanium detector.

The RBS technique, which is appropriate only for light elements analysis (up to silicon or phosphorus), has the advantage over PIXE of distinguishing the isotopes of elements of very low atomic number Z (from chlorine down to boron), as illustrated in Figure I.21, and to provide additionally depth profile information; but at the expense of much more energetic particles to obtain suitable particle deviations (typically about 20 MeV). On the contrary, PIXE enables to resolve identification ambiguities that are always present in the RBS technique because of the depth dependent energy of the scattered particles. Additionally, PIGE is fundamental for analysis of very low Z elements (from potassium down to lithium) with good sensitivity (typically 10-100 μg/g) by detecting the γ-radiation emitted from (p, γ) nuclear reactions, such as $^{19}\text{F}(p, p'\gamma)^{19}\text{F}$ or $^{19}\text{F}(p, \alpha\gamma)^{16}\text{O}$ [I.78]. This technique has however the inconveniences of being suitable only for low Z elements (for incident particles with energies up to a few MeV) and of having the need of several distinct impinging particle energies to perform multi-elemental analysis, since the nuclear reactions involved are of the resonant type.
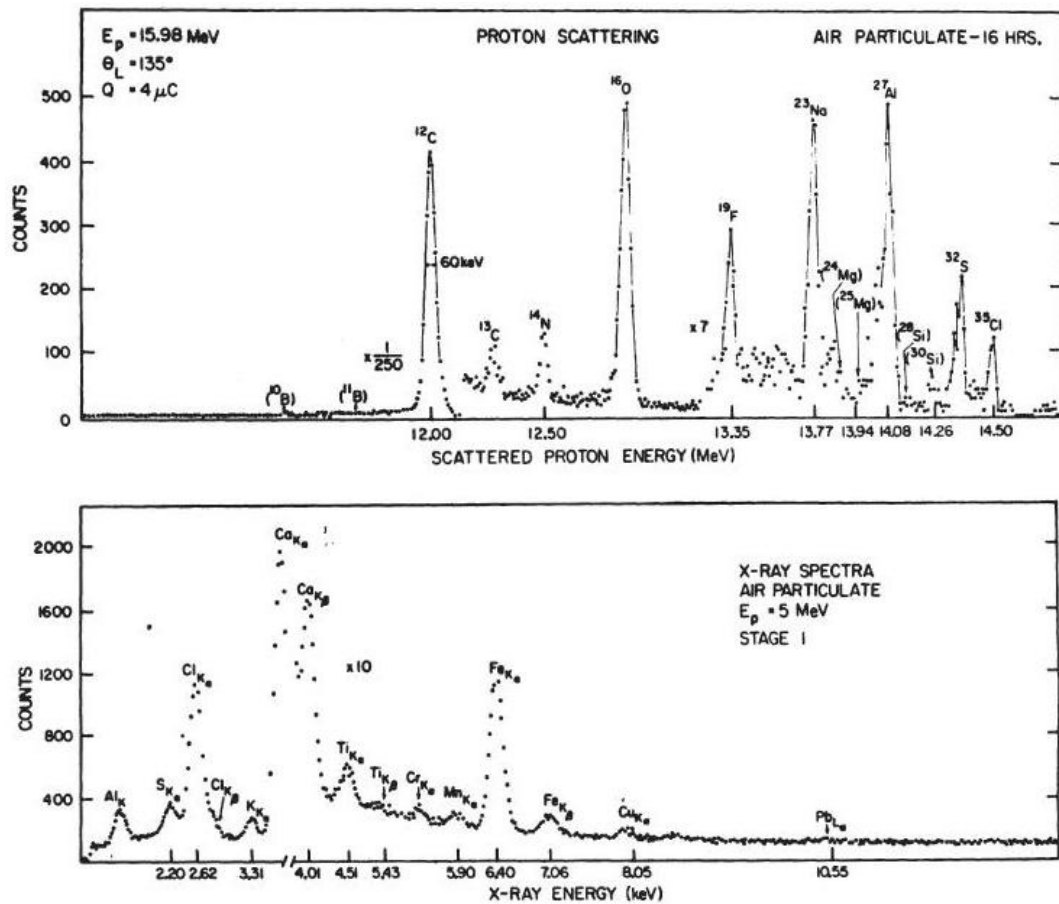
Figure I.21 – Proton scattering (upper) and PIXE (lower) spectra obtained for air particulate sample deposited upon a polystyrene film [I.10].

I.5 SENSITIVITY AND ACCURACY OF THE PIXE TECHNIQUE

I.5.1 DETECTION LIMIT (SENSITIVITY)

One of the main advantages of PIXE as a trace element analytical technique is its high sensitivity. For instance, even in PIXE early years, it was shown that 4×10^{-11} g of Ti deposited on a thin carbon backing could easily be detected [I.8]. Since, for this particular context, the main goal is to detect trace elements in a certain matrix, the sensitivity is therefore defined as minimum detectable amount of matter (in grams or grams per centimetre squared) or the minimum detectable concentration of an element (in Parts Per Million, ppm). As explained earlier, besides the desired characteristic X-ray lines, the PIXE spectrum also inevitably records a continuous bremsstrahlung background whose presence then sets a limit to the sensitivity. As a result, the sensitivity corresponds to the minimum detectable concentrations of trace elements originating a characteristic X-ray line that is distinguishable above the background in a statistically significant way.

Even if several definitions were proposed in the early years of PIXE for the limit of detection, it is now generally assumed that the minimum detection limit (MDL) for a given trace element corresponds to the amount (or concentration) of that element that gives rise to characteristic X-ray peak area in which the number of counts in this peak N_T satisfies the following relation:

$$N_T = 3\sqrt{N_b} \qquad \text{(Eq. I.8)}$$

where N_b is the number of counts in the background under the peak in an interval having a width equal to the Full Width at Half-Maximum (FWHM) of the peak.

Knowing the cross-sections for both X-ray production and continuum radiation background generation, one can calculate the amount of a certain trace element needed to satisfy Equation I.8, i.e. the sensitivity. Such calculations [I.47],[I.79] show that the sensitivity depends on the experimental conditions and that it scales as $\sqrt{\Delta E / (j\,\Omega\,\tau\,)}$, where ΔE is the detector energy resolution, j the collected charge, Ω the solid angle subtended by the X-ray detector and τ the target thickness. As a result, one has to improve these specific parameters to improve the sensitivity. While ΔE and Ω are parameters that can scarcely be changed due to practical considerations and are of no importance for this discussion, much more flexibility is provided by the collected charge j and the target thickness τ. Concerning the collected charge, this can be increased either by a longer irradiation time or by an increase in the beam current. However, running longer irradiations has practical limitations while, on the other hand, a significant increase in the beam current can lead to disastrous consequences as already explained in section I.2.5. On the other hand, the target thickness should be as large as possible, but however within certain limitations. Indeed, besides the fact that moderate target thicknesses are recommended to avoid excessive heating and deterioration of the target, it is on the contrary advisable to have specimens thin enough to hold the thin-specimen criterion so that the slowing-down of the ions and the absorption of the resulting X-rays can both be neglected.

We should also note that in external beam or non-vacuum PIXE (in air or in helium or nitrogen atmosphere) poorer sensitivity is inevitably expected due to an increased background contribution that results from both the interaction of the beam with the exit window material and within the air or chamber gas and the substantial attenuation of soft X-rays by the same gases.

Although a qualitative understanding of the behaviour of the sensitivity with experimental parameters is therefore known, it is unlikely to calculate quantitatively the sensitivity since it is impossible to have an exact estimation of the radiation background yield. Indeed, since the background depends on both the composition of the matrix of the sample and the geometry of the set-up, it is impossible to have a general, simple expression for this cross-section. However, since in most cases of practical interest the matrix and/or the backing material are composed of carbon or organic material, Johansson and Johansson [I.12] and Folkmann *et al.* [I.47] both approximate the

background matrix to pure carbon to simplify the calculation of the radiation background cross-sections. The results of their calculations are presented in Figures I.22, I.23 and I.24.
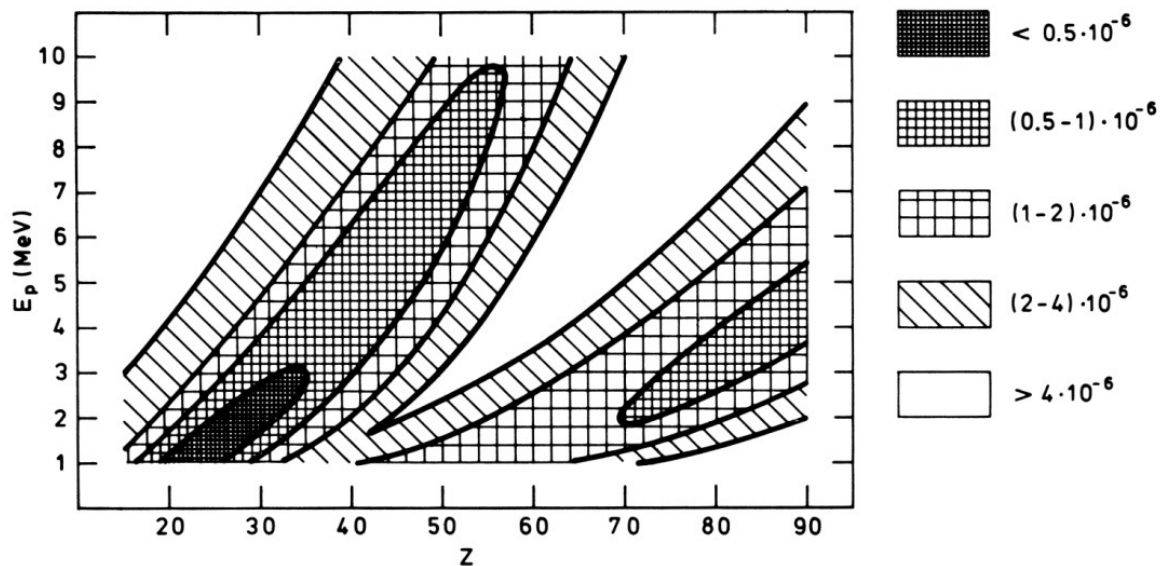

Figure I.22 – Theoretical minimum detectable concentration as a function of the atomic number Z of the sample and the energy of the bombarding protons, E_p [I.12].
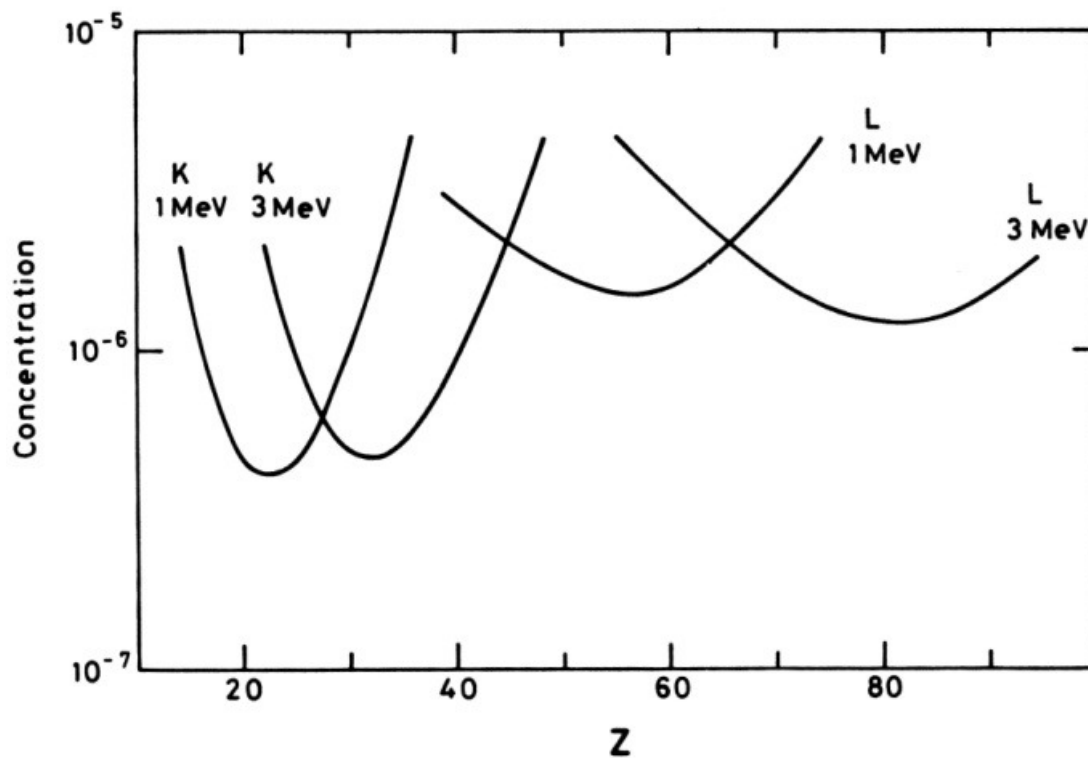

Figure I.23 – Theoretical minimum detectable concentration as a function of the atomic number Z for proton energies E_p of 1 and 3 MeV [I.12].
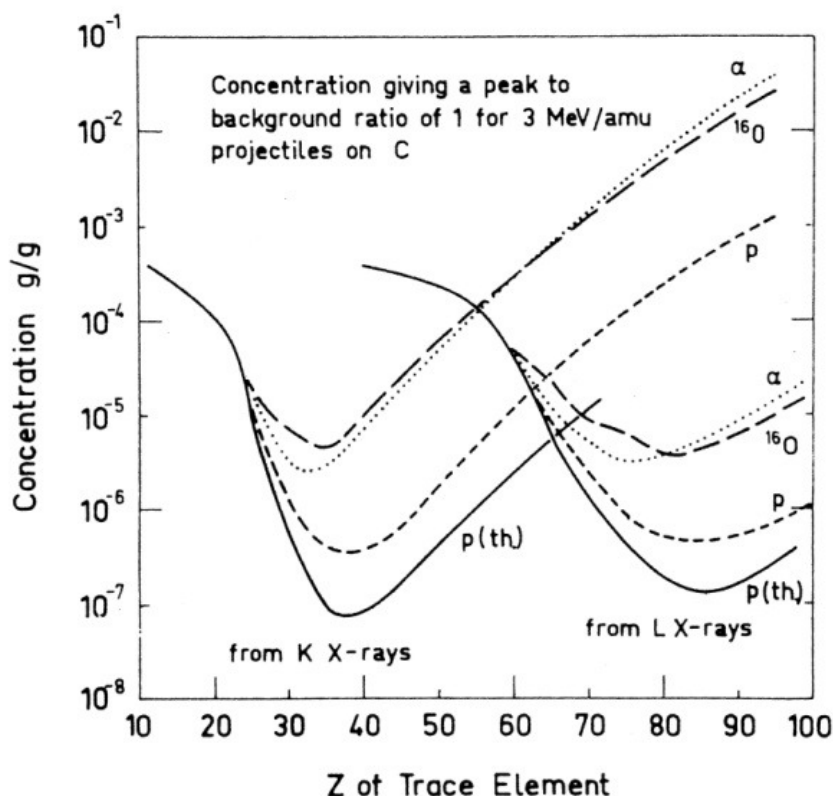
Figure I.24 – Minimum detectable concentration as a function of the atomic number Z for protons, α-particles and ^{16}O ions with energy of 3 MeV/amu [I.47].

While the work of Folkmann *et al.* (Figure I.24) shows that protons are the best choice for impinging particles over the whole periodic table from the sensitivity point of view, Johansson and Johansson have chosen arbitrarily typical values (even if quite conservative ones) of all the experimental parameters to illustrate the effect of beam energy on the sensitivity with atomic number of the target element, Z_T. Figure I.23 shows that all the sensitivity curves, each one corresponding to different proton energies, have a minimum (maximum sensitivity). While the sensitivity for the light elements decreases mainly because of the significant reduction of the fluorescence yield and to the increase in secondary electron bremsstrahlung at low photon energies, the decrease in sensitivity for heavier elements is due to the significant decrease of the X-ray production cross-sections while the background is relatively constant. Interesting is the fact that the maximum sensitivity is achieved for Z=20-30 which is the region of greatest interest in most cases. Therefore, the most appropriate proton energy is about 2 MeV (Figure I.22).

For heavier elements (Z>40), better sensitivity can be achieved by using more likely L- X-rays for analysis rather than K- X-rays. Consequently, by using either K- or L- X-rays a minimum detectable concentration which only varies by about an order of magnitude ($\sim 10^{-6}$) over practically the whole periodic table (elements with Z between 15 and 90) is obtained (Figure I.22). This smooth variation in sensitivity is a very important attribute that distinguishes PIXE as powerful analytical multi-elemental technique. Nevertheless, one should be aware at this point that XRF is a much more practical and less expensive technique when high sensitivity is not required.

Another important characteristic is the fact that the position of maximum sensitivity depends on the energy of the incident protons. This is of great importance from an experimental point of view, since it means that the incident particles energy may be chosen in order to provide maximum sensitivity for a specific Z region.

Although sensitivity is usually defined as the minimum detectable concentration, it can also be expressed in terms of absolute minimum detectable amount of a given trace element in the sample material irradiated by the incident beam. For instance, with typical values of thickness and impinged area of 10^{-4} g/cm^{-2} and 1 cm^2 respectively, a minimum detectable concentration of 1 ppm corresponds to 10^{-10} g, but minimal amounts down to 5×10^{-17} g are theoretically detectable with improved conditions (particularly for high density beams, as it occurs in micro-PIXE) [I.12]. However, we must repeat at this point that the high sensitivity of PIXE has no interest if some trace elements in the material to be analysed are masked by impurities.

I.5.2 ACCURACY

Another characteristic of great importance that has to be taken into account in such analytical multi-elemental analysis is its accuracy. This feature mirrors all the cares taken in all the stages of an analysis, from specimen preparation to data analysis. For instance, issues such as target contamination or possible heat-induced losses during PIXE bombardment (S, Ag, Se and Hg especially) of some elements can result in severe discrepancies in the analysis, as we already mentioned.

Again, there are different ways to define the accuracy of a technique. This can be seen either in terms of repeatability, hence the ability to reproduce successively the same results, or on the other hand in terms of reproducibility, i.e. the aptitude to obtain the same results using totally different experimental conditions. Other ways to define the accuracy of a PIXE procedure consist in analysing certified reference materials [I.80] or in comparing the PIXE results with the ones of other analytical techniques [I.81].

In order to estimate the repeatability of an entire PIXE analytical procedure it is necessary to perform an extensive amount of irradiations of specimens from the same material and then calculate the standard deviation from the spread in the results obtained. This standard deviation should equal the one expected from counting statistic alone when working under optimum conditions but, however, many studies demonstrate that typical experimental standard deviations are slightly worse but still acceptable [I.63].

On the other hand, inter-laboratory comparison exercises [I.82] were also carried out throughout the years to compare analysis results from totally different experimental set-ups. This presents an advantage over the previous evaluation of accuracy since it takes into account eventual differences resulting from others parameters that can vary between experimental arrangements, such as spectra fitting programs [I.83] or detector efficiency calibrations. The results of these measurements indicate that trace element analysis quantification varies within a maximum of 10 % [I.82].

I.6 MOTIVATION OF THE WORK

All these conclusions regarding the sensitivity and the accuracy of the PIXE technique are satisfactory from an experimental point of view. Nevertheless, we still have not mentioned what may be considered as the Achilles´ heel of the PIXE analytical technique: even working in ideal experimental conditions, any quantitative measurement relies on the knowledge of one fundamental parameter whose accuracy cannot be evaluated by some comparison exercise, which is the X-ray production cross-section. Although its accuracy is essential to perform accurate trace element quantifications, available X-ray production cross-sections present typical uncertainties of about 10-20%, which is by far too much. This situation is actually the best scenario, since in some cases the cross-sections needed have not been experimentally determined yet and the values used to perform quantitative analysis are estimations from theoretical calculations, giving rise to even less accurate analytical results.

It seems clear from the above discussion about PIXE accuracy that the data in the literature is either not enough, or even worse, unavailable. Consequently, much work remains to be done in the field to improve the precision and accuracy of PIXE analyses, namely providing and experimentally obtained and accurate X-ray production cross-sections, as pointed out recently by Lapicki [I.84].

In this line of thought, and making use of the recently assembled, although not completed, particle accelerator [I.85] at the Atomic and Nuclear Instrumentation Group (Grupo de Instrumentação Atómica e Nuclear – GIAN) in Coimbra, we decided to carry out the following research work, whose main purpose was the determination of X-ray production cross-sections for low-energy light-ions impinging in light elements since there is an evident lack of these values in the literature [I.84]. Indeed, despite their usefulness, particularly for surface analyses where the bombarding particles must have less than 1 MeV, the determination of such X-ray production cross-sections has scarcely been considered throughout the years. We believe this is due to the additional experimental difficulties brought by the use of incident particles with lower energies, i.e. by the consequently reduced X-ray production cross-sections involved when compared to the ones obtained with impinging particles in the 1-4 MeV energy range. Besides, we also decided to focus our interest in target elements of low atomic number Z_T, for which the lack of data in the literature is even more evident. The lack of accurate data may also be explained by the additional difficulties encountered in the detection of the resultant low energy characteristic X-rays (i.e. below 2 keV) since these X-ray energies are near, or even below, the detectable energy threshold of semiconductor based X-ray detectors usually used with this technique.

In order to carry out successfully such investigation, we developed an entire PIXE experimental set-up based on the referred particle accelerator. Besides, it was fundamental to overcome several experimental difficulties; namely the detection of low-energy X-rays (below 2 keV) with improved detection efficiency, which is necessary

due to the small cross-sections involved. Consequently, conventional Si(Li) detectors do not seem to be the most suitable choice for this particular application, and so alternative X-ray detectors must be used. Since gaseous detectors offer simultaneously large sensitive areas and relatively large detection efficiency for low energy X-rays down to the carbon or K-line (277 eV), this was our choice to perform the work that is presented here.

I.7 REFERENCES

[I.1]   W.C. Röentgen, "On a New Kind of Rays", Proceedings of the Physical Medical Society, 1895.

[I.2]   H.G.J. Moseley, "The high-energy spectra of the elements, Part I", Phil. Mag. 26, pp. 1024-1034, 1913 and H.G.J. Moseley, "The high-energy spectra of the elements, Part II", Phil. Mag. 27, pp. 703-713, 1914.

[I.3]   R. Glocker and H. Schreiber, Ann. Phys. 85, pp. 1089-1102, 1928.

[I.4]   J. Chadwick, Phil. Mag. 24, pp. 594, 1912, J. Chadwick, Phil. Mag. 25, pp. 193, 1913.

[I.5]   E. Merzbacher, B.E. Simmons and H.W. Lewis, "Production of characteristic X-rays by protons of 1.7 to 3 MeV energy", Phys Rev. 91, pp. 943-946, 1953.

[I.6]   E. Merzbacher and H.W. Lewis, "X-ray production by heavy charged particles," Encyclopedia of Physics, Springer-Verlag, Berlin, vol. 34, pp. 166-192, 1958.

[I.7]   J.M. Khan, D.L. Potter and R.D. Worley, "Proposed method for microgram surface density measurements by observation of proton-produced X-rays", J. Appl. Phys. 37, pp. 564-567, 1966.

[I.8]   T.B. Johansson, R. Akselsson and S.A.E. Johansson, "X-ray analysis: elemental trace analysis at the 10^{-12} g level", Nucl. Instr. and Methods 84, pp. 141-143, 1970.

[I.9]   K.M. Barfoot, I.V. Mitchell and H.L. Eschbach, "A comparison of thin and thick target methods of measuring proton induced K-shell ionization cross-sections", Nucl. Inst. and Methods 168, pp. 131-138, 1980.

[I.10] J.W. Nelson, I. Williams, T.B. Johansson, R.E. Van Grieken, K.R. Chapman and J.W. Winchester, "Elemental analysis of aerosols using proton scattering", IEEE Trans. on Nucl. Sci. 21(1), pp. 618-621, 1974.

[I.11] W. Maenhaut, "Multielement analysis of biological materials by particle-induced X-ray emission (PIXE)", Scanning Microscopy 4, pp. 43-59, 1990.

[I.12] S.A.E. Johansson and T.B. Johansson, "Analytical application of particle induced X-ray emission", Nucl. Instr. and Methods 137, pp. 473, 1976.

[I.13] J.D. Garcia, "Inner-Shell ionizations by proton impact", Phys. Rev. A1, pp. 280-285, 1970.

[I.14] J. Bang and J.M. Hansteen, Kgl. Dansk, Videnskab. Selskab. Mat-Fys. Medd 31, no. 13, 1959.

[I.15] J.M. Hansteen and O.P. Mosebeke, Nucl. Phys. A201, pp. 541, 1973.

[I.16] W. Brandt and G. Lapicki, "L-shell Coulomb ionization by heavy charged particles", Phys. Rev. A20, pp. 465-480, 1979.

[I.17] W. Brandt and G. Lapicki, "Energy loss effect in inner shell Coulomb ionization by heavy charged particles", Phys. Rev. A23, pp. 1717-1729, 1981.

[I.18] J.D. Garcia, R.J. Fortner and T.M. Kavanagh, "Inner-shell vacancy production in ion-atom collisions", Rev. Mod. Phys. 45, pp. 111-177, 1973.

[I.19] J.S. Hansen, "Formulation of the Binary-Encounter approximation in configuration space and its application to ionization by light ions", Phys. Rev. A8, pp. 822-893, 1973.

[I.20] H. Paul, "A test of theoretical K-shell ionization cross sections for protons", Nucl. Instr. and Methods B42, pp. 443-448, 1989.

[I.21] E.H.S. Burshop, The Auger effect and other radiationless transitions, Cambridge University Press, New York, 1952.

[I.22] F. Folkmann, "Analytical use of ion-induced x-rays", J. Physics E8, pp. 429-437, 1975.

[I.23] J.M. Khan and D.L. Potter, "Characteristic K-shell X-ray production in magnesium, aluminium and copper by 60 to 500 keV protons", Phys. Rev. 133, pp. 890-894, 1964.

[I.24] G. Basbas, W. Berner and R. Laubert, "Universal cross sections for K-shell ionization by heavy charged particles. I. Low particle velocities", Phys. Rev. A7, pp. 983-1001, 1973

[I.25] R.C. Bearse, D.A. Close, J.J. Malanify and C.J. Umbarger, "Production of $K\alpha$ and $L\alpha$ X-rays by protons of 1.0-3.7 MeV", Phys. Rev. A7, pp. 1269-1272, 1973.

[I.26] R. Lear and T.J. Gray, "K-shell ionization cross sections of selected elements from Fe to As for proton bombardment from 0.5 to 2.0 MeV", Phys. Rev. A8, pp. 2469-2474, 1973.

[I.27] A. Langenberg and J. van Eck, "Carbon, nitrogen, neon and argon K-shell ionization by proton and helium-ion impact: X-ray emission cross sections and fluorescence yields", J. Phys. B9, pp 2421-2433, 1976.

[I.28] H. Tawara, Y, Hachiya, K. Ishii and S. Morita, "K-shell ionization of light elements by proton and helium-3-ion impact", Phys. Rev. A13, pp. 572-577, 1976.

[I.29] M. Milazzo and G. Riccobono, "Cross section for induced x-ray emission in some elements by 950 keV protons", Phys. Rev. A13, pp. 578-583, 1976.

[I.30] K. Sera, K. Ishii, M. Kamiya, A. Kuwako and S. Morita, "K-shell ionization of Al and Cu for 0.5-40 MeV proton bombardment", Phys. Rev. A21, pp. 1412-1418, 1980.

[I.31] W.E. Eichinger and P.J. O´reilly, "K-shell X-ray production in vanadium, cobalt, copper, molybdenum and silver by low velocity protons", Nucl. Instr. and Methods B47, pp. 355-360, 1990.

[I.32] M. Geretschager, Z. Smit and O. Benka, "K-shell ionization cross sections for Si, P, K, Ca, Zn and Ga by protons and carbon ions in the energy range 1-6.4 MeV", Phys. Rev. A41, pp. 123-133, 1990.

[I.33] Y.C. Yu, M.R. McNeir, D.L. Weathers, J.L. Duggan and F.D. McDaniel, "K-shell x-ray-production cross sections in $_6$C, $_8$O, $_9$F, $_{11}$Na, $_{12}$Mg and $_{13}$Al by 0.75 to 4.5 MeV protons", Phys. Rev. A44, pp. 5702-5706, 1991.

[I.34] S. Szegedi, P. Raics and M. Fayez-Hassan, "K X-ray production cross sections for 40-180 keV protons", Journal of Radioanalytical and Nuclear Chemistry 260, pp. 429-433, 2004.

[I.35] T. Scharnagl and W. Hink, "X-ray production cross sections for a thin solid Be target", J. Phys. B13, pp. 4021-4030, 1980.

[I.36] F. Folkmann, C. Gaarde, T. Huus and K. Kemp, "Proton induced X-ray emission as a tool for trace lelement analysis", Nucl. Instr. and Methods 116, pp. 487-499, 1974.

[I.37] A. Yamadera, K. Ishii, K. Sera, M. Sebata and S. Morita, "Quasifree-electron bremsstrahlung induced by the projectile field", Phys. Rev. A23, pp. 24-33, 1981.

[I.38] T.C. Chu, K. Ishii, A. Yamadera, M. Sebata and S. Morita, "Quasifree electron bremsstrahlung induced by 20 MeV proton impact", Phys. Rev. A24, pp. 1720-1725, 1981.

[I.39] K. Ishii and S. Morita, "Continuum X-rays produced by light-ion-atom collisions", Phys. Rev. A30, pp. 2278-2286, 1984.

[I.40] K. Ishii and S. Morita, "Scaling law for a continuum of X-rays produced by light-ion-atom collisions", Nucl. Instr. and Methods B22, pp. 8-71, 1987.

[I.41] K. Ishii and S. Morita, "Bremsstrahlung induced by proton and ^{3}He-ion bombardments in the 1-4 MeV/amu energy range", Phys. Rev. A13, pp. 131-138, 1976.

[I.42] K. Ishii, M. Kamiya, K. Sera and S. Morita, "Directional anisotropy of secondary-electron bremsstrahlung induced by proton bombardment of thin solid target", Phys. Rev. A15, pp. 2126-2129, 1977.

[I.43] A.D. González, M.C. Pacher and J.E. Miraglia, "Retardation effects in atomic bremsstrahlung", Phys. Rev. A37, pp. 4974-4977, 1988.

[I.44] F. Folkmann, K.M. Cramon and N. Hertel, "Angular distribution of particle-induced X-ray emission, Nucl. Instr. and Methods B3, pp. 11-15, 1984.

[I.45] S.A.E. Johansson and J.L. Campbell, "PIXE: A Novel Technique for Elemental Analysis", Wiley, Chichester, 1988.

[I.46] R.L. Watson, C.J. McNeal and F.E. Jenson, Advan. X-ray Anal. 18, pp. 288-291, 1975.

[I.47] F. Folkmann, J. Borggreen and A. Kjeldgaard, "Sensitivity in trace-element analysis by p, α and ^{16}O induced X-rays", Nucl. Instr. and Methods 119, pp. 117-123, 1974.

[I.48] G.E. Coote, "Ion beam analysis of fluorine: its principles and applications", Nucl. Instr. and Methods B66, pp. 191-204, 1992

[I.49] I.V. Mitchell, K.M. Barfoot and H.L. Eschbach, "Ion beam monitoring using thin self-supporting reference foils", Nucl. Instr. and Methods 168, pp. 233-240, 1980.

[I.50] G.F. Knoll, "Radiation detection and measurements", John Willey and Sons, Inc., New York, 2000.

[I.51] P. Horowitz and L. Grodzins, "Scanning proton-induced x-ray microspectrometry in an atmospheric environment", Science 189, pp. 795-797, 1975.

[I.52] J.A. Cookson, "The production and use of a nuclear microprobe of ions at MeV energies2, Nucl. Instr. and Methods 165, pp. 477-508, 1979.

[I.53] G.J.F. Legge and A.P. Mazzolini, "Elemental microanalysis of biological and medical specimens with a scanning proton microprobe", Nucl. Instr. and Methods 168, pp. 563-569, 1980.

[I.54] D.G. Fraser, F. Watt, G.W. grime and J. Takacs, "Direct determination of strontium enrichment on grain boundaries in a garnet lherzolite xenolith by proton microprobe analysis", Nature 312, pp. 352-354, 1984.

[I.55] B.G. Martinsson, "An external beam PIXE/PESA setup for characterization of fine aerosols", Nucl. Instr. and Methods B22, pp. 356-363, 1987.

[I.56] B.H. Kusko, M. Menu, T. Calligaro and J. Salomon, "PIXE at the Louvre museum", Nucl. Instr. and Methods B49, pp. 288-292, 1990.

[I.57] J.-C. Dran, J. Salomon, T. Calligaro and P. Walter, "Ion beam analysis of art works: 14 years of use in the Louvre", Nucl. Instr. and Methods B219-220, pp. 7-15, 2004.

[I.58] N. Grassi, A. Migliori, P.A. Mando and H.C. del Castillo, "Differential PIXE measurements for the stratigraphic analysis of the painting *Madonna dei fusi* by Leonardo da Vinci", X-ray spectrometry 34, pp. 306-309, 2005.

[I.59] E.J. Sternglass, "Theory of secondary electron emission by high-speed ions", Phys. Rev. 108, pp. 1-12, 1957

[I.60] K. Traxel and A. Mandel, "Secondary electron imaging at the Heidelberg proton microprobe", Nucl. Instr. and Methods B3, pp. 594-597, 1984.

[I.61] P.I. Mason, PhD Thesis, University of Surrey U.K., 1980.

[I.62] V.N. Volkov, V.B. Vykhodets, I.K. Golubkov, S.M. Klotsman, P.V. Lerkh and V.A. Pavlov, "Accurate light ion beam monitoring by backscattering", Nucl. Instr. And Methods 205, pp. 73-77, 1983.

[I.63] V. Valkovic, R.B. Liebert, T. Zabel, H.T. Larson, D. Miljanic, R.M. Wheeler and G.C. Phillips, "Trace element analysis using proton-induced X-ray emission spectroscopy" Nucl. Insts. and Methods 114, pp. 573-579, 1974.

[I.64] R.G. Musket and C.W. Price, "Implanted standards for ion microanalysis of oxygen in beryllium", Nucl. Instr. and Methods B42, pp. 245-250, 1989.

[I.65] I.V. Mitchell, H.L. Eschbach and K.M. Barfoot, "A gold and aluminium implanted standard for ion beam experiments", Nucl. Instr. and Methods 168, pp. 169-174, 1980.

[I.66] W.J. Teesdale and J.L. Campbell, "An on-demand beam deflection system for microbeam PIXE analysis", Nucl. Instr. and Methods B52, pp. 93-97, 1990.

[I.67] D.W. Mingay and E. Barnard, "Reduction of the bremsstrahlung background in the proton-induced X-ray emission analysis of insulating samples", Nucl. Instr. and Methods 157, pp. 537-544, 1978.

[I.68] M. Ahlberg, G. Johansson and K. Malmqvist, "Elimination of charging in the proton-induced X-ray emission analysis of insulating samples", Nucl. Instr. and Methods 131, pp. 377-379, 1975.

[I.69] R.G. Musket, "Considerations for application of Si(Li) detectors in analysis of sub-keV ion-induced X-rays", Nucl. Instr. and Methods B15, pp. 735-739, 1986.

[I.70] W.J. Teesdale and J.L. Campbell, "An on-demand beam deflection system for microbeam PIXE analysis", Nucl. Instr. and Methods B52, pp. 93-970, 1990.

[I.71] M. Ahlberg, R. Akselsson, D. Brune and J. Lorenzen, "Proton-induced X-ray analysis of steel surfaces for microprobe purposes", Nucl. Instr. and Methods 123, pp. 385-393, 1975.

[I.72] M. Pajek, A.P. Kobzev, R. Sandrik, R.A. Ilkhamov and S.H. Khusmurodov, "Accurate efficiency determination of a Si(Li) detector in the Si-K and Au-M absorption edge energy region", Nucl. Instr. and Methods B42, pp. 346-358, 1989.

[I.73] H.L. Eschbach, I.V. Mitchell and E. Louwerix, "Use of an ultrahigh vacuum balance for the quantitative assay of evaporated reference layers", Thermochimica Acta 51, pp. 33-43, 1981.

[I.74] H.C. Kaufmann and R. Akselsson, "Non-linear least squares analysis of proton-induced X-ray emission", Advan. X-ray Anal. 18, pp. 353-361, 1975.

[I.75] J.A. Maxwell, W.J. Teesdale and J.L. Campbell, "The GUEPH-PIXE software package", Nucl. Instr. and Methods B43, pp. 218-230, 1989; J.A. Maxwell, W.J. Teesdale and J.L. Campbell, "The GUEPH-PIXE software package – II", Nucl. Instr. and Methods B95, pp. 407-421, 1995, J.A. Maxwell; W.J. Teesdale and J.L. Campbell, "The GUEPH-PIXE software package – III: Alternative data proton database", Nucl. Instr. and Methods B170, pp. 193-204, 2000.

[I.76] A.S. Farooqi, W. Arshed, O.A. Akanle, C. Jeynes and N.M. Spyrou, "Fluorine determination in diet samples using cyclic INAA and PIGE analysis", Journal of Radioanalytical and Nuclear Chemistry 161(1), pp. 71-78, 1992.

[I.77] E.A. Preoteasa, E. Preoteasa, C. Ciortea, D.D. Marin, D. Gurban, M. Gugiu and A. Scafes, "PIXE and PIGE assessment of *in vivo* elemental and physical changes of a composite from a dental filling", X-ray spectrometry 38, pp. 548-556, 2000.

[I.78] Preoteasa, G.E. Coote, "Ion-beam analysis of fluorine – its principles and applications", Nucl. Instr. Methods. B66, pp. 191-204, 1992.

[I.79] W. Maenhaut and K.G. Malmqvist in *Hanbook of X-ray spectrometry* Ed. by R.E. VanGrieken and A.A. Markowicz, Marcel Dekker Inc.,New York, 1993.

[I.80] L.-E. Carlsson, "Accuracy and precision in thick target PIXE-PIGE analysis determined with geological standards", Nucl. Instr. and Methods B3, pp. 206-210, 1984.

[I.81] E. Bombelka, R.W. Richter, H. Ries and U. Watjen, "Large scale intercomparison of aerosol trace element analysis by different analytical methods", Nucl. Instr. and Methods B3, pp 296-300, 1984.

[I.82] D.C. Camp, A.L. Van Lehn, J.R. Rhodes and A.H. Pradzynski, "Intercompariosn of trace element determinations in simulated and real air particulate samples", X-ray spectrometry 4, pp. 123-137, 1975.

[I.83] J.L. Campbell, W. Maenhaut, E. Bombelka, E. Clayton, K. Malmqvist, J.A. Maxwell, J. Pallon and J. Vandenhaute, "An intercomparison of spectral data processing techniques in PIXE", Nucl. Instr. and Methods B14, pp. 204-220, 1986.

[I.84] G. Lapicki, "The status of theoretical L-shell ionization cross-sections by protons", X-ray spectrometry 34, pp. 269-278, 2005.

[I.85] A.M.F. Trindade, "Um Sistema para Aceleração de Iões Positivos a Baixas Energias: Projecto, Construção e Testes", M.Sc. thesis, University of Coimbra, 2006.

– CHAPTER II –

THE PARTICLE ACCELERATOR

This Chapter aims at describing the experimental arrangement we built up to perform our PIXE studies. At the time that my colleague A. Trindade finished his work on the particle accelerator we used [II.1], the experimental set-up (illustrated in Figure II.1) that we further improved and converted into a PIXE set-up was at an early stage. At that time, it allowed to obtain proton beam currents up to only a few nA in the reaction chamber. Moreover, no high voltage HV was applied to the accelerating tube, and therefore the maximum energy of the impinging protons was limited by the voltages of the ion source (up to 5 keV per elementary charge). The ion source was already fully incorporated into the developed particle accelerator and the polarizing high voltages were supplied by an electronic module with fluctuating ground potential [II.1]. The batteries installed (shown in Figure II.1) supplied the power to this electronic module.

Prior to reporting the improvements made to this particle accelerator, we must describe briefly the experimental set-up referred. This description can be simplified by distinguishing 3 main parts (for a detailed description see [II.1]); namely the *ion source,* the *accelerating tube* and the *reaction chamber* (Figure II.1).
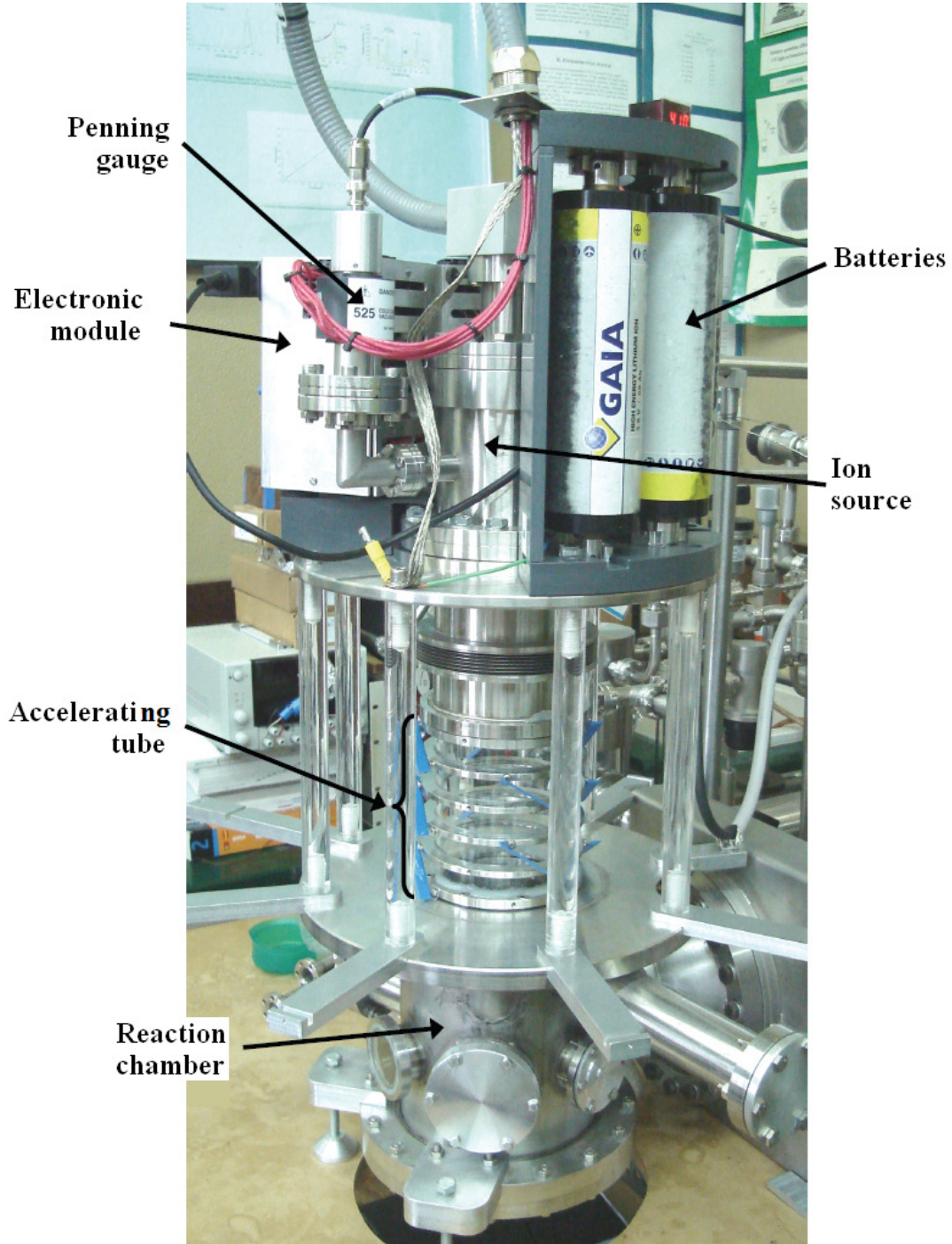
Figure II.1 – Photograph of the particle accelerator built at GIAN by A. Trindade [II.1].

The *ion source* (model IG20 from HIDEN) consists in a vacuum vessel where a gas is inserted and ionized, and whose resultant ions are successively extracted and focused. The gas is inserted into the cage inside the ion source through a very precise needle valve in order to control the incoming gas flux since pressures higher than 10^{-4} Torr are not allowed inside the ion source. As shown in Figure II.2, this cage is biased at a potential V_S higher than the ion source fluctuating ground potential HV, so that electrons are accelerated in its direction and ionize the gas molecules that are inside. These electrons are released, through thermionic effect, from the surface of a filament heated by Joule´s effect due to the flow of a current I_F. The resulting positive ions inside

the cage are then extracted out of the ion source cage because the potential V_E of the extractor is lower than the cage voltage V_S. Furthermore, at the output of the extractor are 3 electrodes with voltages successively equal to 0 V, V_F and 0 V (with V_F lower than V_E), defining an Einzel lens used to focus the emerging ion beam. The voltages V_S, V_E, V_F and the filament current I_F are supplied by a homemade electronic module with fluctuating ground potential that is fed by rechargeable batteries (Figure II.1). The emerging ion beam leaves therefore the ion source focussed and the ions have energy equal to qV_S where q is the ion charge.

The *accelerating tube* isolates electrically the ion source from the reaction chamber and accelerates the ions. It consists of 6 metallic rings alternatively mounted onto 5 insulating glass rings. The metallic rings are connected in series by resistors of high ohmic value (165 MΩ each), defining an equal voltage drop from ring to ring. The high voltage HV used to accelerate the ions during their drift along the accelerating tube is applied to the upper ring which is in electrical contact with the ion source while the lower ring is connected to the reaction chamber and therefore at ground potential. The high voltage HV is consequently the electric potential of reference for the ion source. Since the ions emerge from the source with a maximum energy of 5 keV, the high voltage HV applied to the accelerator (up to 50 kV) defines the energy of the ions when these come out into the reaction chamber.

The *reaction chamber* consists of a cylindrical vacuum vessel which is connected to the accelerating tube through its upper face. As it can be seen in Figure II.1, it has several vacuum sealed flanges in its lateral surface which allow connecting various radiation detectors and all kinds of equipment needed. The larger of these flanges is used to connect the overall particle accelerator to a vacuum system that uses a turbo-molecular vacuum pump to reach a residual vacuum in the reaction chamber in the 10^{-7} Torr range. Besides, the bottom circular flange is used to insert the sample holder.
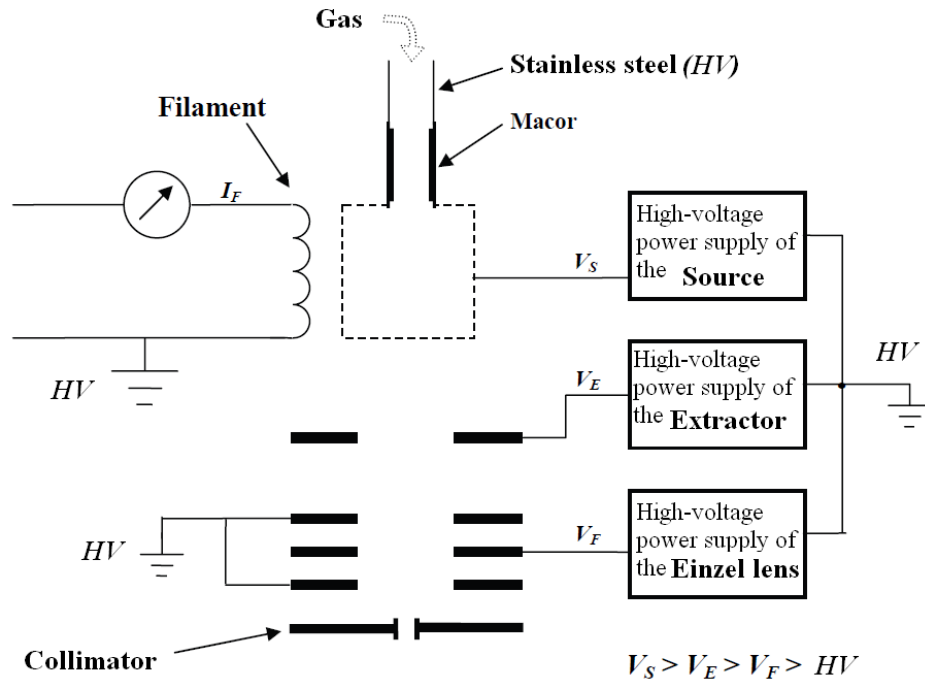

Figure II.2 – Schematic of the ion source.

We have to refer at this point that our colleague A. Trindade still performed important improvements on the experimental arrangement beyond the work described in [II.1], namely the inclusion of an insulating vacuum tube connected to the ion source in order to keep the gas insertion system at ground potential while having the accelerator biased at high voltages (shown in Figures II.3, II.4 and II.5), the replacement of the high voltage power supply used to bias the source cage (V_S) with a more powerful one and the construction of a second electronic unit (also with fluctuating ground potential), described in more detail later on, to polarize the ion selecting device built by us. We have to point out that the replacement of the high voltage power supply of the source cage was fundamental since the limited power delivered by the previous module (1 W) was limiting the maximum value of the filament current I_F to 1.75 A, which was far away from the maximum value of 4.5 A indicated by the manufacturer. Although we are now still far from making full use of the capabilities of this ion source since the new power supply installed (model H50P from EMCO with a power of 15 W) only enables to reach a new improved maximum current filament of 2.20 A, this slight increase in I_F leads to a massive improvement in the ion beam current of a factor of about 1000, as we will see in more detail further in section II.1.

However, many improvements still had to be implemented in order to use this experimental set-up to perform PIXE analysis, namely:

✓ *Safety*: First of all, from the moment that high voltages could be applied to the accelerating tube the top priority was to ensure that the system did not present any danger to the people working with it.

✓ *Ion selecting device*: The ion source naturally originates many different ions for each gas ionized inside it (H^+, HH^+… for the case of H_2) and all these different ions are extracted, accelerated due to their positive charge and reach the Faraday cup placed in the reaction chamber. Since the cross-sections of the interaction processes differ with the type of ions concerned, the insertion of an ion selecting device is essential.

✓ *Beam characterization*: Prior to any target irradiation, it is also fundamental to fully characterize the dimensions and the profile of the beam, as well as the influence of each parameter on it (HV, V_S, V_E, V_F…).

✓ *Reaction chamber components*: Both beam and X-ray collimators, a Faraday cup with a secondary electron suppressor, a movable target holder had to be projected and installed since these were not implemented in the reaction chamber yet. Besides, the installation of the developed X-ray detector (shown in Figures II.3 and II.4) to the existing reaction chamber was also necessary.

Concerning the improvements in the security of the experimental set-up, the idea was to make impossible any kind of hazardous electrical discharge to the worker while still having access to the potentiometers used to control the different voltages of the ion source. As it can be seen in Figure II.1, eight supports were placed at the top of the reaction chamber. These were used to support a metallic cage for the protection from the high voltage HV used to bias the top of the accelerating tube, as shown in Figure II.3.

This metallic cage was designed and built by us and is connected to ground potential, avoiding direct contact with the high voltages. Figures II.4 and II.5 show the cage attachment that follows the insulator pipe that connects the ion source (at high voltage) to the gas insertion system (at ground potential). However, since external access to both the electronic modules and to the needle valve that controls the gas flow in the ion source is indispensable, it was also necessary to create insulated accesses to control each potentiometer of the electronic modules, as well as to the needle valve. This was accomplished by using insulating plastic rods (Figures II.6 and II.7) so that each potentiometer and the precision needle valve could be controlled from the outside of the cage. In the meantime, the displays of the electronic modules that indicate the voltage values could still be seen from outside the cage.
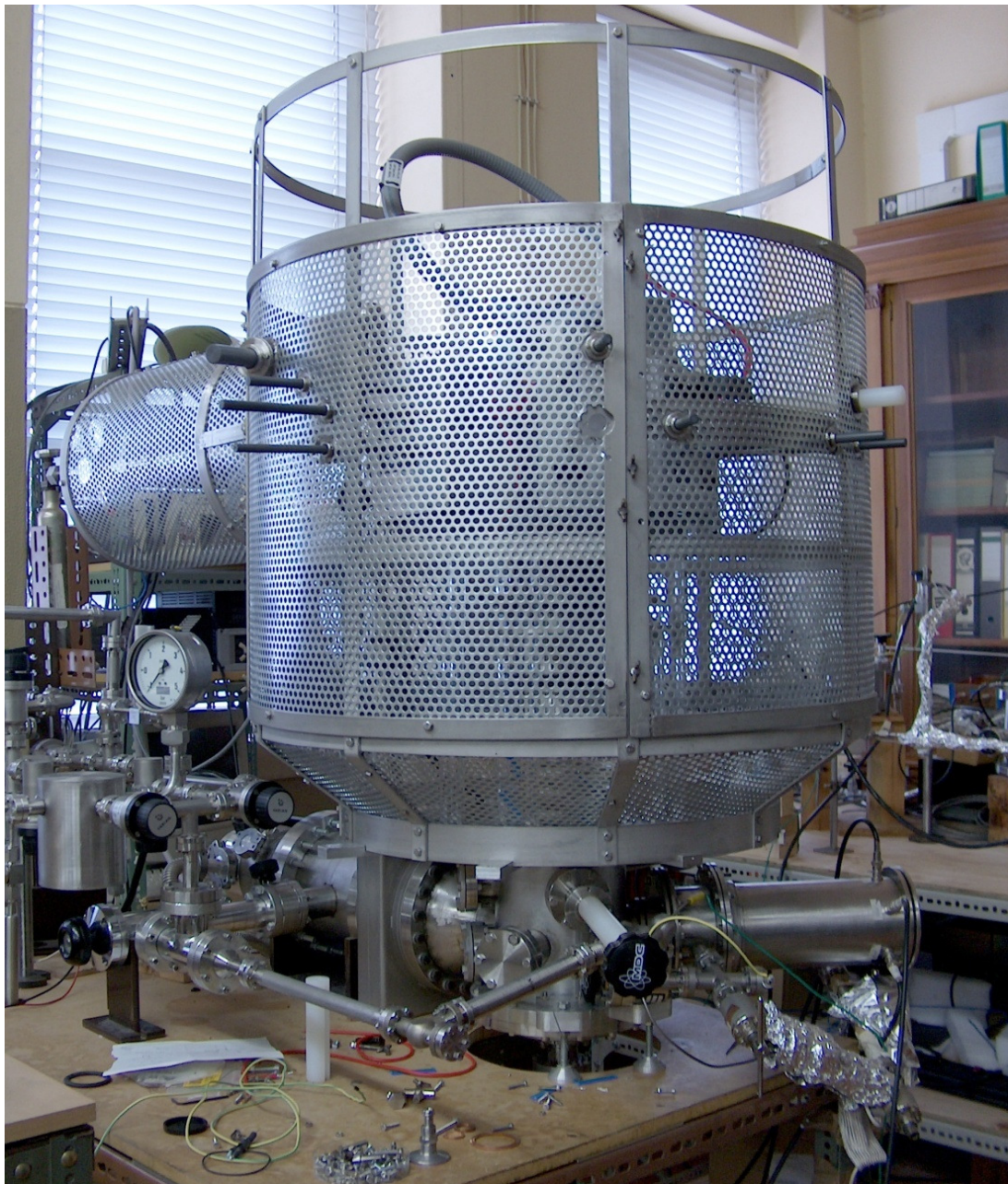
Figure II.3 – Photograph of particle accelerator with the surrounding protecting metallic cage.

Figure II.4 – Another view of the protecting metallic cage surrounding the particle accelerator.
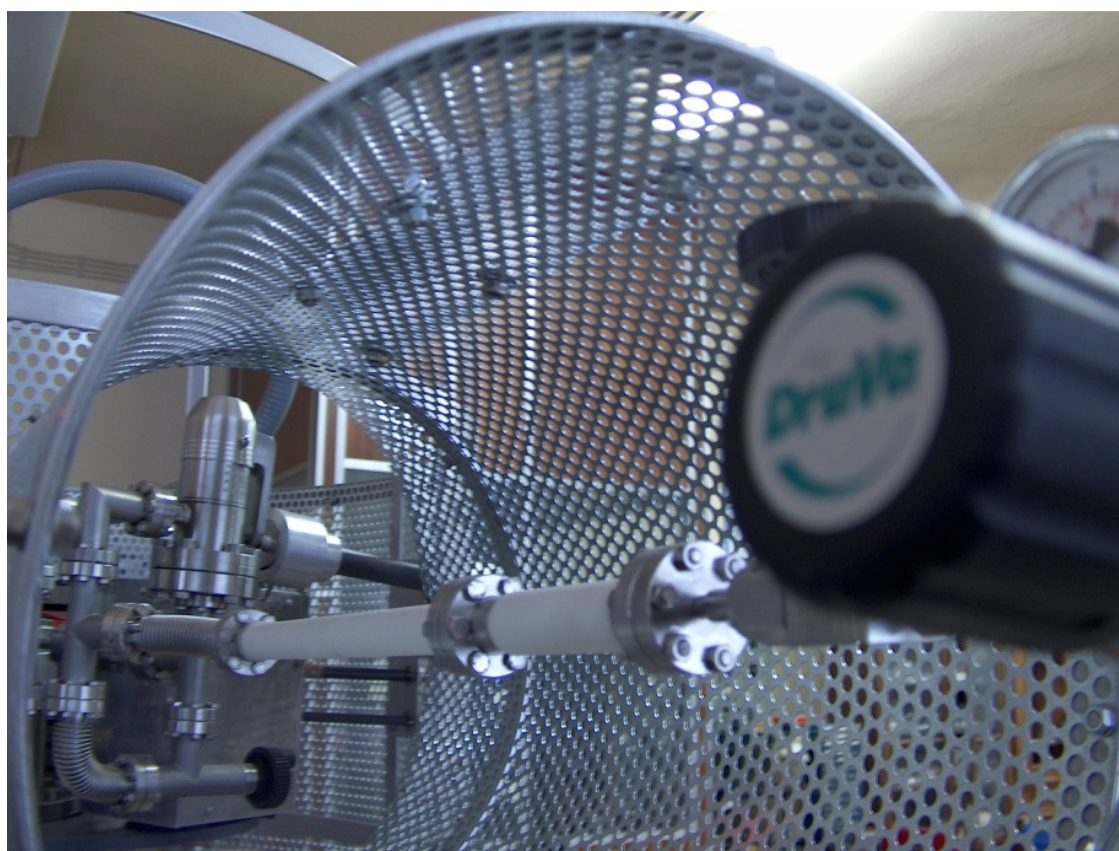
Figure II.5 – Photograph of the extension of the cage that follows the insulating vacuum tube until the gas insertion system.
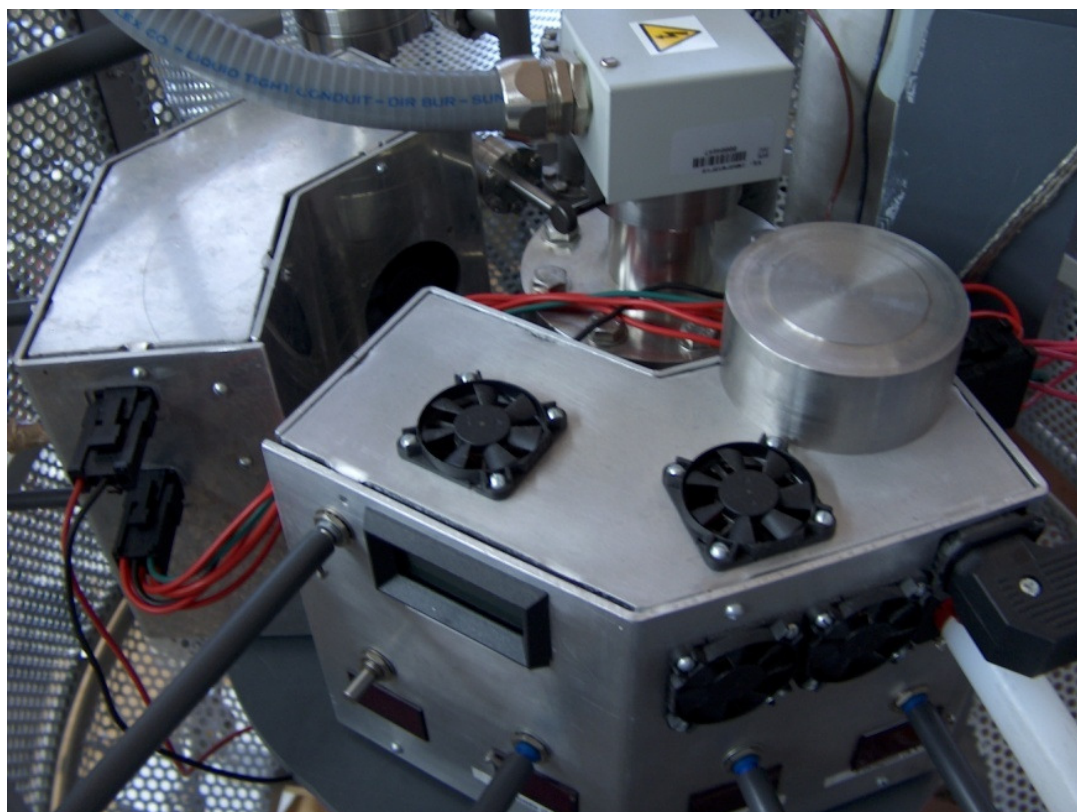
Figure II.6 – Photograph of both electronic modules with the plastic rods used to control the different voltages from the outside of the cage.

Figure II.7 – Photograph of the plastic rods used to control the potentiometers of the electronic modules from outside of the cage.

II.1 BEAM CHARACTERIZATION

Since no ionic current had been measured before with high voltage HV applied to the accelerating tube and with the recently improved electronic module, we decided to first evaluate the total ionic current I_{ion} achievable in the reaction chamber without any collimation restriction before performing any other study. Although all the pieces we projected for 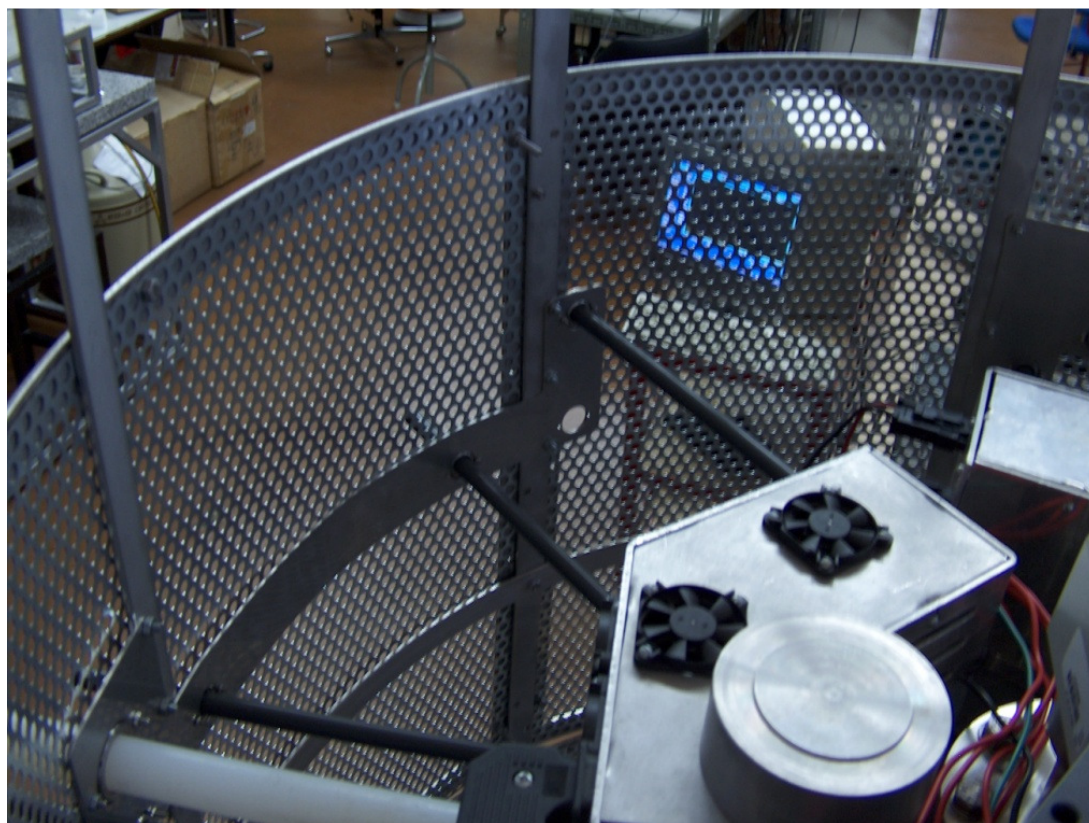the ion selecting device were already built and installed between the ion source and the accelerating tube, this latter was not working yet at this time. Figure II.8 presents the behaviour of I_{ion} with the pressure of hydrogen P_{H2} and for several values of HV. This latter shows that P_{H2} is of great influence on the current I_{ion} measured since an increase by a factor of 10 of the pressure leads to currents about 10 times larger. Besides, Figure II.8 also shows that the high voltage HV applied to the accelerating tube also is of great influence in I_{ion} since the current obtained by applying 30 kV in the accelerating tube is higher than the one without any acceleration voltage by a factor of almost 10. We also concluded from Figure II.8, by comparing the curves of I_{ion} for the two distinct filament currents I_F of 1.75 and 2.20 A (which are the maximum filament currents reachable with the older and the recently improved electronic modules respectively) that I_F has an enormous influence in I_{ion}. Besides, it is clear that the replacement of the power supply of the source cage represents a great improvement since it originates an increase in I_{ion} of a factor of almost 1000.
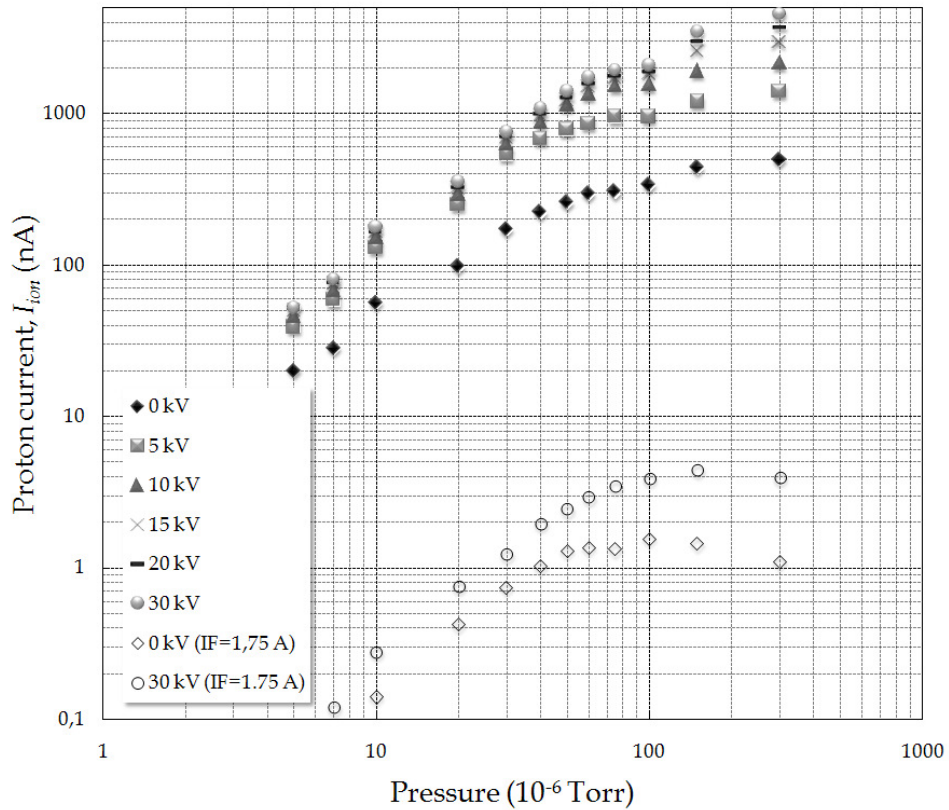

Figure II.8 – Ionic current I_{ion} measured in the reaction chamber as a function of the pressure of hydrogen, P_{H2}, for several high voltages HV applied to the accelerating tube, and for 2 distinct value of I_F of 2.20 A (full symbols) and 1,75 A (open symbols), and with V_S, V_E and V_F equal to 1200, 780 and 730 V respectively.

As mentioned earlier, it was fundamental to characterize the beam profile (namely its intensity and the cross-section dimensions) as a function of the parameters HV, V_S, V_E and V_F in order to size the components of our PIXE set-up. For this purpose, we have projected two segmented circuit boards (Figure II.9), with rectangular quadrants and concentric circular segments, which were placed in the center of the reaction chamber. Each square segment of the circuit board is 20 mm wide while the diameter of the larger concentric ring equals 50 mm. The ionic current received by each electrically isolated segment during irradiation could be measured independently since each segment was connected to a different feedthrough of the reaction chamber. Information about the spatial distribution of the impinging beam was obtained by comparison of the measured currents. We then studied the beam shape as a function of the different parameters of the particle accelerator.
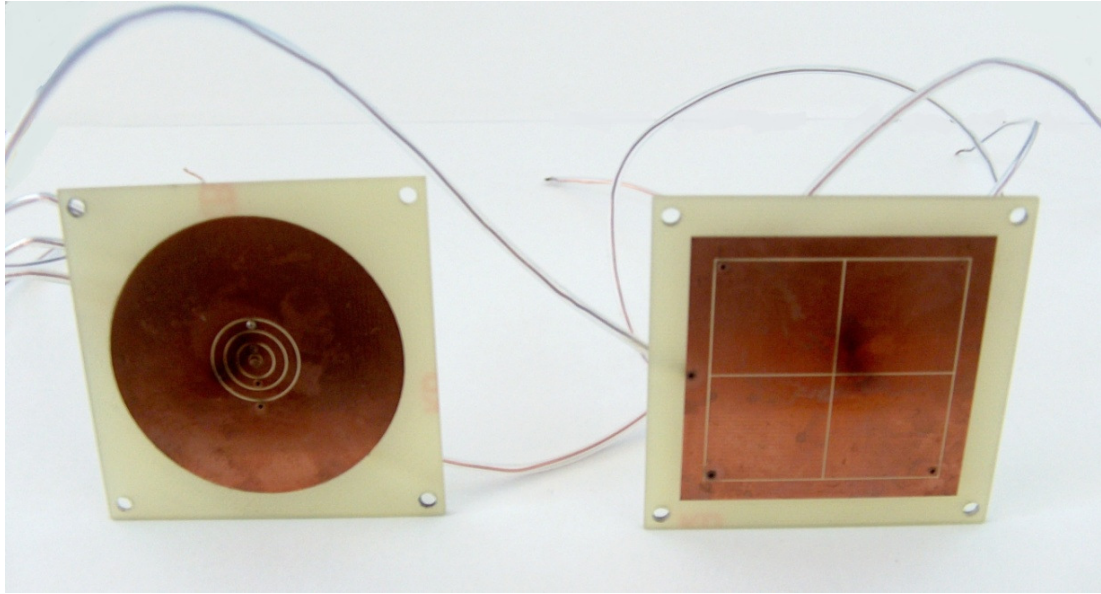
Figure II.9 – Photograph of the circuit boards with concentric (left) and rectangular (right) segments.

We first decided to study the influence of the high voltage HV applied to the accelerating tube on the beam profile. This was made by setting typical values for P_{H2}, I_F, V_S, V_E and V_F and then irradiating alternatively the rectangular and concentric ring segments. As shown in Figure II.10 where current densities are schematically represented for the several segments, the high voltage HV applied to the accelerating tube guarantees that almost all the ionic current is delimited inside a relatively restricted circle of about 5-8 mm in diameter, as intended. However, the beam seems to be slightly deflected from the center of the segmented targets.

In order to study in more detail the beam profile, we looked at the influence of the several parameters of the ion source on it. We therefore varied the voltages V_S, V_E and V_F alternatively, by keeping appropriate values for the remaining ones. Figure II.11 shows that the value of V_S is of little importance in both the distribution and quantity of ions reaching the segmented targets given the appropriate values of V_E and V_F of about approximately V_S-300 V and $0.6V_S$ respectively, as indicated by the manufacturer.
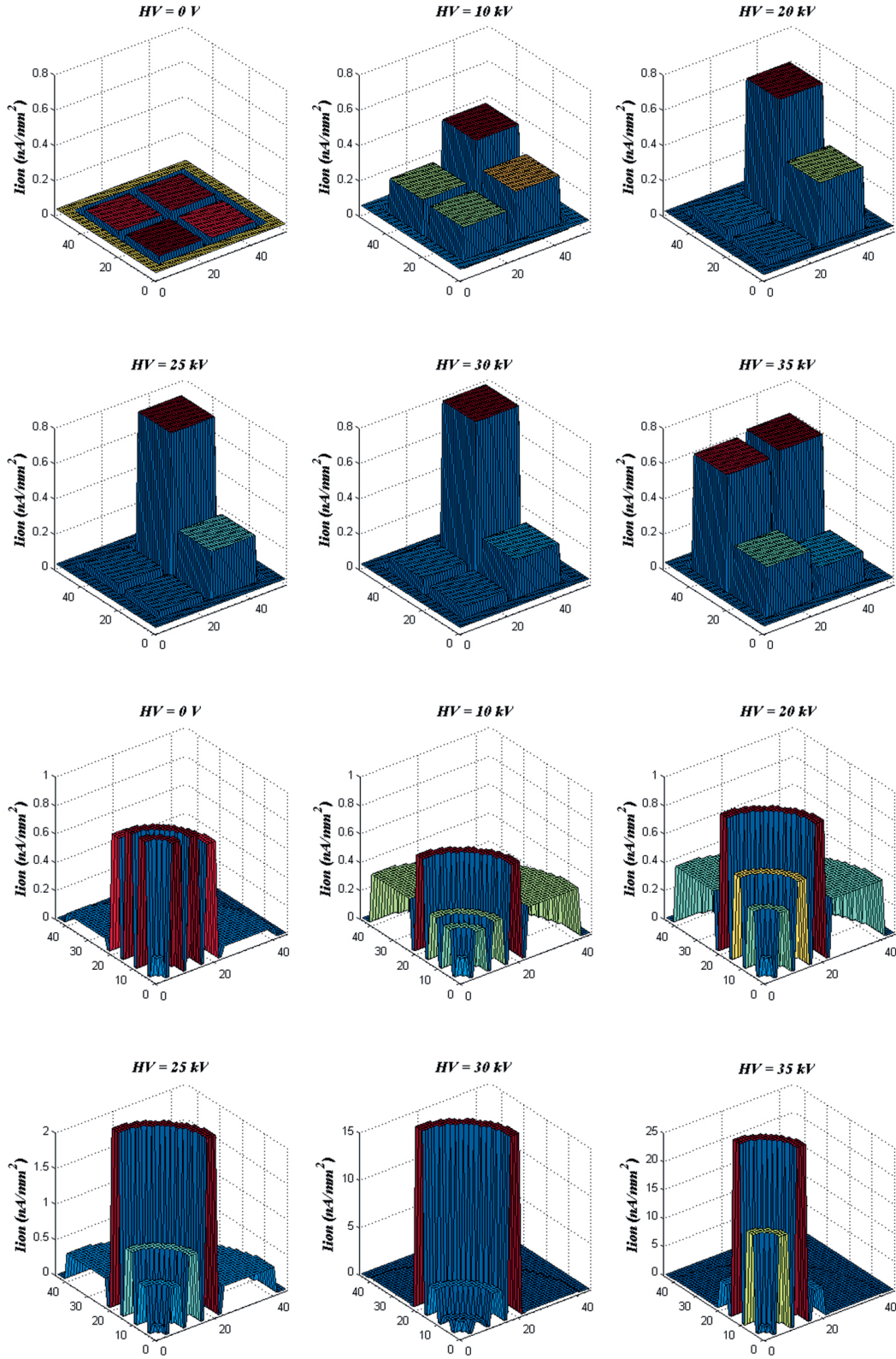
Figure II.10 – Schematic representation of the distribution of the ion beam as a function of the high voltage HV applied to the accelerating tube by using both rectangular (top) and concentric rings (bottom) segments, with P_{H2}, I_F, V_S, V_E and V_F equal to 6×10^{-5} Torr, 2.15 A, 1500 V, 1150 V and 1000 V respectively.

Figure II.11 – Schematic representation of the distribution of the ion beam, with 35 keV protons, as a function of the voltage of the ion source cage V_S by using both rectangular (top) and concentric rings (bottom) segments, with P_{H2} and I_F equal to 6×10^{-5} Torr and 2.15 A, respectively.

We also observed that the value of V_E is neither relevant from both the beam shape and dimensions point of view given the appropriate values of V_F of about $0.6V_S$, although an optimal value of V_E around V_S-300 V, as indicated by the source manufacturer, indeed lead to optimum ionic currents.

On the contrary, Figures II.12 and II.13 clearly show that, for a given set of values for V_S and V_E, the value of the voltage applied to the Einzel lens V_F is of extreme importance concerning the beam profile. Indeed, although almost no ionic current is lost, the ion beam spreads broadly when using inappropriate values of V_F.
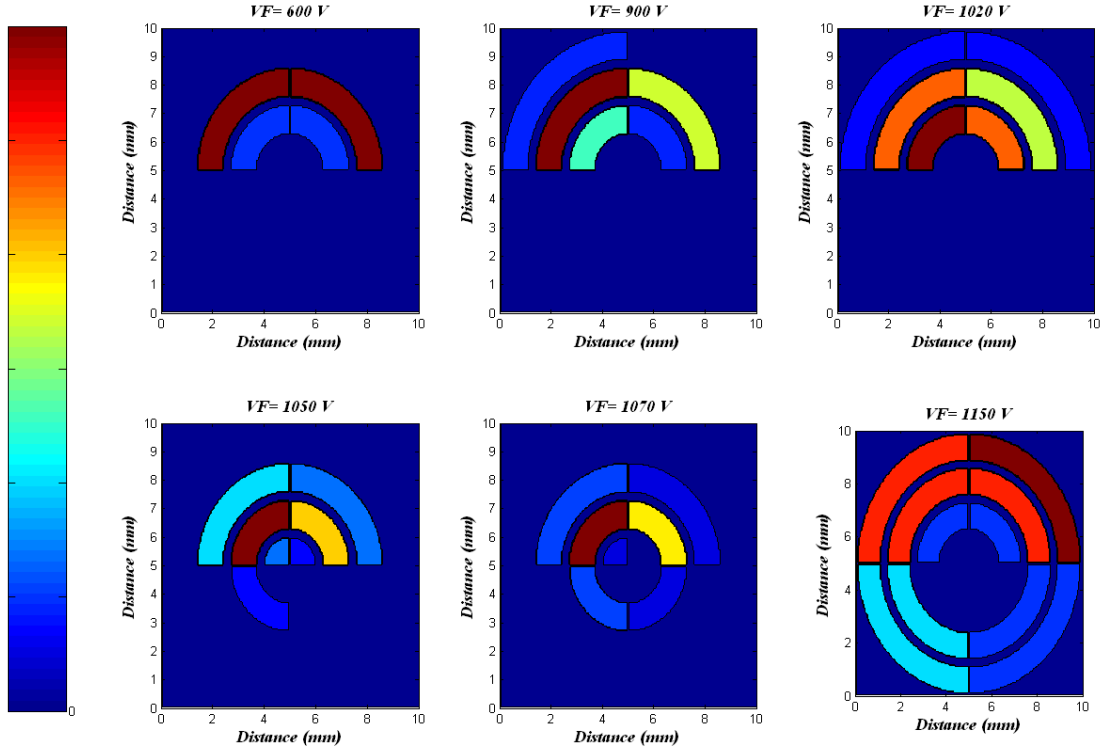
Figure II.12 – Schematic representation at scale of the density distribution of the ion beam current, with 35 keV protons, as a function of the voltage of the Einzel lens V_F by combining the information given by both the rectangular (top) and concentric rings (bottom) segments (Figure II.12), with P_{H2} and I_F, equal to 6×10^{-5} Torr and 2.15 A respectively.
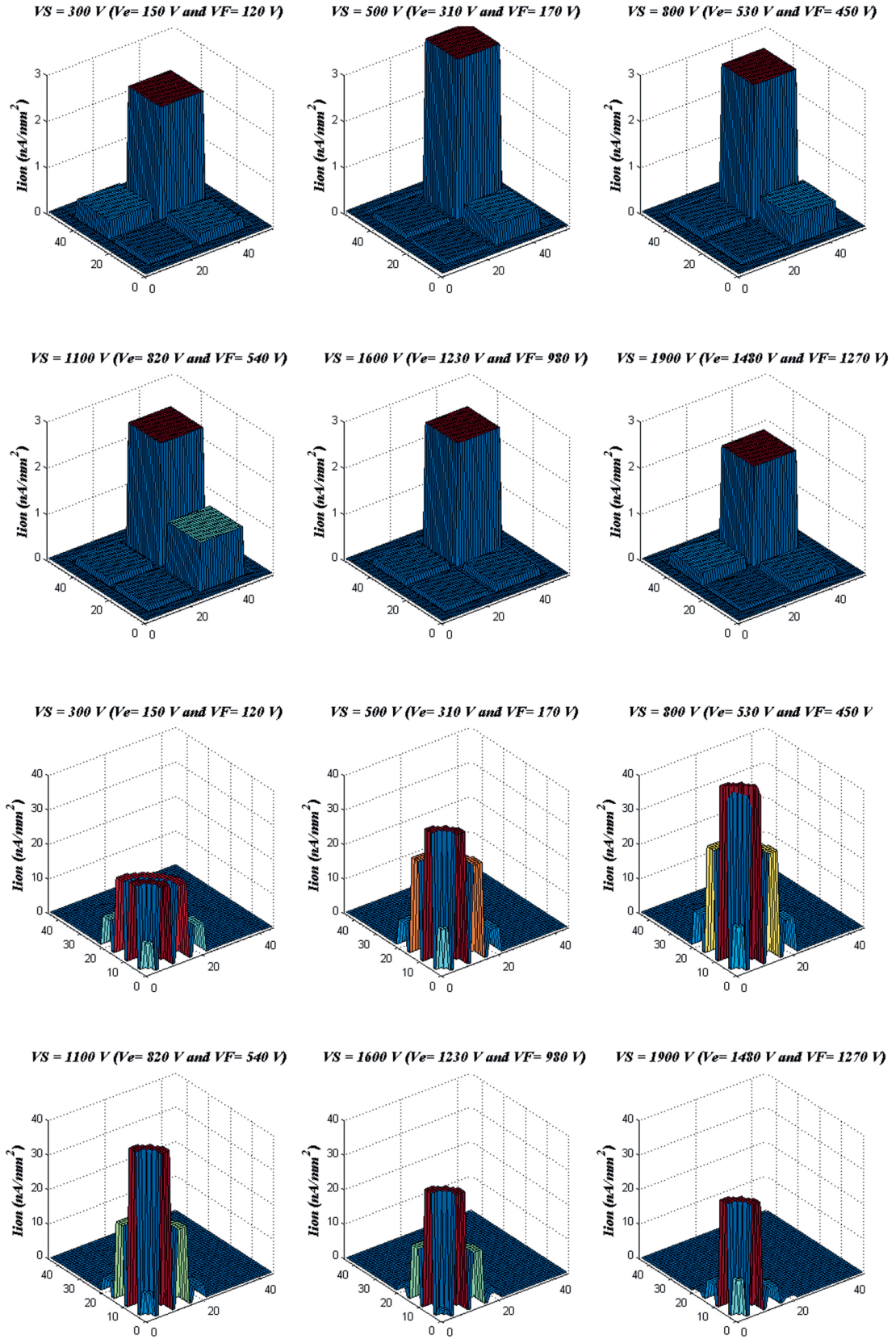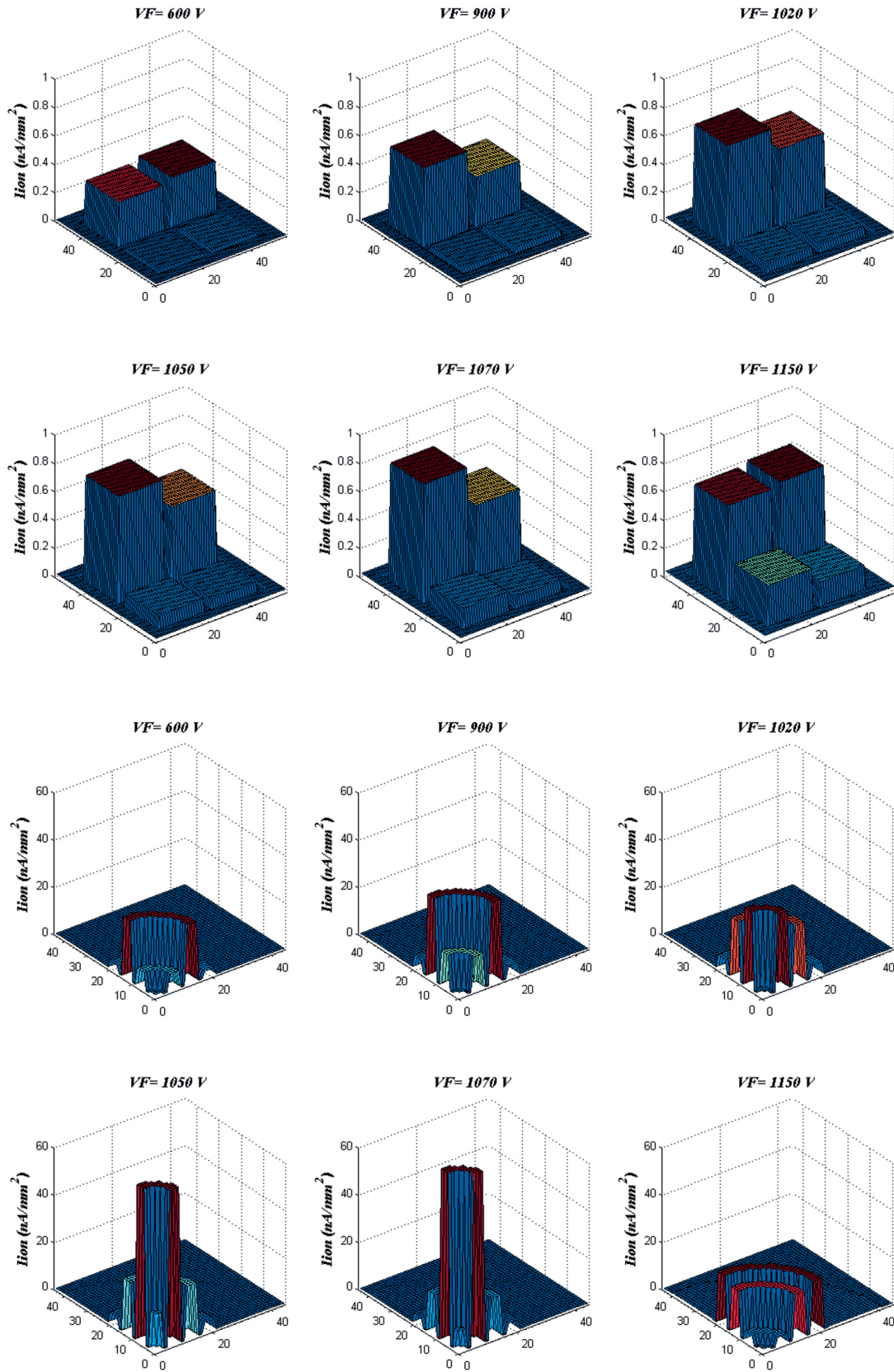
Figure II.13 – Schematic representation of the distribution of the ion beam, with 35 keV protons, as a function of the voltage of the Einzel lens V_F by using both rectangular (top) and concentric rings (bottom) segments, with $P_{H2,}$ I_P, V_S and V_E equal to 6×10^{-5} Torr, 2.15 A, 1500 V and 1150 V respectively.

Another study was carried out in order to evaluate the spread of the ion beam profile along the axis of the reaction chamber (Figure II.14). For this purpose, we used the concentric ring segments at several points along the beam direction above (+) and below (-) the proper position of the irradiated targets (denominated here as z=0) by moving the circuit board with concentric ring segments with the help of a feedthrough with millimetric screw upon which this latter was assembled. As Figure II.14 shows that the ion beam spreads as the deviation from the proper position increases, we can conclude that the parameters of the ion source are indeed optimized for the spot where the samples to irradiate are positioned.
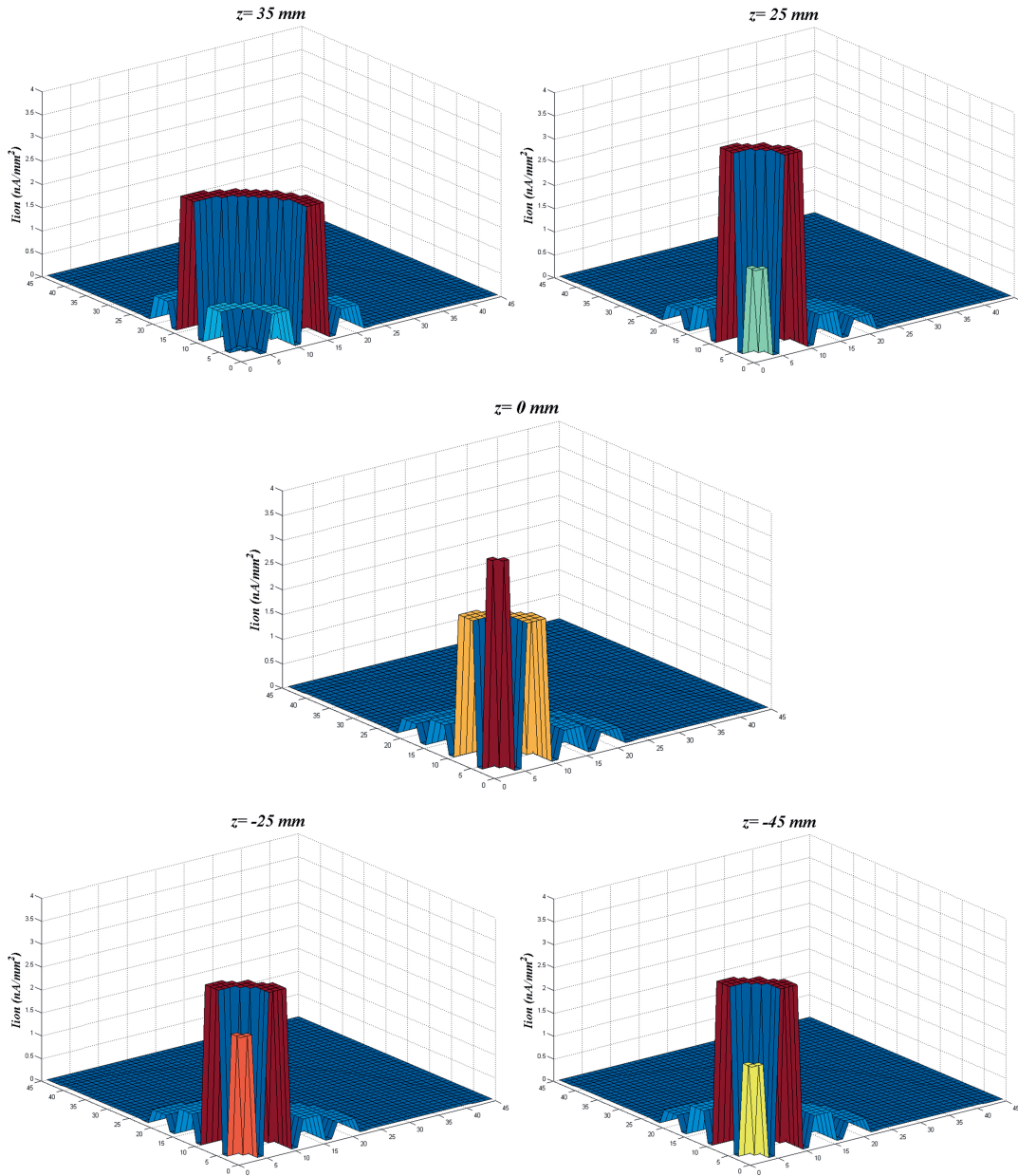

Figure II.14 – Schematic representation of the distribution of the ion beam, with 40 keV energy protons, as a function of position z along the beam direction, obtained by using the concentric rings segments, with P_{H2}, I_F, V_S, V_E and V_F equal to 6×10^{-5} Torr, 2.15 A, 1500 V, 1150 V and 1050 V respectively.

All these studies demonstrate that a large fraction of the total ionic current is invariably collected in only one quadrant, even operating with optimal sets for the voltages of V_S, V_E and V_F, as it can be seen from Figure II.9 where the dark spots in the copper surface correspond to the most irradiated areas. Consequently, we concluded that the overall accelerating tube is deviated from the symmetry axis of the reaction chamber. In fact, even with optimal sets of voltages in the source, for which the inner ring presents high values of current density, the second concentric ring is invariably, and by far, the one with the highest current densities. However, we can also conclude from the studies performed that this deviation is slight (between 1.0 and 2.3 mm away from the symmetry axis) since the third concentric ring constantly presents much lower current densities than the two first ones. Consequently, except for the case where severe beam collimation is required (beams with maximum diameter less than a few millimeters), this slight beam deviation from the symmetry axis was not considered important for our future work. A much more important result from these studies is the confirmation that the great majority of the ion beam is confined within a few millimeters as intended. Such conclusion is verified in Figure II.15 where it is possible to see a small dark ellipse (about 5-6 mm^2) resulting from the beam interaction in a 45º titled thick target with an optimal set of voltages for the source components (for instance, these are 1150, and 1050 V for V_E and V_F respectively with V_S equal to 1500 V). Moreover, Figure II.14 also demonstrates that an optimal set of voltages for the ion source components indeed optimize the beam shape for the postion where the samples are placed since this latter worsens as the target departs from it.
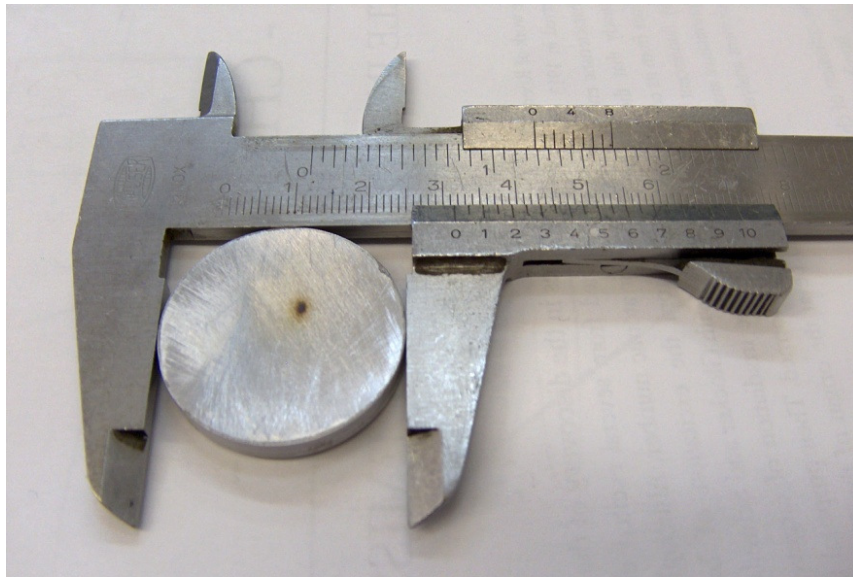
Figure II.15 – Photograph of an aluminium thick target irradiated with protons in the 10-45 keV energy range.

Finally, these studies about the dimensions and the shape of the beam have confirmed that a beam collimator is necessary since residual density currents are still present in the furthest areas from the spot where the targets to be studied will be placed. However, we had to find a compromise concerning beam collimation: on one hand, it is necessary due to both the limited dimensions of some of the targets and the geometry of

the reaction chamber (including defining correctly the detector solid angle) but, on the other hand, it cannot be too severe to provide ion beams with sufficient intensities.

II.2 COMPONENTS OF THE REACTION CHAMBER

Concerning the reaction chamber, we had to project, build and implement all the components necessary in a typical PIXE set-up (as described in section I.2.1) although it has a confined volume. Great care was taken to make the equipment as versatile as possible.

First of all, the X-ray detector we developed (described in Chapter III) needed to fit into the reaction chamber and to simultaneously ensure vacuum seal. This was done by manufacturing a flange adapter (Figure II.16) which was connected simultaneously to one of the exit flanges of the reaction chamber and to the top flange of the X-ray detector.
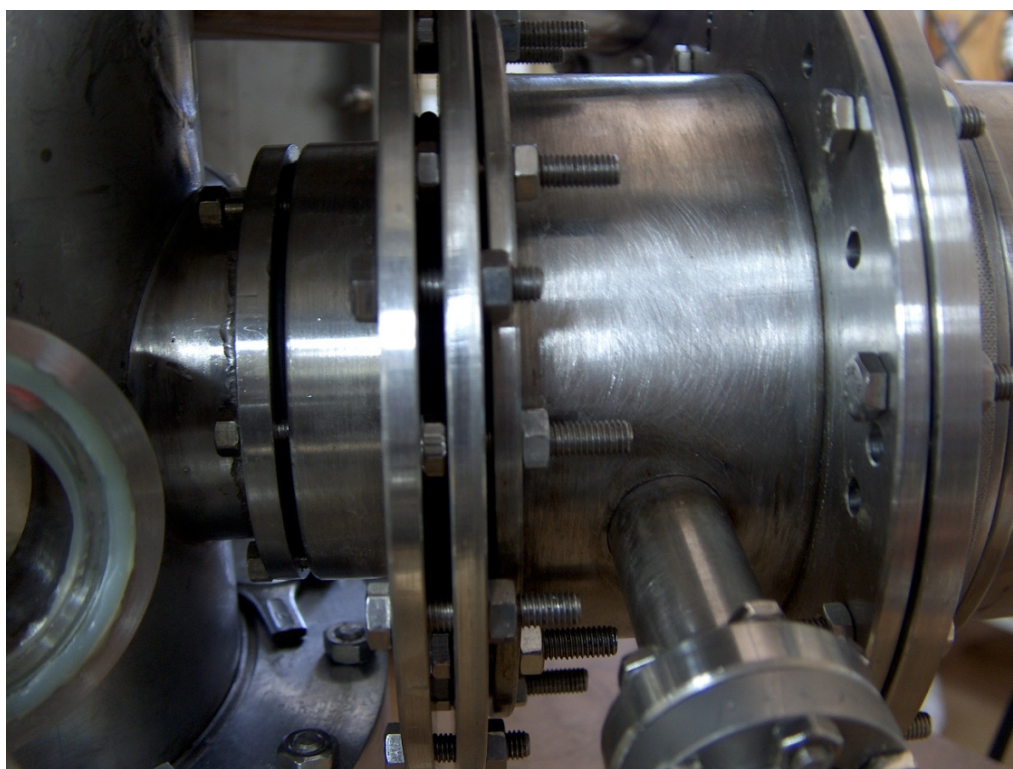
Figure II.16 – The X-ray detector assembled to the reaction chamber with the help of an adapter flange.

As we already mentioned, it was also fundamental to provide beam collimation to guarantee that the beam impinges only on the sample so that the registered X-ray events correspond to the beam interaction with the specimen only. As shown in Figures II.17 and II.18, this was made by inserting 3 parallels rings with 15 mm diameter holes in their center that can additionally house other inner rings with reduced holes of distinct diameters so that it is possible to select different collimation restrictions (as represented

in Figure II.17). The first of these rings is larger than the accelerating tube aperture to ensure that only the ions close to the system axis interact inside the reaction chamber.

Also for collimation purposes, an X-ray collimator was mounted to prevent scattered and/or characteristic X-rays resulting from the interaction of the beam with the collimator material from reaching the detector window. This consists on three parallel rings between the target and the detector window. These rings, also parallels to the detector radiation entrance window, have holes in their center with increasing diameter as the specimen-to-collimator distance increases, as represented in Figure II.17.

In addition, we built a target holder (Figures II.17 to II.19) to keep the specimen in the proper position. The bombarded sample surface defines a 45º angle with respect to both the beam direction and the detector radiation entrance window. As we intended to irradiate thin specimens, this target holder has a hole in its center to allow the beam to reach a Faraday cup located below. The specimen holder (Figure II.18) was built upon a ring that enables rotation of the entire target holder around the axis of the reaction chamber. Besides, the entire target holder was also mounted upon a linear motion feedthrough with millimetric screw that enables to vary precisely its height inside the reaction chamber so that the irradiated sample can be placed properly in front of the X-ray detector. Both these movements allow the optimization of the specimen position.

The Faraday cup, shown in Figure II.18.b), is an electrically insulated metallic disk where the beam is dumped after passing through the thin targets irradiated and whose diameter is much larger than the maximum beam diameter. It is connected to an external charge integrator or to an ammeter through a feedthrough allocated in the bottom flange of the reaction chamber (Figure II.18) to make possible the measurement of the integrated charge of the beam. In order to avoid the escape of secondary electrons from the Faraday cup surface while the beam is impinging on it, which would originate a mistaken measure of the integrated charge, we also installed a secondary electrons suppressor (Figure II.18.b)) a few millimeters above the Faraday cup disk. It consists on a very thin mesh mounted on a circular frame, biased with a negative voltage so that the secondary electrons are forced to remain in the Faraday cup. This ring is connected to a feedthrough so that it can be biased with a negative voltage. Besides, we also projected these reaction chamber elements to enable the irradiation of thick targets for which the beam is dumped in the specimen itself. In this case, beyond measuring the beam current on the target itself, we also modified the beam collimators in order to place another secondary electron suppressor ring upon the sample. This was realized, as it can be seen in Figure II.19, by replacing the rods used to support the collimator rings (Figure II.18) by insulating ones so that the secondary electron suppressor ring is electrically isolated.

Finally, we also have incorporated a beam chopper. It consists of a thick disk placed at the end of a linear motion feedthrough whose linear displacement perpendicularly to the beam direction enables to intercept the beam between the two first collimator rings.

All these components were incorporated in the reaction chamber, as schematically represented in Figure II.17.

Stainless steel

Teflon

Mild steel

Glass
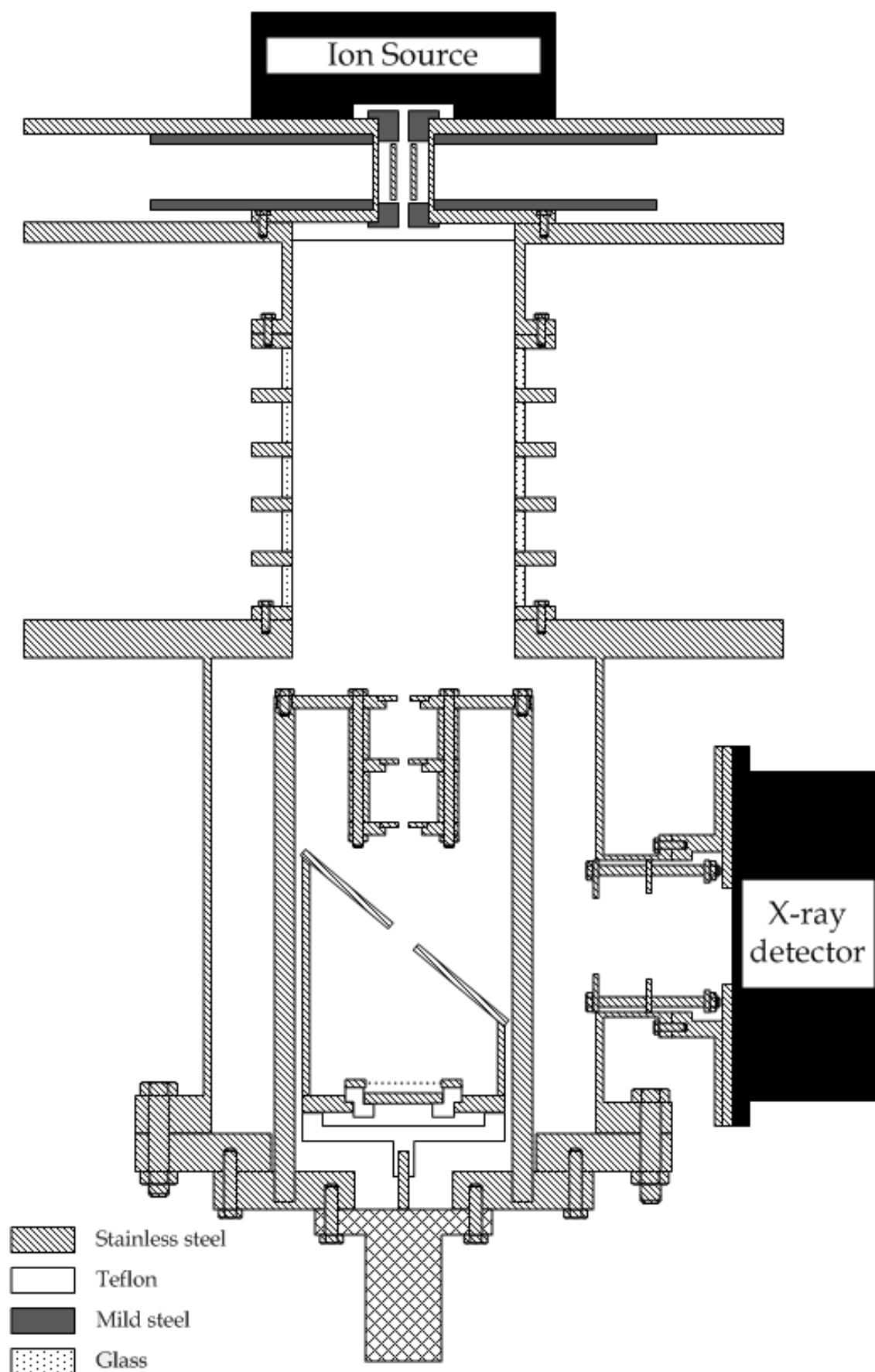
Figure II.17 – Schematic of the PIXE experimental arrangement.

Figure II.18 – Photographs of the target holder assembled on a feedthrough with millimetric screw connected to the bottom flange of the reaction chamber. The left photograph shows the entire set-up, including the beam collimators, while the right one focus on the Faraday Cup with a secondary electron suppressor ring which was used during the irradiation of thin samples.
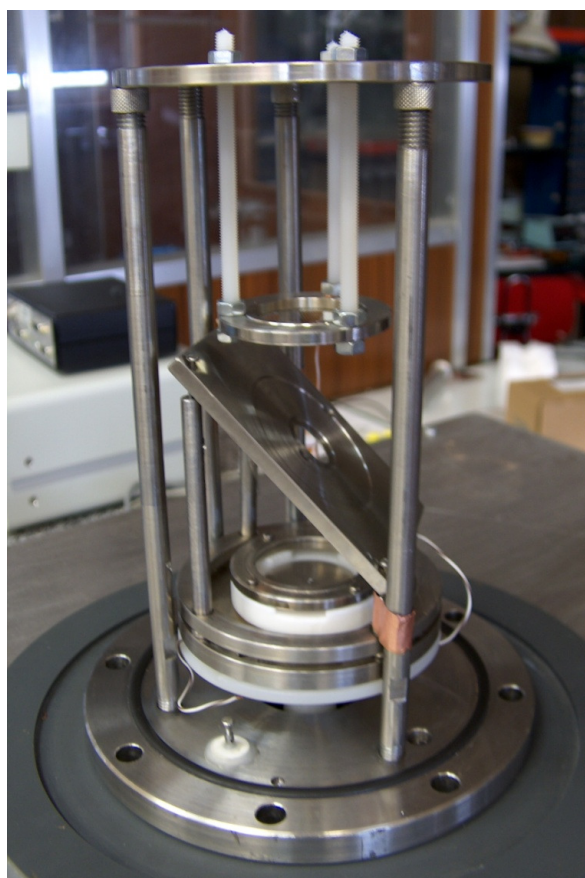
Figure II.19 – Photograph of the target holder with an electrically insulated secondary electron suppressor upon the sample spot which was used during the irradiation of thick samples.

II.3 WIEN FILTER

As mentioned earlier, it was also fundamental to incorporate an ion selecting device in the particle accelerator in order to guarantee that only one kind of ions impinges on the specimens at a time. We decided to build a Wien filter to accomplish this task: this device acts as a velocity filter, and hence as a mass filter for charged particles, and consists of a magnet and a pair of electrostatic plates arranged perpendicularly to magnet poles, as illustrated in Figure II.20.
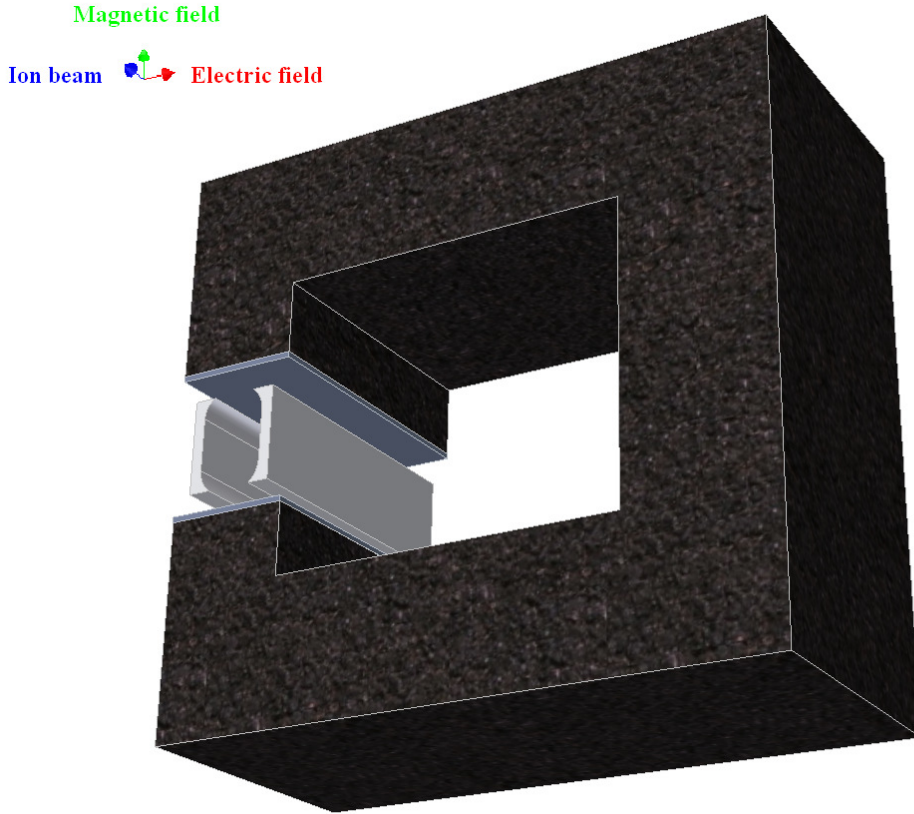
Figure II.20 – Schematic of the Wien filter.

The electric and magnetic fields, $\vec{\varepsilon}$ and $\vec{B}$ respectively, are perpendicular to each other and to the ion trajectory as represented in Figure II.20. The electric and magnetic forces, $\overrightarrow{F_e}$ and $\overrightarrow{F_m}$ respectively, felt by the incoming ions inside the device have therefore the same direction, perpendicular to the beam direction, but with opposite ways. While the electric force F_e felt is the same for all the ions extracted from the source with the same positive charge q (for a given potential difference ΔV between the plates, which equals $2V_{plates}$, where V_{plates} is the absolute value of the voltage applied to each plate), the magnetic force F_m depends on the ion velocity and hence on its mass. The net force $\vec{F}$ felt by the ions is a characteristic of the ion velocity v_i, i.e. of its mass m as shown by the following relationships:

$$\vec{F} = \overrightarrow{F_e} + \overrightarrow{F_m} = q\,(\vec{\varepsilon} + \vec{v} \times \vec{B}\,)$$
(Eq. II.1)

and so

$$F = q \, (\varepsilon - v_i B) \qquad \text{(Eq. II.2)}$$

Equation II.2 shows that it is possible to set the value of the electric field, i.e. of ΔV, so that F vanishes for ions with a certain initial velocity v_{i0}. This initial velocity is determined by the electric potential V_S applied at the ion source cage. Ions of mass m_0 and charge q_0 acquire a kinetic energy equal to $q_0 V_S$ in the ion source and have therefore an initial incoming velocity v_{i0} equal to $\sqrt{2q_0 V_S / m_0}$ when leaving it.

These ions with mass m_0 and charge q_0, for which $v_{i0} = \varepsilon / B$, go through the device unperturbed, exiting the Wien filter while the ions with different q/m ratio therefore feel a non-zero net force $\vec{F}$ and are deviated to one side of the filter because this net force $\vec{F}$ is perpendicular to their motion. This way, we guarantee that only ions with a given velocity, and hence a given q_0/m_0 ratio, go through this filter in direction to the accelerating tube.

Another ion with mass m and charge q, different than m_0 and q_0 respectively, leaving the ion source has an initial velocity v_i (different from v_{i0}) equal to $\sqrt{2qV_S / m}$. This ion consequently suffers a transversal constant acceleration, $\ddot{x}$, described by the following relationship:

$$m\ddot{x} = F = q(\varepsilon - v_i B) = q(v_{i0} B - v_i B) = qB\sqrt{2V_S} \left(\sqrt{\frac{q_0}{m_0}} - \sqrt{\frac{q}{m}} \right) \quad \text{(Eq. II.3)}$$

where x is the coordinate in the direction of both electrical and magnetic forces, which is perpendicular to the direction defined by the motion path of the ions.

Consequently, since both $\dot{x}(0)$ and $x(0)$ are nulls,

$$x(t) = \frac{qV_{plates}}{md} \left(1 - \sqrt{\frac{q \, m_0}{q_0 \, m}} \right) t^2 \qquad \text{(Eq. II.4)}$$

where the plates are biased with $+ V_{plates}$ and $-V_{plates}$. Alternatively, as a function of the distance z travelled within the Wien filter:

$$x(z) = \frac{V_{plates}}{2dV_S} \left(1 - \sqrt{\frac{q \, m_0}{q_0 \, m}} \right) z^2 \qquad \text{(Eq. II.5)}$$

where z is the is the coordinate of the axis defined by the direction of motion of the ions ($z(t = 0) = 0$ and $\dot{z}(t = 0) = v_i$) and d is the distance between the two plates that define the electric field ε.

We projected this Wien filter by taking into account Equation II.5, the components available in the market and the construction restrictions due to limited space between the poles of the magnet acquired.

We first decided to use a permanent magnet rather than an electromagnet in order to avoid both the manufacturing of an additional power supply with fluctuating ground potential and the consequent increase in energy consumption due to the limited power delivered by the batteries. As a result, the filter we built has constant magnetic field and we only can vary the electric field, by varying the voltage difference ΔV between the plates since the distance d separating these is also constant. We acquired a permanent major magnet with a "U" shape, model Major Magnet 862 from Eclipse (schematically represented in Figure II.20 and shown in Figures II.21 and II.22), which is characterized by having a uniform magnetic field of 0.21 T between its 2 parallel poles. These poles are plates of $22.2 \times 52.4 \text{ mm}^2$, separated by 27.3 mm. As shown in Figure II.22, this permanent magnet was placed around but outside the vacuum tube inside which the ions travel and mild steel plates where used upon each of its faces in order to cancel the magnetic field outside the filter. Concerning the electric field, both plates of the filter were biased using an additional electronic module developed by my colleague A. Trindade. We decided to apply the same voltage V_{plates} to both plates, but with opposite polarity, to define the electric field inside the filter rather than to have one plate at ground potential with the other biased with high voltage. This decision enabled to add a second and more precise voltage increment for each plate independently rather than optimizing the voltage value in a single plate with the other one at a fixed potential. The electronic module built therefore enables to vary very precisely the voltage of each plate independently using an additional potentiometer.

We also took into account the following aspects in the projection of this filter:

- ✓ we are considering very light ions, i.e. the ones resulting from the ionization of either H_2 or D_2 gases.
- ✓ independently of the kind of ion considered, all the ions that reach the Wien filter have an energy which is exclusively defined by the source voltage V_S and the ion positive charge q, being therefore equal to qV_S.
- ✓ the maximum value of V_S is 2 kV.
- ✓ we considered the most critical case to size the filter, which is the case of protons due to their lower mass (i.e. their higher incoming velocity), since this implies larger voltage difference ΔV to be applied between the plates for the referred ion to be selected.
- ✓ the Wien filter was placed between the ion source and the accelerating tube (as shown in Figure II.21) to limit the voltages required to select the ions.
- ✓ the exit collimator has to allow the selected ions to go though the filter unperturbed and without any loss of intensity while preventing the other ions from exiting the filter.
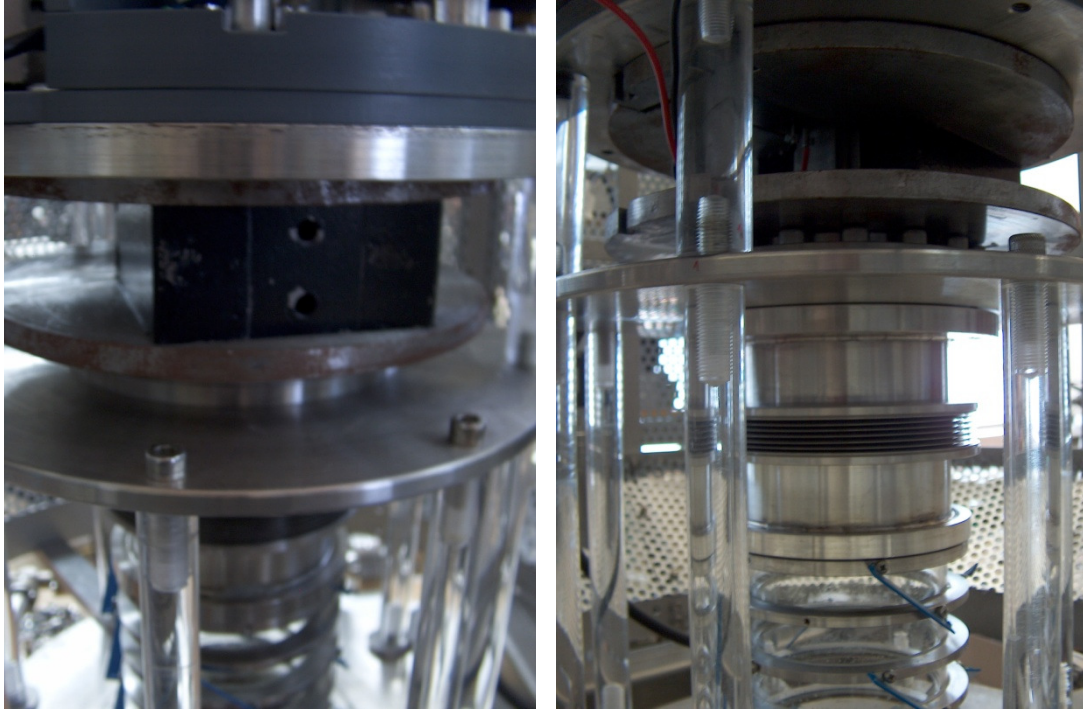
Figure II.21 – Photograph of the permanent magnet with "U" shape with mild steel plates upon each face.
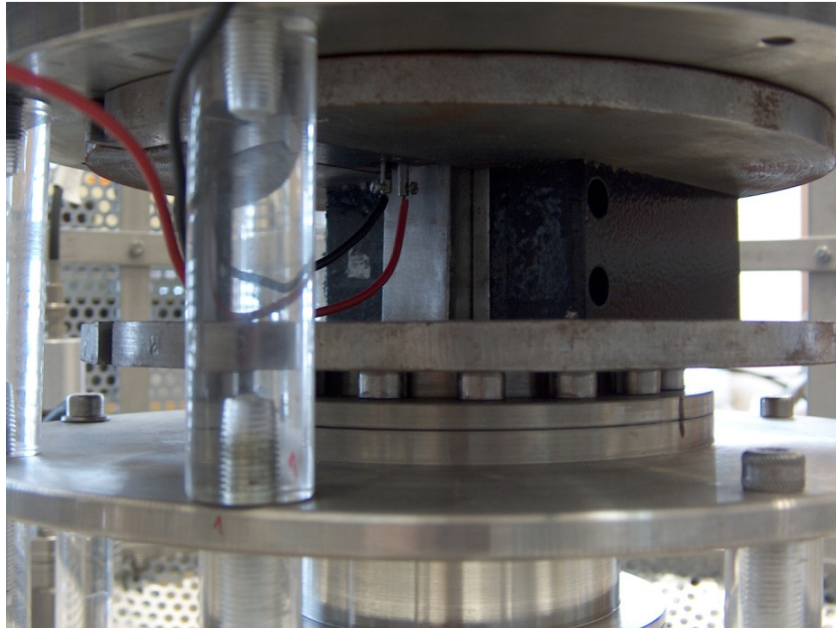
Figure II.22 – Photograph of the permanent magnet surrounding the Wien filter, i.e. the rectangular tube inside which the ions are selected.

Besides, considering the work of Leal-Quiros and Prelas [II.2], we projected plates with tilted edges in order to improve the performance of the filter regarding focusing. We used the Maxwell® software [II.3] to study the electric field force lines as a function of both the dimensions and the shape of the tilted edges for a few cases, as illustrated in Figure II.23, in order to choose a preferred geometry.
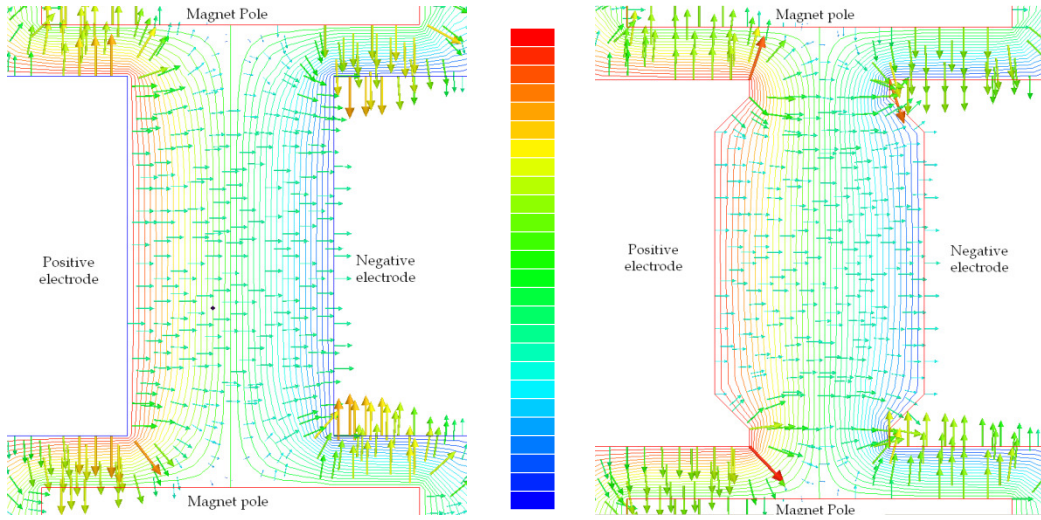
Figure II.23 – Comparison of the electric field line forces for the case of standard rectangular electrodes (left picture) and tilted ones (right picture).

In order to determine the dimensions of the exit collimator we used Equation II.5 which describes the trajectory of ions inside the filter. We considered that this exit diameter had to have a minimum diameter so that the desired kind of ion still exits the filter even when the voltage applied to the plates ΔV has an uncertainty up to 5 % around its optimal value. We also determined the deviation of all the possible kind of ions resulting from the ionization of a given gas when the filter is set for one of these ions to guarantee that only the desired ion specie exits from the filter. An exit collimator diameter of 5 mm was chosen from these calculations. The entrance collimator is shown in Figure II.24 where it can be seen that it is made of mild steel, just as the exit collimator, in order to close the magnetic field lines resulting from the presence of the surrounding permanent magnet.
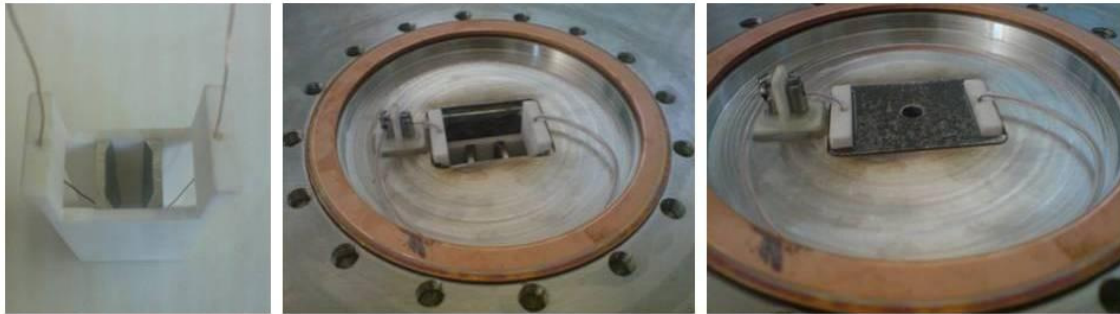
Figure II.24 – Photograph of the inside central region of the Wien filter. The two stainless steel plates define the electric field and are surrounded by an insulator support (left picture); a double feedthrough with insulated wires connected to each plate (picture at the centre) and the top collimator at the entrance of the filter (right picture) is made of mild steel in order to close the circuit of the magnetic field lines (an identical mild steel collimator piece is placed at the output of the filter).

As we finished installing the manufactured Wien filter, we performed a few tests in order to verify that it was working correctly. First of all, without the permanent magnet installed, i.e. without any magnetic field, we tested the filter by studying the minimum voltage of V_{plates} to apply to the plates to guarantee that protons do not exit

the filter as a function of the source cage potential V_S since the incident protons energy is proportional to it. In this case the net force felt by the ion is only due to the electric filed between the plates, and so:

$$m\ddot{x} = F = q\varepsilon = q \; \frac{2V_{plates}}{d} \qquad \text{(Eq. II.6)}$$

where d is the distance between the plates than define the electric field and is equal to 10.8 mm.

Hence, since both $\dot{x}_0$ and x_0 are nuls

$$x = \left(\frac{V_{plates}}{2dV_S}\right) z^2 \qquad \text{(Eq. II.7)}$$

It is therefore possible to relate the minimum voltage of V_{plates} from which, after travelling a distance l corresponding to the length of the filter, the ions are deviated transversely of a distance x of at least 2.5 mm (corresponding to the radius of the exit aperture hole) and hence do not exit the filter. Consequently, the minimum value of V_{plates} from which no ionic current is detected varies linearly with V_S. The results obtained experimentally are presented in Figure II.25 where it is also possible to see that these are in good agreement, within experimental errors, with the expected behaviour. The slight discrepancies between the experimental values and the expected behaviour can eventually be attributed to small uncertainties in either the distance between the plates as well as in their parallelism. Both discrepancies can be attributed to uncertainties during the manufacturing processes or in the assembly of the different pieces.

We then installed the permanent magnet so that the ions travelling into the filter felt simultaneously both electric and magnetic forces. In order to guarantee a proper operation of the filter we studied the behaviour of the voltage V_{plates} to apply to the plates so that the electric and magnetic forces vanish for protons, i.e. that maximizes the ionic current I_{ion} measured in the reaction chamber, as a function of the energy of the incident ions, i.e. of V_S. In this case, protons travel though the filter undeflected since $v_{io} = \varepsilon/B = \sqrt{2q_0 V_S/m_0}$ where $\varepsilon = 2V_{plates}/d$. As a result,

$$V_{plates} = \left(dB\sqrt{\frac{q_0}{2m_0}}\right) \sqrt{V_S} \qquad \text{(Eq. II.8)}$$

The results obtained are presented in Figure II.26 where it is possible to verify that the experimental data are in agreement with the expected behaviour. It is possible to deduce the value of the magnetic field from the fit made to the data obtained experimentally. We determine a value of the magnetic field of 165.7 ± 5.7 mT, which is slightly lower than the value of 210 mT indicated by the manufacturer but however in good agreement with the maximum value of about 180 mT that we measured with a magnetic field meter.
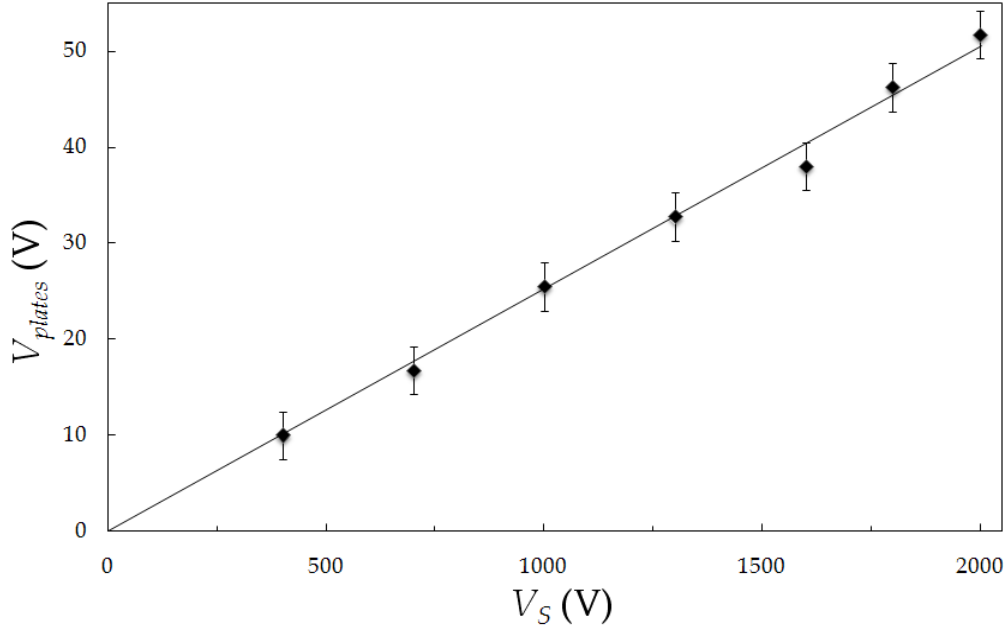
Figure II.25 – Voltage V_{plates} to apply to each plate in order to deflect the protons from the outside the filter without the presence of the magnetic field as a function of the voltage V_s of the source cage.
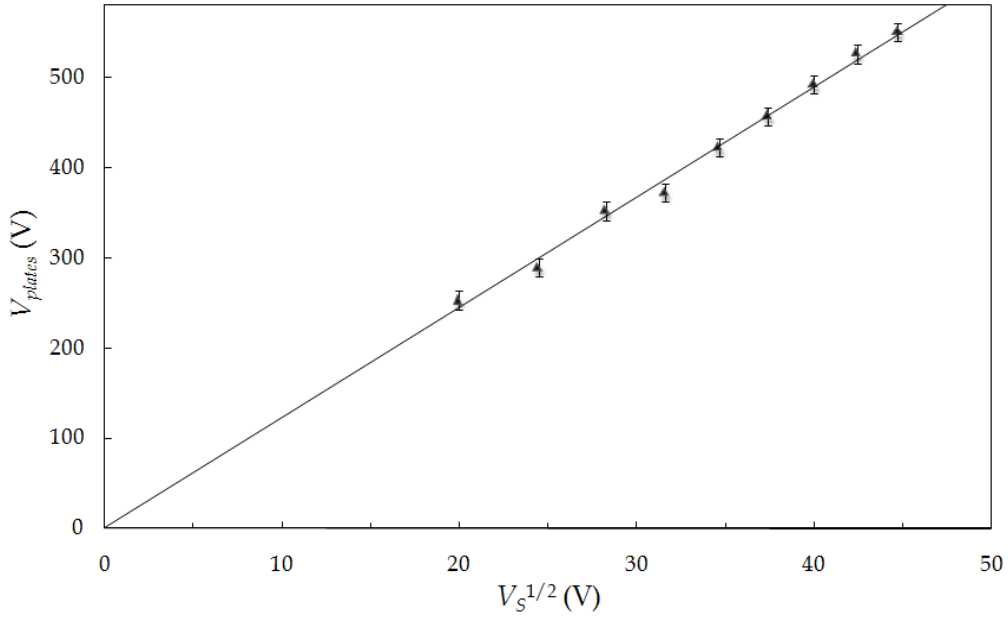
Figure II.26 – Values of V_{plates} in both plates that maximize the ionic current of the filter as a function of $\sqrt{V_S}$.

Despite all the improvements presented in this Chapter, we still have not considered another feature that is essential to carry out this work successfully which is the X-ray detection system. Due to both the very low X-ray production cross-sections expected and the very low energy of the X-ray to detect, a traditional Si(Li) detector cannot be used, as explained earlier in Chapter I, to register the fluorescence spectra. For these reasons, we built and characterized the performance of an X-ray detector which we

optimized for this particular application. This X-ray detector, a Gas Proportional Scintillation Counter, is the subject of the following Chapter.

II.4 REFERENCES

[II.1] A.M.F. Trindade, "Um Sistema para Aceleração de Iões Positivos a Baixas Energias: Projecto, Construção e Testes", M.Sc. thesis, University of Coimbra, 2006.

[II.2] E. Leal-Quiros and M.A. Prelas, "New tilted-poles Wien filter with enchanced performance", Rev. Sci. Instrum. 60(3), pp. 350-357, 1989.

[II.3] http://www.ansoft.com/products/em/maxwell/

– CHAPTER III –

THE X-RAY DETECTION SYSTEM

As referred at the end of Chapter I, the X-ray detection system is a fundamental feature in the framework of these PIXE studies since it has to present simultaneously a large detection area and a good efficiency for the detection of soft X-rays below 2 keV because of the very low cross-sections expected. For these reasons, and despite their much better performance in terms of energy resolution, neither wavelength dispersive X-ray detectors, X-ray calorimeters, nor conventional Si(Li) or other semiconductor based radiation detectors typically used in PIXE set-ups are suitable choices to carry out these studies successfully. On the contrary, despite leading to poorer energy resolutions, room temperature gaseous X-ray detectors fulfil both these requirements. Besides, gaseous detectors are easily adaptable to the existing reaction chamber without the insertion of any additional radiation window, which is fundamental to obtain improved detection efficiency for soft X-rays.

One can distinguish two types of gaseous radiation detectors to perform X-ray spectrometry: gas avalanche multiplication detectors (proportional counters) and gas proportional scintillation counters (GPSC). Both produce output pulses with amplitudes proportional to the number n of primary electrons resulting from the X-ray interaction with the filling gas; n being approximately proportional to the energy E_X of the incident X-ray. Since n is small, about 200-300 primary electrons for a 5.9 keV photon in pure Xe, an amplification stage is required prior to further electronic treatment of the detector signal.

The different processes used to achieve the signal amplification are what distinguish GPSCs from gas avalanche electron multipliers. While gas avalanche electron multipliers use charge amplification, the signal amplification in GPSC relies on the production of secondary scintillation light which has the advantage of leading to much reduced statistical fluctuations and thus to improved energy resolutions when compared to those obtained in PCs (about 8 % for 5.9 keV X-rays with a GPSC [III.1] instead of at least 11 % for a PC [III.2]). Moreover, GPSCs present several other advantages over PCs. For instance, the absence of space charge effects in GPSC (since charge multiplication is avoided) allows to operate at considerably high counting rates, up to typically 10^4 counts/s, which is fundamental to our particular application since not only the X-ray detection system will register the counts from the X-ray fluorescence peaks (that do not represent any problem due to the expected low cross-sections involved) but also the bremsstrahlung continuous that has a high counting rate. Another important advantage of GPSCs over PCs, which is fundamental for our work, is their performance for the detection of very low energy X-rays, an application where GPSCs are particularly competitive since they can outperform even solid-state detectors in the 0.2-1 keV range [III.3].

For all these reasons, we decided to build a GPSC to register the X-ray spectra of our PIXE studies.

III.1 THE GAS PROPORTIONAL SCINTILLATION COUNTER

The Gas Proportional Scintillation Counter (GPSC) has been introduced by Conde and Policarpo in 1967 [III.4]. It consists of a vessel filled with a noble gas and in its most conventional design it has two distinct regions: the absorption/drift region and the secondary scintillation region as illustrated in Figure III.1.
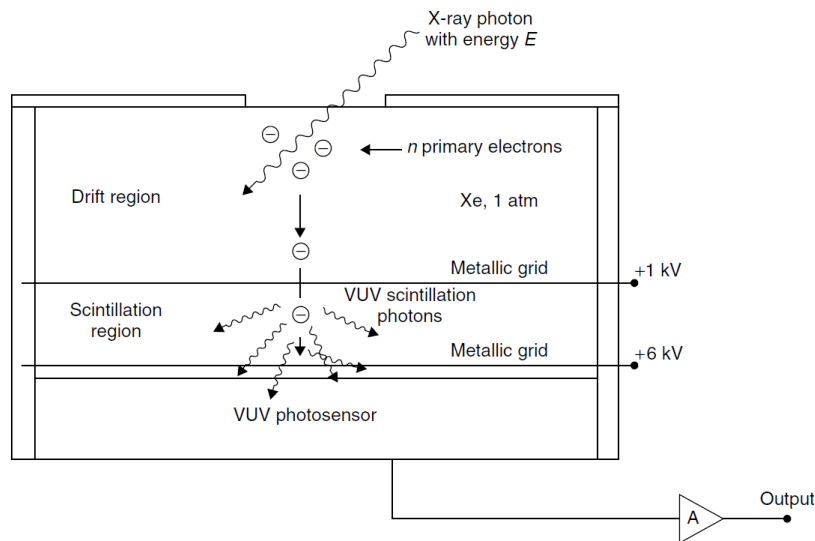

Figure III.1 – Schematic of the Gas Proportional Scintillation Counter [III.1].

The incident ionizing radiation of energy E_X up to typically 50 keV is absorbed, mostly by photoelectric effect [III.1], in the noble gas medium of the absorption/drift region where a number n of primary electrons is produced, and which is in good approximation proportional to the energy E_X. Thanks to a weak reduced electric field in this absorption/drift region, E_d/p (typically about 0.1 V cm^{-1} Torr^{-1}), these primary electrons drift towards the secondary scintillation region where the reduced electric field E_s/p is higher, since it must be above the threshold for excitation of the filling gas but however lower than its threshold for ionization. This way, the drifting electrons gain enough energy between collisions to excite, but not to ionize, the gas atoms whose de-excitation leads to the emission of secondary scintillation light. This secondary scintillation light is characteristic of the filling gas and is then detected by a photosensor that produces an electrical signal proportional to the amount of light detected and thus to the absorbed radiation energy E_X.

Since the efficiency of production of secondary scintillation light is high for noble gases, the signal amplification is high and has the advantage of presenting less statistical fluctuations than the charge amplification processes used in the competitive detectors. For example, up to 500 VUV photons per primary electron can be produced in Xenon per cm per bar [III.5].

GPSCs are usually filled with pure Xe at slightly above atmospheric pressure because this particular noble gas combines a large secondary scintillation yield and a large photoelectric cross-section to a small average energy to create a primary electron-ion pair, which is usually denominated as w-value ($w=E_X/\bar{n}$), and also a small Fano factor F defined as the relative variance of $\bar{n}$, $F = \sigma_n/\bar{n}$.

Three distinct GPSC geometries have been implemented in the last decades; namely the spherical anode geometry [III.6], the cylindrical geometry [III.4] and the uniform electric field one [III.7]. The latter geometry is the most used due to its improved performance.

On the other hand, several alternative filling gas and/or photosensors have been the subject of many publications throughout the years. While photomultiplier tubes (PMT) were almost exclusively used in the early years of the GPSC, several kinds of photosensors are nowadays used depending on the detector application [III.1].

A detailed description of the GPSC can be easily found in several review papers and books [III.1],[III.8] and is therefore not presented here since it is not the purpose of this work. Nevertheless, it is inevitable to relate some of the characteristics of the GPSC for the understanding of the choices made concerning the projection/optimization of the X-ray detector that was built.

Since we expect low counting rates, we need to build a large sensitive area GPSC. As all the photosensors available have inevitably finite dimensions, this implies compensating the decreasing amount of secondary scintillation light reaching the photosensor, because of solid angle effects, with the radial coordinate of the point of absorption of the radiation. As explained in [III.9],[III.10], there are two ways to compensate the radially decreasing amount of the VUV secondary scintillation light reaching the photosensor (and so the decreasing detector output signal amplitude) and

therefore avoiding the consequent degradation of the energy resolution for high detection areas. The first consists of increasing radially the detection efficiency of the secondary scintillation light, by using either masks with radially decreasing transmission covering the photosensor or photosensors with radially increasing efficiency, in order to keep constant the amount of secondary scintillation light detected independently of the point of absorption. The second method relies on increasing radially the intensity of the secondary scintillation produced in the scintillation region, i.e. the number of VUV photons produced, by increasing radially the electric field between these grids. This latter technique was successfully implemented by using a curved grid [III.9]-[III.11] since it led to improved performance for radiation windows with diameters up to 40 mm [III.12].

However, the implementation of such technique is of little or no interest if the photosensor used has, independently of the resultant GPSC performance, a limited sensitive area as it is the case of Large Area Avalanche Photodiodes (LAAPD) [III.13]. On the other hand, only few photosensors enable the detection of very soft X-rays below 2 keV, the others being too noisy electronically. Despite all the recent publications about alternative photosensors as wire chambers with photosensitive vapours like tetraaminoethylene (TMAE) [III.14], Large Area Avalanche Photodiodes (LAAPD) [III.15], microstructures covered with photocathode films like Gas Electron Multipliers (GEM) in single and multistage versions [III.16],[III.17], Micro Hole and Strip Plates (MHSP) [III.18] or Microstrip Plates (MSP) [III.19], the Photomultiplier Tube (PMT) remains the only photosensor that fulfils both these two fundamental requirements.

On the other hand, our goal of detecting very low energy X-rays with a GPSC has another consequence. Despite being the preferred GPSC filling gas due to its several advantages [III.1], pure Xe also presents an important disadvantage in the detection of soft X-rays because of its large atomic number. Indeed, the short absorption length of soft X-rays in pure Xe at atmospheric pressure (few hundred μm for energies below 1 keV) is at the origin of the loss of primary electrons to the detector entrance window by diffusion and backscattering [III.20]. A consequent spectra distortion thus appears as a low energy tail which worsens the energy resolution and the peak-to-valley ratio. Numerous papers report several techniques which aim to reduce this undesirable spectra distortion, either by increasing the electric field in the absorption region [III.21] or by eliminating the absorption region with the so called driftless GPSC [III.22]. The latter authors have shown very good results in attenuating this distortion, but the technique requires elaborate electronic pulse processing. Alternatively, significant performance improvements were also observed using another simple method which consists in filling the detector with a lighter gaseous mixture in order to increase the X-ray absorption length [III.23]. Besides, the addition of a lighter gas to Xe not only leads to longer X-ray absorption lengths and so to reduced tails in the energy spectrum [III.20] but can also lead to Penning mixture effects which may originate improved Fano factors and *w*-values. For instance, the use of Ne-Xe mixtures as an alternative to pure Xe has already been studied with good results in reducing the low energy tail distortion, although these do not exhibit the expected energy resolution improvement [III.23]. This was attributed to the

lower secondary scintillation yields and larger *w*-values of Ne-Xe mixtures in comparison to pure Xe ones.

In this line of thought, and by taking into account the recognized potential of Ar-Xe mixtures as a valid alternative to pure Xe [III.24]-[III.27], we considered the use Ar-Xe mixtures as GPSC filling gas for soft X-ray detection. This decision relies on the fact that not only Ar-Xe mixtures provide longer absorption lengths than pure Xe, but they also potentially present similar or even improved energy resolutions, *w*-values [III.27], Fano factors and secondary scintillation yields in comparison to pure Xe [III.24]-[III.26]. Indeed, some Ar-Xe mixtures have larger ionization yields than pure Ar or pure Xe for α-particles [III.24] and a similar behaviour is expected for X-rays. However, the larger ionization yields must arise from the non-metastable Penning effect since the metastable Penning effect is energetically impossible for Ar-Xe mixtures.

Therefore, although the increase in the absorption length is not expected to be as large as for Ne-Xe mixtures [III.23], Ar-Xe mixtures appear as a good compromise between detector performance and reduction of the spectra distortion.

Due to the particular requirements that our PIXE X-ray detection system has to fulfil for our application, we have carried out the present work, which consists in studying the performance of a large area GPSC using a curved grid to delimit the absorption and scintillation regions and filled with pure Xe and Ar-Xe mixtures for the detection of X-rays in the 0.1-10 keV energy range. Particular attention was paid to the 0.1-2 keV energy range, where performance improvements are expected by using Ar-Xe mixtures instead of pure Xe as the filling gas.

III.2 CONSTRUCTION OF A LARGE DETECTION AREA GPSC

III.2.1 DESCRIPTION OF THE EXPERIMENTAL SYSTEM

The design of this GPSC had to take into account its optimization for the detection of soft X-rays in the 0.1-10 keV energy range and a large detection area, but it also had to fit to the reaction chamber of the particle accelerator. Additionally, we also intended to make it as versatile as possible. The projection of this GPSC therefore took into account the following considerations:

✓ *Drift region length sizing* to ensure that the incident radiation of maximum energy (about 10 keV) is fully absorbed in the detector volume independently of the filling gas (i.e. even with high Ar concentration mixtures).

✓ *Scintillation region length sizing* to guarantee the production of enough secondary scintillation light to detect very low energy X-rays. The detector has been designed in order to collect a maximum amount of VUV secondary scintillation photons, especially for Ar-Xe mixtures with low Xe percentages (for which the

threshold for ionization and the light yield is expected to be much lower than for pure Xe).

✓ *Large detection area*: i.e. both large sensitive area radiation window and a large area photosensor combined with a curved grid.

✓ *Low electronic noise level* to enable the detection of X-rays down to 200 eV with improved energy resolutions to distinguish characteristic X-rays from neighbouring elements of the periodic table.

✓ *Adaptability* of the GPSC to the PIXE experimental set-up.

✓ *Versatility* by allowing the use of different radiation windows with different geometry, material and/or thickness. This was made by using a common window holder for all the windows we built.

✓ *Improved detection efficiency* by minimizing the X-ray absorption in the detector entrance window and maximizing the radiation absorption in the absorption/drift region of the detector.

✓ *Possibility to adapt a vacuum sealed vessel* on the detector top flange in order to perform studies concerning the detection of very low energy X-rays.

The GPSC projected for these studies is depicted in Figure III.2 and shown in Figure III.3. All the pieces have been designed and projected tri-dimensionally using the Autodesk Inventor® software and then machined in the workshop of the Physics Department.
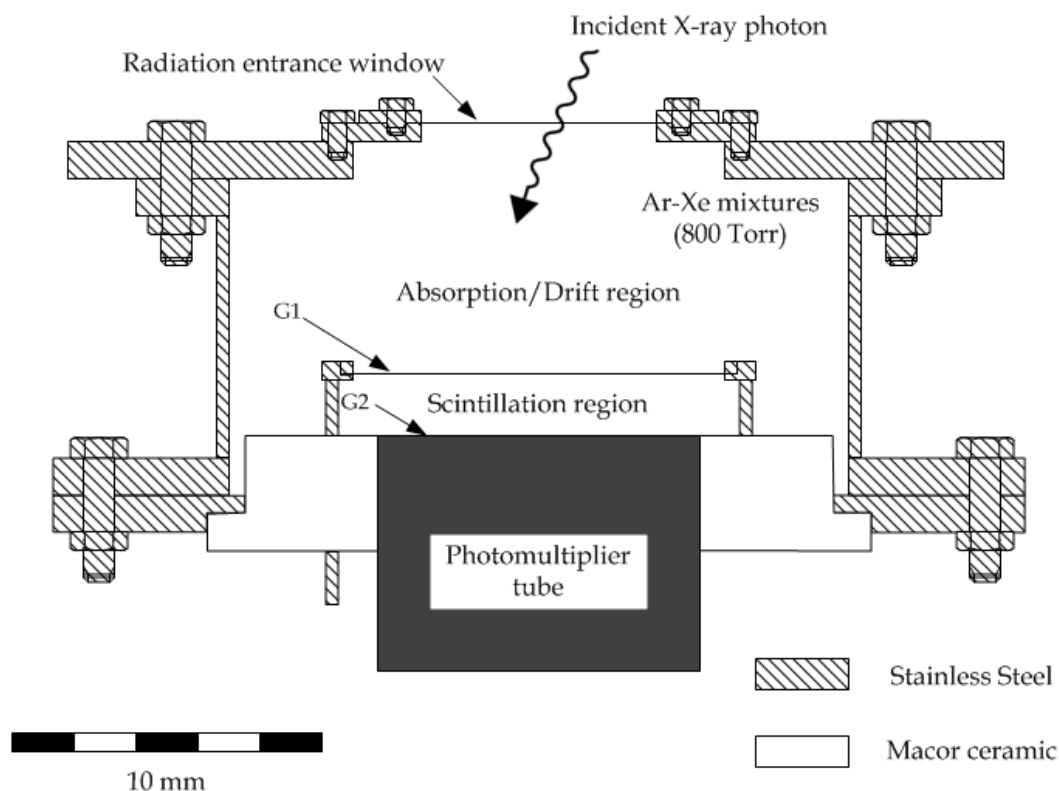
Figure III.2 – Schematic of the Gas Proportional Scintillation Counter built.

Figure III.3 – Photograph of the Gas Proportional Scintillation Counter.

The detector has a 105 mm internal diameter stainless steel cylinder body, 2 mm thick, which was grounded during the experiments. The vessel is vacuum sealed by compressing the top and bottom flanges against the detector body using Viton o-rings seals. A Macor® ring (Figure III.2) was fixed with an insulating and low vapour pressure epoxy (BB-2116 from TRA-BOND) to the detector body for insulating both the feedthrough of grid G1 biasing and the PMT tube from the grounded detector steel body (Figure III.2).

Special care was taken with the top flange (Figure III.3) since, not only it is supposed to seal the detector and to accommodate different radiation windows using the same holder (as we will see further in this Chapter), but it also had to be coupled to the PIXE system through an adapter (already shown in Figure II.3). Moreover, it has additionally been designed to house a vacuum sealed vessel (Figure III.4) where several targets of light elements were placed to be excited with α-particles from a ^{244}Cm radioactive source in order to obtain different X-ray energies corresponding to their K_α and K_β fluorescence lines. These different X-ray energies were used when testing the detector performance.

The detector cylindrical body is 57 mm long and has a 46.5 mm thick absorption/drift region and a 11.2 mm long scintillation region. As shown in Figure III.5, the 46.5 mm thick drift region guarantees the absorption of X-rays up to 10 keV even using Ar-Xe mixtures with large Ar concentration. These two regions are separated by a grid, G1, built from a mesh, made of 80 μm diameter wires distributed in a 1 mm pitch rectangular patch, framed onto a stainless steel ring. This ring is supported by 3 pillars, one of them being the feedthrough used to bias this grid. While the beginning of the absorption/drift region is naturally the radiation entrance window, the

end of the scintillation region is the PMT photocathode surface because a second chromium grid, G2, with 1 mm thick crossed-stripes was vacuum evaporated onto it to optimize the collection of secondary scintillation light [III.28].
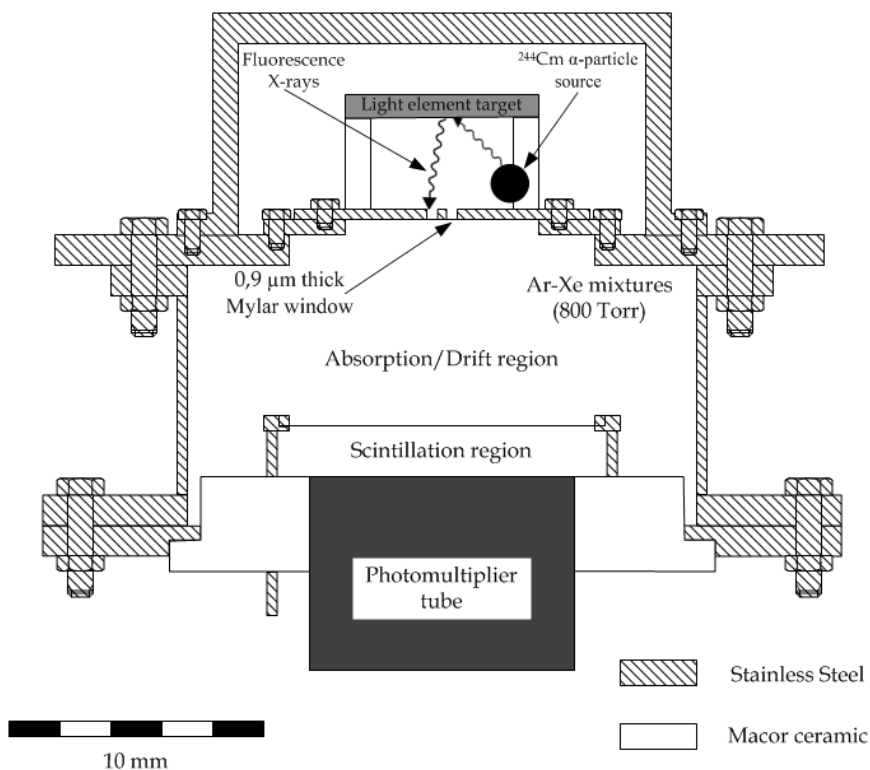
Figure III.4 – Schematic of the GPSC with the vacuum sealed vessel described on its top to ensure that fluorescence X-rays reach the radiation window by evacuating the air between the sample and the detector.
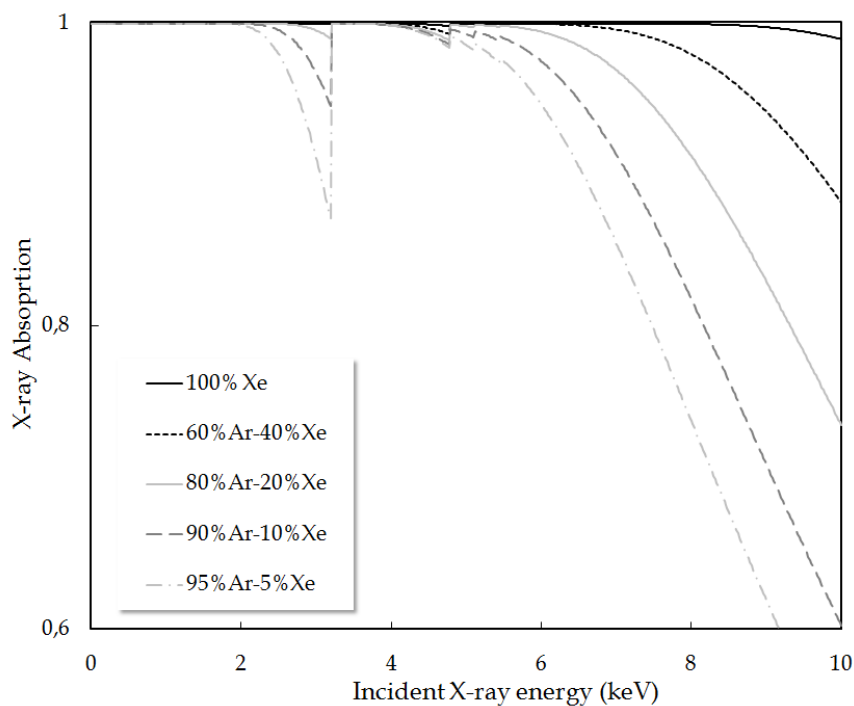
Figure III.5 – X-ray absorption in the 46.5 mm thick absorption/drift region as a function of the incident X-ray energy for pure Xe and several Ar-Xe mixtures at 800 Torr [III.29].

III.2.2 VACUUM SYSTEM

The detector was coupled to a high vacuum system, schematically represented in Figure III.6, which includes an evacuation system and a gas admission system that uses ultra pure (purity above 99.9995 %) rare gases (Ne, Ar, Kr or Xe). The high vacuum system is mainly made of DNCF16 pipes and ultra high-vacuum valves. A turbo-molecular pump (with a pumping speed of 150 l.s^{-1}) connected to a mechanical pump are used in this vacuum system. These pumps are the ones used to evacuate the particle accelerator set-up described in Chapter II.
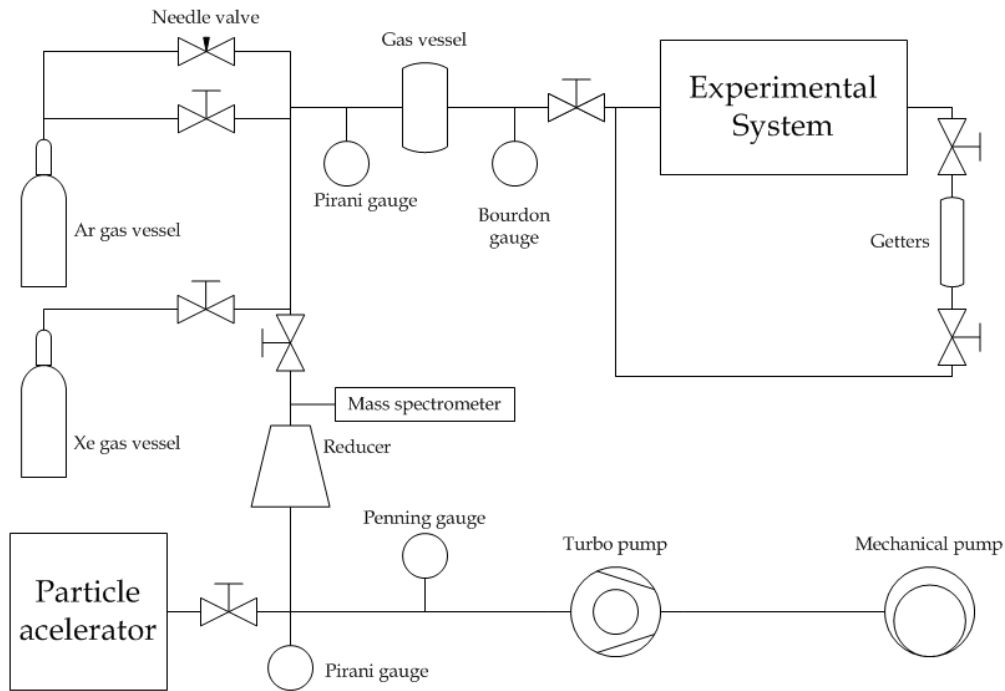
Figure III.6 – Schematic of the high-vacuum system used to both evacuate the detector and fill it with Ar, Ne, Ke or Xe based mixtures.

The vacuum measurement is guaranteed with both a Pirani type gauge and a Penning one (vacuum measurements in the 10^{-3}-1000 and 10^{-8}-10^{-2} Torr ranges, respectively) (Figure III.6). On the other hand, the pressure measurement needed during the detector filling process is assured, for pressures up to 5 atms, by a Pirani and a Bourdon transducers. Although the turbo-molecular pump enables the pressure in the vacuum line to decrease down to about 1×10^{-7} Torr, the gas system and the detector chamber were typically evacuated down to 5×10^{-7} Torr prior to filling. The detector was then filled at slightly above atmospheric pressure to avoid vessel contamination from air.

As shown in Figure III.6, the detector cylindrical body has 2 lateral exits to DNCF16 flanges to tack the detector to a closed piping circuit and to the vacuum system. This closed circuit around the detector is used to connect it to a purification system, composed by a tube filled with tens of getters (model ST 707/washer/833 from SAES) that consist in small rings of an alloy of Zr, Fe and Va that absorbs (via a 3 steps

adsorption mechanism: surface dissociation, surface sorption and bulk diffusion) any undesired chemical active impurity (mainly H_2O and N_2 in our case) when maintained at a temperature of about 150-180 ºC. Due to the high temperature of the getters, the gas continuously goes through these by convention guaranteeing therefore continuous purification.

III.2.3 RADIATION WINDOWS

As mentioned before, the top detector flange has been designed to enable exchanging the radiation window without affecting the detector body. This care was taken because of expected difficulties in obtaining/acquiring windows that meet all the requirements for this particular application: i.e. vacuum sealing, large area, enough mechanical strength to bear atmospheric differential pressure, but still thin enough to allow transmission of soft X-rays down to 200 eV. The top flange was designed with a dedicated inner flange for the entrance window, placed onto it with an o-ring seal, in order to experiment different windows and several ways to use them.

The materials selected for the radiation window were chosen by taking into account both their mechanical strength (to bear the difference of pressures when evacuation operations are needed both inside and outside the detector vessel), permeability, X-ray transmission for soft X-rays and available thicknesses. Although Beryllium has been commonly used in the last decades, we did not choose this option due to its high toxicity and price (about 1500 € for a few cm^2 of a 0.25 μm thin foil [III.30]) and low mechanical resistivity when compared to other possible materials. Besides, it has the disadvantage of presenting almost no X-ray transmission in the 200-300 eV energy range and hence for the 277 eV Carbon K_α line (Figure III.7). We then considered the use of thin plastic films, like Kapton® or polypropylene, with Mylar® as our final choice since it was the only one available with thicknesses below a few micrometers.

However, all these polycarbonate based materials are naturally extremely difficult to handle with such low thicknesses. Their use for manufacturing vacuum sealed windows that stand significant differences of pressure brings extreme experimental difficulties. For this reason, we used a 75 μm thick and 38 mm diameter Kapton® window to perform our first studies with this GPSC. Although its large diameter enables to carry out performance studies for large detection areas, its thickness forbids the detection of soft X-rays (Figure III.8).

Additionally, in order to detect soft X-rays down to 200 eV we manufactured a second radiation window (shown in Figure III.9) from a 0.9 μm thick Mylar® film glued onto a 4 mm thick stainless steel frame. Since the detector was filled at slightly above atmospheric pressure and will be operating with vacuum in the other side of the radiation window, we had to ensure that such a thin Mylar® film stands atmospheric differential pressure. In order to manufacture a window with significant sensitive area and that stands this pressure difference, we built a window frame with 6 circular holes 1.5 mm in

diameter circularly distributed 1.5 mm apart around a similar seventh hole centred in the middle of the frame in such a way that each of these holes has sufficiently low area to stand the atmospheric pressure when evacuation operations are needed. The active area of this window is 12.4 mm^2.
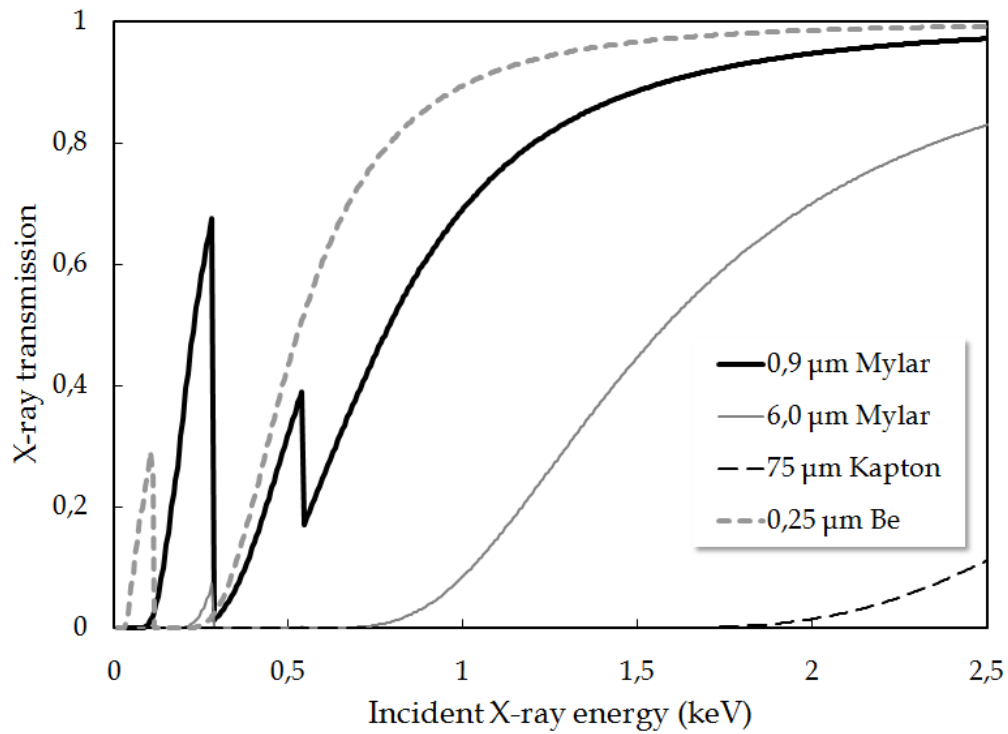
Figure III.7 – X-ray transmission as a function of the incident X-ray energy for different materials [III.29].
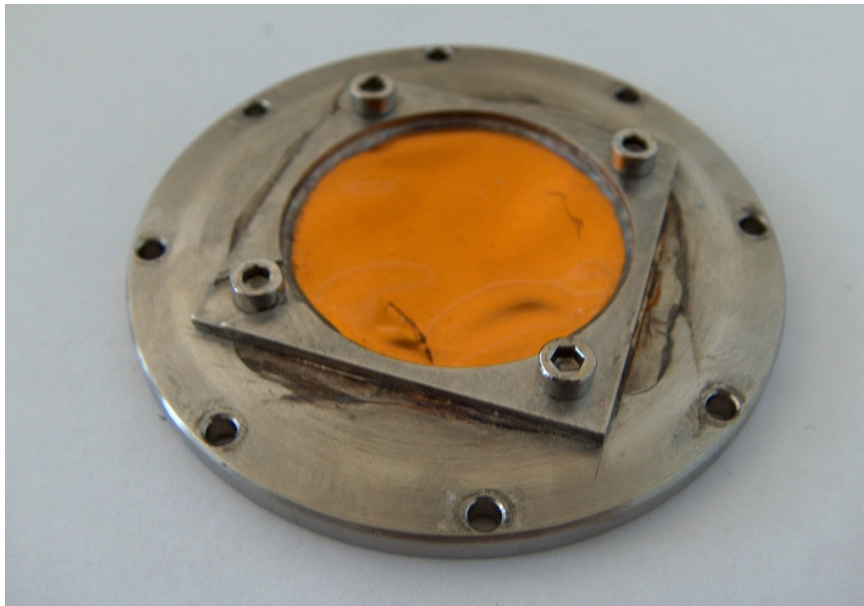
Figure III.8 – Large area radiation window, 38 mm diameter, made of a 75 μm thick Kapton® film.
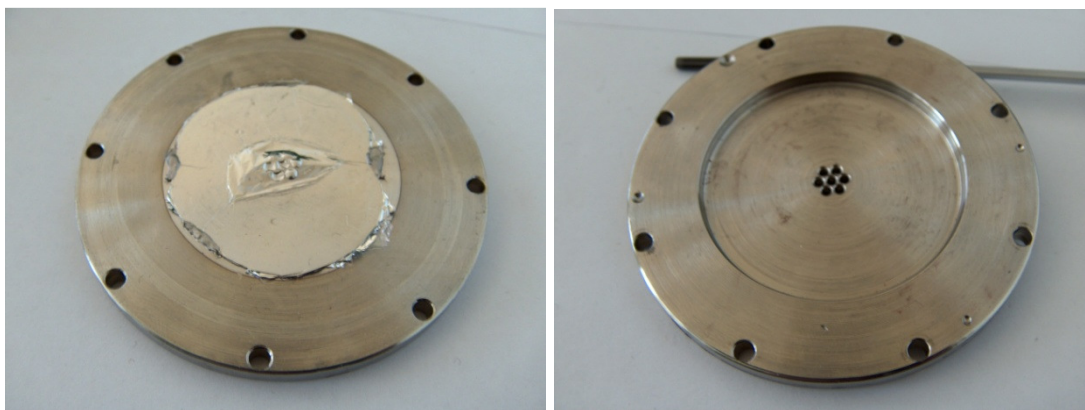
Figure III.9 – Inside (left) and outside (right) sides of the second radiation window used in the studies concerning the detector performance in the detection of soft X-rays in the 0.1-10 keV range.

Finally, although this second window enables us to make all the studies concerning the detector performance in the detection of soft X-rays, it has neither sufficient sensitive area nor enough mechanical strength to stand the repeated evacuation operations needed in our PIXE experimental arrangement. A third radiation window was therefore built combining simultaneously improved soft X-ray detection and large detection area. We decided to use a 6.0 μm thick Mylar® film glued onto another 4 mm thick stainless steel frame because it seemed to be a good compromise between mechanical strength safety while presenting large sensitive areas and good X-ray transmission down to 1 keV, which is enough for the first PIXE studies we planned since these aim to detect the K-line from aluminium, whose energy is 1.487 keV. Again, we built a radiation window that consists of a multitude of holes that enable to maximize the pressure difference supported by the thin film. This way, a large detection area of 192 mm^2 was easily achieved with improved mechanical strength. This X-ray window is schematically represented in Figure III.10 where it is possible to see that the edges of each hole were smoothed in order to avoid damaging the thin film.
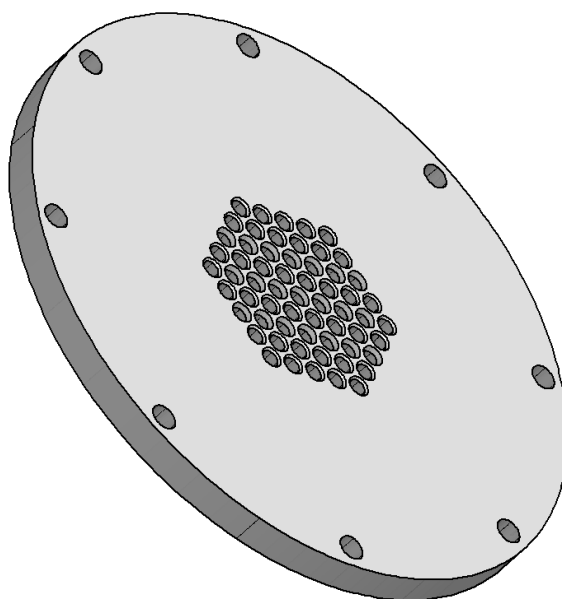
Figure III.10 – Schematic of the inside side of the third window built. This is the side upon which the 6 μm thick Mylar® film is glued, showing the smooth edges of each individual drilled hole.

We have to refer at this point that, for all the three radiation windows manufactured, a thin layer of Aluminium (about 50 nm thick) was evaporated under vacuum onto the plastic film to insure electrical conductivity of the radiation window with the detector body. This was necessary to guarantee uniformity of the electric field in the drift region.

III.2.4 DETECTOR POLARIZATION

As we explained before, the detector window and body have to be grounded to be used in the PIXE set-up. This constraint imposes the use of a ceramic ring (represented in Figure III.2) to insulate electrically the PMT from the metallic vessel as well as the need to polarize the PMT with fluctuating voltages in its cathode and its anode.

The PMT (model 9266QB from Electron Tubes) was chosen because its photocathode of fused silica has relatively high detection efficiency for the VUV secondary scintillation light of Xe and also provides high gains up to 7×10^6. As shown in Figure III.2, the PMT window (2" in diameter) is the end of the scintillation region. Since a uniform electric field has to be applied in this region (between G1 and the PMT optical window external surface) to produce the secondary scintillation light, a chromium grid G2 has been evaporated onto the PMT window under vacuum, with 1 mm wide crossed-stripes with a pitch of 2.5 mm. The grid pattern was obtained by a second evaporation with the mask rotated 90º. We also evaporated a chromium thin layer on the lateral external surface of the PMT cylinder to establish electrical contact between the chromium evaporated grid G2 and the PMT cathode. These latter are therefore at the same potential, V_k.

Since the detector window is grounded, the grid G1 is biased with a positive voltage V_G (typically 500 V) through the feedthrough represented in Figure III.2 so that a uniform reduced electric field, E_a/p, directs the primary electrons towards the scintillation region. In the scintillation region, the high voltage V_k applied to G2 (up to 6000 V) defines a uniform reduced electric field, E_S/p, higher than E_a/p but below the ionization threshold of the filling gas, as explained in section III.1. Finally, the amplification of the detector signal by the PMT is obtained by establishing a voltage drop V_{PMT} between the PMT's cathode and anode. Since the high voltage applied to the cathode is V_k, the PMT anode is biased with a positive voltage V_a higher than V_k, so that $V_{PMT}=V_a$-V_k (typically about 1000 V).

Concerning the PMT polarization, we used the voltage divider distribution indicated by the manufacturer (schematized in Figure III.11), to which we added a resistor R_S, placed between the PMT cathode and ground potential and the capacitors C_1, C_2 and C_3 between the last dynodes (d_8, d_9 and d_{10} in Figure III.11). The values of the different components involved, i.e. of the capacitors and the resistors, were determined by taking into account the PMT specifications; namely the maximum current and voltage applicable to the PMT's anode, cathode and between dynodes.
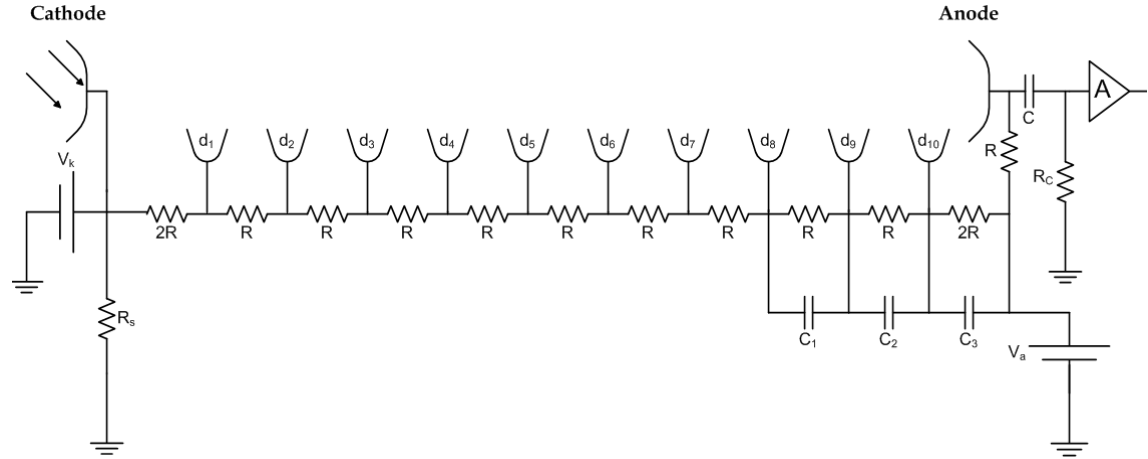
Figure III.11 - Schematic of the polarization circuit of the PMT. R, R_S and R_C equal 0.5, 9.4 and 1 MΩ respectively while C_1, C_2, C_3 and C equal 0.1, 0.1, 1 and 0.1 nF respectively.

The capacitors C_1, C_2 and C_3 were added in the last amplification stages, where the signal charge is already significant, in order to stabilise the voltage drop between consecutive dynodes due to the presence of the charge signal itself, since the charge provided by the capacitor is much larger than the one due to the detector signal.
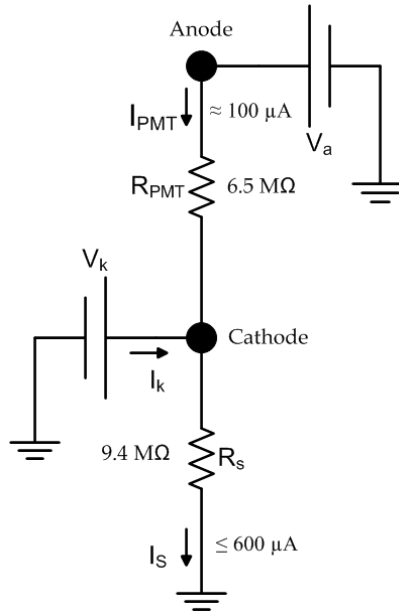
Figure III.12 – Simplified representation of the PMT polarization circuit.

As illustrated in Figure III.12, the voltage divider of the PMT can be represented as a resistor R_{PMT} (which equals 13R) between its cathode and anode. Figure III.12 points out that R_{PMT} and R_S compose a voltage divider. Since the value of V_k depends strongly on the filling gas used because the thresholds for scintillation and ionization are expected to decrease with decreasing Xe concentrations, the value of the resistor R_S was determined to guarantee that, independently of the filing gas considered, a minimum voltage drop V_{PMT} between the PMT´s cathode and anode is applicable, even for low values of V_k (i.e. around the threshold for scintillation for mixtures with low Xe

concentrations). On the contrary, R_S also simultaneously ensures that, for high values of V_k up to 6000 V (i.e. around the threshold for ionization for mixtures with high Xe concentrations and pure Xe), the power supply used to bias to PMT´s cathode does not exceed the possible current delivered (1 mA in our case). It also ensures that the power supplies used for V_k and V_a never work in the "accepting current" mode.

The charge signal from the PMT anode is collected through a capacitor C followed by a resistor R_C at ground potential into the preamplifier. This RC filter eliminates the DC component due to the anode biasing. The temporal constant of this filter, $R_C C$, must be much higher than the drift time of the electron cloud in the scintillation region of the detector (about 0.1-1 µs) and still much lower than the average time between events (1 ms for a 10^3 events/s count rate). The collected charge was then integrated in a Canberra 2005 charge sensitive preamplifier which is used due to its good signal-to-noise ratio. There, the charge signal is converted into a voltage one and simultaneously amplified by a factor of 5.

The outcoming voltage signals were then amplified with a Tennelec TC243 linear amplifier which differentiates the pulses (with a shaping time in the 2-8 µs range). Simultaneously this latter amplifies the pulses with a variable gain to adjust their amplitude to the 0-8 V range of the multichannel analyser (MCA) (Nucleus model PCA-II with 1024 channels) where the energy spectrum is processed.

We have to point out that extreme care was taken in order to reduce the electronic noise to its minimum value during the experiments. Beyond opting for high voltage power supplies with low ripple voltage to avoid significant fluctuations in the PMT amplification, we also wrapped the PMT and the electronic components needed for its polarization into a cylindrical metallic tube (Figure III.3), in order to shield it from interfering electronic noise. Besides, the tube was painted in black inside to avoid any refection of the light passing through the PMT glass, and was also used to prevent incoming light from the surroundings.

III.2.5 PRELIMINARY RESULTS

Prior to any study concerning Ar-Xe mixtures as the filling gas of GPSCs, we characterized the GPSC performance in an already known application, i.e. with pure Xe at atmospheric pressure as the filling gas. The radiation window used to perform these preliminary studies was the 38 mm diameter Kapton® one, which enables the detection of X-rays down to 2-3 keV. The first studies concerning the performance of the developed GPSC were made with an ^{55}Fe radioactive source emitting the characteristic K_α and K_β lines of Manganese (with energies of 5.895 and 6.492 keV respectively). A Chromium thin film (15 µm thick) was used as a filter to absorb the K_β line while allowing the K_α line to go through it. The resulting mono-energetic X-ray beam was collimated through a 2 mm diameter hole in a Lead absorber centered in front of the 75 µm thick Kapton® radiation window used in this study.

The detector grid and the PMT cathode were biased so that the reduced electric fields in the absorption/drift and scintillation regions, E_a/p and E_S/p respectively, equals 0.1 and 5 V cm^{-1} Torr^{-1} in order to correspond to the best operating conditions for a GPSC [III.1]. Each pulse-height distribution obtained in the MCA was then fitted to a gaussian curve superimposed on a linear background by using the Grid-Least-Squares-Method in order to determine the peak amplitude, the gaussian centroid, c, and its Full Width at Half Maximum (FWHM). The energy resolution R is then defined as the ratio FWHM/c.

As referred earlier, the detector has been designed with a considerably long scintillation region (11.6 mm) in order to guarantee the production of a large amount of VUV secondary scintillation photons even for Ar-Xe mixtures with low Xe concentrations for which lower scintillation efficiencies are expected. Due to high voltage power supply limitations, this choice limits the E_S/p value to 5.3 V cm^{-1} Torr^{-1}, which is slightly lower than the threshold for ionization in pure Xe [III.31]. This maximum E_S/p value was nevertheless enough for a good detector performance since an energy resolution of 7.7 % was obtained for 5.9 keV X-rays with pure Xe as the filling gas.

As a test to the performance of this GPSC filled with pure Xe, we carried out the analysis of some materials [III.32],[III.33]. As shown from the characteristic X-ray spectra of Figures III.13 and III.14, which we obtained by exciting the targets with α-particles from a ^{244}Cm radioactive source, the detector can separate clearly characteristic X-rays peaks from neighbour elements (except for very soft X-rays); showing therefore that it is suitable to carry out our PIXE studies due to its superior performance over standard PCs.
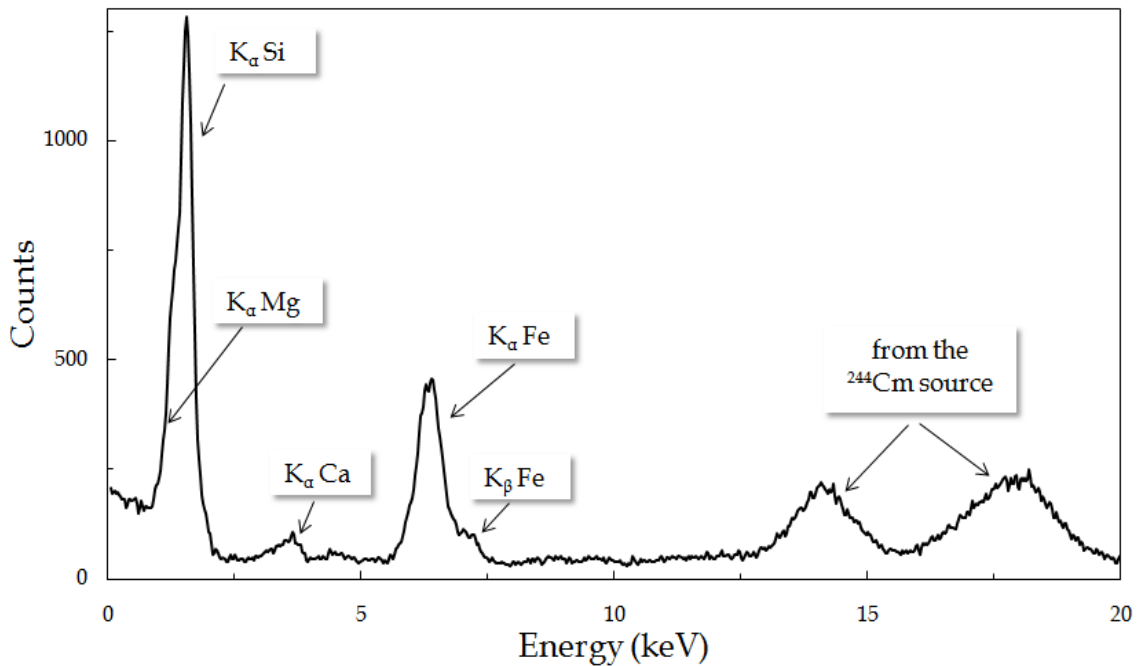
Figure III.14 – Typical X-ray fluorescence spectrum obtained by exciting a sherd obtained from the excavation of the Castro de Vieito in North of Portugal with a ^{244}Cm α-particle source [III.33]. For this particular application, we used the 0.9 µm thick Mylar® window in order to detect such soft X-rays.
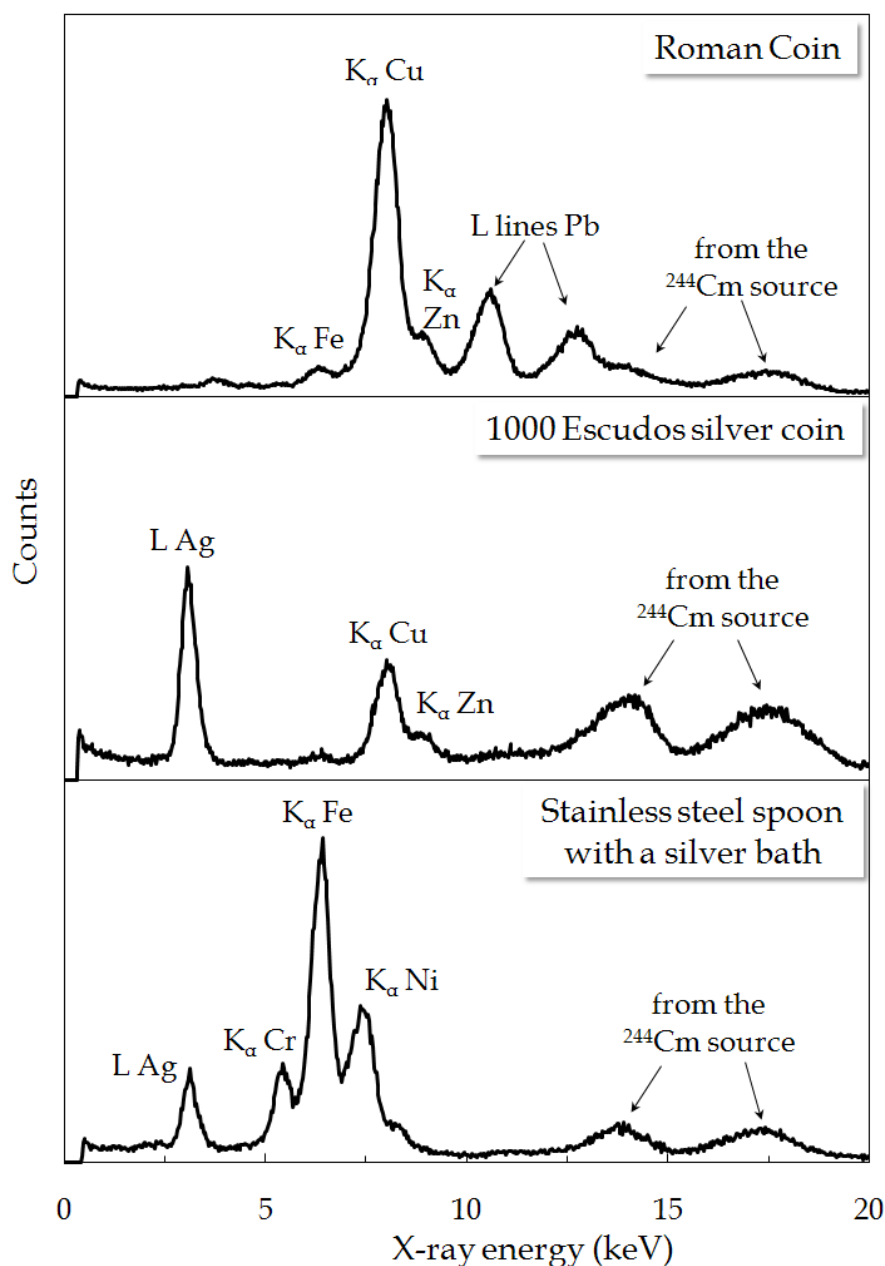
Figure III.13 – X-ray fluorescence spectra obtained by exciting with a ^{244}Cm α-particle source some old pieces of interest [III.32].

Besides, we also considered the influence of the counting rate on the detector performance, although we do not expect high counting rates during our PIXE studies due to the very low X-ray production cross-sections expected. In the latter studies, spectra were acquired by keeping the counting rate lower than 1000 counts/s to prevent any slight performance deterioration. While spectra were obtained for a 150 counts/s rate with an energy resolution of 7.7 %, this latter worsens up to 8.2 % with a rate of 20 000 counts/s. Moreover, we have to point out that the peak centroid c shifts 150 eV to higher energies because of pile-up effects with high counting rates. For

these reasons, the spectra of the following studies have been acquired with a maximum counting rate of 1000 counts/s.

III.3 AR-XE MIXTURES

Since the purpose of this work is to study the potential of Ar-Xe mixtures as an alternative to pure Xe as the filling gas of GPSCs, we performed several studies to characterize such mixtures. Not only have these studies naturally dealt with the relevant characteristics of any GPSC filling gas such as their electroluminescence yield, excitation and ionization thresholds, w-values and Fano factors, but we also paid particular attention to the performance of this Ar-Xe filled GPSC in two specific applications of interest to carry out our PIXE studies, namely large sensitive area and the detection of very low energy X-rays.

III.3.1 CHARACTERIZATION OF AR-XE MIXTURES

Since the signal amplification stage of a GPSC relies on the electroluminescence of the filling gas, we began by studying the secondary scintillation yield of Ar-Xe mixtures, i.e. the number of scintillation photons produced per X-ray photon per unit of distance drifted and per unit of gas pressure Y^x/p, as a function of the reduced electric field applied to the scintillation region E_S/p. This study also allowed us to obtain for each Ar-Xe mixture considered the thresholds for scintillation, E_{sci}/p, and ionization, E_{ion}/p, as well as the best operating conditions, i.e. the values of E_S/p and of the reduced electric field in the absorption region, E_a/p, that originate the best performance.

For each Ar-Xe mixture considered, we have acquired pulse-height distributions (Figure III.15), using a planar grid G1 to delimit the absorption/drift and scintillation regions and a 2 mm diameter collimated beam of 5.9 keV X-rays. Curves of the secondary scintillation yield Y^x/p (proportional to the gaussian centroid c of the pulse-height distribution) and of the energy resolution R were obtained as a function of the electric fields used in both absorption and scintillation regions, E_d/p and E_S/p respectively, keeping constant the PMT voltage, V_{PMT}.

As shown in Figure III.16, the reduced electroluminescence yield, Y^x/p, increases linearly with the reduced electric field in the scintillation region E_S/p for all the studied mixtures, until the ionization threshold E_{ion}/p is reached, with a behaviour similar to pure Xe [III.34]. Above E_{ion}/p, the pulse amplitude begins to increase exponentially due to charge multiplication. However, as reported in [III.35] for pure Xe, the energy resolution continues to improve for values of E_S/p slightly higher than E_{ion}/p until a value we called E_m/p, showing that a slight charge multiplication contributes to an improvement of the detector performance. However, for E_S/p values higher than E_m/p,

we observe a deterioration of R and a clear exponential gain rise due to charge multiplication (Figure III.16).

We can notice that, although Y^x/p is larger for Ar-Xe mixtures than for pure Xe in the low reduced electric field region, its upper value decreases as the Xe concentration in the mixture decreases, originating, in the best operating conditions, a smaller detector pulse amplitude than for the pure Xe case. This decrease in Y^x/p is explained by the slight reduction of the scintillation yield as the Ar concentration increases in the mixture [III.24]-[III.26], together with a shift of the scintillation light spectrum to lower wavelengths, a region where the efficiency of the PMT used decreases. This effect also explains the observed deterioration of R with decreasing Xe concentrations.

We also determined the scintillation threshold, E_{sci}/p of each investigated Ar-Xe mixture by considering the extrapolated x intercept of the linear fits to the experimental data of the non-normalized Y^x/p below E_{ion}/p. Figure III.16 shows that the scintillation threshold also decreases for lower Xe concentrations, an effect that was also observed for Ne-Xe mixtures [III.36] and was explained in terms of the energetic balance between the energy gained by the electrons between collisions from the electric field and their energy loss through collisions with the filling gas atoms. Indeed, although the electron energy loss by collision with the filling gas atoms, which is about $2m/M$ (with m the electron mass and M the atom mass), is larger for Ar than for Xe atoms, the collision cross-section of electrons in Ar is lower and so the electrons reach the energy necessary for excitation of the filling gas atoms at lower reduced electric fields, E_{sci}/p. This energetic balance is responsible for the larger scintillation yield observed for Ar-Xe mixtures in the low E_S/p region when compared to the pure Xe.
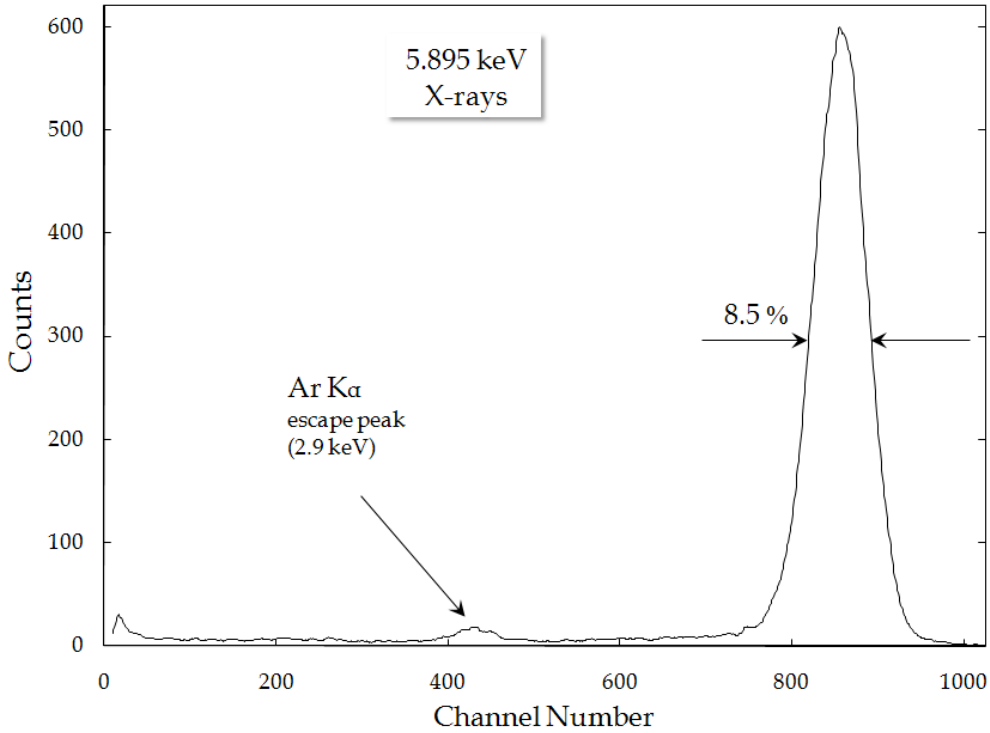
Figure III.15 – Typical energy spectrum obtained for 5.9 keV X-rays from the ^{55}Fe radioactive source and using 95%Ar-5%Xe mixture as the filling gas.
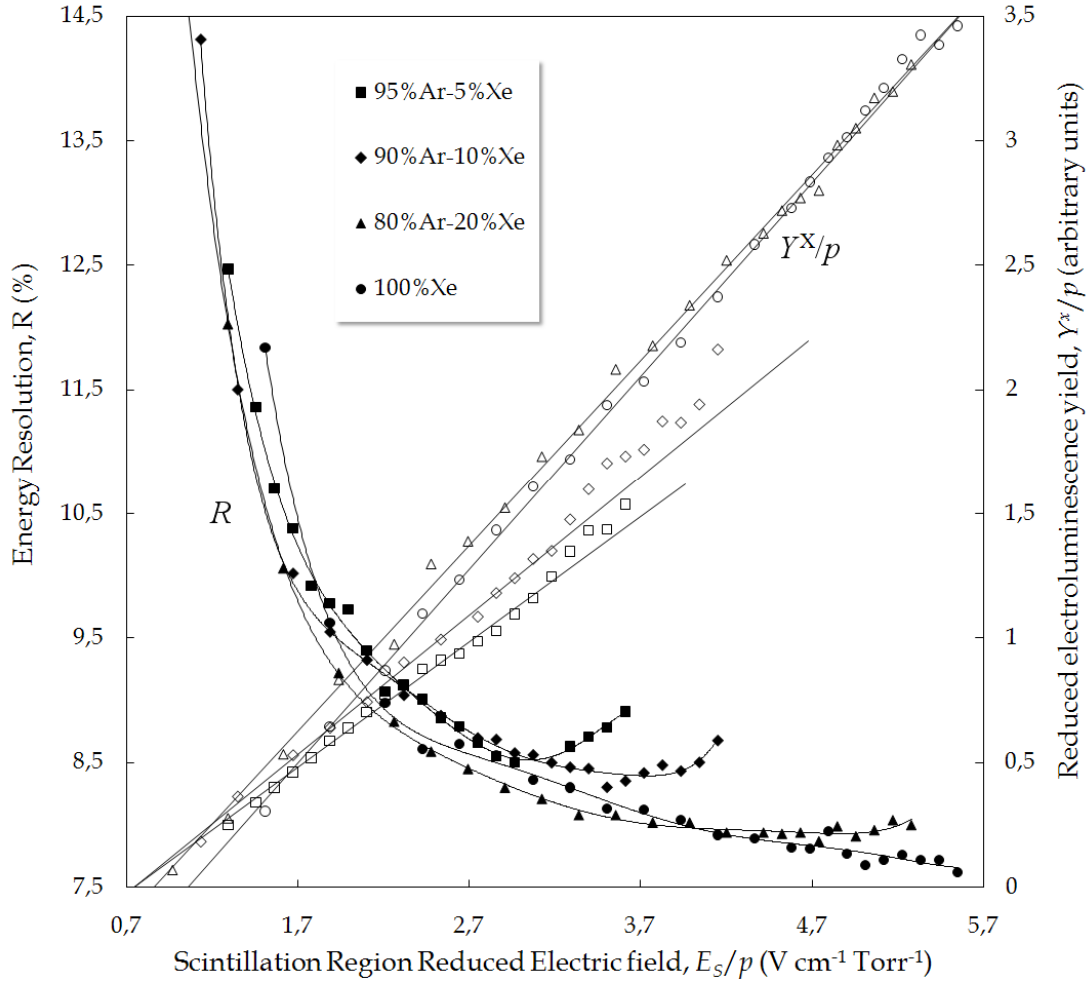
Figure III.16 – Reduced electroluminescence yield, Y^x/p, (open symbols) and energy resolution, R, (full symbols) for 5.9 keV X-rays as a function of the reduced electric field in the scintillation region, E_S/p, for different Ar-Xe mixtures (E_a/p was kept constant).

The operating electric fields in the absorption and scintillation regions, E_a/p and E_m/p, which originate the best detector performance, the thresholds E_{sci}/p and E_{ion}/p and the best energy resolution achieved are summarized in Table III.1 for each studied mixture. Due to the referred high voltage power supply limitations, E_{ion}/p and E_m/p were not determined for pure Xe and for the 60%Ar-40%Xe mixture, and so the indicated 5.7 V cm^{-1} Torr^{-1} value is a lower limit. Both E_a/p and E_m/p decrease with increasing Ar concentration. This is also the behaviour observed for E_{sci}/p, except for the 99%Ar-1%Xe mixture.

Although the R values for pure Xe and 80%Ar-20%Xe are very similar, we did not obtain the performance improvement observed in [III.37] for Ar-Xe mixtures when compared to pure Xe. We believe that this is due to the fact that the efficiency of the CsI covered microstrip plate used in[III.37] increases towards lower wavelengths [III.38], a wavelength region to which the scintillation light shifts as the Ar concentration increases in the mixture, compensating in this way the slight reduction in the total scintillation yield of the Ar-Xe mixtures as Xe concentration decreases [III.24]-[III.26]. We note however that the performance of the GPSC instrumented with the PMT is superior to the GPSC

that uses a CsI covered microstrip plate (MSP) as the photosensor, since in the latter case the best R value obtained for 5.9 keV X-rays and 80%Ar-20%Xe was about 11 % [III.37].

TABLE III.1
EXPERIMENTAL VALUES OF E_A/P, E_{SCI}/P, E_{ION}/P AND E_M/P AND THE BEST ENERGY RESOLUTION R ACHIEVED FOR THE DIFFERENT AR-XE MIXTURES STUDIED

	100% Xe	40% Xe	20% Xe	10% Xe	5% Xe	3% Xe	1% Xe
E_a/p (± 0.02) (V cm^{-1} $Torr^{-1}$)	0.20	0.20	0.13	0.07	0.07	0.07	0.07
E_{sci}/p (± 2%) (V cm^{-1} $Torr^{-1}$)	1.08	0.97	0.87	0.76	0.74	0.73	0.85
E_{ion}/p (± 0.1) (V cm^{-1} $Torr^{-1}$)	≥ 5.7	≥ 5.7	4.9	3.2	3.1	2.8	2.3
E_m/p (± 0.1) (V cm^{-1} $Torr^{-1}$)	≥ 5.7	≥ 5.7	5.0	3.6	3.5	3.0	2.8
Best R (%)	7.7	7.8	7.8	8.3	8.5	9.1	11.5

In order to determine the Fano factors of the Ar-Xe mixtures considered we used the following analytical tool, already reported in many works [III.39]-[III.41]: for reduced electric fields in the scintillation region E_S/p below the threshold for ionization E_{ion}/p, the energy resolution R of a GPSC is given by [III.1]

$$R = 2.355 \sqrt{\frac{Fw}{E_X} + \frac{K}{A} + V_n}$$ (Eq. III.1)

where A, the pulse amplitude, is proportional to the intensity of the secondary scintillation, F represents the Fano factor, E_X is the energy of the incident X-ray, w is the w-value, K is a constant that describes the statistical fluctuations introduced by the photosensor that detects the scintillation light, and V_n is a term, usually small, that describes the contribution of the electronic noise of the detection system to the energy resolution.

However, neglecting the fluctuations introduced by the electronic noise, which are quite small in our case, from Equation III.1 we can write

$$R^2 = 5.546 \left(\frac{Fw}{E_X} + \frac{K}{A} \right)$$ (Eq. III.2)

where A is proportional to the centroid channel, c, of the Gaussian fitted to the spectrum main peak.

Therefore, in a plot of R^2 versus the reciprocal of the pulse amplitude $1/A$ (as shown in Figure III.17 for the 99%Ar-1%Xe mixture) the extrapolation to infinite

amplitudes (i.e. $1/A \rightarrow 0$) gives the square of the so-called intrinsic energy resolution, R_{int}, since then $R^2 \rightarrow R^2_{int} = 5.546 \ (Fw/E_X)$ (Equation III.3). Consequently, the Fano factor F can be obtained from the value of R_{int} if E_X and w are known.
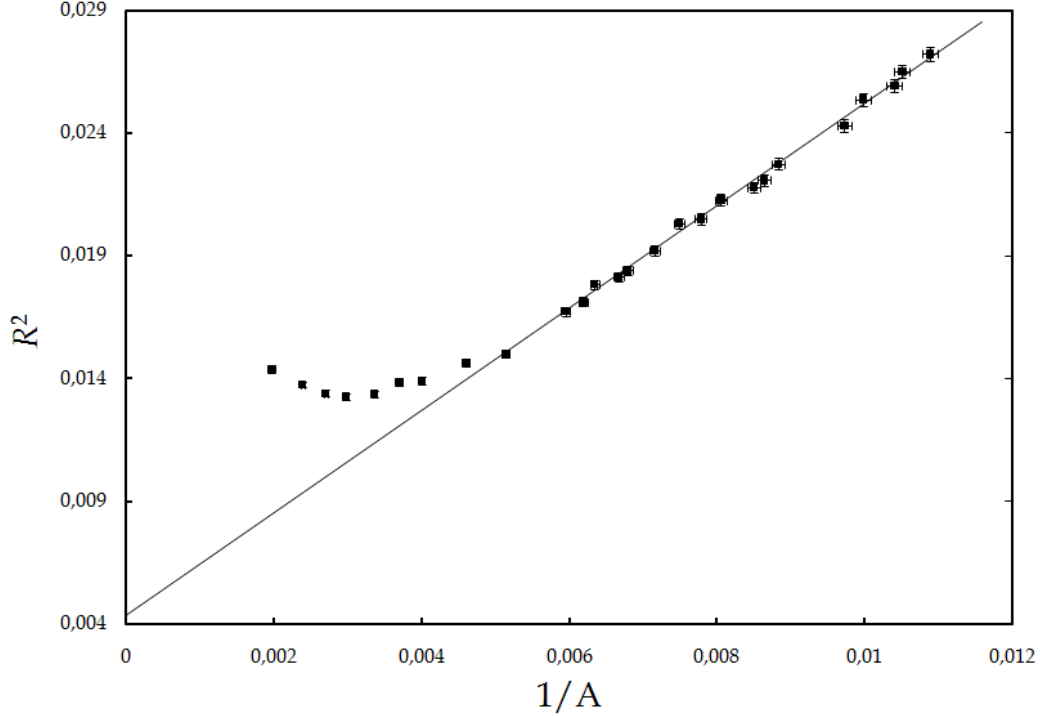
Figure III.17 – R^2 as a function of the reciprocal pulse height amplitude, $1/A$, (in arbitrary units) for the GPSC filled with 99%Ar-1%Xe. The errors bars are about the size of the dots.

For each Ar-Xe mixture studied, the experimental data for R^2 and $1/A$ were fitted to straight lines with the least squares method with errors in both coordinates. These errors were obtained in the way described below. Low values of $1/A$ were not considered since they deviate from the linear behaviour. For the example shown in Figure III.17, the lowest value of $1/A$ included in the fit was 0.005. This is due to the fact that these experimental data points were obtained with high values of E_S/p, for which ionization already occurs.

The errors in the $1/A$ coordinate were obtained from the errors in A, Δ_A, which are due mainly to instabilities of the photomultiplier power supply and are estimated to be 1% of A, i.e. $\Delta_{1/A} = 0.01/A$. The errors in the R^2 coordinate, Δ_{R2}, were estimated from the errors in the Gaussian fit to the experimental pulse-height distributions $\Delta_R = \pm \ 0.05$ (in units of %). Therefore, $\Delta_{R2} = 2R\Delta_R = \pm \ 0.10 \ R \ (\%^2)$.

The least squares method gives the best parameters of the linear fits to Equation III.3. These results allowed us to determine R_{int}, Fw and then F for 5.9 keV X-rays and several Ar-Xe mixtures, which are listed in Table III.2 and shown in Figure III.18, together with their errors.

The only w-values available in the literature for Ar-Xe mixtures are the ones from [III.27] and are therefore the ones we used to carry on our calculations of the Fano factors. However, since no w-values for mixtures with low Xe concentrations (1%, 3%

and 5%) were available, we assumed that these values do not differ significantly from the 10 % Xe mixture ones for the investigated mixtures and used the *w*-value of 21.5 eV in these cases to estimate the Fano factors for these mixtures.

TABLE III.2
EXPERIMENTAL RESULTS OF R_{INT}, Fw, W AND F FOR THE STUDIED AR-XE MIXTURES
AND FOR 5.895 KEV X-RAYS

Xe %	R_{int} (%)	Fw (eV)	w (eV) (from[III.27]])	F
1	6.67 ± 0.21	4.73 ± 0.29	_	≈ 0.22
3	6.77 ± 0.09	4.87 ± 0.12	_	≈ 0.23
5	6.98 ± 0.05	5.18 ± 0.07	_	≈ 0.24
10	7.18 ± 0.04	5.48 ± 0.06	21.42 ± 0.21	0.256 ± 0.004
20	7.14 ± 0.02	5.41 ± 0.03	21.64 ± 0.21	0.250 ± 0.003
40	7.25 ± 0.02	5.59 ± 0.03	21.63 ± 0.21	0.258 ± 0.003
100	7.19 ± 0.02	5.49 ± 0.03	21.61 ± 0.21	0.254 ± 0.003
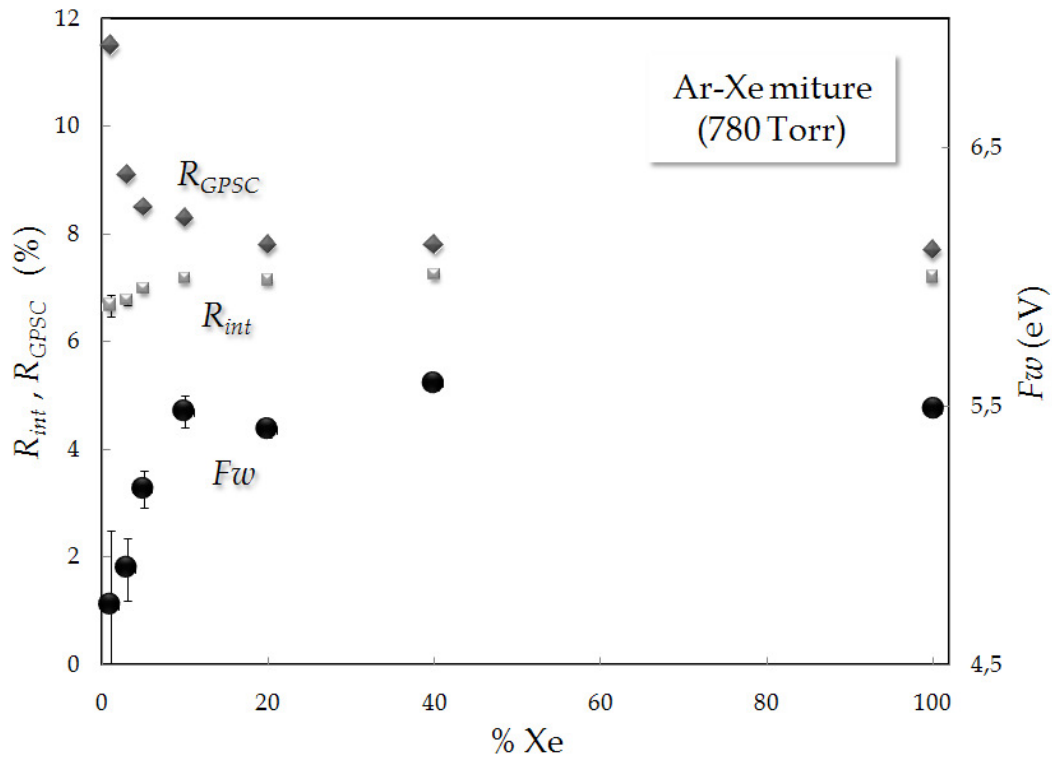
Figure III.18 – Intrinsic energy resolutions R_{int}, Fw and energy resolutions R_{GPSC} obtained experimentally with the present GPSC filled at 780 Torr with Ar-Xe mixtures as a function of the concentration of Xe.

As shown in Table III.2, the experimentally measured Fano factors tend to decrease with increasing Ar concentrations corresponding to Xe contents below 10%. This can be attributed to Penning effects that lower the fluctuations in the number of

primary electrons released, as was observed before for Ne-Xe mixtures [III.42]. However, while the latter are metastable Penning mixtures and therefore exhibit such behaviour for Xe concentrations below 5 %, Ar-Xe ones are non-metastable Penning mixtures which reveal Penning effects for Xe concentrations below about 8-10 % [III.43].

In Table III.3 we compare the Fano factor results obtained in this work with the ones available in the literature, some of them for radiation other than 5.9 keV X-rays, as indicated in the Table. Results for α-particles are also included for comparison, though the physical processes involved are different from those for X-rays.

As shown in Table III.3, the results for the Fano factors have significant discrepancies, that cannot be attributed only to the use of radiations other than the ^{55}Fe X-rays. The result obtained for pure Xe in this work, 0.254 ± 0.003 is in good agreement with some of the experimental (0.26 [III.46]) and simulation (0.24 [III.58] and 0.3 [III.42]) values published, but deviates strongly, by a factor of more than two, from other results [III.39],[III.54] and [III.59]. This also applies to the values obtained for Ar-Xe mixtures [III.39].

Such large differences may be due to geometric effects arising from the use of a GPSC with spherical geometry. In fact, in a parallel grid geometry GPSC the secondary scintillation is always produced uniformly along a straight electric field line connecting the parallel grids and so, the fraction of light reaching the PMT remains constant as the voltage between the grids is varied, varying only its intensity. In a spherical anode geometry like the one used in [III.39], the secondary scintillation is produced non-uniformly along a line that extends away from the anode, and so, as the voltage increases, the fraction of light reaching the PMT due to anode shadowing and eventually other geometry effects, will depend on the applied voltage, eventually distorting the plots of the type of Figure III.17. Another source of plot distortion may result from noisy photosensors that increase the energy resolution for small A values, and so for large $1/A$. This originates an increase in the slope of the straight line fit, which leads to intercepts at lower values of R^2 and so to lower Fano factors.

These and other effects related to charge multiplication, fluctuations in the yield of the secondary scintillation, or impurities can eventually explain the discrepancies obtained by the different authors for the Fano factor values. However, since the energy resolution achieved in the present work for Xe (Table III.2) is as good as the best published results it is unlikely that the large Fano factors we obtained result from impurity effects.

Comparing the w-values and the Fano factors of Ar-Xe mixtures to the ones for 100% Xe, it seems that these mixtures represent a valid alternative as detection media for gaseous X-ray detectors, either in standard proportional counters or in gas proportional scintillation counters.

TABLE III.3

FANO FACTORS AND W-VALUES FOR PURE AR, PURE XE AND THEIR MIXTURES AT ATMOSPHERIC PRESSURE
FOR 5.9 KEV X-RAYS

Mixture	Fano Factor			w-value (eV) [III.27]
	Previous experimental results	Simulation results	This work	
100% Ar	0.19 for 5.68 MeV α-particles [III.44] <0.40 ± 0.03 for 1.49 keV X-rays [III.39] 0.23 ± 0.05 (extrapolation to infinite pressures) [III.45] 0.30 ± 0.04 [III.48] $0.20^{+1.0}_{-0.02}$ [III.49] 0.22 for 6.0 MeV α-particles [III.50]	0.17 [III.44] 0.16 for electrons [III.51] 0.15 [III.52] 0.16 [III.53]		
99%Ar-1%Xe			≈ 0.22	
97%Ar-3%Xe			≈ 0.23	
95%Ar-5%Xe	<0.14±0.03 for 1.49 keV X-rays [III.39]		≈ 0.24	
90%Ar-10%Xe			0.256±0.004	21.42±0.21
80%Ar-20%Xe	<0.16±0.02 for 1.49 keV X-rays [III.39]		0.250±0.003	21.64±0.21
76%Ar-24%Xe	<0.23± 0.02 for 1.49 keV X-rays [III.39]			
60%Ar-40%Xe			0.258±0.003	21.63±0.21
20%Ar-80%Xe	<0.21± 0.03 for 1.49 keV X-rays [III.39]			
100% Xe	0.13 ± 0.01 [III.54] 0.17± 0.007 [III.55] <0.15 ± 0.03 for 1.49 keV X-rays [III.39] 0.26 [III.46] <0.12 [III.40] 0.29±0.02 for 5.3 MeV α-particles [III.56] <0.15 ± 0.01 for 1.49 keV X-rays [III.57] 0.13 ± 0.02 [III.59]	0.304 [III.47] 0.17 [III.44] 0.21 [III.41] 0.30 [III.42] 0.24 [III.58]	0.254±0.003	21.61±0.21

III.3.2 LARGE DETECTION AREAS

The fact that the reduced electroluminescence yield Y^x/p of Ar-Xe mixtures increases linearly from a threshold with the reduced electric field in the scintillation region E_s/p, with a behaviour similar to pure Xe, makes possible the implementation of the curved grid technique [III.9],[III.10] when using Ar-Xe mixtures, and with the shape of the grid similar to the one used for pure Xe.

For this reason, we have tested the performance of this GPSC with the ellipsoidal grid of [III.12] as G1 (instead of the planar one) for different Ar-Xe mixtures and using the 38 mm diameter window. In Figure III.19 we present the spectra obtained for 80%Ar-20%Xe and 5.9 keV X-rays with both planar and curved grids as G1, and compare these spectra with the one obtained for a 2 mm diameter collimated beam. We can observe that a distortion appears as a low energy tail on the left of the gaussian distribution, due to solid angle scintillation losses for off-centred absorbed X-rays, which are also responsible for a slight decrease in the position of the centroid of the distribution and for a deterioration of the energy resolution R observed for large detection areas. Comparing the spectra with planar and curved grids, we can observe significant improvements achieved when the elliptical grid is used, namely a smaller spectrum distortion and improvements in both the detector pulse amplitude and its energy resolution.
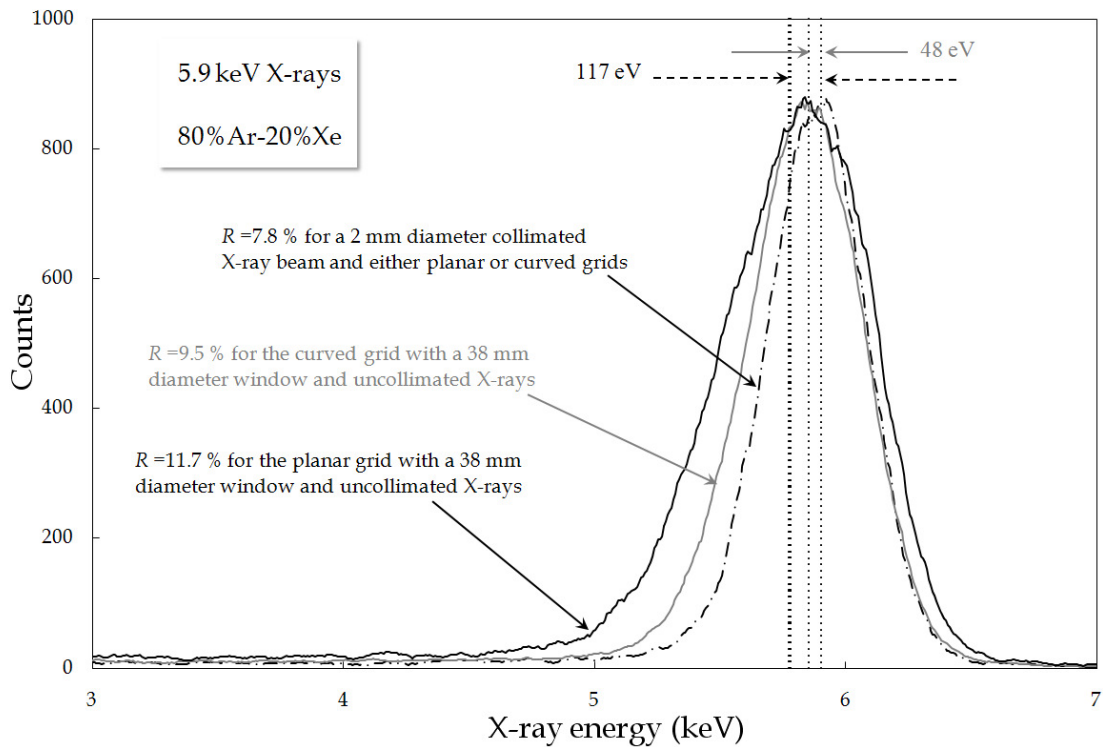
Figure III.19 – Energy spectra obtained with 80%Ar-20%Xe for a 2 mm diameter collimated beam and using the full 38 mm diameter detection area for both the planar and the curved grids.

For each Ar-Xe mixture, we obtained for 5.9 keV X-rays the detector pulse amplitude normalized to the value obtained for a 2 mm diameter collimated beam and its

energy resolution as a function of the window diameter. The results were obtained with both planar and curved grids. For each grid, 4 different voltages ΔV were applied to the scintillation region, as illustrated in Figure III.20 for the 80%Ar-20%Xe case, since for a certain grid curvature, the ΔV that best compensates solid angle distortions depends on the gas. For the 80%Ar-20%Xe case (Figure III.20), the degradation of R with increasing window diameters is minimized and the decrease in the pulse amplitude is almost inexistent when 4600 V are applied to the scintillation region. A similar behaviour was observed for all other Ar-Xe mixtures studied, and the best operating voltage ΔV was different for each studied mixture as expected.
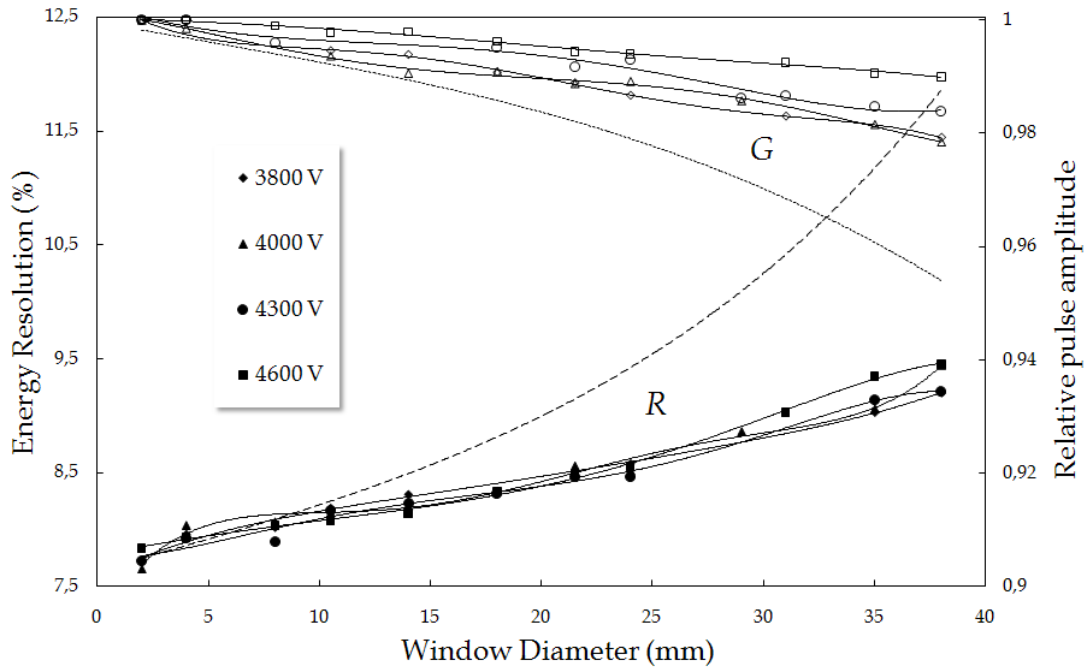
Figure III.20 – Detector relative pulse amplitude G (open symbols) and energy resolution R (full symbols) for the 80%Ar-20%Xe mixture as a function of the window diameter for 4 different voltages ΔV in the scintillation region using the elliptical grid (solid lines) and the planar grid for ΔV =4600 V (dotted and slashed lines).

In Figure III.21 we present, for each mixture studied, the ratio between the energy resolutions R and between the relative pulse amplitudes G obtained with the planar and the curved grids, identified with the subscripts p and c, respectively. As already referred, the behaviour is similar for all the mixtures studied, in particular comparing with the pure Xe case, showing that the shape of the curved grid effectively compensates the solid angle distortion for all the studied mixtures. Since this compensation ideally occurs for a specific voltage difference in the scintillation region, which is gas dependant, these voltages ΔV are the ones that appear in Figure III.21 for each mixture.

We can observe that while the energy resolution improvement is almost independent of the filling gas considered, the relative gain compensation seems to worsen as the Xe concentration decreases in the mixture.
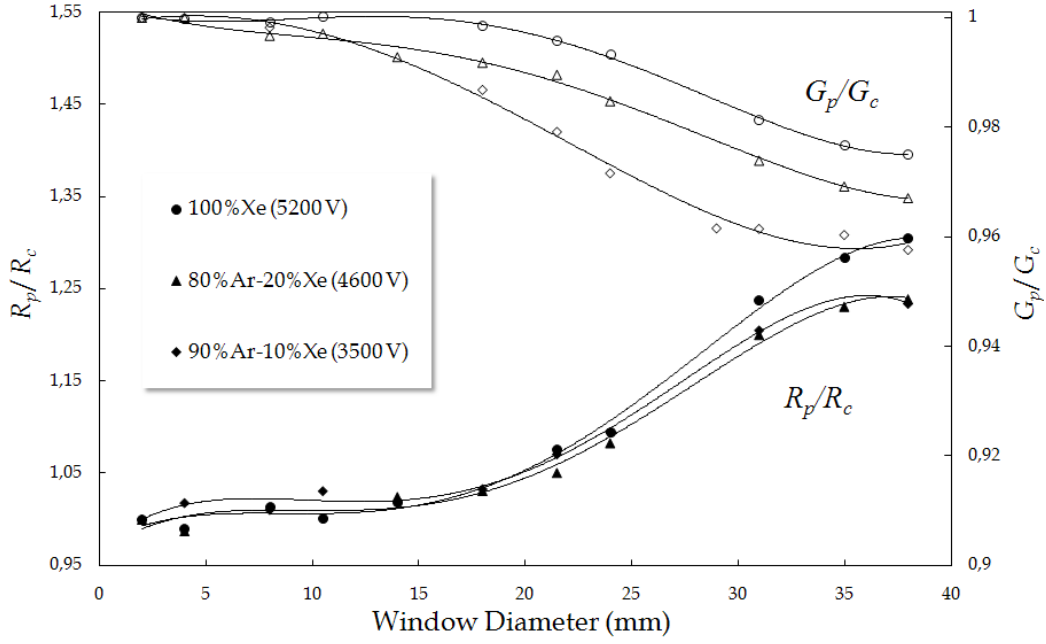
Figure III.21 – Ratios between the detector relative pulse amplitudes G (open symbols) and energy resolutions R (full symbols) as a function of the window diameter, and obtained with the planar grid (p) and the curved one (c) with the best operating voltages for each Ar-Xe mixture.

III.3.3 SOFT X-RAYS DETECTION

We then installed the 0.9 µm thick Mylar® window on the detector top flange and used the experimental set-up as schematized in Figure III.4 to detect low energy X-rays below 2 keV. Prior to the detection of any soft X-rays we calculated the detection efficiency of the present detector filled with pure Xe (Figure III.22) since the knowledge of such parameter is fundamental to carry on quantitative PIXE studies. Such calculations were performed in a way described in [III.3] by taking into account the transmission of both Mylar® and Al layers [III.29] and the loss of primary electrons by backscattering to the detector window [III.20], which depends on the filling gas used.
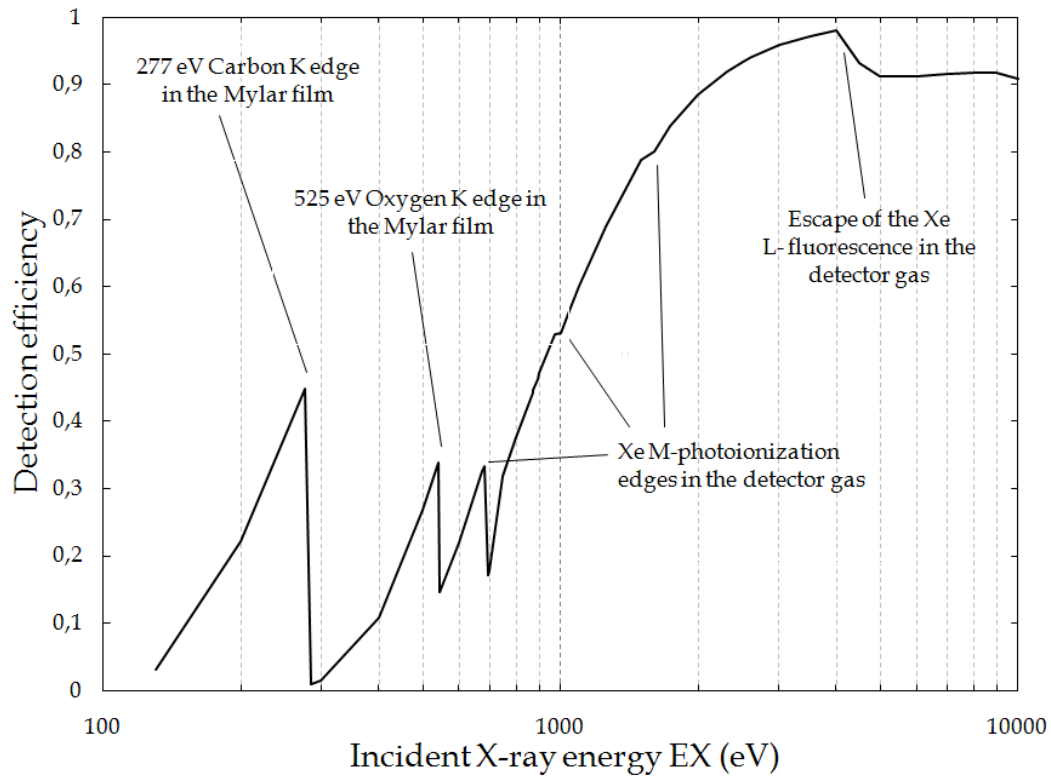
Figure III.22 – Calculated detection efficiency of the present GPSC filled with pure Xe as a function of the energy E_X of the incident X-ray.

X-ray spectra were obtained for several X-ray energies E_X and for several Ar-Xe mixtures with 100%, 40%, 20%, 10% and 5% Xe concentrations, as shown in Table III.4 and Figures III.23 and III.24. For each Ar-Xe mixture studied the reduced electric fields in both absorption and scintillation regions were chosen in order to reach the optimal energy resolution, keeping the PMT voltage constant.

These different X-ray energies E_X correspond to the unfiltered K_α and K_β fluorescence lines of various elements from C to Ge, obtained by exciting pure or compound element targets with α-particles from a 30 kBq ^{244}Cm radioactive source placed under vacuum as shown in Figure III.4. As we can observe in Figure III.24, the spectra present high counting rates in the very low energy region. This behaviour is due to the presence of electronic noise and of the C and O X-ray fluorescence K-lines resulting from the interaction of the incident X-rays with the C and O atoms present in the Mylar® window.

The performance of the GPSC is evaluated in terms of both the energy resolution R and the Peak-to-Valley ratio (PVR) [III.23], which is defined as the ratio of the counts at the centroid c and the average number of counts for 5 points located at a distance of 1.5 FWHM from the peak [III.60]. The PVR gives a quantitative measurement of the distortion of the spectrum in the low energy region.

TABLE III.4

ENERGY RESOLUTIONS, R, OBTAINED FOR THE GPSC FILLED WITH SEVERAL AR-XE MIXTURES
FOR THE Kα X-RAYS FROM LOW ATOMIC NUMBER ELEMENTS

Element	Kα line energy E_x (eV)	R (%) ± 0.1				
		5% Xe	10% Xe	20% Xe	40% Xe	100% Xe
C	277	-	-	57.5	42.6	37.2
O	525	34.5	33.4	30.4	24.7	24.1
F	677	24.4	24.0	24.3	22.3	21.9
Mg	1254	17.5	17.5	18.3	18.1	16.9
Al	1487	15.3	15.9	15.7	15.3	15.7
Si	1740	14.7	14.7	14.5	14.4	13.7
S	2307	13.2	12.9	12.9	12.5	11.7
Cl	2622	12.9	12.8	12.3	11.8	11.5
Ca	3690	10.2	10.0	9.7	9.7	9.4
Ti	4508	9.5	9.5	9.4	9.1	8.8
V	4949	9.4	9.4	9.3	9.2	8.8
Cr	5411	9.3	9.0	9.0	9.0	8.7
Mn	5895	9.2	8.6	8.6	8.6	8.4
Co	6925	8.7	7.9	8.1	8.5	7.6
Ni	7422	8.5	8.1	7.9	7.8	7.6
Cu	8041	8.4	8.1	7.8	7.5	7.4
Zn	8631	8.1	7.9	7.7	7.5	7.3
Ge	9876	7.9	7.8	7.5	7.5	7.1

Figure III.23 – Experimental pulse height-distributions in pure Xe and 60%Ar-40%Xe for the 277 and 525 eV Kα fluorescence lines from C and O respectively.
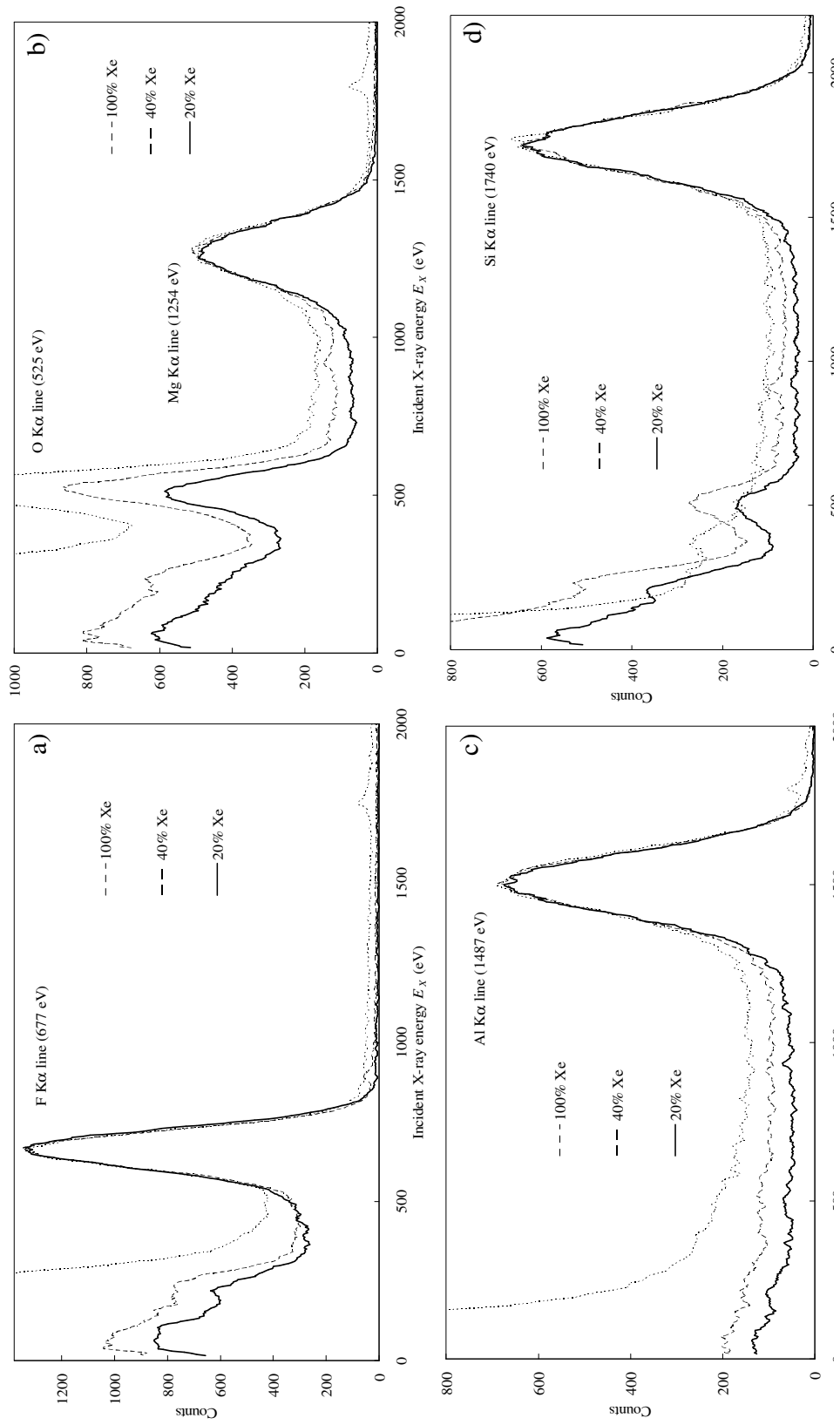
Figure III.24 – Experimental pulse height-distributions in pure Xe, 60%Ar-40%Xe and 80%Ar-20%Xe for a) 677 eV, b) 525 eV and 1254 eV , c) 1487 eV and d) 1740 eV X-rays (F, O, Mg, Al and Si Kα fluorescence lines respectively).

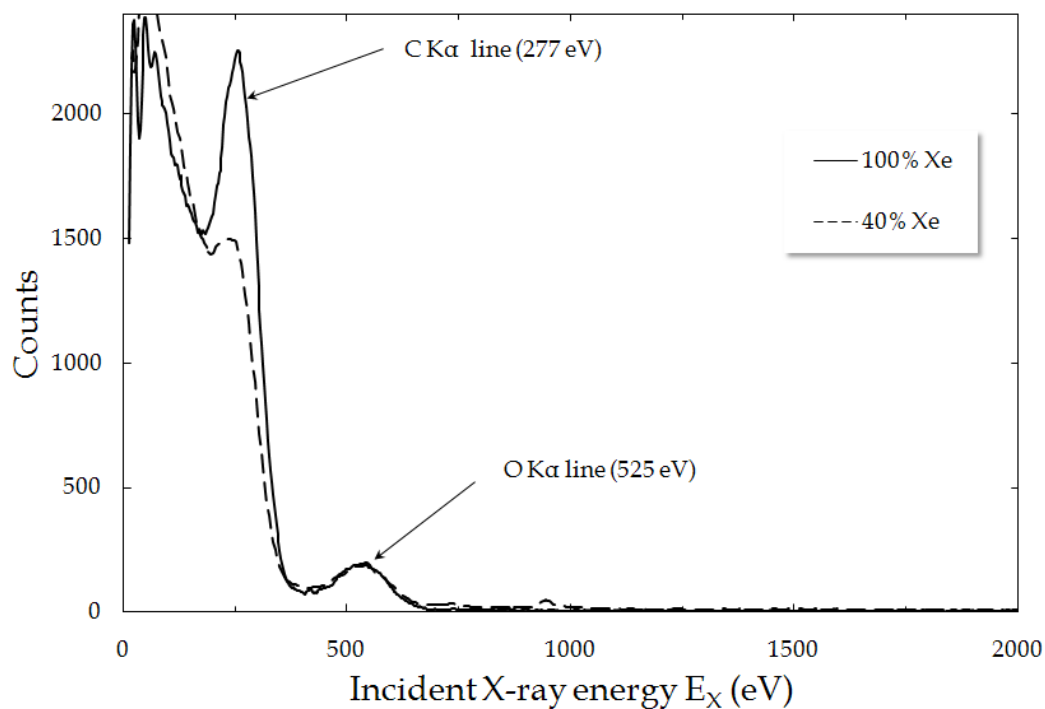Table III.5 shows that the PVR generally improves by a factor of about 2 or 3 as the Ar concentration increases in the mixture. This behaviour shows that the loss of primary electrons to the detector window is reduced with the addition of Ar, as it can be seen in the spectra shown in Figure III.24. However, these improvements in the reduction of the spectra distortion do not result in the expected improvement of the energy resolution, R, as shown in Table III.4. Indeed, R remains approximately constant for pure Xe and the Ar-Xe mixtures. This might be explained by the slightly lower scintillation yield of Ar-Xe mixtures when compared to pure Xe.

Moreover, this improvement in the PVR is not achieved for the C and O K_α lines (277 eV and 525 eV respectively) (Figure III.23) since the absorption length is shorter in Ar than in Xe for the 250-630 eV energy range. This also explains why the energy resolution R worsens with increasing Ar concentrations in this energy range (Table III.4). In fact, the carbon peak becomes almost undistinguishable from the low energy tail, becoming impossible to determine its energy resolution for low Xe concentrations (Table III.4).

Figure III.25 confirms that the energy resolution R is approximately proportional to the square root of the reciprocal X-ray energy $1/E_X$ [III.1], except for the data corresponding to very low energy X-rays which are over the linear behaviour. This is due to the significant worsening of R below approximately 1 keV resulting from the low energy tail distortion. Small deviations apart from this linear behaviour can also be attributed to the expected discontinuities in the Fano factors F and the w-values for Ar-Xe mixtures with the X-ray energy E_X. Indeed, such variations in F and w have been studied before for pure Xe [III.61] and Ne-Xe mixtures [III.42], but no data is available in the literature for Ar-Xe mixtures.

TABLE III.5

PEAK-TO-VALLEY RATIOS FOR DIFFERENT SOFT X-RAY ENERGIES AND FOR THE GPSC FILLED WITH PURE XE AND AR-XE MIXTURES

% Xe	Peak-to-Valley ratios			
	F Kα line (677 eV)	Mg Kα line (1254 eV)	Al Kα line (1487 eV)	Si Kα line (1740 eV)
100	2.9	2.9	4.8	6.2
40	4.4	3.4	6.7	8.8
20	4.9	6.9	9.7	14.2
10	3.2	8.2	10.5	14.7
5	2.7	6.9	11.0	15.7

We have also observed, as illustrated in Figure III.26, that the response of the detector is linear within the experimental error, apart from the discontinuities at the Xe L-, Xe M- and Ar K- edges [III.62], which is of great importance for registering PIXE spectra. We have also noticed that the discontinuities at the Xe L- and M-edges decrease as the Xe concentration decreases while the Ar K-edge becomes more pronounced as the Ar concentration increases. The values of these discontinuities in the

linearity were calculated in a way described in [III.61]. Discontinuities of 63 and 37 eV were obtained in pure Xe for the Xe L- and M- edges respectively for instance, values which are in good agreement with the published data [III.61],[III.63],[III.64].
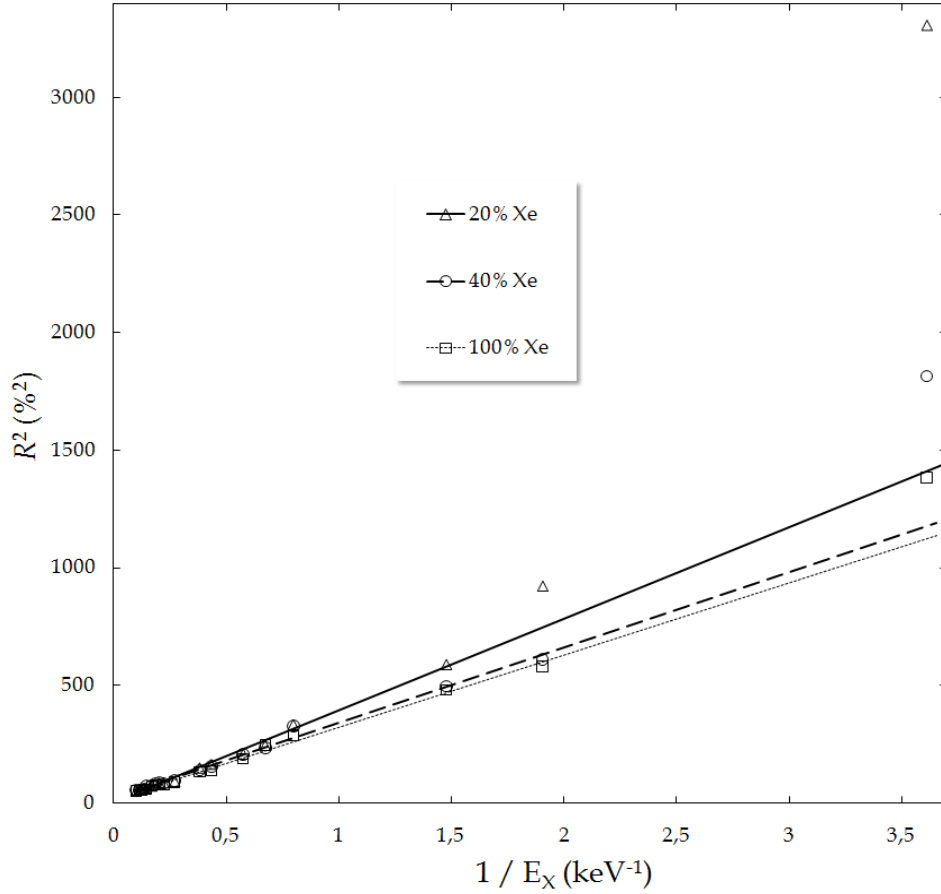
Figure III.25 – Plot of R^2 as a function of the reciprocal X-ray energy, $1/E_X$.

We have shown that, although no performance improvement was achieved by using Ar-Xe mixtures instead of pure Xe, the performance of the present GPSC filled with Ar-Xe mixtures is similar to the one reached with pure Xe as the filling gas. Indeed, energy resolutions of 7.8 % were obtained for 5.9 keV X-rays with either 60%Ar-40%Xe or 80%Ar-20%Xe mixtures while a value of 7.7 % was reached with pure Xe. We can also conclude that similar, or even improved, secondary scintillation yields, w-values, Fano factors can be achieved with Ar-Xe mixtures.

Concerning large detection area with Ar-Xe mixtures as the filling gas, it was shown that the curved grid technique allows a good compensation for all the studied mixtures, with the best operating voltages depending on the gas mixture.

Moreover, the GPSC filled with Ar-Xe mixtures presents energy resolutions for soft X-rays that, apart from the 250-630 eV energy range, almost as good as the ones obtained for pure Xe. These mixtures have also the great advantage of exhibiting improved peak-to-valley ratios (PVR) as the Xe concentration decreases from 100% down to 5%. This improvement in the PVR is particularly important regarding the use of the present GPSC to acquire PIXE spectra since Ar-Xe mixtures filled GPSCs therefore

enable reaching improved sensitivities for soft X-rays below 2 keV when compared to pure Xe filled GPSCs.

For all these reasons, the use of large area GPSCs with Ar-Xe mixtures was shown to be a good alternative to pure Xe to register PIXE spectra.
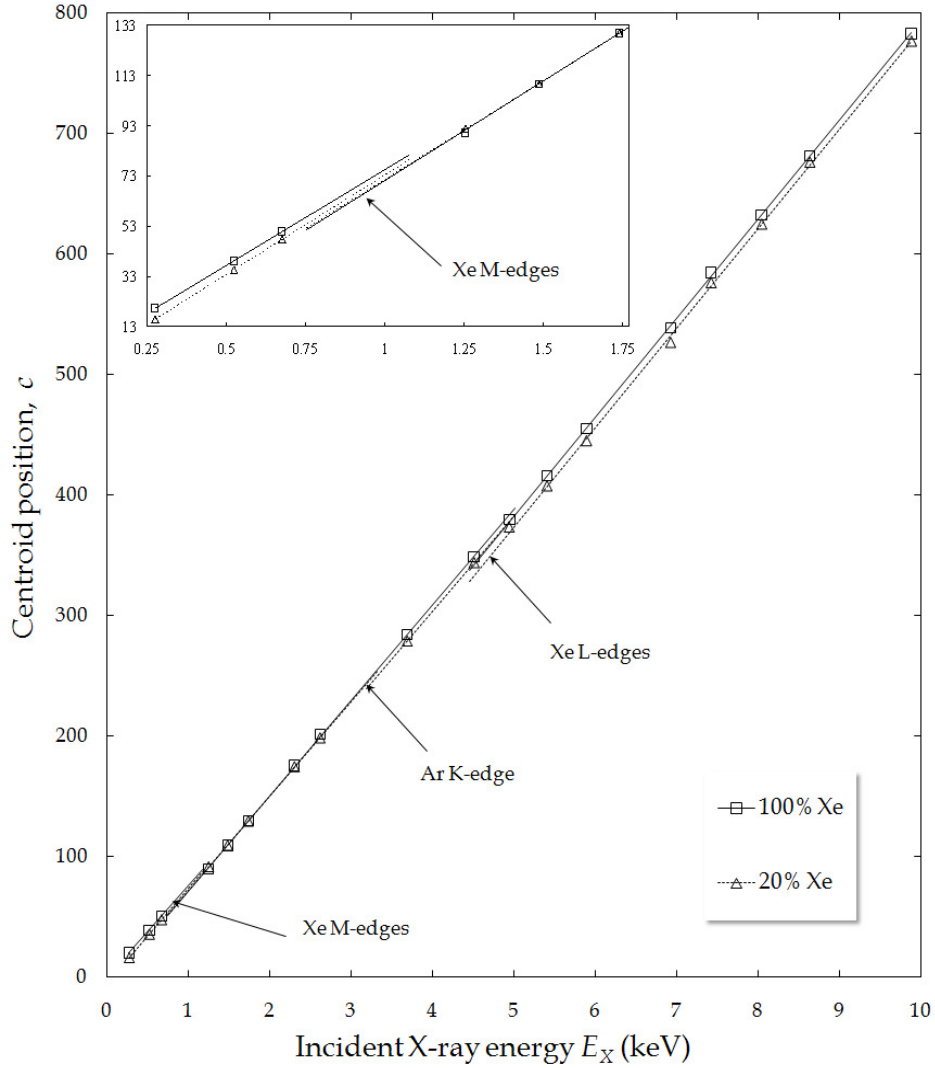
Figure III.26 – Centroid position c as a function of the incident X-ray energy E_X for pure Xe and 80%Ar-20%Xe.

III.4 PRIMARY SCINTILLATION

In addition to the studies concerning Ar-Xe mixtures as the detection media in GPSCs, we also performed another distinct study with the developed GPSC: an investigation on the primary scintillation produced by weakly ionizing radiation in Xe in the gas phase. The slow-down of the electrons resulting from the absorption of an ionizing radiation in a noble gas produces both excited and ionized atoms from collisions

with electrons. The primary scintillation is the result of the radiative decay of the excited species produced directly during the radiation absorption or indirectly after electron-ion recombination.

The primary scintillation is produced in the noble elements during the formation of the primary electron cloud following the absorption of ionizing radiation (i.e. X- and γ-photons or heavy particles) and its relevance relies on its application in several fields, such as time coincidence measurements or Time Projection Chambers (TPC). A recent private communication with David R. Nygren (from the Lawrence Berkeley National Laboratory) concerning his last work [III.65] which aims to measure both primary and secondary scintillation in a TPC in order to study the double β-decay of ^{136}Xe in gas phase, combined to an evident lack of available information in the literature, encouraged us to perform the following study to measure the primary scintillation yield in pure Xe.

Indeed, some previous works concerning the primary scintillation [III.66]-[III.68] deal with condensed noble gases (usually in liquid state), and/or heavily ionizing radiation such as α-particles, but the published results for the direct interaction of X-rays are scarce particularly due to difficulties in detecting such small amounts of light.

For pressures above ~10 Torr in Xenon, the excited- and ion-dimers Xe_2^* and Xe_2^+ are easily formed in three body collisions (Equations III.5 and III.8). Then, the primary scintillation produced (Equations III.6 and III.10) consists essentially of the UV continuum characteristic of the decay of the Xe_2^* excimer (excited dimer) states (peaked at ~173 nm) [III.69].

As pointed out by Kobayashi *et al.* [III.70], there are 2 mechanisms leading to the production of primary scintillation, namely:

excitation luminescence, which follows excitation by electron impact

$$e^- + Xe \rightarrow Xe^* + e^- \qquad \text{(Eq. III.4)}$$

$$Xe + Xe + Xe^* \rightarrow Xe + Xe_2^* \qquad \text{(Eq. III.5)}$$

$$Xe_2^* \rightarrow Xe + Xe + h\nu \qquad \text{(Eq. III.6)}$$

and *recombination luminescence*, which follows ionization by electron impact

$$e^- + Xe \rightarrow Xe^+ + 2\,e^- \qquad \text{(Eq. III.7)}$$

$$Xe + Xe + Xe^+ \rightarrow Xe + Xe_2^+ \qquad \text{(Eq. III.8)}$$

$$Xe_2^+ + e^- \rightarrow Xe_2^{**} \rightarrow Xe_2^* \qquad \text{(Eq. III.9)}$$

$$Xe_2^* \rightarrow Xe + Xe + h\nu \qquad \text{(Eq. III.10)}$$

both reactions leading to the production of Xe_2^*, followed by the emission of a VUV scintillation photon with energy hv.

While in the case of condensed media and/or heavily ionizing particles the recombination component [III.71] is strong due to the large concentration of primary electrons and of noble gas positive ions along the radiation track, this primary scintillation component is much weaker, or even inexistent, in the case of weakly ionizing radiation (such as electrons or X- and γ-rays) interacting in gas phase noble gases [III.72]-[III.75], leading therefore to much weaker primary scintillation yields. This difference is experimentally evidenced by comparing published data for the average energy spent to produce a primary scintillation photon, W_s, in liquid and gaseous mediums. While Chepel *et al.* [III.76] measured W_s of 18.3 ± 1.5 eV and 17.1 ± 1.4 eV for 59.54 keV γ-rays and α-particles respectively in liquid Xe (in liquid phase the primary scintillation receives a much stronger contribution from recombination), much larger values of W_s of 76 ± 12 eV have been measured by Parsons *et al.* [III.74] for 60 keV γ-rays in Xe and 90%Xe-10%He at 20 atm.

Nevertheless, even in gas phase, the recombination component can still be important for heavily ionizing particles. In this case, its contribution is expected to decrease with increasing applied electric fields.

We used the GPSC experimental set-up to detect 5.9 keV X-rays from a [55]Fe radioactive source, just as we explained in section III.2.5. However, in this particular application, we took special attention to the detector output pulse resulting from the primary scintillation, beyond the usual detector signal output resulting from the detection of the secondary scintillation. The production of primary scintillation light occurs due to the de-excitation of the excimers resulting from the radiation interaction, whose lifetimes are short (about a few tens of *ns* [III.77]), while the production of secondary scintillation takes place only after the drifting of the primary electron cloud towards G1 (i.e. tens of μs latter). As a result, the primary scintillation can be considered as a prompt signal in comparison to the detector signal output, and so its signal appears prior to the one due to the secondary scintillation, as represented in Figure III.27. Figure III.27 represents both primary and secondary scintillation pulses amplitudes, which were measured with a TDS 1012 Tetronix digital oscilloscope. Although it is difficult to distinguish the primary scintillation signal from the electronic noise because of its very low amplitude (only about 0.5 mV after electronic amplification and with a high PMT gain), we managed to obtain a clear distinction of the primary scintillation pulse from noise by averaging out the noise level close to zero, making therefore possible its measurement: the digital oscilloscope was triggered not with the primary scintillation pulse but later with the secondary scintillation pulse, at a low threshold of ~10-20 mV in order to observe simultaneously the primary scintillation pulse, and averages of 128 pulses were taken for both the primary and secondary scintillation signals. These averaged pulses were then recorded so that the amplitudes of both signals were determined by fitting these to gaussian curves. We also related the separation between the centroids of the gaussian fits to the time δ separating the two peaks, i.e. events. To avoid saturation when

measuring the amplitude of the secondary scintillation pulses, we reduced the gain of the linear amplifier by a factor of 10, as compared to the primary scintillation case, and this factor was taken into account when comparing the primary with the secondary scintillation amplitudes.
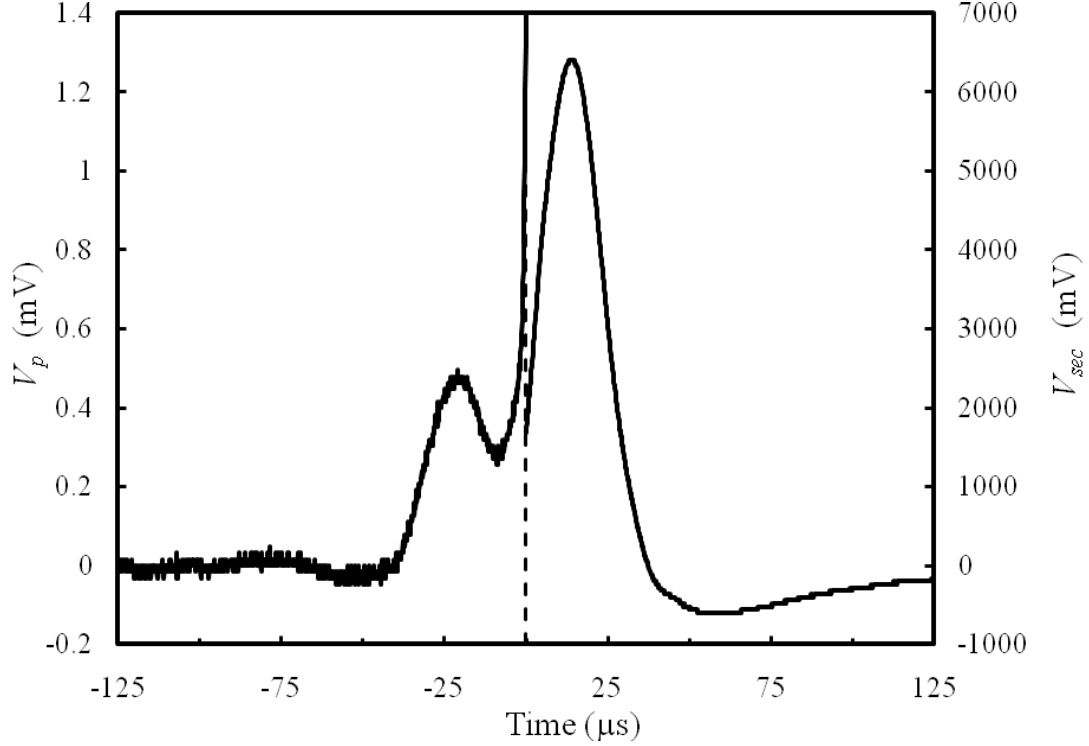
Figure III.27 – Primary (left panel) and secondary (right panel) scintillation pulses obtained for 5.9 keV X-rays.

However, we have to take into account that this averaging technique relies on the following assumptions:

✓ First of all, any comparison between both scintillation pulse amplitudes is only possible under the fair assumption that the primary and secondary scintillation have the same spectral distribution (peaked at 173 nm); otherwise the non-uniformity of the PMT efficiency for different wavelengths would forbid any comparison.

✓ Besides, the absorption point of the X-ray is considered to be constant to guarantee that the solid angle subtended by the PMT photocathode remains the same. This condition has also to be taken into account to consider that the drifting time of the primary electron cloud towards G1 is constant, since we considered a constant time difference between the primary scintillation pulse and the secondary scintillation one. Otherwise, we would be averaging pulses with different amplitudes and centred at different instants. This condition is almost verified for 5.9 keV X-rays since their absorption length in Xe at 800 Torr (2.62 mm [III.78]) is much shorter than the 46.5 mm drift distance D travelled by the primary electrons cloud before reaching G1.

Because of this latter reason, this technique can no longer be used for X-rays with energies higher than about 8-10 keV with a GPSC filled at atmospheric pressure. On the other hand, for X-rays below about 4 keV, the primary scintillation signal is, even using this averaging technique, less distinguishable from the electronic noise. As a result, this averaging technique is only viable for X-rays in the 4-10 keV energy range.

We first plotted in Figure III.28 the time difference δ between the 2 peaks of Figure III.27 as a function of E_d/p to confirm that the first pulse preceding the secondary scintillation pulse corresponds in fact to the primary scintillation signal. This delay δ of the secondary scintillation pulse in relation to the signal from the primary scintillation is due, as already explained, to the time that the primary electrons take to drift through the remaining part of the 46.5 mm deep absorption region towards grid G1.

Indeed, the observed delays δ in the 25-34 μs range for E_d/p in the 0.05-0.4 Vcm^{-1} Torr^{-1} range are consistent with published drift velocities of about 1-2 mm/μs for electrons in Xe for this E_d/p range [III.47],[III.79]. Besides, the fact that the time lag δ between primary and secondary scintillation pulses decreases as E_d/p increases is also expected since the drift velocity of the electrons increases with increasing E_d/p.

Figure III.28 – Delay δ between the secondary and the primary scintillation pulses as a function of the reduced electric field E_d/p in the GPSC drift region, when the field applied in the secondary scintillation region is E_{sec}/p = 2.9 V cm^{-1} Torr^{-1} in Xe at 800 Torr.

We then studied the amplitudes of both primary and secondary scintillation pulses, V_p and V_{sec} respectively, as a function of the reduced electric field E_d/p applied in the drift region; with a constant reduced electric field in the secondary scintillation region E_{sec}/p of 2.9 Vcm^{-1} Torr^{-1}. As expected, and with exception for very low electric

fields $E_d/p < 0.05$ Vcm^{-1} Torr^{-1} for which allowance for primary electron recombination is larger, the amplitude V_{sec} remains approximately constant within the experimental errors (Figure III.29). The small drop in V_{sec} at higher E_d/p may be explained by the lower transmission of electrons from the absorption/drift to the scintillation region due to the smaller difference between E_d/p and E_s/p [III.80]. On the other hand, the amplitude V_p does not seem to be sensitive to increasing E_d/p, within the experimental error. This experimental error in V_p is considerably large, as it can be seen in Figure III.29, but this is expected since it involves the measurement of a signal with very small amplitude.
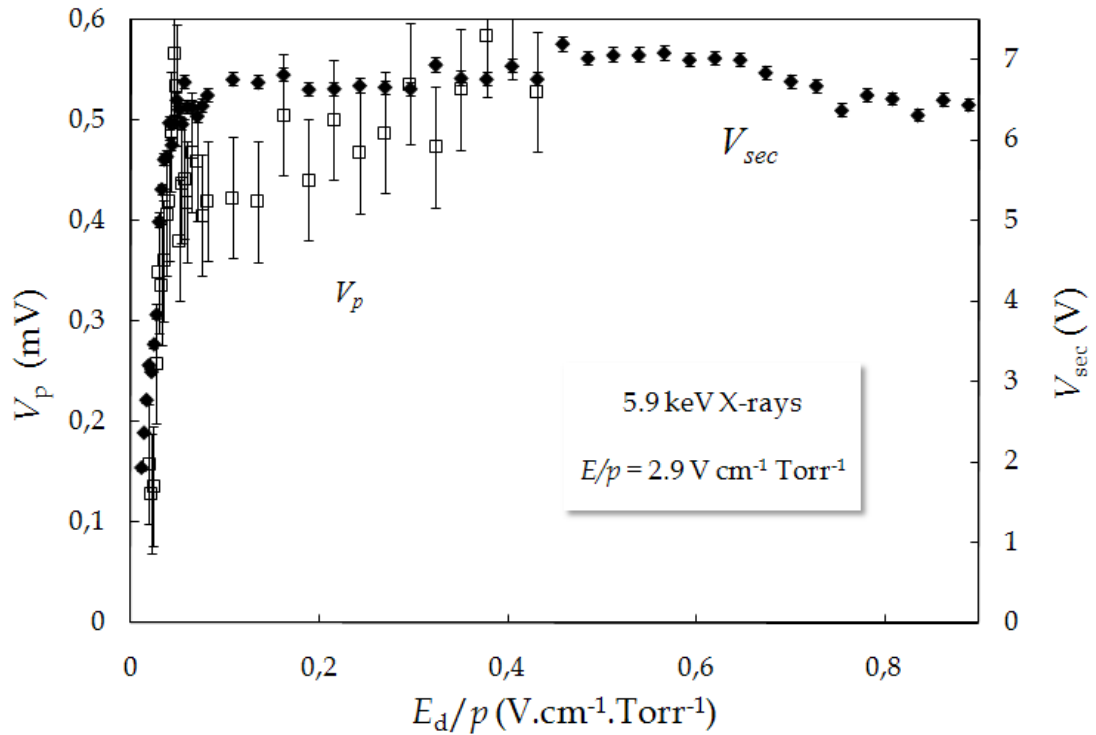
Figure III.29 – Amplitudes V_p and V_{sec} of the primary ($\square$) and secondary ($\blacklozenge$) scintillation pulses as a function of the reduced electric field E_d/p in the GPSC drift region, when the field applied in the secondary scintillation region is $E_{sec}/p = 2.9$ V cm^{-1} Torr^{-1} in Xe at 800 Torr.

In Figure III.30 we plotted the ratio V_{sec}/V_p between the secondary and primary scintillation pulse amplitudes. We observed that, for $E_d/p > 0.05$ Vcm^{-1} Torr^{-1}, the V_{sec}/V_p ratio remains approximately constant within the experimental error and equals $(14.2 \pm 2.1) \times 10^3$. The V_{sec}/V_p ratio shows a slight trend to decrease with E_d/p because of the already referred small drop in V_{sec} at higher E_d/p. This constant value of the ratio proves that the recombination process gives a negligible contribution to the primary scintillation yield for 5.9 keV X-rays in Xe gas at 800 Torr.
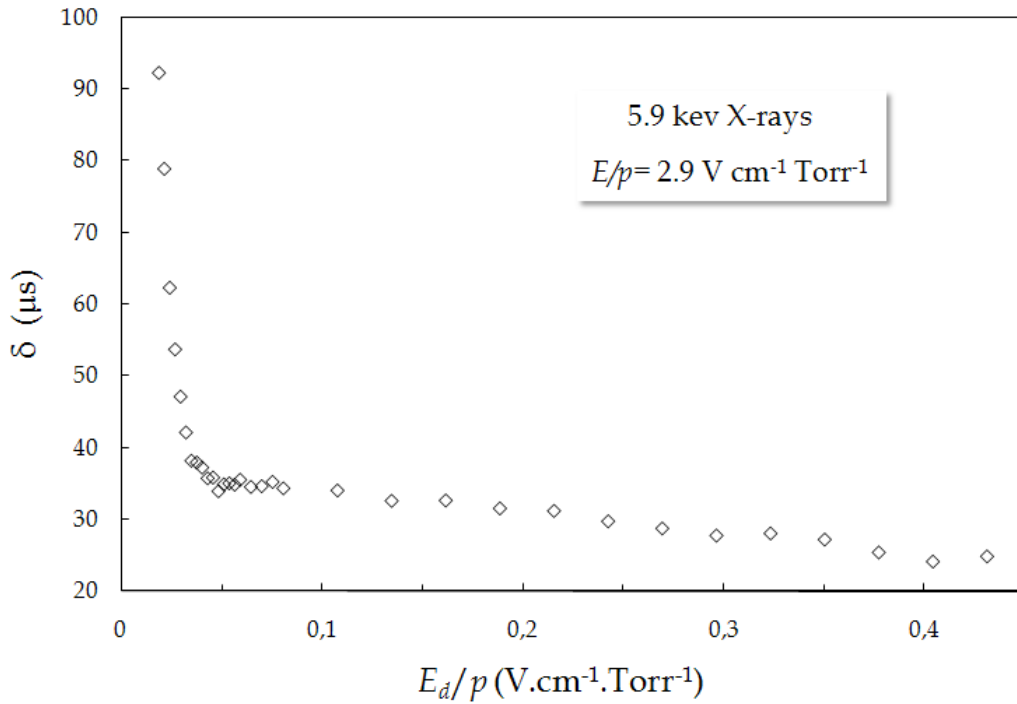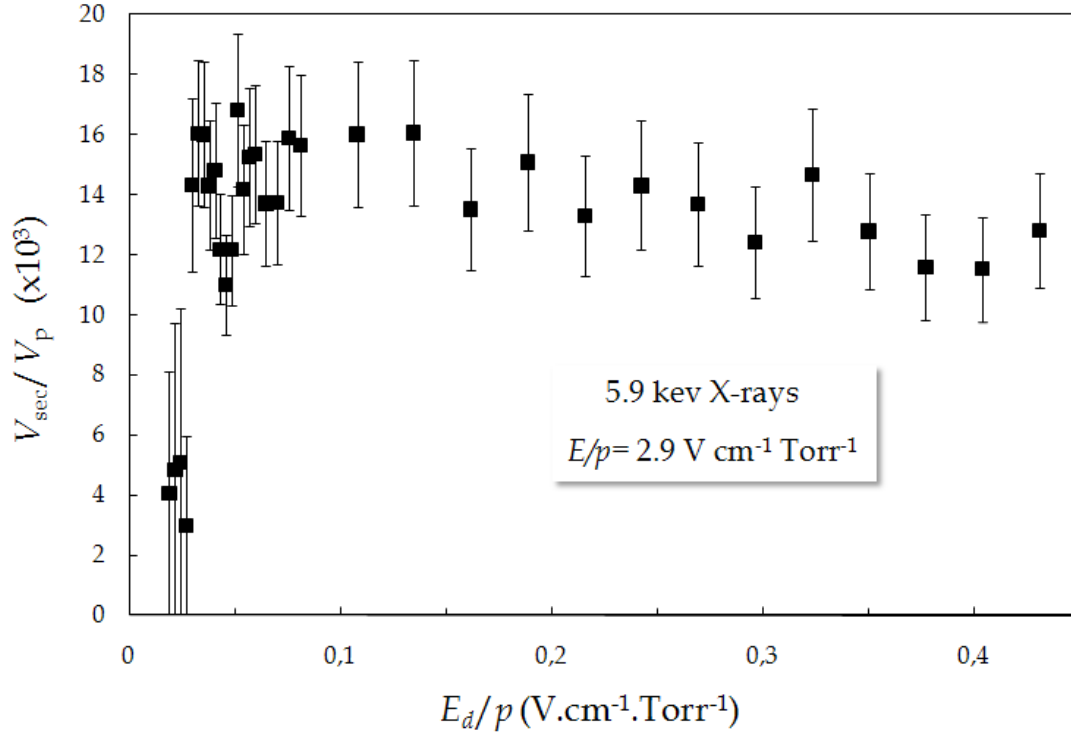
Figure III.30 – Ratio V_{sec}/V_p between the secondary and the primary scintillation pulse amplitudes as a function of the reduced electric field E_d/p in the GPSC drift region, when the field applied in the secondary scintillation region is $E_{sec}/p = 2.9$ V cm^{-1} Torr^{-1} in Xe at 800 Torr.

The experimental value of the ratio V_{sec}/V_p combined to the knowledge of the secondary scintillation yield enables the determination of the primary scintillation yield since the amplitudes V_{sec} and V_p are proportional to the average numbers n_{sec} and n_p of secondary and primary scintillation photons reaching the PMT, so that:

$$\frac{V_{sec}}{V_p} = \frac{n_{sec}}{n_p}$$

(Eq. III.11)

Concerning n_p, this can be related to the number of primary scintillation photons per X-ray event m as $n_p = Tm\bar{\Omega}$ where T is the grid optical transmission and $\bar{\Omega}$ is the average of the solid angles $\Omega(x)$ subtended by the PMT window at each scintillation point along the drift region weighted by the X-ray absorption rates $g(x) = (1/\lambda)\, e^{-x/\lambda}$ where λ is the x-ray absorption length ($\lambda=0.262$ cm for $E_X=5.9$ keV in Xe at $p=800$ Torr and so $\lambda<<D$ as needed).

As illustrated in Figure III.31, the solid angles $\Omega(x)$ subtended by the PMT window are given by $\Omega(x) = 2\pi\left(1 - (D + d\text{-}x)/\sqrt{(D + d\text{-}x)^2 + R^2}\right)$ with x measured from the detector entrance window (else by $\Omega(x') = 2\pi\left(1 - x'/\sqrt{(x')^2 + R^2}\right)$ with $x'=D+d\text{-}x$) and where D and d are the lengths of the absorption/drift and scintillation regions respectively and R the radius of the PMT photocathode (which equals 2.4 cm).

120

Figure III.31 – Schematic of the Gas Proportional Scintillation Counter.

On the other hand, n_{sec} equals $NL\int_D^{D+d}\Omega(x)dx$, where N is the average number of primary electrons per X-ray event ($N = E_X/w$) and L is the secondary scintillation yield per primary electron and per cm. The behaviour of the pressure reduced secondary scintillation yield, L/p, is well established: below the threshold for ionization, it increases linearly with the pressure reduced electric field E_S/p, according to the empirical relation

$$\frac{1}{p}L = A\frac{E_S}{p} - B$$ (Eq. III.12)

first reported in 1977 in [III.81], and afterwards investigated in detail with accurate Monte Carlo calculations [III.82]. The values obtained in [III.82] for the constants A and B (x in cm, E_S in V cm^{-1}, p in Torr, and T=293 K) are A= 0.1389 photons electron^{-1} V^{-1} and B= 0.1325 photons electron^{-1} cm^{-1} Torr^{-1}, which are also in good agreement with the recently published absolute measurements [III.83].

As a result,

$$\frac{V_{sec}}{V_p} = \frac{n_{sec}}{n_p} = \frac{NL\int_D^{D+d}\Omega(x)dx}{Tm\bar{\Omega}} = \frac{\frac{E_X}{w}L\int_D^{D+d}\Omega(x)dx}{Tm\bar{\Omega}}$$ (Eq. III.13)

Considering the value V_{sec}/V_p =14.2 ×10^3 obtained experimentally and by introducing w=21.61 eV [III.84], L=216 photons electron^{-1} cm^{-1} (calculated from Equation III.12 with the pressure p=800 Torr and E_{sec}/p = 2.9 V cm^{-1} Torr^{-1}), T=0.84 (calculated on geometrical grounds for the grid used), $\int_D^{D+d}\Omega(x)dx = 5.62$ cm, and $\bar{\Omega} = 0.52$, we deduced the value m=53 ± 8 for the number of primary scintillation

photons produced when a X-ray photon with an energy E_X of 5.9 keV is absorbed in Xe at 800 Torr. The error in m was determined by taking into account the error associated to the ratio V_{sec}/V_p, this latter being itself calculated by taking into account the errors in both V_{sec} and V_p.

Finally, we also have deduced that the average energy W_s expended to produce a primary scintillation photon ($W_s=E_X/m$) is $W_s=111 \pm 16$ eV for $E_X=5.9$ keV in Xe at 800 Torr.

The obtained value of W_s is in agreement with an estimation that was made by comparing the Xe electron impact scattering cross sections σ_{ion} for ionization and σ_{exc} for excitation from [III.47]: this estimation relies on the assumption that the ratio W_s/W between the values W_s for primary scintillation and W for primary ionization approximately equals the ratio $\sigma_{ion}/\sigma_{exc}$. As we can observe in Figure III.32, where we both plot σ_{exc} and σ_{ion} together with the ratio $\eta = \sigma_{ion}/\sigma_{exc}$ as a function of electron energy ε, this ratio η varies only from about 4 to 9 in the ε range from 100 eV to 10 keV. Since $W{\sim}22$ eV, this implies an expected value for W_s to be in the 80-200 eV, which is compatible with the value we deduced experimentally.
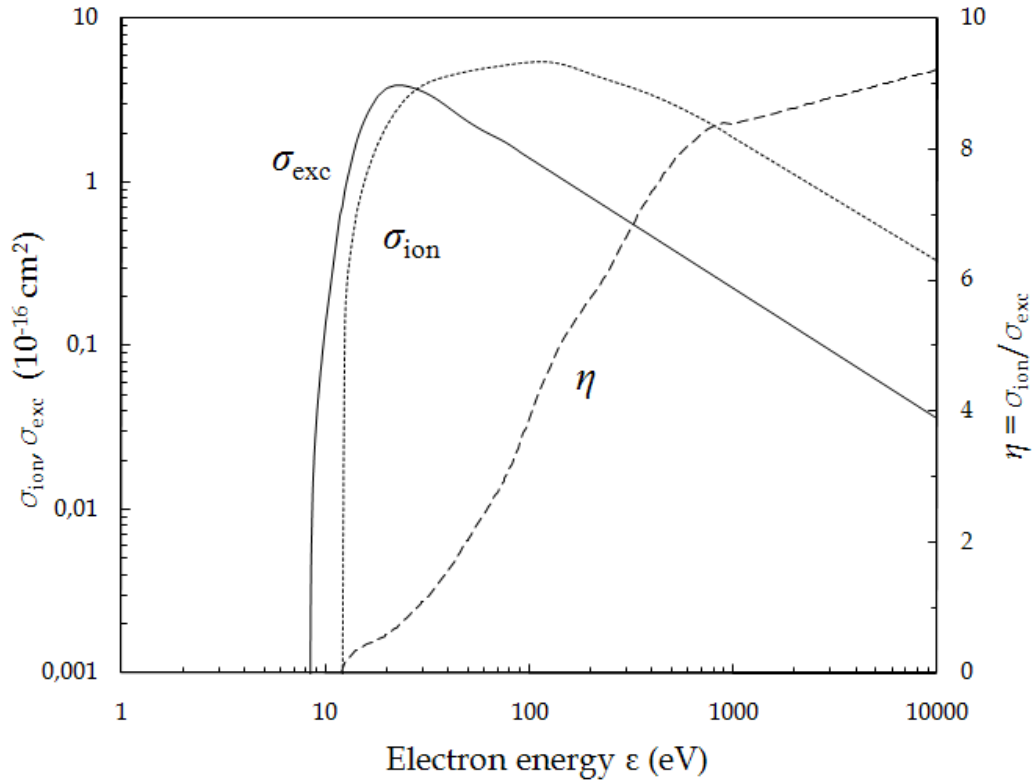
Figure III.32 – Electron impact scattering cross sections σ_{exc} for excitation and σ_{ion} for ionization in Xe, together with the ratio $\eta = \sigma_{ion}/\sigma_{exc}$.

The experimental value $W_s=111 \pm 16$ eV we obtained for 5.9 keV X-rays in Xe at atmospheric pressure is somewhat larger than the value 76 ± 12 eV measured by Parsons *et al.* [III.74] for 60 keV γ-rays at 20 atm which was mentioned before. Nevertheless, these values are quite compatible within the frame of our previous

discussion since we expected larger W_s as the energy decreases and the detection media becomes less dense. Also for these reasons, our experimentally obtained value of W_s in gaseous Xe is much larger than for α-particles, for which the values 34.3 ± 1.6 eV and 49.6 ± 1.1 eV have been measured at atmospheric pressure by Saito *et al.* [III.66] and Miyajima *et al.* [III.67] respectively. A qualitative comparison confirms again our previous discussion concerning the contribution of the recombination process in the primary scintillation yield.

III.5 REFERENCES

[III.1]   C.A.N Conde, "Gas Proportional Scintillation Counters for X-ray spectrometry" in *X-ray Spectrometry: Recent Technological Advances*, pp. 195-216, 2004.

[III.2]   L.P.M.M. Carita, S.J.C. do Carmo, F.P. Santos, and C.A.N. Conde, "The Gridded-Microstrip Gas Chamber as a High Energy Resolution Gaseous X-Ray Detector",IEEE Trans. Nucl. Sci. 54(5), pp. 1779-1783, 2007.

[III.3]   F.I.G.M. Borges, J.M.F. dos Santos, T.H.V.T. Dias, F.P. Santos and C.A.N. Conde, "A gas proportional scintillation counter for x-ray spectrometry in the 0.1-3 keV range", X-ray Spectrometry 33(2), pp. 124-127, 2004.

[III.4]   C.A.N. Conde e A.J.P.L. Policarpo, "A gas proportional scintillation Counter", Nucl. Instr. and Methods 53, pp. 7, 1967.

[III.5]   T.H.V.T Dias, "Physics of noble gas x-ray detectors: a Monte Carlo study" in *Linking the gaseous and condensed physics of matter: the behaviour of slow electrons*. Edited by L.G. Christophorou, E. Illenberger and W.F. Schmidt, NATO ASI Series B: Physics 326, pp. 553, Plenum Press, New-York, 1994.

[III.6]   A.J.P.L. Policarpo, M.A.F. Alves, M.C.M. dos Santos and M.J.T. Carvalho, "Improved resolution for low energies with gas proportional scintillation counters", Nucl. Instr. And Methods 102, pp. 337-348, 1972.

[III.7]   C.A.N. Conde, M.C.M. Santos, M. Fatima, A. Ferreira and C.A. Sousa, "Argon scintillation counter with uniform electric field", IEEE Trans. Nucl. Sci. 22(1), pp. 104-108, 1975.

[III.8]   F.I.G.M. Borges, "Detectores de radiação X de baixa energia baseados em misturas de Xénon e Néon", PhD Thesis, University of Coimbra, 2003.

[III.9]   C.A.N. Conde, J.M.F. dos Santos and A.C.S.S.M. Bento, "Gas proportional scintillation counter for ionizing radiation with medium and large size radiation windows and/or detection volumes", U.S. Patent 5517030, May 14, 1996.

[III.10] C.A.N. Conde, J.M.F. dos Santos and A.C.S.S.M Bento, "Gas proportional scintillation counter for ionizing radiation with medium and large size radiation windows and/or detection volumes", European Patent EP 0616722 BI, December 30, 1998.

[III.11] C.A.N. Conde, J.M.F. dos Santos and A.C.S.S.M. Bento, "New concepts for the design of large area gas proportional scintillation counters", IEEE Trans. Nucl. Sci. 40(4), pp. 452-454, 1993.

[III.12] R.M.C. Silva, J.M.F. dos Santos, and C.A.N. Conde, "An ellipsoidal grid gas proportional scintillation counter", Nucl. Instr. and Methods A422, pp. 305-308, 1999.

[III.13] J.A.M. Lopes, J.M.F. dos Santos and C.A.N. Conde, "A large area avalanche photodiode as the VUV photosensor in gas proportional scintillation counters", Nucl. Instr. and Methods A454, pp. 421-425, 2000.

[III.14] D.F. Anderson, "A Xenon Gas Scintillation Proportional Counter Coupled to a Photoionization Detector", Nucl. Instr. and. Methods 178, pp. 125-130, 1980.

[III.15] D.S. Covita, J.A.M. Lopes, M. Szawlowski, and J.M.F. dos Santos, "High-Pressure Xenon GPSC/LAAPD for Hard X-Ray Spectrometry", IEEE Trans. Nucl. Sci. 51(4), pp. 1492-1496, 2004.

[III.16] D. Mormann, A. Breskin, R. Chechik, P. Cwetanski, B.K. Singh, "A gas avalanche photomultiplier with CsI-coated GEM", Nucl. Instr. and Methods A478, pp 230-234, 2002.

[III.17] J.A.M. Lopes, J.M.F. dos Santos, C.A.N. Conde, R.E. Morgado, "A new integrated photosensor for gas proportional scintillation counters based on the gas electron multiplier (GEM)", Nucl. Instr. and Methods A426, pp. 469-476, 1999.

[III.18] E.D.C. Freitas, J.F.C.A. Veloso, A. Breskin, R. Chechik, F.D.Amaro, L.F. Requicha Ferreira, J.M. Maia, J.M.F. dos Santos, "Micro-Hole & Strip Plate Based Photosensor", Nucl. Instr. And Methods A580., pp. 214-217, 2007.

[III.19] S.J.C. do Carmo, L.P.M.M. Carita, F.I.G.M. Borges and C.A.N. Conde, "A gas proportional scintillation counter with KI and KBr-Covered microstrip plate as photosensor: Experimental Results", Trans. Nucl. Sci. 54(4), pp. 1257-1262, 2007.

[III.20] F.I.G.M. Borges, F.P. Santos, T.H.V.T. Dias, P.J.B.M. Rachinhas, C.A.N. Conde and A.D. Stauffer, "Xenon-Neon Gas Proportional Scintillation Counters for X-rays below 2 keV: A Monte Carlo simulation study", IEEE Trans. Nucl. Sci. 49(3), pp. 917-922, 2002.

[III.21] F.P. Santos, J.M.F. dos Santos, T.H.V.T. Dias and C.A.N. Conde, "Pulse-Height spectrum distortion in Xenon gaseous detectors for soft X-rays", IEEE Trans. Nucl. Sci. 42(4), pp. 611-614, 1995.

[III.22] D.G. Simons and P.A.J. de Korte, "Soft X-ray energy resolution and background rejection in a driftless gas scintillation proportional counter", Nucl. Instr. and Methods A277, pp. 642-656, 1989.

[III.23] F.I.G.M. Borges, F.P. Santos, J.M.F. dos Santos, T.H.V.T. Dias, P.J.B.M. Rachinhas and C.A.N. Conde, "Xenon-Neon Gas Proportional-Scintillation Counters for X-rays below 2 keV: Experimental Results", IEEE Trans. Nucl. Sci 50(4), pp. 842-846, 2003.

[III.24] S. Kubota, "Non-metastable Penning effect in the Alpha-particle ionization of inert gas mixtures", J. Phys. Soc. of Japan 29(4), pp. 1017-1029, 1970.

[III.25] T. Takahashi, S. Himi, M. Suzuki, J. Ruan and S. Kubota, "Emission spectra from Ar-Xe, Ar-Kr, Ar-N_2, Ar-CH_4, Ar-CO_2 and Xe-N_2 gas scintillation proportional counters", Nucl. Instr. and Methods 205, pp. 591-596, 1983.

[III.26] H. Brunet, A. Birot, H. Dijols, J. Galy, P. Millet and Y. Salamero, "Spectroscopic and kinetic analysis of the VUV emissions of argon and argon-xenon mixtures: II. Energy transfer in Ar-Xe mixtures", J. Appl. Phys B15, pp. 2945-2967, 1982.

[III.27] F.L.R. Vinagre and C.A.N. Conde, "Penning effects in Ar-Xe mixtures at atmospheric pressures: Absolute W-value measurements for 5.9 keV X-rays", Conference Record of the IEEE-1999 Nuclear Symposium and Medical Imaging Conference, vol. 2, pp. 651-653, 2000.

[III.28] J.M.F. dos Santos, A.C.S.S.M. Bento and C.A.N. Conde, "The dependence of the energy resolution of gas proportional scintillation counters on the scintillation region to photomultiplier distance", IEEE Trans. Nucl. Sci. 39(4), pp. 541-545, 1992.

[III.29] http://henke.lbl.gov/optical_constants/

[III.30] http://www.goodfellow.com/

[III.31] F.I.G.M. Borges, J.M.F. dos Santos, T.H.V.T. Dias, F.P. Santos, P.J.B.M. Rachinhas and C.A.N. Conde, "Operation of gas proportional scintillation counters in a low charge multiplication regime", Nucl. Instr. and Methods A422, pp. 321-325, 1999.

[III.32] F.I.G.M Borges, S.J.C. do Carmo, T.H.V.T. Dias, F.P. Santos, F.P.S.C. Gil, A.M.F. Trindade, R.M. Curado da Silva and C.A.N. Conde, "Performance of a room temperature gas proportional scintillation counter in X-ray analysis of metallic alloys excited with alpha particles", Advances in X-Ray Analysis 51, pp. 249-254, 2008.

[III.33] B.F.O. Costa, G. Pereira, A.J.M. Silva, M. Ramos Silva and S.J.C. do Carmo, "Mossbauer study of Haltern 70 amphora sherds from Castro do Vieito, North of Portugal", Journal of Physics: Conference Series 217, nº 012060, 2010.

[III.34] C.A.N. Conde, L.F.R. Ferreira, M.F.A. Ferreira, "Secondary scintillation output of xenon in a uniform-field gas proportional scintillation counter", IEEE Trans. Nucl. Sci. 24, pp. 221-224, 1977.

[III.35] F.I.G.M. Borges, J.M.F. dos Santos, T.H.V.T. Dias, F.P. Santos, P.J.B.M. Rachinhas and C.A.N. Conde, "Operation of gas proportional scintillation counters in a low charge multiplication regime", Nucl. Instr. and Methods A422, pp. 321-325, 1999.

[III.36] F.I.G.M. Borges, J.M.F. dos Santos, S. Kubota and C.A.N. Conde, "Electroluminescence yield for λ>165 nm in neon-xenon mixtures: experimental results", IEEE Trans. Nucl. Sci. 44(3), pp. 464-467., 1997.

[III.37] C.M.B. Monteiro, J.F.C.A. Veloso, J.M.F. dos Santos and C.A.N. Conde, "The performance of the GPSC/MSGC hybrid detector with Argon-Xenon gas mixtures", IEEE Trans. Nucl. Sci. 49(3), pp. 907-911, 2002.

[III.38] G.R. Carruthers, "Magnetically focused electronographic image converters for space astronomy applications", Applied Optics 8-3, pp. 633-638, 1969.

[III.39] E.P. Lima, M. Salete S.C.P. Leite, M.A.F. Alves, and A.J.P.L. Policarpo "Fano factors of rare gases and their mixtures", Nucl. Instr. and Methods 192, pp. 575-581, 1982.

[III.40] T.Z. Kowalski, A. Smith, and A. Peacock, "Fano factor implications from gas scintillation proportional counter measurements", Nucl. Instr. and Meth. Phys. Res. A279, pp. 567-572, 1989.

[III.41] T.H.V.T. Dias, F.P. Santos, P.J.B.M. Rachinhas, F.I.G.M. Borges, J.M.F. dos Santos and C.A.N. Conde, "Xenon-neon gas proportional scintillation counters: experimental and simulation results", J. Appl. Phys. 85(9), pp. 6303-6312, 1999.

[III.42] F.P. Santos, T.H.V.T. Dias, P J.B.M. Rachinhas, C.A.N. Conde and A.D. Stauffer, "Monte Carlo simulation study of the Fano factor, w-value, and energy resolution for the absorption of soft x rays in xenon-neon gas mixtures" J. Appl. Phys. 89(12), pp. 8202-8213, 2001.

[III.43] R.Z. Fuzesy, J. Jaros, L. Kaufman, J. Marrimer, S. Parker, V. Perez-Mendez and S. Redner, "A gas mixture for multi-wire chambers with high proportional gains", Nucl. Instr. and Methods 100, pp. 267-268, 1972.

[III.44] G.D. Alkhazov, A.P. Komar and A.A. Vorob´ev, "Ionization fluctuations and resolution of ionization chambers and semiconductor detectors", Nucl. Instr. and Methods 48, pp. 1-12, 1967.

[III.45] A. Hashiba, K. Masuda, T. Doke, T. Takahashi and Y. Fujita, "Fano factor in gaseous argon measured by the proportional scintillation method", Nucl. Instr. and Meth. Phys. Res. 227, pp. 305-310, 1984.

[III.46] F.I.G.M. Borges, J.M.F. dos Santos, S. Kubota and C.A.N. Conde, "Light yield and Fano factor in xenon gas proportional scintillation counters", Proceedings of SPIE – The International Society for Optical Engineering, "EUV, X-Ray and gamma ray instrumentation for astronomy VII" 2808, pp. 613-616, 1996.

[III.47] T.H.V.T. Dias, F.P. Santos, A.D. Stauffer and C.A.N. Conde, "Monte-Carlo simulation of X-ray absorption and electron drift in gaseous Xenon", Phys. Rev. A48(4), pp. 2887-2902, 1993.

[III.48] C.M.B. Monteiro, J.A.M. Lopes, P.C.P.S. Simões, J.M.F. dos Santos and C.A.N. Conde, "An argon gas proportional scintillation counter with UV avalanche photodiode scintillation readout", IEEE Trans. Nucl. Sci. 48(4), pp. 1081-1086, 2001.

[III.49]   M. Kase, T. Akioka, H. Mamyoda, J. Kikuchi and T. Doke, "Fano factor in pure Argon", Nucl. Instr. and Methods 227, pp. 311-317, 1984.

[III.50]   A.P. Komar, A.A. Borob´ev and V.A. Korolev, "Measurement of the ionization fluctuations produced by α particles in argon", Soviet Phys.-Doklady 6(2), pp. 131-133, 1961.

[III.51]   M.A. Prasad and K. Unnikrishnan, "Statistical distribuition of ionization yields in gases from electron irradiation", Phys. Rev. A23(4), pp. 2082-2084, 1981.

[III.52]   K. Unnikrishnan and M. A. Prasad, "Energy deposition by electrons in Argon", Radiation Research 80(2), pp. 225-232, 1979.

[III.53]   G.D. Alkhazov, "Ionization fluctuations in gases", Soviet Phys.-Tecnhical Phys. 16(9), pp. 1540-1546, 1972.

[III.54]   D.F. Anderson, T.T. Hamilton, W.H.-M. Ku and R. Novick, "A large area gas scintillation proportional counter", Nucl. Instr. and Methods 163, pp. 125-134, 1979.

[III.55]   A.J.P.L. Policarpo, M.A.F. Alves, M. Salete S.C.P. Leite and M.C.M. dos Santos, "Detection of soft X--rays with a xenon proportional scintillation counter", Nucl. Instr. and Methods 118, pp. 221-226, 1974.

[III.56]   N. Ishida, J. Kikuchi and T. Doke, "Fano factor in xenon", Phys. Rev. A46(3), pp. 1676-1679, 1992.

[III.57]   M.M.F. Ribeirete, A.J.P.L. Policarpo, M. Salete S.C.P. Leite, M.A.F. Alves and E.P. Lima, "Fano factors of Krypton-xenon mixtures", Nucl. Instr. and Methods 214, pp. 561-563, 1983.

[III.58]   Dayashankar and K. Unnikrishnan, "Ionization yield fluctuations in xenon due to energy degradation of electrons", Phys. Letters A99(2-3), pp. 81-83, 1983.

[III.59]   J.A.M. Lopes, J.M.F. dos Santos, R.E. Morgado and C.A.N. Conde, "A xenon gas proportional scintillation counter with UV-sensitive large area avalanche photodiode", IEEE Trans. Nucl. Sci. 48(3), pp. 312-319, 2001.

[III.60]   R.M. Keyser, "Characterization of room temperature detectors using the proposed IEEE standard", Ortec, Oak Ridge. (Available in *http://www.ortec-online.com/papers/roomtemp_det.pdf*)].

[III.61]   T.H.V.T. Dias, J.M.F. dos Santos, J.P.B.M. Rachinhas, F.P. Santos, C.A.N. Conde, and A.D. Stauffer, "Full-energy absorption of X-ray energies near the Xe L- and K-photoionization thresholds in xenon gas detectors: simulation and experimental results". J. Appl. Phys. 82(6), pp. 2742-2753, 1997.

[III.62]   http://www.csrri.iit.edu/periodic-table.html

[III.63]   J.M.F. dos Santos, C.A.N. Conde and A.C.S.S.M. Bento, "The energy linearity of gaseous xenon radiation detectors for X-rays with energies between 2 and 60 keV: Experimental results", Nucl. Instr. and Methods A324, pp. 611-613, 1993.

[III.64]   F.I.G.M. Borges, T.H.V.T. Dias, F.P. Santos, P.J.B.M. Rachinhas, J.M.F. dos Santos and C.A.N. Conde, "An investigation of the M-discontinuities in the response of xenon gas detectors to X-rays in the 0.1-2 keV range", Nucl. Instr. and Meth. A505, pp. 242-246, 2003.

[III.65]   D. Nygren, "Optimal detectors for WIMP and 0-υ ββ searches: Identical high-pressure xenon gas TPCs?", Nucl. Instr. and Methods A581, pp. 632-642, 2007.

[III.66]   K. Saito, H. Tawara, T. Sanami, E. Shibamura and S. Sasaki, "Absolute number of scintillation photons emitted by alpha particles in rare gases", Trans. Nucl. Sci. 49(4), pp. 1674-1680, 2002.

[III.67]   M. Miyajima S. Sasaki and E. Shibamura, "Absolute number of photons produced by alpha-particles in liquid and gaseous xenon", Nucl. Instr. and Methods B63, pp. 297-308, 1992.

[III.68]   A. Pansky, A. Breskin, A. Buzulutskov, R. Chechik, V. Elkind and J. Va'vra, "The scintillation of CF_4 and its relevance to detection science", Nucl. Instr. and Methods A354, pp. 262-269, 1995.

[III.69]   M. Suzuki and S. Kubota, "Mechanism of proportional scintillation in argon, krypton and xenon", Nucl. Instr. and Methods 164, pp. 197-199, 1979.

[III.70]   S. Kobayashi, N. Hasebe, T. Igarashi, M.-N. Kobayashi, T. Miyachi, M. Miyajima, H. Okada, O. Okudaira, C. Tezuka, E. Yokoyama, T. Doke, E. Shibamura, V.V. Dmitrenko, S.E. Ulin and K.F. Vlasik, "Scintillation luminescence for high-pressure xenon gas", Nucl. Instr. and Methods A531, pp. 327-332, 2004.

[III.71]   E. Aprile, A.E. Bolotnikov, A.I. Bolozdynya, T. Doke, *Noble gas detectors*, Wiley-VCH Verlag GmbH & Co. KGaA, Weinheim, 2006.

[III.72]   T. Doke, K. Masuda and E. Shibamura, "Estimation of absolute photon yields in liquid argon and xenon for relativistic (1 MeV) electrons", Nucl. Instr. and Methods A291, pp. 617-620, 1990.

[III.73]   T. Meinschad, L. Ropelewski and F. Sauli, "Detection of primary and field-enhanced scintillation in xenon with a CsI-coated GEM detector", Nucl. Instr. and Methods A547, pp. 342-345, 2005.

[III.74]   A. Parsons, T.K. Edberg, B. Sadoulet, S. Weiss, J. Wilkerson, K. Hurley, R.P. Lin and G. Smith, "High pressure gas scintillation drift chambers with wave-shifter fiber readout", IEEE Trans. Nucl. Sci. 37, pp. 541, 1990.

[III.75]   L. Periale, V. Peskov, C. Iacobaeus, T. Francke, B. Lund-Jensen, N. Pavlopoulos, P. Picchi and F. Pietropaolo, "The development of gaseous detectors with solid photocathodes for low-temperature applications", Nucl. Instr. and Methods A535, pp. 517-522, 2004.

[III.76]   V. Chepel, M.I. Lopes, V. Solovov, "Primary scintillation yield and α/β ratio in liquid xenon", Radiation Physics and Chemistry 74, pp. 160-167, 2005.

[III.77]   Y.K. Akimov, "Scintillations of noble gases and their applications (Review)", Instruments and Experimental Techniques 41, pp. 1, 1998.

[III.78]   http://physics.nist.gov/PhysRefData/Xcom/html/xcom1.html

[III.79]   J.L. Pack, R.E. Voshall, A.V. Phelps and L.E. Kline, "Longitudinal electron diffusion coefficients in gases: noble gases", J. Appl. Phys. 71, pp. 5363-5371, 1992.

[III.80]   F.I.G.M. Borges and C.A.N. Conde, "Electron transport and grid transmission in noble gas radiation detectors", Proceedings of the *Symposium on Atomic, Surface and Cluster Physics* – SASP1994, pp. 436-437, 1994.

[III.81]   C.A.N. Conde, L.F.R. Ferreira, and M.F.A. Ferreira, "Secondary scintillation output of xenon in a uniform field gas proportional scintillation counter", IEEE Trans. Nucl. Sci. 24, pp. 221-224, 1977.

[III.82]   F.P. Santos, T.H.V.T. Dias, A.D. Stauffer and C.A.N. Conde, "Three-dimensional Monte Carlo calculation of the VUV electroluminescence and other electron transport parameters in xenon", J. Phys. D: Appl. Phys 27, pp. 42-48, 1994.

[III.83]   C.M.B. Monteiro, L.M.P. Fernandes, J.A.M. Lopes, L.C.C. Coelho, J.F.C.A. Veloso, J.M.F. dos Santos, K. Giboni and E. Aprile, "Secondary scintillation yield in pure xenon", JINST 2, P05001, 2007.

[III.84]   F.L.R. Vinagre and C.A.N. Conde, "A technique for the absolute measurement of the *w*-value for X-rays in counting gases", Nucl. Instr. and Methods A450, pp. 365-372, 2000.

– CHAPTER IV –

PIXE STUDIES

The first PIXE experiments that we performed were conducted by bombarding several samples with protons in the 10-45 keV energy range. These intended to guarantee that our experimental set-up was working properly; regarding both the particle accelerator, the X-ray detection system and the data processing procedures. However, as explained in Chapter I, the data in the literature available for comparison is scarce or even inexistent for this low energy ion range, i.e. below 100 keV. Indeed, the works of Basbas *et al.* [IV.1], Szegedi *et al.* [IV.2] and Khan and Potter [IV.3], that present results for thick aluminium and/or copper targets irradiated with low energy protons down to 25, 40 and 60 keV respectively, are the few exceptions. Even so, the values presented in [IV.1] are not absolute X-ray yield measurements but results normalized to the value presented in [IV.3] for 100 keV protons.

We decided to irradiate aluminium targets first since this particular element is subject of study in these three works. Besides, aluminium has the advantage of being a conducting material and we also have the possibility of manufacturing extremely thin aluminium samples through vacuum evaporation techniques. Three distinct approaches can be applied experimentally to determine aluminium X-ray production cross-sections, each having naturally its own advantages and inconvenients over the others; namely:

    ✓ *Self-supporting thin target*: in this case, the incident ions go through a thin self-supporting specimen of known thickness. By thin we mean targets whose thickness is thin enough so that the bombarding ions only lose a

very small part of their initial energy in a way that the X-ray yield measured results from the interaction of ions with approximately constant energy.

✓ *Thin target upon a substrate*: the incident ions impinge on a thin specimen of known thickness which is deposited upon a thick substrate, usually made of a carbon based material in order to avoid simultaneously any unwanted characteristic X-rays from the backing material where the beam is dumped and an additional large amount of bremsstrahlung. This approach enables to irradiate thin targets which hold the thin target criterion but with much easier sample preparation procedures.

✓ *Thick target yield*: the impinging ions are totally slowed down and stopped in a thick specimen. The emitted X-rays consequently correspond to the interaction of the incident ions at different energies (integral from their initial impinging energy to 0) for which the X-ray production cross-sections are different.

Our first attempt in determining experimentally X-ray production cross-sections was through the irradiation of *self-supporting thin targets* of known thickness (section I.3.1) since this approach leads to more precise experimental results since the impinging ions keep, within good approximation, a constant energy while travelling through the sample. Moreover, corrections due to self-absorption effects are not needed since the emitted X-rays travel very small distances in the target before leaving the sample. Also, a reduced bremsstrahlung background is present in the PIXE spectra since no X-rays are originated from the interaction of the ions with the baking material. The ion beam, after crossing and interacting with the thin specimen, is dumped in a Faraday cup with a secondary electron suppressor (Figure II.18) where the ionic current is measured.

Nevertheless, this approach also presents experimental problems of great importance; namely the accurate knowledge of the specimen thicknesses and the difficult preparation and handling of such thin samples. For our particular application, this latter practical difficulty is even more severe due to the very low energy of the incident protons which implies the use of extremely thin films. For instance, the range of 50 keV protons in aluminium is about 500 nm and, if it is intended that the incident protons lose only 5 % of their initial energy, the maximum thickness of the film should be 40 nm [IV.4]. Of course, for lower energies, the targets will have to be even thinner. Despite the practical difficulties in the manufacture of such thin films, we prepared several films with thicknesses in the 40-300 nm range by vacuum evaporating high-purity aluminium onto glass plates covered by a thin layer of liquid soap. The thin evaporated specimens were then extracted away from the glass by submerging the aluminium coated glass plates in water and floating the thin films. The thin aluminium samples were then carefully deposited upon a Teflon support with a hole in the centre, which was covered by the thin target film and placed in the ion beam trajectory. The hole of this Teflon support is larger than the ion beam cross-section so that the ions interact only with the sample, being afterwards dumped in the Faraday cup. However, these thin targets did not stand irradiations for more than a few minutes before being destroyed, even for beams of

very low intensity. This was of course far from being enough to acquire PIXE spectra satisfactory from a statistical point of view. Besides, although we managed to handle samples with thicknesses down to only 40 nm, these were still too thick to hold the thin target criterion for protons of energy below 30 keV. Another important limitation we had when manufacturing these thin films was the difficulty in the accurate measurement of the specimen thicknesses, despite the use of a thickness meter during the vacuum evaporation.

In view of all these difficulties, we decided to try alternative approaches.

We then considered the irradiation of *thin targets upon a substrate*. These latter consist in thin targets of known thickness, also obtained by vacuum evaporation, but with the difference that the film target is evaporated on a thick backing material in which the ion beam is dumped. The measurement of the ion beam current is therefore performed on the bombarded target. This alternative avoids the severe practical difficulties concerning the specimen handling and allows the irradiation of these thin targets for much longer periods, but at the expense of a slight worsening of the sensitivity due to the presence in the PIXE spectrum of bremsstrahlung from the backing material where the beam is dumped. We prepared thin films by evaporating aluminium deposited upon carbon based substrates. This enabled us to prepare films with thickness down to 10 nm since no handling of the sample was necessary. However, the difficulty regarding the inaccuracy in the specimen thickness remained. Also, an additional issue appears due to the use of carbon based substrates since the current measurement can no longer be done in a Faraday cup below the target, such measurement being particularly complicated when irradiating insulating samples.

Since it is not possible to determine X-ray production cross-sections with accuracy without a precise knowledge of the thickness of the thin specimen irradiated, we could not proceed with any valid study with such targets. Considering these disadvantages, we decided to perform our studies using thick targets (section I.3.2). This decision has resulted in a much simpler target preparation, but however at the expense of a much more complex analytical data processing.

The irradiation of *thick targets* enables an indirect calculation of X-ray production cross-sections through the experimental determination of the *thick target yield curve*. In this case, the knowledge of the specimen thickness is no longer required and almost no sample preparation is necessary, avoiding so several practical difficulties. However, the energy of the impinging ions is no longer constant and the X-ray yield registered results from the interaction of protons with different energies. As explained in section I.3.2 (Equation I.6), the number of characteristic X-rays $N_{p,Z}$ of the p- (K-, L- or M-) X-ray line in the PIXE spectrum due to the irradiation of a thick target of atomic number Z_T is related to the X-ray production cross-section $\sigma_{p,Z}^{X}(E)$ through the following relationship:

$$N_{p,Z} \ = \ N_p \ \left(\Omega/4\pi\right) \ \epsilon_{p,Z} \ n \, \rho \int_0^{x_0} e^{-\mu \frac{\sin \theta}{\sin \varphi}(x_0 - x)} \ \sigma_{p,Z}^{X}(E) \ dx \qquad \text{(Eq. IV.1)}$$

where x is the beam direction, x_0 the range of the incident particles in the target in this direction, μ the target absorption coefficient for its own characteristic X-ray line, θ and φ the angles between the incident beam and the specimen surface and between the specimen surface and the detector axis direction respectively, ρ the density of the target, N_p the number of impinging protons, $\Omega/4\pi$ the solid angle subtended by the detector, $\epsilon_{p,Z}$ the detector efficiency for the considered p-line of the element Z (taken from data of Figure III.22) and n the number of target atoms per gram (which equals N_{AV}/A_Z where N_{AV} is Avogadro´s number).

The *thick target yield* $I_{p,Z}(x_0)$, defined as the number of X-rays produced in a thick target per impinging proton of initial energy E_0 with range x_0 [IV.1],[IV.5], is therefore related to the number of X-rays counts $N_{p,Z}$ in the PIXE spectrum through

$$I_{p,Z}(x_0) = \frac{N_{p,Z}}{N_p \left(\Omega/4\pi\right) \epsilon_{p,Z}} \quad = n\,\rho\, \int_0^{x_0} e^{-\mu\frac{\sin\theta}{\sin\varphi}(x_0-x)} \; \sigma_{p,Z}^X(E)\, dx \quad \text{(Eq. IV.2)}$$

It is possible to obtain an expression relating the X-ray production cross-section $\sigma_{p,Z}^X(E)$ and the thick target yield $I_{p,Z}(x_0)$ by differentiating Equation IV.2 using the following relationship

$$\frac{d}{d\lambda}\left[\int_{u(\lambda)}^{v(\lambda)} f(x,\lambda)\, dx\right] = \int_{u(\lambda)}^{v(\lambda)} \frac{\partial}{\partial\lambda}\left(f(x,\lambda)\right) dx \quad + f(v,\lambda)\frac{dv}{d\lambda} \; - f(u,\lambda)\frac{du}{d\lambda}$$
$$\text{(Eq. IV.3)}$$

For $\varphi = \theta$, we obtained:

$$\sigma\left[E(x)\right] = \frac{1}{n\rho}\left[\frac{dI_{p,Z}}{dx} + \mu\, I_{p,Z}(E(x))\right] = \frac{1}{n}\left[\frac{dI_{p,Z}}{dE}\frac{dE}{d(\rho x)} + \frac{\mu}{\rho} I_{p,Z}(E(x))\right]$$
$$\text{(Eq. IV.4)}$$

and consequently,

$$\sigma\left[E\right] = \frac{1}{n}\left[\frac{dI_{p,Z}}{dE} S(E) + \frac{\mu}{\rho} I_{p,Z}(E)\right] \qquad \text{(Eq. IV.5)}$$

where $S(E)$ is the target stopping power at energy E (in keV cm^2/g).

Equation IV.5 shows that X-ray production cross-sections can be calculated, given the value and the slope of the thick target yield function $I_{p,Z}(E)$. The value of $dI_{p,Z}/dE$ is obtained analytically through the fit of the experimentally obtained thick target yield curve $I_{p,Z}$ as a function of the incident ion energy E_p, as explained in [IV.1],[IV.5].

We registered PIXE spectra with the developed GPSC by bombarding an aluminium thick target, 31 mm in diameter (shown in Figure II.15). The sample was

irradiated by protons with energy in the 10-45 keV range and the determination of the integrated charge was performed through the measurement of the ion beam current directly on the bombarded sample. This was made by isolating electrically the target and by connecting it to an electrometer through one of the feedthroughs placed in the bottom flange of the reaction chamber (Figure II.19). A typical PIXE spectrum is presented in Figure IV.1 for a thick aluminium sample bombarded by 40 keV protons.
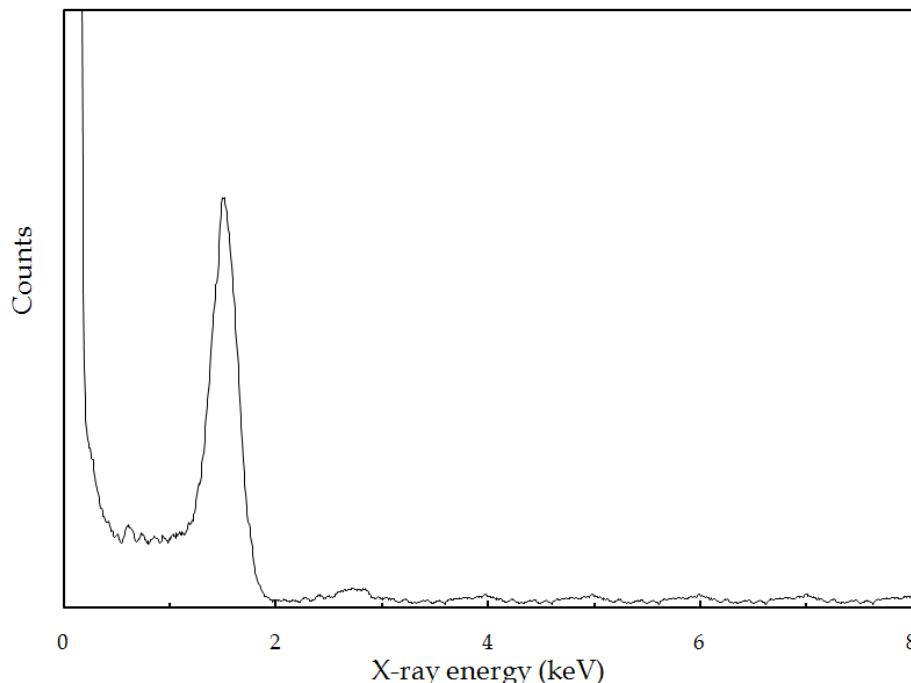

Figure IV.1 – PIXE spectrum obtained by irradiating an aluminium thick target with 40 keV protons.

Our decision of irradiating aluminium targets is not only due to the fact that this particular element is one of the few for which there is published data in the literature for such low velocity protons, but it is also because this particular element seems to be a good compromise between the difficulty in detecting the soft X-rays from lighter elements, i.e. below 1 keV, and the difficulty in obtaining relevant X-ray yields from heavier elements for which the X-ray production cross-section decreases considerably.

Besides, aluminium is a conducting material, which is another important advantage since we observed that the irradiation of insulated targets (either insulating materials or properly insulated conducting samples) leads to considerable changes in the PIXE spectra. As illustrated in Figure IV.2, the irradiation of non-conducting targets leads to PIXE spectra that present considerably higher X-ray yields and bremsstrahlung per integrated charge unit, resulting in much worse signal-to-noise ratios. This phenomenon is in agreement with observations related in [IV.6] and is due to the fact that the target becomes highly positively charged due to the ion bombardment, as already referred in Chapter I.
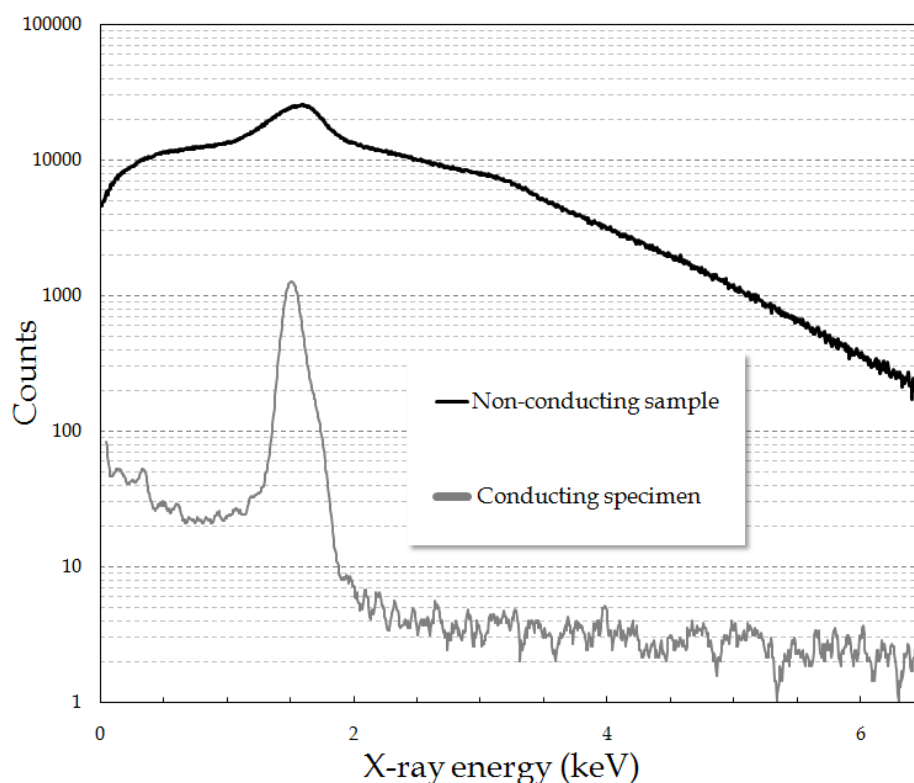
Figure IV.2 – Spectra from a thick aluminium target bombarded with 40 keV protons, with a total integrated charge of 70 μC in both cases, with and without electrical contact established between the sample and ground potential.

Additionally, by examining the GPSC output signal with an oscilloscope during the irradiation of non-conducting targets with a constant proton beam current, we observed that the X-ray counting rate registered by the GPSC is not constant. Indeed, it varies periodically, increasing massively first until it suddenly returns to its original state. This effect occurs because of the build-up of the electric potential of the target due to the accumulation of beam charge, followed by a rapid discharge that releases a flux of energetic electrons through the sample material. During charge build-up, electrons in the vicinity of the target (both secondary electrons from the sample irradiated and electrons from the residual gas) are accelerated towards the highly positively charged target. These energetic electrons hit the target, producing X-rays with enhanced yields observed in the same way as electron excitation leads to X-rays in the EPMA technique (as referred in Chapter I, the X-ray production cross-sections for electrons of tens of keV are similar to the ones for MeV protons). This effect has been reported through the years in the work of Pillay and Peisach [IV.7]-[IV.9] who not only observed this phenomenon, which they named CHarge-Induced X-ray fluorescence (CHIX), but also carried out several studies in order to get a better understanding of it. In one of these studies, they recorded time-resolved spectra to monitor the X-ray yield and showed that the discharges produced in non-conducting targets can be recognized by a periodic increase in X-ray counting rate [IV.10]. These observations are in agreement with the effect we observed.

Although the CHIX enhanced X-ray yield is not significant for impinging ions with energy higher than 1 MeV since the relevant X-ray production cross-sections for PIXE are particularly large for such energetic ions, i.e. about 1-100 barn, this effect

was shown to be particularly relevant with low energy ions [IV.8], i.e. when considering an energy range where ion induced X-ray production cross-sections are considerably low (10^{-2}-10^{-5} barn). Indeed, since this enhanced CHIX X-ray yield remains relatively constant with low-energy ions while the relevant PIXE contribution falls considerably with decreasing energy of the incident particles, the CHIX contribution to the X-ray yield increases dramatically becoming by far the dominant effect at low ion energies in insulating targets [IV.8]. This behaviour at low ion energies therefore explains the enormous differences we observed between the PIXE spectra of insulated and conducting samples bombarded with 40 keV protons (Figure IV.2).

We point out that CHIX is a strong alternative to PIXE regarding PIXE-induced XRF (XSQR) studies since large X-ray fluxes are obtained even with low beam currents [IV.9],[IV.11].

IV.1 MEASUREMENT OF THE BEAM CURRENT

Even when irradiating conducting samples for which the CHIX effect does not occur, great care has to be taken to measure accurately the integrated beam charge. Indeed, secondary electrons resulting from the beam interaction with the target can escape the bombarded sample leading to an additional false positive current and hence to an overestimate of the integrated charge. Therefore systematic errors in the observed X-ray yield per unit charge will appear if suppression of these secondary electrons is not made. The release of these secondary electrons can be minimized by inserting a negatively biased grid in front of the target, as shown in Figure II.19.

We studied the dependence of the measured current, I_{MES}, with the negative voltage applied to the grid, V_G, concluding that it decreases as V_G increases in absolute value, reaching a constant value, I_{ION}, which is the current due to the charge of the ions in the beam only, i.e. when there are no secondary electrons leaving the sample. In Figure IV.3, we present the ratio between I_{MES} and I_{ION} as a function of absolute value of V_G for different H_2 pressures and it can be seen that, in all cases, this ratio drops to one as $-V_G$ increases. Moreover, Figure IV.3 shows that the escape of the secondary electrons increases with increasing H_2 pressures. This can be explained by the fact that the number of molecules in the vicinity of the target increases for higher residual pressures, making the interaction of the secondary electrons with the gas molecules and therefore their escape from the target easier. On the contrary, no dependence of I_{MES} with the energy E_p of the impinging protons was observed. Moreover, irradiations of targets of different elements have showed that the dependence of the ratio I_{MES}/I_{ION} with $-V_G$ varies among the elements as it can be seen in Figure IV.4; confirming the observations described by Traxel and Mandel in [IV.12].

We also confirmed that the value of V_G does not influence the number of X-rays events registered in the PIXE spectra as long as the parameters of the ion source remain constant.
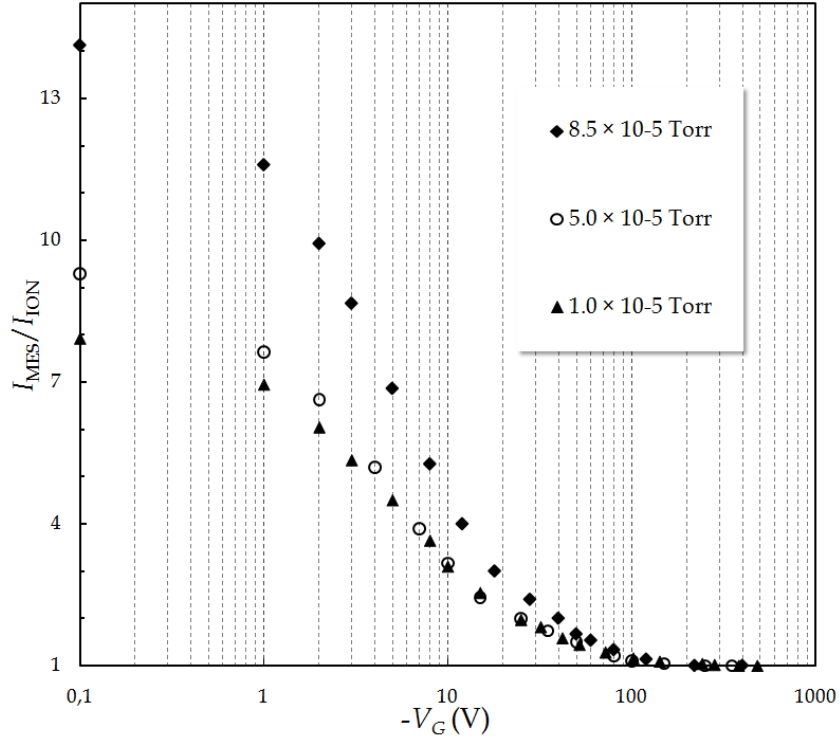
Figure IV.3 – Ratio between the measured current I_{MES} and the actual proton current $I_{ION,}$ obtained by suppression of the secondary electrons, in a copper target irradiated by 35 keV protons as a function of the voltage V_G applied to the secondary electron suppressor grid for several H_2 pressures inside the reaction chamber.

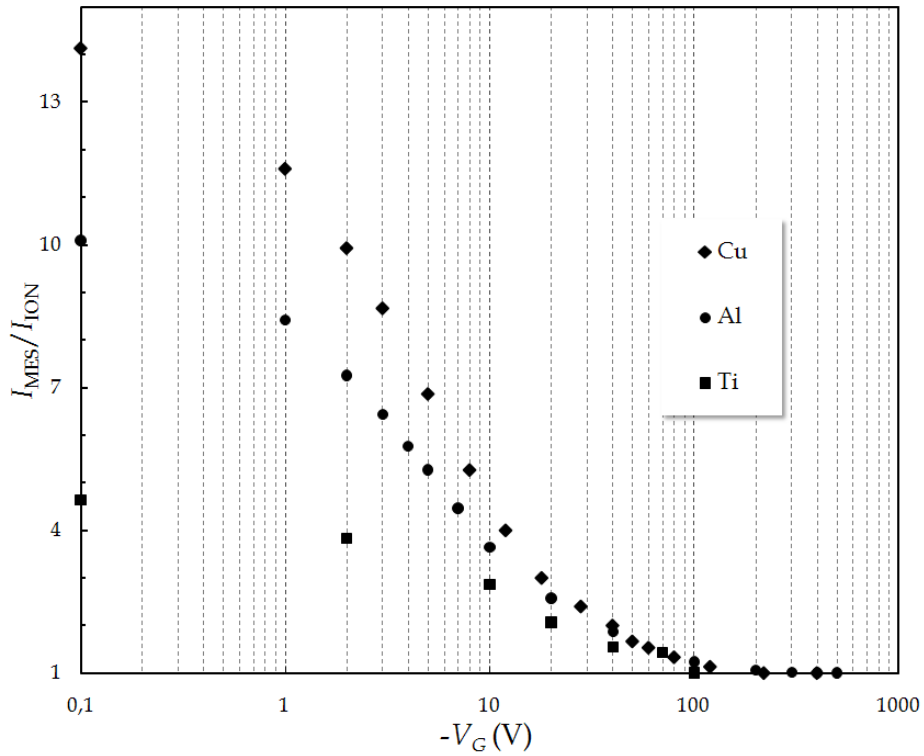Figure IV.4 – Ratio between the measured current I_{MES} and the actual proton current I_{ION}, obtained by suppression of the secondary electrons, in a aluminium (●), titanium (■) and copper (♦) thick targets irradiated by 35 keV protons as a function of the voltage V_G applied to the secondary electron suppressor grid. The residual pressure inside the reaction chamber was 8.0×10^{-5} Torr.

IV.2 INFLUENCE OF THE RESIDUAL HYDROGEN PRESSURE

We also considered the influence of the residual H_2 pressure in the reaction chamber on the performance of the PIXE set-up because we observed that the vacuum in the reaction chamber increases massively from the moment the H_2 gas is injected into the ion source. This is due to the lack of a radiation window separating the ion source and the overall particle accelerator, including the reaction chamber, to guarantee the transmission of the low-energy protons (range of less than 500 nm in solids[IV.4]). A worsening of the residual vacuum from $2\text{-}3 \times 10^{-6}$ Torr up to the $10^{-4}\text{-}10^{-3}$ Torr range could be observed as the H_2 gas was inserted in the ion source. A mass spectrometer confirmed that this high residual pressure is mainly composed by hydrogen gas. This worsening of the vacuum in the reaction chamber is critical and inevitable in our particular case since we are forced to operate the ion source with high H_2 fluxes to maximize the intensity of the proton beams since the filament current I_F achievable in the ion source with the actual electronic module is limited (section II.1).

We also observed that, even keeping the proton current that impinges on a thick target constant, the residual H_2 pressure inside the chamber influences the number of X-ray counts recorded in the PIXE spectra. In addition to this unexpected effect, we also observed that, for large H_2 pressures inside the ion source, a "residual" current on the target, I_{RES}, was always measured even without having ions hitting it, i.e. when using the Wien filter to deviate all the possible ions from its exit collimator. Moreover, we also observed that this "residual current" I_{RES} originates X-rays characteristic of the target element. The results concerning the dependence of the X-ray counts with the residual pressure can be observed in Figure IV.5 where both total and residual counts obtained for an aluminium thick target irradiated with a constant proton beam current of 200 nA are presented. For each pressure, the number of counts originated by the proton beam alone is therefore the difference between the two bars.

In Figure IV.6, we present the ratio between the residual current and the current measured when protons bombard the target, I_{RES}/I_{MES}, also as a function of the residual pressure, concluding that this ratio also increases with pressure. From Figures IV.5 and IV.6 we can observe that both the residual X-ray counts and the residual current are a significant part of the total and that both increase with increasing H_2 pressures, becoming predominant in the total of counts registered. The same behaviour was observed for titanium and copper thick targets.

We believe that these unexpected phenomena can be explained by the collision of neutral atoms or molecules with the target, since it is possible to measure a "residual" current I_{RES} on target for high H_2 pressures even when the filter Wien is polarized to guarantee that all the possible ions are deviated from the target. Such neutral particles/molecules can be originated by the interaction of the protons produced in the ion source with the H_2 molecules eventually before entering the Wien filter. Indeed, collisions of protons with H_2 molecules leading to fast neutral hydrogen atoms have cross-sections up 10^{-15} cm^2 range for protons energies with energy in the 1-50 keV

range [IV.13], showing that this interaction is likely to occur at pressures above about 10^{-6}-10^{-5} Torr. Such deterioration of the ion beam with poor vacuums has already been described in [IV.14], where the degradation of proton beams is shown to occur in poor vacuum conditions. Besides, Figure IV.6 shows that the behaviour is the same for all the targets used, confirming therefore that this phenomenon is due only to the higher H_2 concentration in both the accelerator tube and reaction chamber.

The "residual" current I_{RES} measured therefore can eventually correspond mainly to the escape of secondary electrons form the target when this latter is hit by those fast neutral atoms. This hypothesis was confirmed increasing the negative voltage V_G of the secondary electron suppressor ring. For high values of V_G, the measured current dropped to zero showing that the "residual" current is indeed due to secondary electrons that leave the target.

Since we are interested in determining the X-ray yield for protons, we must remove the contributions of both the "residual" measured X-ray counts and current once we have concluded that these are not due to protons. With this in mind we defined an "effective" X-ray yield as the number of X-ray counts in each spectrum due to the proton beam, obtained from the difference between measured and residual counts, divided by the current due to protons which is also the difference between the measured and residual currents. This effective X-ray yield is represented in Figure IV.7 for a titanium thick target and we can observe that this effective yield also increases with the increase of H_2 pressure in the reaction chamber, indicating eventually that the proton beam is also perturbed by the increase of H_2 in its path towards the target.

Consequently, it is clear that the PIXE spectra have to be acquired with minimal residual H_2 pressure. However, on the other hand, the limitation in the maximum current available in ion source filament with the existing electronic module forces us to use high values of H_2 pressure within the ion source to obtain acceptable proton currents on target. Due to these limitations we expect to register X-ray yields somewhat larger than the expected ones due to the unavoidable contribution of this competitive process to the PIXE spectra (Figure IV.7). This residual contribution can be reduced if the gas evacuation in the reaction chamber during irradiations is improved or else if the current in the ion source filament, I_F, could be increased.

However we should point out that independently of the operating H_2 pressure we still observed that the number of recorded counts in the PIXE spectrum varies linearly with the integrated charge, as expected.
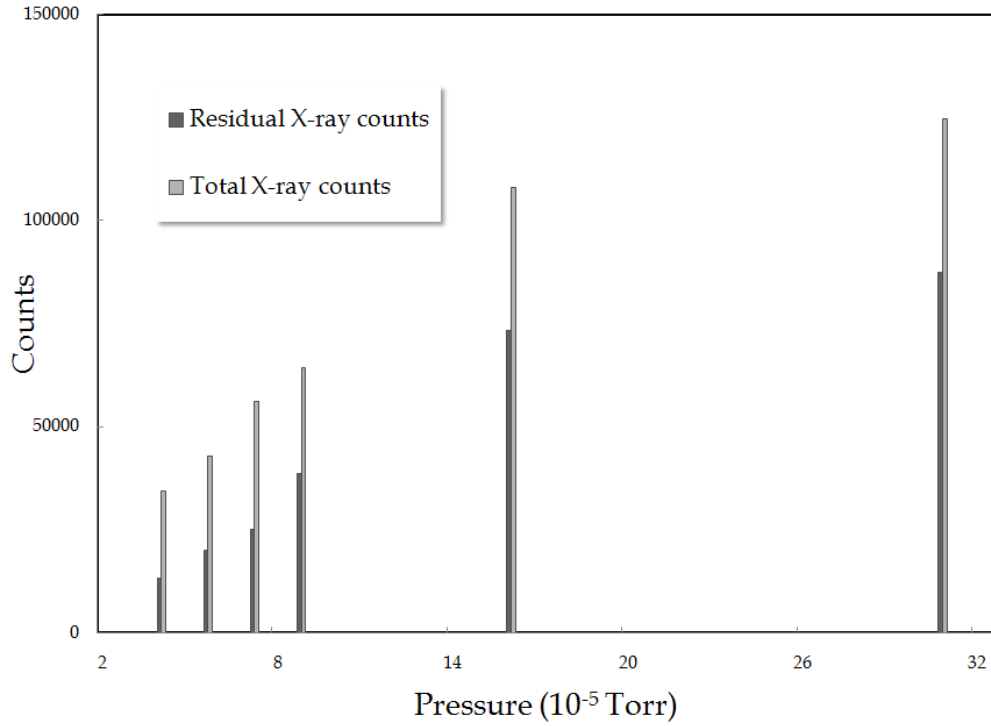
Figure IV.5 – "Total" and "Residual" X-ray yields from an Aluminium thick target irradiated by 35 keV protons with a constant current of 200 nA as a function of the residual H_2 pressure during irradiation. The error in the presented X-ray yields is of 5 %.
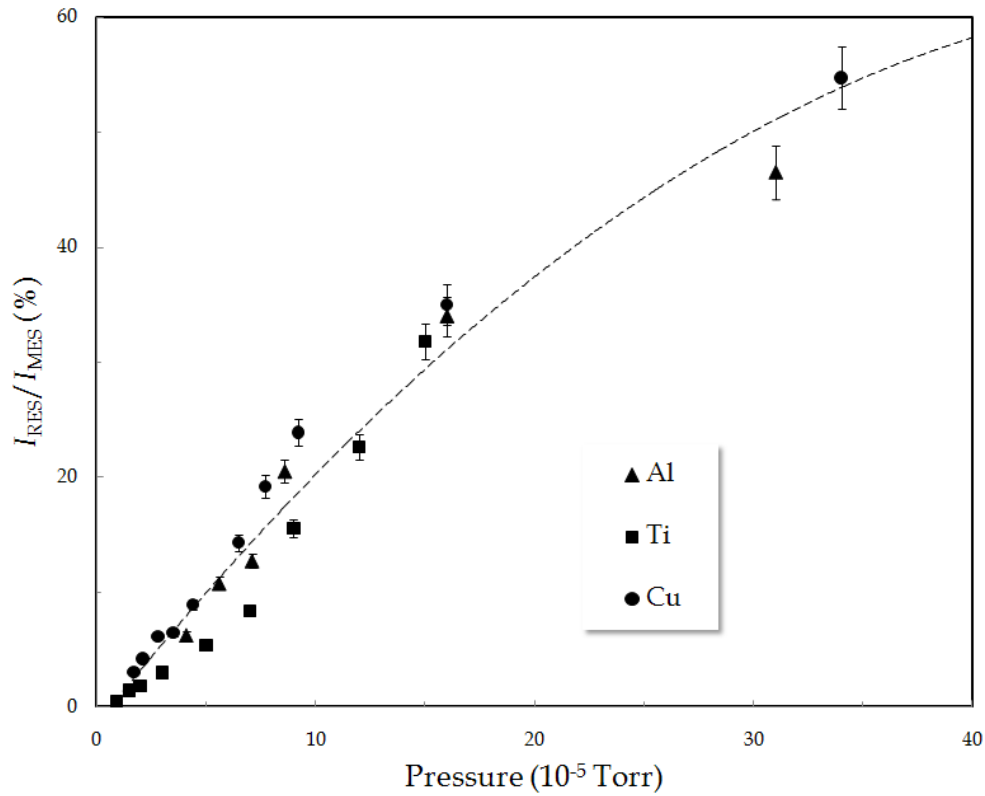

Figure IV.6 – Ratio I_{RES}/I_{MES} of the residual current I_{RES} to the measured one I_{MES} with the Wien filter set to let proton go through it, for Aluminium (▲), Titanium (■) and Copper (●) thick targets irradiated by 35 keV protons as a function of the residual H_2 pressure. The curve is only guide for the eyes.
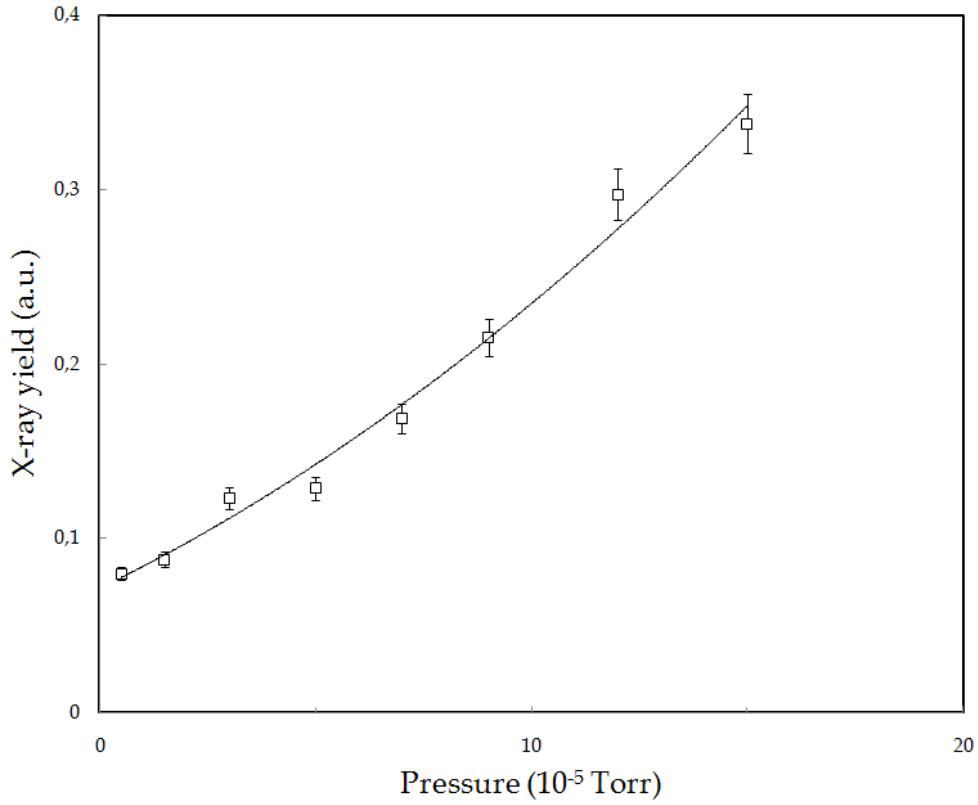
Figure IV.7 – "Effective" X-ray yield for a Titanium thick target irradiated by 35 keV protons as a function of the residual H_2 pressure. The curve is only guide for the eyes.

IV.3 THICK TARGET YIELD CURVE AND DEDUCED X-RAY PRODUCTION CROSS-SECTIONS

After having observed the behaviour of the experimental set-up and having optimized it regarding both the voltage V_G and the operating H_2 pressure, we registered PIXE spectra while bombarding the aluminium thick target with protons of energy E_p in the 10-45 keV range with a step of 5 keV in order to obtain the thick target X-ray yield curve $I(E_p)$ for the K-line of aluminium.

As already referred, the X-ray yield $I(E_p)$ at a given energy E_p, is defined as the number of characteristic X-ray events, N, originated due to the impact of a proton of energy E_p on the target. N is also related to the number of X-ray events registered by the radiation detector used through Equation IV.2, this latter being the number of counts in the peak of the pulse-height distribution obtained for the aluminium K-line. With this purpose, the pulse-height distributions registered were fitted to gaussian functions superimposed on a linear background. $I(E_p)$ was then determined using Equation IV.2, where the integrated charge was obtained through the measurement of the proton current with an electrometer connected to the target, the solid-angle Ω subtended by

the GPSC was calculated to be 0.0188 sr and its detection efficiency for the aluminium K_a line was calculated 0.45.

The results for the thick target yields $I(E_p)$ obtained for aluminium bombarded with protons of energy E_p in the 10-45 keV range are presented in Table IV.1 and Figure IV.8. We have also included in Figure IV.8 the published data from [IV.3] for comparison. We have estimated the error in the number N of counts in the peak to be of ±1% because of the low statistic of the recorded spectra and the error in the integrated charge to be ±5 % due to the difficulties encountered in maintaining a fixed impinging current during the long acquisition times. The error in the calculated X-ray yields $I(E_p)$ was estimated through the error propagation formula (Table IV.1).

Figure IV.8 shows that our experimentally obtained X-ray yields $I(E_p)$ are in good agreement with the results from [IV.3]. Concerning the dependence of the X-ray yield curve with the energy of the impinging protons E_p, Figure IV.8 shows that this latter is qualitatively satisfactory although we have to point out that the X-ray yields registered for proton energies higher than 25 keV seem to present a lower increase than expected. We attributed this phenomenon to the deterioration of the proton beam due to the poor vacuum which leads, as described in [IV.14], to protons with lower energies than expected. Indeed, as the proton energy increases, the cross-sections involved in the H^+-H_2 interactions also increase, allowing the protons to lose a fraction of their energy and to therefore originate lower X-ray yields. For this reason, when we fitted the $I(E_p)$ points obtained experimentally to a curve of the power type we have only considered the $I(E_p)$ points for E_p below 25 keV. As a result, X-ray production cross-sections were determined only for protons energies lower than 25 keV (Table IV.1 and Figure IV.9).

As it can be observed in Figure IV.8, there is a relatively good agreement between the general trend exhibited by the $I(E_p)$ curve and the published data from Khan and Potter [IV.3]. Such behaviour shows that the experimental system is working correctly although quantitative measurements may present the small discrepancies as long as the referred limitation remains. As already mentioned, the limitation regarding the residual H_2 pressure might be at the origin of larger X-ray yields than expected (Figure IV.7). Indeed, an improved (i.e. lower) operating H_2 pressure might lead to lower X-ray yields which would be in better agreement with the few data available in the literature [IV.1]. Consequently, the slopes of the $I(E_p)$ curve that we calculated are expected to be somewhat larger than they should, leading therefore inevitably to larger X-ray production cross-sections σ_X than expected.

TABLE IV.1

ALUMINIUM THICK TARGET YIELD TABLE

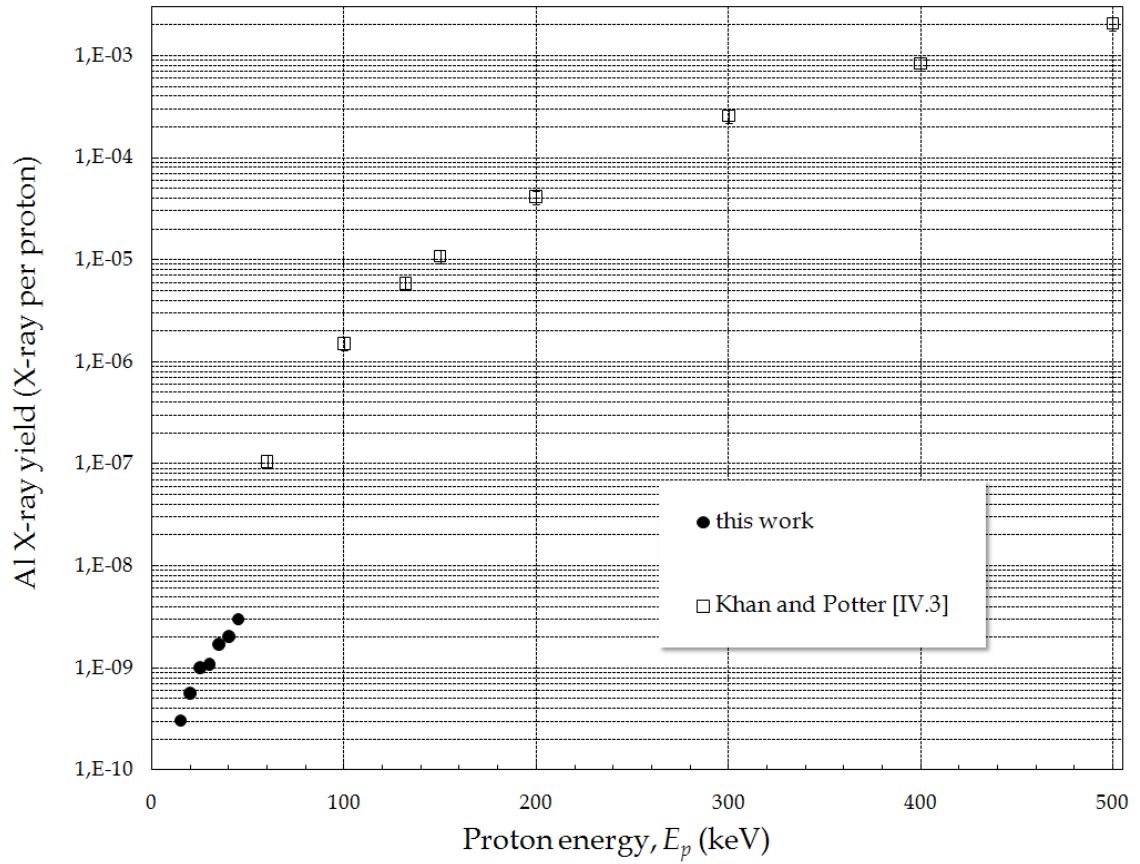| Proton energy E_p (keV)	Al thick target X-ray yield		$S(E_p)$ [IV.15] (10^5 keV cm²/g) $\pm$ 10 %	dI/dE_p (X-ray/proton keV) $\pm$ 40 %	$\sigma_X (E_p)$ (barn) $\pm$ 40 %
	$I(E_p)$ (X-ray/proton)	$I_{fit}(E_p)$ (X-ray/proton)			
15	$(3.06 \pm 0.16) \times 10^{-10}$	2.99×10^{-10}	3.483	5.36×10^{-11}	8.43×10^{-4}
20	$(5.62 \pm 0.29) \times 10^{-10}$	5.88×10^{-10}	3.867	7.44×10^{-11}	1.30×10^{-3}
25	$(1.01 \pm 0.05) \times 10^{-9}$	0.98×10^{-9}	4.157	9.60×10^{-11}	1.81×10^{-3}
30	$(1.09 \pm 0.06) \times 10^{-9}$	-	4.373	-	-
35	$(1.71 \pm 0.09) \times 10^{-9}$	-	4.529	-	-
40	$(2.02 \pm 0.10) \times 10^{-9}$	-	4.638	-	-
45	$(2.99 \pm 0.15) \times 10^{-9}$	-	4.709	-	-

Figure IV.8 – Thick target yield for aluminium K-characteristic X-rays as a function of the incident proton energy E_p. The error in the experimental points is inferior to the size of the dots.

Table IV.1 also lists the slopes of the thick target yield curve, dI/dE_p, for proton energies E_p below 25 keV. These were analytically calculated using the fitting to the thick target yield curve.

This fit was obtained by adjusting the experimentally obtained $I(E_p)$ values only for proton energies E_p of 15, 20 and 25 keV to a power curve of the $A(E_p\text{-}1.487)^B$ type for E_p higher than 1.487 keV since its corresponds to the energy of the K_α line from aluminium and no X-ray yield can consequently be obtained for lower energies, and where E_p is expressed in keV and A and B are constants.

The constants A and B were obtained through the least square method using the following method: a change of variable, from E_p to E_p' with $E_p' = E_p\text{-}1.487$, was made so that the fitting function becomes $I(E_p')=AE_p'^B$. Alternatively, we can also write that $ln(I(E_p')) = ln(A) + Bln(E_p')$. This way we have calculated the values of $ln(A)$ and B together with their errors by performing a linear regression on the $[ln(I(E_p')), ln(E_p')]$ values pairs. The values of $A = (1.14\pm0.43) \times 10^{-12}$ and $B = 2.14 \pm 0.13$ were obtained. We noticed that the errors in A and B are far from being negligible, but this is due to the fact that we are considering only three points to perform a fit to the $I(E_p)$ curve. Table IV.1 presents the fitted X-ray yields $I_{fit}(E_p)$ which differ by no more than 5 % from the measured yields $I(E_p)$. The slopes dI/dE_p', which equal the slopes dI/dE_p, are therefore given by $ABE_p'^{B\text{-}1}$. The error in dI/dE_p' was calculated through the error propagation formula and was shown to be not inferior to 40 % because of the relatively high errors obtained for A and B. These large errors in A and B are mainly due to the very low number of points available to the fitting, imposed by the already mentioned limitations of the experimental set-up.

Given the values of $I(E_p)$ and dI/dE_p for each energy E_p considered, we determined the corresponding K- X-ray production cross-sections for aluminium, σ_X, through Equation IV.5 and by using the stopping-power values from [IV.15]. The results are resumed in Table IV.1 and presented in Figure IV.9. The error in the cross-sections was calculated by considering both the referred errors in the X-ray yield and its slope (Table IV.1) and the error of the stopping-power values. Although this latter parameter is known with good accuracy for protons with MeV energy, the uncertainty increases up to 10 % for low energy particles.

As shown in Figure IV.9, there is a fairly good agreement between our experimentally obtained X-ray production cross-sections for aluminium and the trend of other reported data. The tendency to higher σ_X values than the reported data is explained as already mentioned by the higher X-ray yields we obtained.
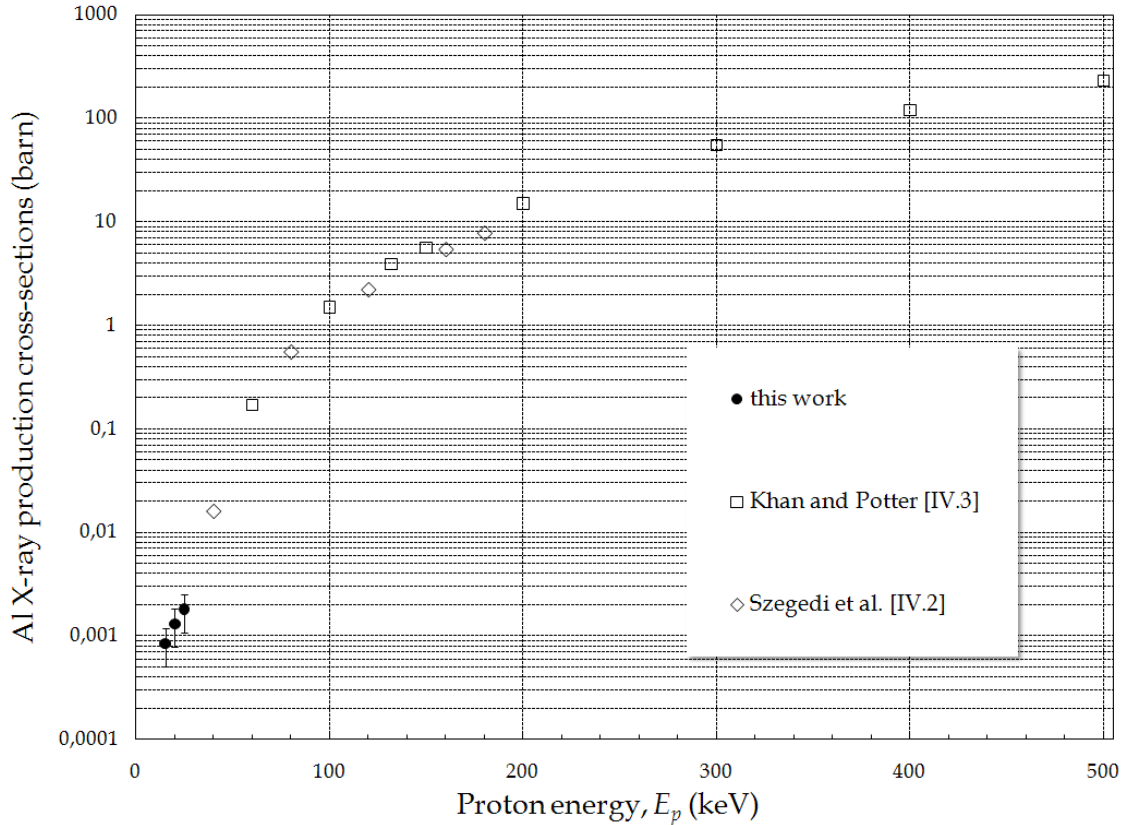
Figure IV.9 – X-ray production cross-sections for aluminium, obtained in this work (●) and by other authors (□ and ◊), as a function of the incident proton energy E_p.

Although these first results for an aluminium thick target were promising with the discrepancies obtained explained by the present limitations of the experimental set-up, the same quantitative agreement was not obtained for heavier elements, such as titanium or copper, so these results are not presented here. Indeed, although the general trend of the $I(E_p)$ curves obtained experimentally regarding their dependence with the energy of the impinging protons E_p was in agreement with published data, namely the fact that the increase of the X-ray yield with increasing energies E_p is more pronounced as the target atomic number Z_T increases (the X-ray yield increases with about E_p^4 for Z_T above 25 [IV.16]), the results obtained were quantitatively far from acceptable. Since the discrepancies observed between our results and the expected ones seem to increase with the target atomic number Z_T, we believe that some competitive process might be involved, whose cross-section depends strongly on Z_T. Studies at several residual H_2 pressures point to our limitations concerning the minimal H_2 operating pressure inside the reaction chamber to be at the origin of such discrepancies.

IV.4 FUTURE WORK

Although these first experimental results are promising, the referred limitations of the experimental set-up did not allow us to perform more accurate and reliable studies

with other elements and/or ions. Improvements in the experimental arrangement therefore appear to be fundamental to determine more accurate X-ray production cross-sections. Besides, there is also plenty of space for improvements that will allow the use of this experimental set-up to carry on studies distinct from PIXE. This section aims to present possible improvements that may be implemented and studies that can be made with this set-up.

The first measurements presented here have shown that it is fundamental to improve, i.e. decrease, the residual H_2 pressure during irradiations. Since no physical barrier can be placed between the ion source and the overall particle accelerator and the reaction chamber due to the reduced range of these low energy protons, the decrease of the pressure inside the system can be achieved by implementing two distint approaches. The first consists in placing a short flange immediately after the ion source and connecting it to an extra vacuum pump station. This additional vacuum system would have to be electrically isolated from the ion source since this latter would be at high voltage. Such improvement would enable the gas inserted into the ion source to be evacuated before entering the Wien filter, therefore avoiding any interaction of the protons with the residual gas molecules. Alternatively, a simple liquid nitrogen trap was shown to be a good alternative to complex vacuum systems. On the other hand, another way to decrease significantly the residual H_2 pressure is by reducing significantly the flux of H_2 gas needed by the ion source. This can be done by increasing the maximum current I_F delivered to the ion source filament by the electronic module since the module currently used is far from making full use of the capabilities of the ion source. This change would also lead to much shorter data acquisition times and enable the determination of even smaller X-ray production cross-sections, as it is the case for heavier elements, since much higher proton beam currents I_{ION} could be obtained on target. Both suggestions have the disadvantage of requiring massive interventions in the upper structure of the particle accelerator containing the ion source, the electronic modules and the batteries. However, the importance of these alterations and the resulting improvements we expect in the performance of the particle accelerator are enough to justify their implementation. In fact, none of these have been executed yet because of both the delay that such interventions would inevitably impose in the conclusions of this work and the high cost of the material needed to perform these changes. However, both improvements will be implemented in the near future.

As soon as these improvements are implemented, we expect the ion beam currents on target to increase significantly, making possible to obtain high ion beam currents even with severe beam collimation. As a result, the possibility of using this experimental arrangement to perform micro-PIXE analysis is under study. In this case, a motorized and vacuum-compatible scanning device will be necessary to scan the target under the beam. Moreover, software has to be developed in order to build 2D images containing multi-elemental concentration distributions from the recorded PIXE spectra.

As the irradiation of heavier elements involving much smaller X-ray production cross-sections will be possible with the expected significant increase in beam current, the need to detect X-rays with higher energy will appear. We are therefore also planning to install another X-ray detector in the reaction chamber. This detector, which may be either a conventional Si(Li) detector or another GPSC, optimized for the detection of harder X-rays up to 100 keV, may be placed in direct contact with the vacuum of the reaction chamber or else outside this latter by using an exit flange with a convenient radiation window.

Regarding the accelerating tube, we are also planning to add more insulated rings and to improve their electrical isolation in order to bias it with voltages up to about 100-200 keV. The resulting more energetic ions would allow the determination of X-ray production cross-sections for heavier target elements, and in particular the detection of the L- soft X-ray lines from medium and heavy elements with the developed GPSC since these are not detected with conventional Si(Li) detectors. This improvement in the energy of the incident ions would also allow the use of self-supporting thin specimens since the minimum thickness necessary to hold the thin target criterion would then increase significantly, leading to samples with sufficient mechanical strength to stand both handling and irradiation. Moreover, such more energetic ions would also make possible the use of this particle accelerator to perform thickness measurements. Finally, this latter improvement is of particular importance to use this particle accelerator as a nuclear-microprobe since it would enable depth profiling studies of the target by varying the range of the ions, i.e. E_p [IV.17].

Another field particularly interesting to explore is the use of this particle accelerator to induce and study low-energy nuclear reactions. Indeed, as higher voltages of at least 150 keV can be applied to the accelerating tube, it is possible to induce several (p,γ) nuclear reactions [IV.18],[IV.19].

Although the sample holder device we built was appropriate to perform the studies presented here due to its versatility, this latter is not suitable for analyzing several specimens in sequence. We are considering using one of the lateral flanges of the reaction chamber (Figure II.3) to place a sample ladder, horizontally oriented, holding several samples at a time. This will be mounted onto a feedthrough with longitudinal movement in order to intercept the beam patch, rather than positioning the samples through the bottom feedthrough as we have done up to now. Such device will enable target exchange without breaking the vacuum, resulting so in considerable time savings. Additionally, we are planning to use at least one of the spots of this multi-specimen holder to place radioactive sources (properly shielded to guarantee that these do not interfere during the acquisition of the spectra) in order to calibrate the X-ray detector without breaking the vacuum.

After the implementation of these improvements, we are also planning to acquire PIXE spectra by irradiating targets with other ions; namely from deuterium or helium and eventually determining X-ray production cross-sections for these ions.

Finally, the ions produced in the present experimental set-up can also be used to perform XSQR (PIXE-induced XRF), i.e. to induce X-ray fluorescence (XRF), by irradiating non-conducting targets. Indeed, large fluxes of X-rays are easily generated through the referred CHIX phenomenon when rapid and simple Energy Dispersive X-Ray Fluorescence (EDXRF) studies are required.

As a result, it seems clear that these first experimental results represent only the beginning of a set of possible experiments using the set-up developed during the work reported here, and that much work can still be done with this particle accelerator especially if some improvements are implemented. Some of the suggestions presented here are already being implemented and the others are currently under study.

IV.5 REFERENCES

[IV.1]   G. Basbas, W. Brandt and R. Laubert, "Universal cross sections for L-shell ionization by heavy charged particles. I. Low particle velocities", Phys. Rev. A7, pp. 983-1001, 1973.

[IV.2]   S. Szegedi, P. Raics and M. Fayez-Hassan, "K X-ray production cross sections for 40-180 keV protons", Jour. Radioanal. Nucl. CHem. 260(2), pp. 429-433, 2004.

[IV.3]   J.M. Khan and D.L. Potter, "Characteristic K-shell X-ray production in Magnesium, Aluminium, and Copper by 60- to 500- keV protons", Phys. Rev. 133, pp. 890-894, 1964.

[IV.4]   http://physics.nist.gov/PhysRefData/Star/Text/programs.html.

[IV.5]   M. Rashiduzzaman Khan, D. Cumpton and P.E. Francois, "Proton-Induced X-ray production in titanium, nickel, copper, molybdenum and silver", J. Phys. B9, pp. 455-460, 1976.

[IV.6]   M. Ahlberg, G. Johansson and K. Malmqvist, "Elimination of charging in the proton-induced X-ray emission analysis of insulating samples", Nucl. Instr. and Methods 131, pp. 377-379, 1975.

[IV.7]   M. Peisach, A.E. Pillay and C.A. Pineda, "Enhanced X-ray yields in PIXE analysis of some binary metal fluorides", Nucl. Instr. and Methods B75, pp. 14-16, 1993.

[IV.8]   R.C.M. Mboweni, C.A. Pineda, M. Peisach and A.E. Pillay, "A PIXE study of abnormal X-rays from binary fluorides with protons in the range 0.4-2 MeV", Nucl. Instr. and Methods B85, pp. 138-141, 1994.

[IV.9]   A.E. Pillay and M. Peisach , "Development of a charge-induced X-ray fluorescence process using ion-beams: an improvement of the XSR technique", J. Radioanal. Nucl. Chem. 246, pp. 291-298, 2000.

[IV.10] A.E. Pillay and M. Peisach, "Enhanced PIXE yields from insulated metal targets", J. Radioanal. Nucl. Chem. 237, pp. 35-40, 1998.

[IV.11] A.E. Pillay, "PIXE and charge-induced X-rays (CHIX): are they complementary or competitive?", J. Radioanal. Nucl. Chem. 241, pp. 227-2259, 1999.

[IV.12] K. Traxel and A. Mandel, "Secondary electron imaging at the Heidelberg proton microprobe", Nucl. Instr. and Methods B3, pp. 594-597, 1984.

[IV.13] T. Tabata and T. Shirai, "Analytic cross sections for collisions of H^+, H_2^+, H_3^+, H, H_2 and H^- with hydrogen molecules", Atomic Data and Nuclear Data Tables 76, pp. 1-25, 2000, S.K. Allison, "Experimental results on charge-changing collisions of hydrogen and helium atoms and ions at kinetic energies above 0.2 keV", Reviews of Modern Physics 30(4), 1958.

[IV.14] E.M. Kellogg, "Ion-Gas collisions during beam acceleration", IEEE Trans. Nucl. Sci. 12, pp. 242-246, 1965.

[IV.15] Stopping-power and range tables for electrons, protons and helium ions (available at: http://www.nist.gov/physlab/data/star/index.cfm).

[IV.16] F. Folkmann, "Analytical use of ion-induced x-rays", J. Physics E8, pp. 429-437, 1975.

[IV.17] I. Brissaud, J.P. Frontier and P. Reignier, "Evaluation of depth profiling with PIXE", Nucl. Instr. and Methods B12, pp. 235-244, 1985.

[IV.18] S. Szegedi and S.M. Ibrahim, "Possible use of low voltage accelerators in PIXE analysis", Journal of Anal. and Nucl. Chem. 209(1), pp. 201-210, 1996.

[IV.19] T. Freye, H. Lorenz-Wirzba, B. Cleff, H.P. Trautvetter and C. Rolfs, "Voltage calibration of low-energy accelerators", Z. Physik A281, pp. 211-218, 1977.

– CHAPTER V –

CONCLUSIONS

In this work, a recently built particle accelerator was studied, characterized, improved and used together with a PIXE experimental set-up we developed in order to determine cross-sections for the production of X-rays induced by low energy protons in the 10-50 keV energy range. An X-ray detection system based on a large detection area GPSC filled with Ar-Xe mixtures and optimized for the detection of soft X-rays in the 0.2-2 keV energy range was designed, built and adapted to the PIXE arrangement in order to register the PIXE spectra. Moreover, this X-ray detector was also used to perform a distinct study dealing with the primary scintillation induced by 5.9 keV X-rays absorbed in gaseous Xe at atmospheric pressure. The overall experimental PIXE arrangement was used in order to obtain X-ray production cross-sections in aluminium for 15, 20 and 25 keV protons. Although the first PIXE results obtained are promising, we believe that some limitations of the particle accelerator are responsible for the lack of more accurate results.

At the time we began the works described in this dissertation, the particle accelerator we used was at a very early stage: positive ions were already produced but these were not accelerated and there was no ion selecting device. Besides, the beam current obtained so far in the reaction chamber was far from being sufficient to perform any quantitative PIXE study and the beam profile was unknown. We therefore have implemented several improvements on this set-up before using it to irradiate samples and

perform the X-ray production cross-section studies planned. We first have designed and built a Wien filter which was used to select protons. Before biasing the accelerating tube in order to accelerate these protons, we had to build a security cage for the particle accelerator. When biasing was possible, studies were carried out in order to characterize the beam dimensions and its cross-section, as well as the influence of each parameter of the ion source on it. Concerning the ion source, the electronic module associated was improved leading to improved currents measured in the reaction chamber about a thousand times larger than before. Finally, the reaction chamber was totally equipped to perform PIXE studies: beam and X-rays collimators and secondary electron suppressor grids were built and installed around a versatile sample holder which was designed in order to enable the irradiation of both thin and thick targets.

We also have built an X-ray detection system based on a Gas Proportional Scintillation Counter (GPSC) to register the PIXE spectra. Since this X-ray detector was projected and optimized for this particular application, this latter had to fulfil some requirements specific for the purpose of the present work, namely the detection of soft X-rays down to 200 eV and having a large detection area due to the very small cross-sections involved. For instance, the need of having a large radiation window forced us to instrument this GPSC with an ellipsoidal grid to delimit the absorption and scintillation regions, rather than a planar one as it is usually the case, in order to attenuate the performance degradation observed in large detection area GPSCs, resulting from solid angle variations for off-centered absorbed X-rays. In addition, since this X-ray detector was projected to detect soft X-rays induced by the interaction of the accelerated protons with targets of light elements, we decided to study its performance for Ar-Xe mixtures rather than with pure Xe as the filling gas. This decision is related to the performance deterioration observed in Xe filled GPSCs when detecting soft X-rays below 2 keV because of the loss of primary electrons to the detector window.

The potential of Ar-Xe mixtures as a GPSC filling gas was studied by characterizing relevant characteristic such as their electroluminescence yield, the excitation and ionization thresholds, the w-values and Fano factors. The detector performance was evaluated in terms of the detector gain, the energy resolution and the Peak-to-Valley Ratio (PVR). Ar-Xe mixtures were shown to be a good alternative to pure Xe as the filling gas of GPSCs.

The developed GPSC was additionally used to perform another different study, concerning the primary scintillation yield induced by X-rays in pure gaseous Xe at atmospheric pressure. In this study, we detected the primary scintillation light produced by 5.9 keV X-rays absorbed in pure gaseous Xe and quantified its intensity by comparing its signal to the one due to the secondary scintillation light yield through an averaging technique developed by us. We have demonstrated than the average energy spent to create a primary scintillation photon in gaseous Xe at atmospheric pressure, W_S, is equal to 111 ± 16 eV.

Finally, preliminary studies were conducted with the present PIXE arrangement in order to study the influence of some relevant parameters of the experimental set-up during irradiation. Afterwards, in order to determine cross-sections for X-ray production in light elements, we first have irradiated both self-supporting thin targets with thickness down to 40 nm and thin targets deposited upon a plastic substrate. Due to several experimental limitations resulting from the use of the thin films, X-ray production cross-sections results were finally obtained for aluminium by irradiating thick targets with protons in the 10-45 keV energy range and through the determination of the thick target yield curve. The first results are promising since these were shown to be in good agreement with the very few published data. However, some remaining limitations of the particle accelerator did not allow us to perform more accurate studies. We have identified those limitations and presented possible improvements aiming at eliminating these. Future work has also been suggested in order to make full use of the capabilities of the PIXE experimental set-up we developed. Some of these suggestions are already being implemented.